Bifacial Photovoltaic Performance and Optimization in Mid-to-High Latitudes

by

Erin Tonita

A thesis submitted to the University of Ottawa
in fulfillment of the thesis requirement for the degree of
Doctor of Philosophy in Physics

Ottawa, Ontario, Canada, 2025

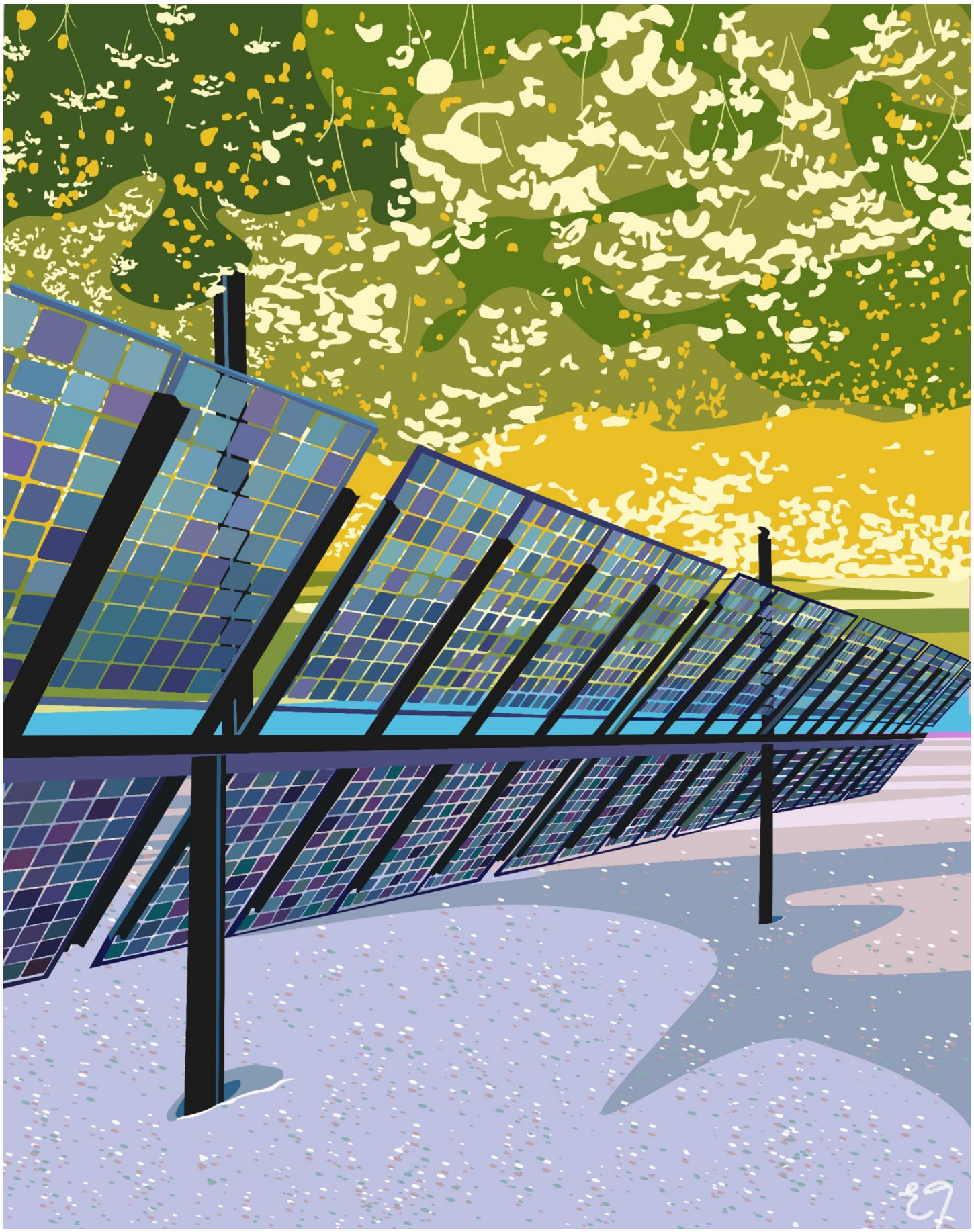

"I have scarcely touched the clay, and I am made of it"
Antonio Porchia, *Voices*.

Examining Committee Membership

The following folks served on the Examining Committee for this thesis.

Supervisor:	Karin Hinzer University Research Chair in Photonic Devices for Energy Vice-Dean, Research, Faculty of Engineering School of Electrical Engineering and Computer Science University of Ottawa
Internal Examiner:	Jean-Michel Ménard Associate Professor Department of Physics University of Ottawa
Internal Examiner:	Liang Chen Professor Department of Physics University of Ottawa
External Examiner:	John Armitage Professor Emeritus Department of Physics Carleton University
External Examiner:	Jennifer Braid Adjunct Professor Case School of Engineering Case Western Reserve University

Abstract

As early as the 1980s, photovoltaic (PV) modules have been deployed in high latitude regions to power buildings and equipment. However, it is only in recent years that significant PV deployments have begun to occur in these regions thanks to the continued drop in PV module costs. Historically, PV technologies have been deployed in low-to-mid latitude locations where solar resource is high and the economics of PV were more suitable. In these regions snowfall is rare or non-existent. This thesis supports efforts to bridge the knowledge gap between PV systems designed, operated, characterized, and modelled in low-to-mid latitudes and PV systems in high latitude, northern locations. Bifacial PV technologies are, in particular, explored due to their added benefits in regions with regular snowfall and cloud cover. The research presented in this thesis spans from the cell-level to the system-level and includes both experimental and modelling work.

One of the main challenges for PV systems in high latitudes is predicting their performance under high latitude operating conditions. This is particularly challenging for bifacial PV technologies where the added complexity of rear-side light is heavily influenced by the surrounding environment and illumination conditions. In this thesis, emerging high efficiency and high bifaciality silicon heterojunction solar cells are simulated and measured under high latitude operating conditions. A methodology for testing bifacial devices indoors that incorporates the effects of additional illumination from rear-side ground cover is developed.

Several bifacial PV system-level models are discussed and explored in this thesis for simulating mid-and-high latitude PV systems, including emerging vertical PV designs. Vertical PV systems have been deployed in recent years in smaller-scale sites ($<$1 MW) due to their suitability in high latitudes and in agri-photovoltaic applications. The effects of varied row spacing and module tilt are explored as a function of latitude, and empirical equations are developed for calculating system row spacing given deployment latitude and configuration (fixed-tilt, tracked, or vertical systems). The sensitivity of bifacial PV energy yield models to input albedo is explored via the calculation of spectral albedo mismatch as a function of latitude for 10 different ground cover scenarios, demonstrating a tendency towards increased modelling uncertainty in high latitudes.

This thesis also presents the highest latitude location model validation effort to-date at 65°N and validates five PV models for emerging vertical bifacial PV systems. Vertical PV systems are found to have higher modelling uncertainty than equator-facing fixed-tilt systems, however hourly and seasonal trends are generally well predicted by the models. Finally, the degradation of PV systems in cold, snowy climates is reviewed and new analysis is presented for four PV systems $>$60°N. PV systems deployed in cold climates tend to degrade slower than

warmer climates, which is an indication that PV systems in high latitudes may out-live their lower-latitude counterparts.

Overall, the six papers presented in this thesis support continued development of mid-to-high latitude PV and demonstrate that PV technologies can be used to provide reliable, seasonal electricity. PV systems must be designed with high latitude environmental conditions in mind, higher tolerances to uncertainty, and to meet northern energy priorities.

Acknowledgements

First of all, I would like to thank my supervisor, Prof. Karin Hinzer, for her support, honesty, insight, and many good laughs. I am very grateful to have done this degree under your supervision and feel incredibly lucky to have been a part of your lab. Thank you to Dr. Chris Valdivia for teaching me the value of tracked changes, backing up your data, and every other useful scientific skill in the grad-student handbook during my early years at SUNLAB. Thank you, Christine, for holding it all together. To all the students of SUNLAB throughout my years that have shared this special part of life with me - thank you for your curiosity, playfulness, and drive to see a better world. In particular, thank you to Annie, Mandy, and RJ for journeying through the new lands of bifacial PV with me, sharing in the tides of experimental highs and simulation lows.

Thank you to the many collaborators and researchers from other institutions who have shared wisdom, labs, and data with me. Thank you to Prof. Michael Ross and Simon Geoffroy-Gagnon for your generosity of knowledge and perspective on renewable energy in Canada's North. Thanks to Prof. Mariana Bertoni for hosting me in the DE*f*ECT Lab many moons ago and sharing samples across the border. Thank you to Michael Martinez-Szewczyk for learning the silicon heterojunction fabrication line with me, and continuing to support my research with solar cell data for many years later.

Thank you to the many folks at NREL for hosting me for 6-months this past year. Dr. Silvana Ovaitt, thank you for your generosity of spirit, fierce vision, and special power of uplifting and believing in the women around you so hard that they learn to shine in the sun. Dr. Chris Deline, thank you for welcoming me into the Reliability Group at NREL and providing last-minute tech wizardry to save all my data. Dr. Dirk Jordan, thank you for mentoring my foray in the field of degradation rate analysis and giving me the space and support for leading a rather cool project. Byron McDanold and Joshua Parker, thank you immensely for all of your field expertise. To all the other countless people who supported my exchange with their time troubleshooting high performance computers, ingesting data, helping me with paperwork, providing feedback on my test-bed designs, and hauling 80/20 and cement bricks through the mud - thank you!

Thank you to Chris Pike and Henry Toal of the Alaska Center for Energy and Power for generously sharing your test-site data, experiential knowledge, and passion for renewable energy in Alaska. It's been incredibly exciting to learn from you both.

Thank you to Dr. Ross Cheriton for supervising my part-time work in astrophotonics at the National Research Council of Canada and for sharing your passion for astronomy, tiny chips, and the magic combination of the two.

Outside of the PV world, big thank yous to: My family, for always making me feel home wherever you are. Mom, for your unending warmth, endless support, wild stories, and many phone calls & visits. The Spicy Busters, for paying their taxes consistently and on time. Fahja, for teaching me math with pennies on the kitchen floor and special relativity around the campfire. Gramps, for keeping the curiosity alive and always valuing education. Céline for generously sharing your home, relentless positivity, and (nearly) all the letters of the alphabet with me for five whole years. B, K, and W for motivating me to finally start learning French after decades of dreaming about it. H, for being the best third wheel and sharing your music. É and C, for generously sharing your francophone home with me and putting up with all my "quats", "corPs", and après/avant confusion. A, T, A, V, and J, for all the fondue nights. M, A, L, and M, for being the best neighbours. S and N, for sharing your home, many fluffy pets, board games, car, and everything else with immense kindness. L, L, and M, for your long-distance friendships that we can carry around the country. R, for our many schemes, plots, and tomfoolery. My bandmate, for all the circles we wrote during this degree. My chums, for all the usual silly nonsense and for sharing your beautiful lives with me. A, for laughing, dancing, singing, crying, pasta-flinging, gardening, and dreaming with me throughout this whole time (and also for sharing your Seattle thesis angel). And to Gavin, for being endlessly patient, supportive, and joyful, for doing the hard work of speaking exclusively French to me during the stage where I could barely say "je veux un chien", and reading 13 french children's novels with me... all this to make my proudest accomplishment of this past six years be learning a second language instead of getting this degree - ha! And, to Gavin, again, for consistently being the type of person to remind me to look at the stars.

Finally, thank you to the brave women of my past whose intelligence and strength created an environment where I could someday do something so whimsical as getting a PhD in Physics.

❄ ❄ ❄

This thesis was written on the unceded ancestral territory of the Anishinaabe Algonquin Nation.

Statement of Originality

I hereby declare that I am the sole author of this thesis. Chapters 1-3 provide background information for contextualizing my thesis research. Chapter 4 presents an original overview of high latitude environmental conditions, and broadly discusses the implications of these environmental characteristics on photovoltaics. The remaining chapters are composed of original research led by myself and either published or submitted to peer-reviewed scientific journals. Unless otherwise stated, all simulations and experiments were performed by me, alongside corresponding data analysis. Further details on the contributions of co-authors to publications are provided proceeding their placement in this thesis. Furthermore, the novelties of each publication are also provided before their placement.

All poetry and art has been created by myself, the author of this thesis, without the use of Artificial Intelligence, and has been presented in this thesis for *la joie de vivre*.

Contributions

The research presented in this thesis has led to the following publications and presentations.

Journal Articles

1. **E. M. Tonita**, D. C. Jordan, S. Ovaitt, H. Toal, K. Hinzer, C. Pike, and C. Deline, "Long-term photovoltaic system performance in cold, snowy climates," Submitted for publication August 22, 2024. Revision submitted January 13, 2025.

2. **E. M. Tonita**, S. Ovaitt, H. Toal, K. Hinzer, C. Pike, and C. Deline, "Vertical bifacial photovoltaic system model validation: study with field data, various orientations, and latitudes," Submitted for publication July 25, 2024. Revision submitted October 29, 2024.

3. **E. M. Tonita**, C. E. Valdivia, A. C. J. Russell, M. Martinez-Szewczyk, M. I. Bertoni, and K. Hinzer, "Quantifying spectral albedo effects on bifacial photovoltaic module measurements and system model predictions," *Progress in Photovoltaics: Research and Applications*, 1-13 (2023). https://doi.org/10.1002/pip.3789

4. **E. M. Tonita**, A. C. J. Russell, C. E. Valdivia, and K. Hinzer, "Optimal ground coverage ratios for tracked and fixed-tilt photovoltaic systems for latitudes up to 75°N," *Solar Energy*, 258, 8-15 (2023). https://doi.org/10.1016/j.solener.2023.04.038

5. **E. M. Tonita**, C. E. Valdivia, A. C. J. Russell, M. Martinez-Szewczyk, M. I. Bertoni, and K. Hinzer, "A general bifacial photovoltaic method to predict system performance," *Joule*, 7(1), 5-12 (2023). https://doi.org/10.1016/j.joule.2022.12.005

6. **E. M. Tonita**, C. E. Valdivia, M. Martinez-Szewczyk, M. R. Lewis, M. I. Bertoni, and K. Hinzer, "Effect of air mass on current losses in bifacial silicon heterojunction solar cells," *Solar Energy Materials and Solar Cells*, 230, 111293 (2021). https://doi.org/10.1016/j.solmat.2021.111293

Conference Proceedings

1. **E. M. Tonita**, C. E. Valdivia, K. Hinzer, "The role of spectrum in encapsulated bifacial silicon heterojunction solar cell carrier loss," *48th IEEE Photovoltaic Specialists Conference Proceedings*, (2021). https://doi.org/10.1109/PVSC43889.2021.9519009

2. **E. M. Tonita**, M. R. Lewis, C. E. Valdivia, M. I. Bertoni, and K. Hinzer, "Temperature-dependent carrier generation and recombination rates in bifacial silicon heterojunction solar cells," *OSA Advanced Photonics Congress*, (2020). https://doi.org/10.1364/PVLED.2020.PvTu2G.4

3. **E. M. Tonita**, C. E. Valdivia, and K. Hinzer, "Study of carrier transport in bifacial silicon heterojunction solar cells under high air mass illumination," *47th IEEE Photovoltaic Specialists Conference Proceedings*, (2020). https://doi.org/10.1109/PVSC45281.2020.9300663

4. M. R. Lewis, **E. M. Tonita**, C. E. Valdivia, R-J K. Obhi, M. I. Bertoni, and K. Hinzer, "Angular-dependence of bifacial silicon heterojunction solar cells for high latitudes," *46th IEEE Photovoltaic Specialists Conference Proceedings*, (2019). https://doi.org/10.1109/PVSC40753.2019.8980857

Conference Presentations & Seminars

1. **E. M. Tonita**, S. Ovaitt, H. Toal, C. Pike, K. Hinzer, and C. Deline, "Validating irradiance models for high-latitude vertical bifacial photovoltaic systems," *52nd IEEE Photovoltaic Specialists Conference (PVSC)*, Seattle, USA (2024). www.nrel.gov/docs/fy24osti/89633.pdf

2. **E. M. Tonita**, "Status of PV in Canada," *The High Latitude Photovoltaic Workshop*, Pitea, Sweden (2024). (**Invited Talk**). www.sandia.gov/app/uploads/sites/243/dlm_uploads/2024/03/3.6-TonitaErin_Canada_20240314.pdf

3. **E. M. Tonita**, D. Jordan, S. Ovaitt, H. Toal, C. Pike, K. Hinzer, and C. Deline, "Cold climate degradation: An analysis of double-axis tracked, E-W vertical, and fixed-tilt photovoltaic deployments in Alaska," *Photovoltaic Reliability Workshop (PVRW)*, Golden, Colorado (2024). www.nrel.gov/docs/fy24osti/89053.pdf

4. **E. M. Tonita**, A. C. J. Russell, C. E. Valdivia, and K. Hinzer, "Optimal row spacing for monofacial and bifacial fixed-tilt and tracked photovoltaic systems up to 75°N," *50th IEEE Photovoltaic Specialists Conference (PVSC)*, San Juan, Puerto Rico (2023).

5. **E. M. Tonita**, C. E. Valdivia, A. C. J. Russell, and K. Hinzer, "Impact of spectral versus broadband albedo on bifacial photovoltaic device models," *Photonics West*, San Francisco (2023).

6. **E. M. Tonita**, C. E. Valdivia, A. C. J. Russell, M. Martinez-Szewczyk, M. I. Bertoni, and K. Hinzer, "A general bifacial photovoltaic method to predict system performance with albedo," *PVPMC Workshop*, Salt Lake City (2022). https://pvpmc.sandia.gov/app/uploads/sites/243/2022/10/ETonita_PVPMC_2022.pdf

7. **E. M. Tonita**, C. E. Valdivia, M. Martinez-Szewczyk, M. I. Bertoni, and K. Hinzer, "Three general methods for predicting bifacial photovoltaic performance including spectral albedo," *49th IEEE Photovoltaic Specialists Conference (PVSC)*, Philadelphia (2022).

8. **E. M. Tonita**, "Solar power in a diesel-locked Arctic: mitigating greenhouse gases with bifacial photovoltaics," *Advanced Electronics and Photonics Seminar Series*, National Research Council of Canada, (2022). (**Invited Seminar**).

9. **E. M. Tonita**, C. E. Valdivia, M. I. Bertoni, and K. Hinzer, "Impact of surface texture and spectra on bifacial silicon solar cells," *Numerical Simulation of Optoelectronic Devices (NUSOD)*, Virtual (2021).

10. **E. M. Tonita**, C. E. Valdivia, K. Hinzer, "The role of spectrum in encapsulated bifacial silicon heterojunction solar cell carrier loss," *48th IEEE Photovoltaic Specialists Conference (PVSC)*, Virtual (2021).

11. **E. M. Tonita**, M. R. Lewis, C. E. Valdivia, M. I. Bertoni, and K. Hinzer, "Temperature-dependent carrier generation and recombination rates in bifacial silicon heterojunction solar cells," *Optical Society of America Advanced Photonics Congress*, Virtual (2020).

12. **E. M. Tonita**, C. E. Valdivia, and K. Hinzer, "Study of carrier transport in bifacial silicon heterojunction solar cells under high air mass illumination," *47th IEEE Photovoltaic Specialists Conference (PVSC)*, Virtual (2020).

13. **E. M. Tonita**, M. R. Lewis, C. E. Valdivia, and K. Hinzer, "High-latitude bifacial silicon heterojunction solar cell modelling," *Canadian Semiconductor Science and Technology Conference (CSSTC)*, Saskatoon, Canada (2019).

14. **E. M. Tonita**, M. R. Lewis, C. E. Valdivia, and K. Hinzer, "Optimizing bifacial silicon heterojunction solar cells for high-latitude," *Numerical Simulation of Optoelectronic Devices (NUSOD)*, Ottawa, Canada (2019).

15. **E. M. Tonita**, M. R. Lewis, C. E. Valdivia, and K. Hinzer, "Bifacial silicon heterojunction solar cells under high-latitude conditions," *Photonics North*, Quebec City, Canada (2019).

16. S. Ovaitt, D. Kern, C. Deline, S. Johnston, E. Palmiotti, **E. Tonita**, D. Jordan, and P. Hacke, "Investigating bifacial module degradation: Insights from the DuraMAT field study," *DuraMAT Webinar*, Online (2024). www.youtube.com/watch?v=XAW0ihBXLpQ

17. R-J K. Obhi, **E. M. Tonita**, M. R. Lewis, C. E. Valdivia, M. I. Bertoni, and K. Hinzer, "Angle dependent quantum efficiency measurements of bifacial silicon solar cells," *Photonics North*, Online (2020).

18. M. R. Lewis, A. C. J. Russell, **E. M. Tonita**, C. E. Valdivia, J. E. Jaysom, M. I. Bertoni, and K. Hinzer, "Impact of bifacial photovoltaic cell characteristics on module energy yield in high latitude locations," *Photonics West*, San Francisco CA (2020).

19. M. R. Lewis, C. E. Valdivia, **E. M. Tonita**, R-J K. Obhi, M. I. Bertoni, and K. Hinzer, "Effect of encapsulation bifacial silicon heterojunction solar cell operation for high latitudes," *29th International Photovoltaic Science and Engineering Conference (PVSEC)*, Xi'an, China (2019).

20. M. R. Lewis, **E. M. Tonita**, C. E. Valdivia, R-J K. Obhi, M. I. Bertoni, and K. Hinzer, "Angular-dependence of bifacial silicon heterojunction solar cells for high latitudes," *Numerical Simulation of Optoelectronic Devices (NUSOD)*, Ottawa, Canada (2019).

21. M. R. Lewis, **E. M. Tonita**, C. E. Valdivia, R-J K. Obhi, M. I. Bertoni, and K. Hinzer, "Modelling of bifacial silicon heterojunction solar cells for Arctic applications," *46th IEEE Photovoltaic Specialists Conference (PVSC)*, Chicago, USA (2019).

Other Scholarly Contributions

The following lists the scholarly contributions made during the course of this degree which are not related to the subject of this thesis.

1. **E. M. Tonita**, L. Szulakowska, J. Baxter, E. L. Flannigan, N. J. Narayanan, and J. M. Ménard, "Physics-graduate student employment in a digital world," *Physics in Canada* (2021). (Magazine article). https://pic-pac.cap.ca/index.php/Issues/showpdf/article/v77n2.0-a4166.pdf

2. **E. M. Tonita**, V. Artyshchuk, J. Weber, S. Janz, A. Densmore, S. Sivanandam, E. de Mooij, J. H. Schmid, P. Cheben, D. Xu, K. Hinzer, and R. Cheriton, "Design and testing of an on-sky astrophotonic telescope platform for on-chip instrumentation," *Proceedings of SPIE Astronomical Telescopes & Instrumentation*, (2022). (Conference Proceeding). https://doi.org/10.1117/12.2622465

3. **E. M. Tonita**, V. Artyshchuk, J. Weber, S. Janz, A. Densmore, S. Sivanandam, E. de Mooij, J. H. Schmid, P. Cheben, D. Xu, K. Hinzer, and R. Cheriton, "Design and testing of an on-sky astrophotonic telescope platform for on-chip instrumentation," *SPIE Astronomical Telescopes & Instrumentation*, Montreal (2022). (Conference Presentation). https://doi.org/10.1117/12.2619244

4. R. Cheriton, A. Densmore, **E. Tonita**, V. Artyshchuk, S. Sivanandam, J. Weber, E. de Mooij, M. Vachon, S. Wang, J. Zhang, M. Milanizadeh, O. Lardiere, K. Jackson, J. Veran, M. Saad-Bin-Alam, J. Schmid, D. Xu, P. Cheben, and J. Siegfried, "On-sky demonstration of astrophotonic CO2 correlation sensing using silicon ring resonator filters," *Proceedings of SPIE Astronomical Telescopes & Instrumentation*, (2024). (Conference Presentation). https://doi.org/10.1117/12.3020837

5. R. Cheriton, **E. Tonita**, V. Artyshchuk, A. Densmore, S. Sivanandam, E. de Mooij, P. Cheben, D. Xu, J. H. Schmid, K. Hinzer, and S. Janz, "On-sky demonstration

of astrophotonic fiber Fabry-Perot correlation spectroscopy," *Proceedings of SPIE Astronomical Telescopes & Instrumentation*, (2022). (Conference Proceeding). https://doi.org/10.1117/12.2619244

6. S. Sivanandam R. Cheriton, P. Zavyalova, P. R. Herman, E. Deibert, **E. Tonita**, V. Artyshchuk, E. de Mooij, S. Janz, and A. Densmore, "Astrophotonic solutions for spectral cross-correlation techniques," *Proceedings of SPIE Astronomical Telescopes & Instrumentation*, (2022). (Conference Proceeding). https://doi.org/10.1117/12.2629996

7. R. Cheriton, **E. M. Tonita**, V. Artyshchuk, A. Densmore, S. Sivanandam, E. de Mooij, D. Xu, J. H. Schmid, P. Cheben, and S. Janz, "Fiber Fabry-Perot filter correlation spectroscopy for real-time radial velocity determination and astrophotonic gas sensing," *Proc. SPIE PC12008, Photonic Instrumentation Engineering IX*, PC1200809 (2022). (Conference Proceeding). https://doi.org/10.1117/12.2610397

Table of Contents

Examining Committee v

Abstract vi

Acknowledgements viii

Statement of Originality x

List of Figures xix

List of Tables xxii

List of Abbreviations xxiii

List of Symbols xxvi

1 Introduction 1

1.1 Thesis outline 8

2 Physics of semiconductors & solar cells 10

2.1 Semiconductor materials 11

2.1.1 Crystal and energy band structure 12

2.1.2 Density of states 14

2.1.3 Carrier concentration . . . 15
2.1.4 Conductivity and mobility . . . 18
2.1.5 Drift and diffusion . . . 19
2.1.6 Generation and recombination . . . 20
2.1.7 The transport equations . . . 24
2.1.8 Optical properties . . . 24
2.2 Photovoltaic energy conversion . . . 25
2.2.1 p-n junctions . . . 25
2.2.2 Current-voltage characteristics . . . 28
2.3 Light trapping . . . 32
2.4 Efficiency limits . . . 33
2.5 Solar resource . . . 35
2.5.1 Irradiance components . . . 36
2.5.2 Albedo . . . 37
2.6 Drift-diffusion modelling . . . 38

3 Fundamentals of bifacial photovoltaics **43**
3.1 Solar cell design . . . 45
3.2 Module design . . . 47
3.3 System design . . . 48
3.4 System modelling . . . 50
3.4.1 Sky models . . . 51
3.4.2 Irradiance transposition models . . . 51
3.4.3 Electrical models . . . 54
3.4.4 Select bifacial photovoltaic models . . . 55

4 High latitude environmental conditions **60**

4.1 Available solar resource 61

4.2 Ambient temperature 65

4.3 Snow 67

4.4 Impact on system design & performance 69

5 Bifacial photovoltaic cell characterization & measurement **75**

5.1 Effect of air mass on current losses in bifacial silicon heterojunction solar cells . 75

5.2 A bifacial photovoltaic device measurement method incorporating albedo . . . 87

6 Latitude trends for bifacial photovoltaic systems **103**

6.1 Ground coverage ratios for tracked and fixed-tilt photovoltaic systems for latitudes up to 75°N 103

6.2 Effect of spectral albedo on bifacial photovoltaic module measurements and system model predictions 118

6.3 Vertical bifacial photovoltaic system model validation 133

6.4 Long-term photovoltaic system performance in cold, snowy climates 147

7 Summary & outlook **168**

References **172**

Glossary **192**

List of Figures

1.1 Renewable energy mix in northern countries . . . 2
1.2 Photovoltaic deployment trends and projections . . . 4
1.3 Historic emissions and electricity mix in Canada . . . 6
1.4 Electricity emissions, PV potential, and installed PV capacity across Canada . 7

2.1 Diamond lattice, zincblende lattice, and the first Brillouin zone . . . 12
2.2 Detailed and simplified energy band structures of silicon and GaAs . . . 13
2.3 Fermi-Dirac distribution and density of states functions for conduction and valence bands . . . 15
2.4 Energy band diagrams and number densities of electrons and holes in intrinsic and doped semiconductors . . . 17
2.5 Energy band diagram of an intrinsic semiconductor under a voltage bias . . . 18
2.6 A schematic of photogeneration and thermalization alongside recombination mechanisms of radiative, SRH, Auger, and surface recombination. . . . 21
2.7 The formation of a p-n junction . . . 26
2.8 p-n junction behaviour at short-circuit, maximum power, and open-circuit . . . 27
2.9 Internal quantum efficiency, external quantum efficiency, and spectral responsivitiy 29
2.10 I-V curve with important points labelled . . . 30
2.11 Equivalent circuit of a solar cell with parasitic resistances . . . 31
2.12 Effect of illumination intensity and temperature on I-V curves and EQE . . . 32
2.13 Example ray paths for different textured surfaces . . . 33

2.14 The single-junction solar cell detailed balance efficiency limit 34
2.15 The standard solar spectrum and varied air masses 35
2.16 Components of solar irradiance: DNI, DHI, and GHI 37
2.17 Example albedometer 38
2.18 Spectral and broadband albedos for select ground conditions 39
2.19 Workflow of Sentaurus tools and input and output files 40
2.20 A schematic workflow of Sentaurus drift-diffusion modelling for textured bifacial solar cells. 42

3.1 Irradiance sources for bifacial PV systems. 44
3.2 A schematic of common monofacial and bifacial silicon solar cell designs . . . 46
3.3 Module components and layers for monofacial and bifacial modules. 47
3.4 Diagram showing how PV cells get packaged into modules which then become deployed PV systems. Bypass diodes are shown above the module for illustrative purposes. 48
3.5 Schematic diagram of various portrait and landscape PV mounting architectures, with varying tier number. 48
3.6 Common PV system configurations 49
3.7 Example clear-sky day PV production curves 50
3.8 A schematic of the Perez sky model with beam irradiance, circumsolar irradiance, isotropic diffuse irradiance, and horizon brightening effects labelled. 52
3.9 View factor, ray tracing, and finite-element methodologies for irradiance transposition 53
3.10 Schematic workflow of DUET 59

4.1 Annual solar resource latitude trends 61
4.2 Monthly trends for GHI, ambient temperature, and albedo 62
4.3 Average monthly map of the northern hemisphere for solar insolation, surface temperature, and albedo 63
4.4 Sun position trends as a function of latitude 64

4.5 Latitude trends for diffuse fraction and air mass 65
4.6 Annual average ambient temperature latitude trends 66
4.7 Annual average albedo latitude trends 67
4.8 Example photovoltaic systems deployed in high latitude regions 68
4.9 Visual summary of key technical impacts of northern environmental conditions on photovoltaic systems 69
4.10 Annual cumulative plane-of-array insolation at different latitudes 70
4.11 Annual plane-of-array insolation relative to south-facing fixed-tilt PV systems as a function of deployment latitude. 71
4.12 Monthly plane-of-array insolation at different latitudes 72
4.13 Imags of snow shedding patterns 73
4.14 Distribution of module operating temperature in Alaska and an example efficiency temperature coefficient 74

List of Tables

3.1 Bifaciality of select modern silicon solar cell technologies. 46
3.2 Bifacial photovoltaic models. 56

List of Abbreviations

a-Si:H hydrogenated amorphous silicon 46, 76, 77

ACEP Alaska Center for Energy and Power 8, 134, 135, 149

Al-BSF aluminium back surface field 5, 45, 46

AM air mass 36, 64, 65

ARC anti-reflection coating 32, 45

CdTe cadmium telluride 119

CWEC Canadian Weather-year for Energy Calculation 49

DAT double-axis tracker 49, 50

DHI diffuse horizontal irradiance 36, 51, 61, 64

DNI direct normal irradiance 36, 37, 51, 61

DOS density of states 14, 15

DUET Dual-sided Energy Tracer 49, 51, 55–58, 88, 105, 119, 133, 134, 169

EQE external quantum efficiency 28, 31, 39, 77, 119

EVA ethylene-vinyl acetate 47

FCC face-centered cubic 12, 13

FF fill factor 30

GaAs gallium arsenide 13, 35, 119

GCR ground coverage ratio 104

GHG greenhouse gas 6

GHI global horizontal irradiance 36, 37, 51, 52, 61, 64, 65, 72

HIT heterojunction with intrinsic thin-layer 46

IBC interdigitated back-contact 5

IEC International Electrotechnical Commission 44, 87, 88, 169

IQE internal quantum efficiency 28

IR infrared 35, 36, 65

ITO indium tin oxide 76, 77

ITRPV International Technology Roadmap for Photovoltaics 5

NOCT nominal operating temperature 54, 58

NREL National Renewable Energy Laboratory 3, 5, 8, 9, 56, 57, 134, 135, 149

NSRDB National Solar Radiation Database 61, 65

PERC passivated emitter rear-contact 5, 45, 46, 148

PLR performance loss rate 147, 170

POE polyolefin elastomer 47

PV photovoltaic 1–9, 25, 30–33, 36–38, 44, 45, 47–58, 60, 69–74, 76, 87, 88, 103, 104, 118, 133, 134, 147–149, 168–170

PVCZ Photovoltaic Climate Zone 147, 148

RMSE root-mean-square error 133, 134, 170

SAM the System Advisor Model 52, 56, 57, 70, 72, 133, 134, 169

SAT single-axis tracker 49, 50, 70, 87, 103, 104, 169

SHJ silicon heterojunction 5, 9, 46, 73, 76, 77, 88, 118, 119, 148, 168

SMARTS Simple Model of the Atmospheric Radiative Transfer of Sunshine 38

SRH Shockley-Read-Hall 22, 23

SRI Scaled Rear Irradiance 87, 88, 118

STC Standard Test Conditions 44, 55, 57

TCAD technology computer-aided design 38

TCO transparent conducting oxide 46

TMM transfer matrix method 41

TMY typical meteorological year 49, 58, 61, 65–67, 70, 72

TOPCon tunnel oxide passivated contact 5, 46

UV ultraviolet 35, 60, 65, 168

VF view factor 51, 56

List of Symbols

A Area. 31

B_{rad} Radiative recombination coefficient. 21

$\mathcal{B}$ Bifacial gain. 44

C_{aug} Auger recombination coefficient. 22

D_n Diffusion coefficient for electrons. 20, 23

D_p Diffusion coefficient for holes. 20, 23

E_{fn} Quasi-Fermi level for electrons. 17, 18, 28

E_{fp} Quasi-Fermi level for holes. 17, 18, 28

E_i Fermi level. 16, 17

E_c Conduction band energy. 13–15

E_f Fermi-level energy. 15, 16, 18

E_g Bandgap energy. 13, 34

E_v Valence band energy. 13, 14

E Energy. 14

G_n Total electron generation rate. 24

G Irradiance. 54

J_0 Dark saturation current density. 29, 34

J_{dark} Dark current density. 31

$J_{diffusion}$ Diffusion current density. 19

J_{drift} Drift current density. 19

J_{mp} Current at maximum power. 30

J_n Current density of electrons. 24

J_{sc} Short-circuit current. 28, 34

J Current density. 19

L_n Electron diffusion length. 23

L_p Hole diffusion length. 23

N_a Density of ionized acceptors. 17, 26, 27

N_c Effective density of states for the conduction band. 16

N_d Density of ionized donors. 17, 26, 27

N_s Surface trap density in cm^{-2}. 23

N_v Effective density of states for the valence band. 16

P_{inc} Incident power. 31

P_{rated} Nameplate power rating of a PV module. 55

P_{mp} Maximum power. 30

P Power. 30

R_{aug} Auger recombination rate. 22

R_{rad} Radiative recombination rate. 21

R_{sh} Shunt resistance. 31

R_{SRH} SRH recombination rate. 22

R_{surf} Surface recombination rate. 23

R_s Series resistance. 31

$\mathcal{R}$ Reflectivity. 28

R_n Total electron recombination rate. 24

R Reflection coefficient. 25

S Surface recombination velocity. 23

T_{amb} Ambient temperature. 54

T_{cell} Cell temperature. 54

T_{mod} Module temperature. 54

T_{NOCT} Nominal operating temperature. 54

$\mathcal{T}$ Transmittance. 28

T Temperature. 15, 34

U_0 Constant heat transfer coefficient of the Faiman model. 54

U_1 Convective heat transfer coefficient of the Faiman model. 54

V_{bi} Built-in potential. 27

V_{mp} Voltage at maximum power. 30

V_{oc} Open-circuit voltage. 31

V Voltage. 17

a_{bb} Broadband albedo. 38

$A(\lambda)$ Spectral albedo. 38

a Albedo. 37

α Absorption coefficient. 25

$\Delta\mu$ Difference in electron and hole quasi-Fermi levels. 17

∇n Concentration gradient for electrons. 20

∇p Concentration gradient for holes. 20

γ Temperature coefficient for efficiency. 55

η Power conversion efficiency. 30

$\mathbf{E}$ Electric field. 19, 24

ϵ_s Static dielectric constant. 24, 27

EY_{bi} Bifacial energy yield. 44

EY_{mo} Monofacial energy yield. 44

$f(E)$ The Fermi-Dirac distribution function. 15, 16

$g(E)$ density of states. 14, 15

GUI Upwelling irradiance from the ground. 37

$\hbar$ Plank's constant. 14

k_B Boltzmann constant. 15

κ Extinction coefficient. 25

m^* Effective mass. 14

$\mu_{carrier}$ Mobility limited by carrier-carrier scattering processes. 19

μ_{defect} Mobility limited by defect scattering processes. 19

μ_{doping} Mobility limited by ionized impurity scattering processes. 19

μ_n Electron mobility. 18, 20

μ_{phonon} Mobility limited by phonon scattering processes. 19

μ_p Hole mobility. 18, 20

m Ideality factor. 29

n_0 Electron number density in equilibrium. 20

n_i Intrinsic carrier density. 16, 17

n_r Real part of the complex index of refraction. 25

n_s Electron number density at the surface of a material. 23

n_t Electron number density when the Fermi level is equal to the energy of a trap state, t. 22

$\tilde{n}$ Complex index of refraction. 24

n Electron number density. 15, 16, 18

p_0 Hole number density in equilibrium. 20

p_s Hole number density at the surface of a material. 23

p_t Hole number density when the Fermi level is equal to the energy of a trap state, t. 22

$\Phi_p(E)$ Photon flux. 28

φ_{Jsc} Short-circuit current bifaciality coefficient. 44

φ_{Pmp} Maximum power point bifaciality coefficient. 44, 45

φ_{Voc} Open-circuit voltage bifaciality coefficient. 44

ϕ Electrostatic potential. 24

p Hole number density. 15, 16, 18

q Elementary charge. 18, 27

SR Spectral response. 28

$\tau_{rad,n}$ Radiative minority carrier lifetime in an p-doped semiconductor. 21

$\tau_{rad,p}$ Radiative minority carrier lifetime in an n-doped semiconductor. 21

τ_{SRH} SRH minority carrier lifetime. 22

θ_c Spectral response. 32

t Time. 24

v_T Thermal surface velocity. 23

v_w Wind speed. 54

v Drift velocity. 19

Φ Work function. 25

λ Wavelength. 25, 28

ω_{scr} Total width of the space charge region. 27

Ω Capture cross section in cm^2. 23

Chapter 1

Introduction

For the world to reach net-zero
We need renewables in the North.
Solar energy could be one hero
This thesis follows henceforth.

.

Sunlight is abundant
(At least for half of the year).
Research in this field is not redundant
And PV performance is not so clear.

.

Thus in this work, we seek out answers
For how to solar power northern nations.
We show bifacial & vertical PV are enhancers
For future decarbonizations.

❄ ❄ ❄

During the course of this PhD, global installed solar photovoltaic (PV) capacity grew from $\sim$500 GW to $>$1.6 TW, more than doubling all previous cumulative installed capacity and beginning the terawatt age of PV [1]. PV technologies are poised to reach between 30-70 TW of installed capacity by 2050 under net-zero 2050 pathways [2]. To achieve this large growth in PV capacity, PV modules must be deployed across the world, on the utility-scale.

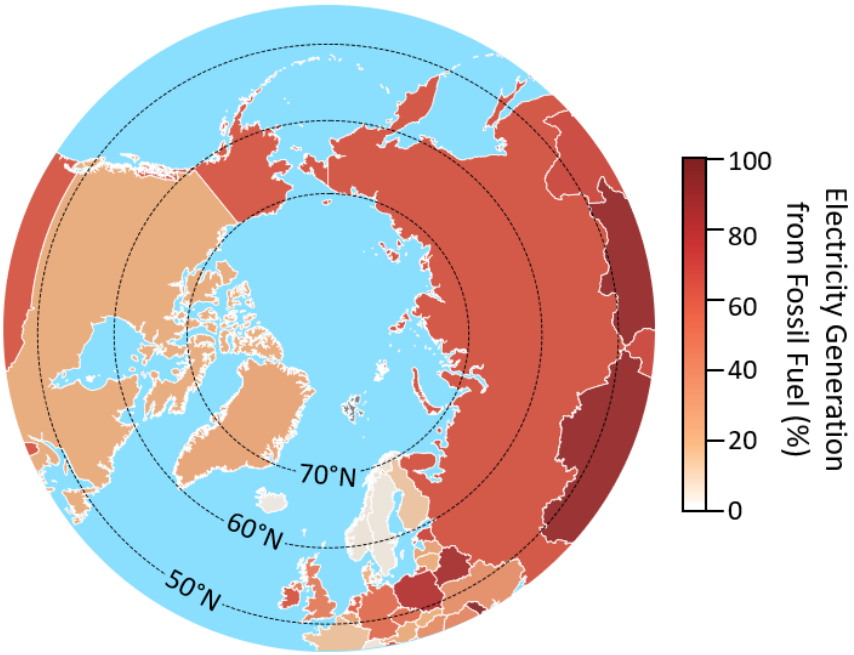

Figure 1.1: The percentage of electricity generation per country which comes from coal, oil, or gas. Country values for 2021, as compiled from the International Energy Agency [6].

Photovoltaics in High Latitudes

PV technologies have been deployed in high latitude, northern locations to power equipment and buildings as early as the 1980s [3, 4]. However, significant development in high latitudes have been limited in the past due to the prohibitively high cost of solar modules. With the dropping costs of PV modules, PV is now one of the cheapest forms of available electricity in most areas of the world [5] and may be deployed in markets previously unavailable, such as high latitude and cold climate regions.

Here, I consider Canada as a whole to be a "high latitude" country from the perspective of historic deployments of PV, with most PV deployments in North America occurring along coastal regions in the USA. Northern latitudes are primarily the focus of this thesis due to the local geography of the author (being Ottawa, Canada) and limited populated land mass near the South Pole. However, research conducted in northern high latitudes will naturally apply to other regions in the southern hemisphere which also experience regular snowfall and cold temperatures.

The need in the North is not negligible. Figure 1.1 shows the percentage of electricity that

was generated in 2021 using fossil fuels per country [6]. To achieve net-zero electricity grids by 2050, a rapid ramp in northern renewable deployments must occur over the next few decades.

The cold climate PV industry is relatively young, especially given module lifetimes are between 25-30 years and long-duration knowledge of PV performance in the field is limited. Research is required to know how to optimize and adapt PV deployments for northern environmental conditions, electricity grids, and energy priorities. Despite renewable energy leadership in the Nordics and Iceland, the solar industry in these countries is still in its early years to meet the growing needs caused by electrification [7, 8]. Best practices for PV in cold climates are still in the process of being developed, tested, and refined.

Current research fields for PV in high latitude locations include research on the interaction between PV arrays and snow, frost, ice, and permafrost [9–12]; the integration of PV with agricultural practices ("agri-PV") [13, 14], into building design [15, 16], and hybrid diesel microgrids [17–22]; the environmental impacts of PV on sensitive and precious northern ecosystems [23, 24]; socioeconomic impacts [25, 26]; the long-term reliability of PV under frequent and harsh seasonal cycling [3, 4, 27–33]; and best practices for mounting, operation, and maintenance [34–37].

In this thesis, the characterization and optimization of PV solar cells and systems is discussed under northern environmental conditions. Chapter 4 provides a detailed overview of high latitude environmental conditions and the impact these unique conditions have on PV system design, while Chapters 5 and Chapter 6 present original research on the characterization and optimization of mid-to-high latitude PV. In Chapter 6, original research is also presented on PV system-level model uncertainty and validation in high latitudes, and an analysis and review of PV degradation rates in cold climates is presented. A detailed thesis outline is provided in Section 1.1 at the end of this chapter.

Deployment trends

The dropping costs of PV modules was mentioned above as one of the main drivers for increased PV deployments in high latitude locations. Figure 1.2 shows the PV module price learning curve between 1976 and 2018, historic record silicon solar cell and module efficiencies, solar cell technology trends, and trends in the location of PV deployments.

The "learning curve" presented in Fig. 1.2A, shows that the average cost of PV has been decreasing by 28% per doubling of the installed capacity [38]. Depending on the analysis time period, the PV learning curve has been reported as between 20-29% [43].

Fig. 1.2B shows the historic record efficiencies for single-junction crystalline silicon solar cells and modules, taken from the National Renewable Energy Laboratory (NREL) record efficiency

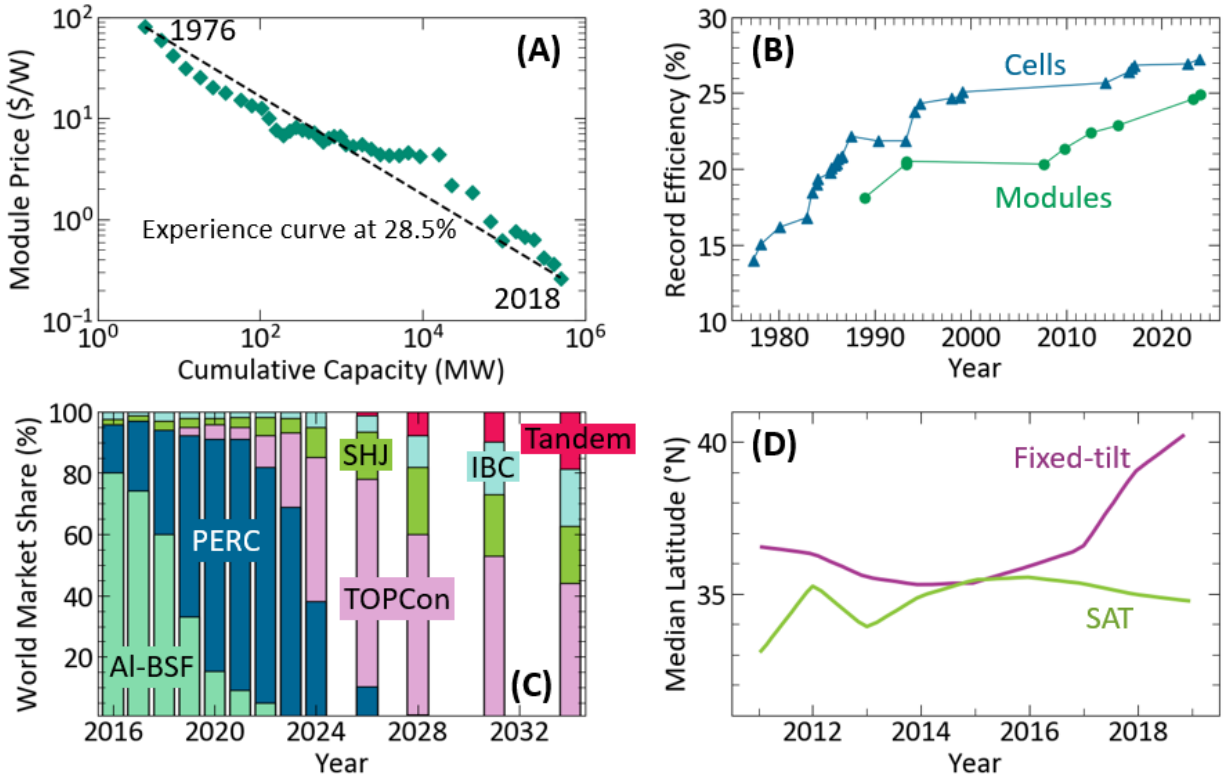

Figure 1.2: (A) PV module cost learning curve, from Ref. [38]. (B) Record historic silicon single-junction solar cell and module efficiencies, from Ref. [39]. (C) Historic [40] and projected [41] GW-manufacturing scale solar cell technology trends, showing Al-BSF, PERC, TOPCon, SHJ, IBC, and silicon-based tandem technologies. (D) Median latitude of 736 utility-scale PV plants in the continental USA from Ref. [42]. PV plants are separated into fixed-tilt (non-tracking) and and single-axis trackers (SAT) and by the year where the PV plant began commercial operation.

charts [39]. Record cell efficiencies are now around 27% while modules are 25%. These increased efficiencies in time are a result of technological advancements in silicon solar cell design. Fig. 1.2C shows the historic and projected trends in solar cell design, with values from the International Technology Roadmap for Photovoltaics (ITRPV) [40, 41]. Aluminium back surface field (Al-BSF) technologies have now been phased out in favour of passivated emitter rear-contact (PERC) cells. N-type solar cell technologies of tunnel oxide passivated contact (TOPCon) and silicon heterojunction (SHJ) design are anticipated to grow and overcome PERC popularity in upcoming years. Interdigitated back-contact (IBC) cells are expected to grow to a lesser extent due to their increased complexity [41]. Tandem cells using silicon as a bottom junction are expected to begin to grow on the market over the next decade, due to their ability to overcome the 1-junction efficiency limit, described in Section 2.4 of this thesis. Common silicon solar cell designs, such as PERC, TOPCon, and SHJ are described in more detail in Section 3.1.

Bifacial photovoltaics - PV cells and modules which produce electricity from photons absorbed from both front and rear sides - are significantly growing in world market share compared to traditional single-sided monofacial designs. Bifacial PV is further described in this thesis in Chapter 3. Bifacial cells are expected to compose 90% of all manufactured solar cells this year (2024) [41] and NREL estimates that 50-75% of all installations in 2022 were bifacial [44]. Bifacial benefits have been shown to tend to increase with latitude [45–48], making them a promising technology choice for installations in cold climates. Further details can be found in Section 4.4.

Fig. 1.2D shows deployment location latitude trends, as digitized from Ref. [42]. In this work, Bolinger *et al.* examined the centroid latitude of 736 utility-scale PV plants which began commercial operation between 2007 and 2019 in the USA, representing >90% of the US utility-scale PV fleet. Since 2015, the median latitude of fixed-tilt PV deployments has been rising, demonstrating a recent northward trend in PV deployments, and highlighting the importance of this research field.

Photovoltaics in Canada

The northern country and home of this thesis' author, Canada, generates ∼20% of its electricity using fossil fuel resources, leading to around ∼80 Mt of CO_{2e} emissions per year [49], as visualized in Figure 1.3. Further renewable energy developments are required to reach net-zero emission goals and to fulfill projected energy requirements given an electrifying world.

Fossil fuel consumption varies across Canada. Figure 1.4 shows electricity and PV trends across the 10 provinces and 3 northern territories of Canada. Fig. 1.4A shows the annual total

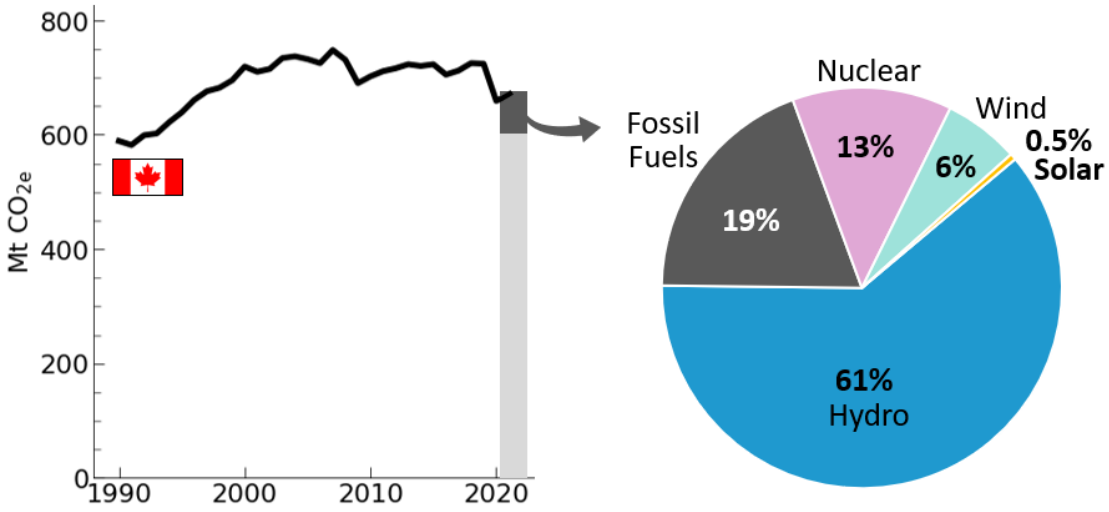

Figure 1.3: Historic emissions and electricity mix in Canada. Historic data is from Ref. [49], while electricity mix data is from Ref. [50] for 2022.

electricity emissions per province and territory in 2020, highlighting high emissions particularly in the prairie provinces of Alberta and Saskatchewan [51]. When examining the greenhouse gas (GHG) intensity of electricity generation throughout Canada (Fig. 1.4B) [51], regions with lower population and high fossil fuel consumption are also highlighted, showing high emissions intensity in the northern territories and some regions of Atlantic Canada.

Natural Resources Canada has calculated the annual PV potential - or predicted annual energy yield per installed capacity - for monofacial latitude-tilt fixed-tilt PV arrays across Canada [52, 54]. This data is reproduced in Fig. 1.4C. This analysis highlights the potential for PV technologies to offset CO_2 emissions particularly in the Canadian prairies where electricity emission intensity is high. It also highlights that there are many regions in northern Canada where PV potential is $>$1000 kWh/kWp. PV electricity generation can be improved compared to these values yet by using high-efficiency bifacial modules and optimizing PV system designs for high latitude environments. The impact of design choices, such as these, on PV potential is presented in Section 6.4.

Fig. 1.4D shows the reported installed capacity of PV across Canada in 2022, according to the Canadian Renewable Energy Association [53]. Installed capacity across Canada grew by 26% from 2021 to 2022 to a total capacity in Canada of $\sim$4 GW. In the past, most PV deployments occurred in Ontario due to government incentives, however in recent years much of the development has shifted to Alberta where solar resource is particularly high. In 2022, $\frac{3}{4}$ of new renewable energy projects in Canada were in Alberta [53]. Significant development

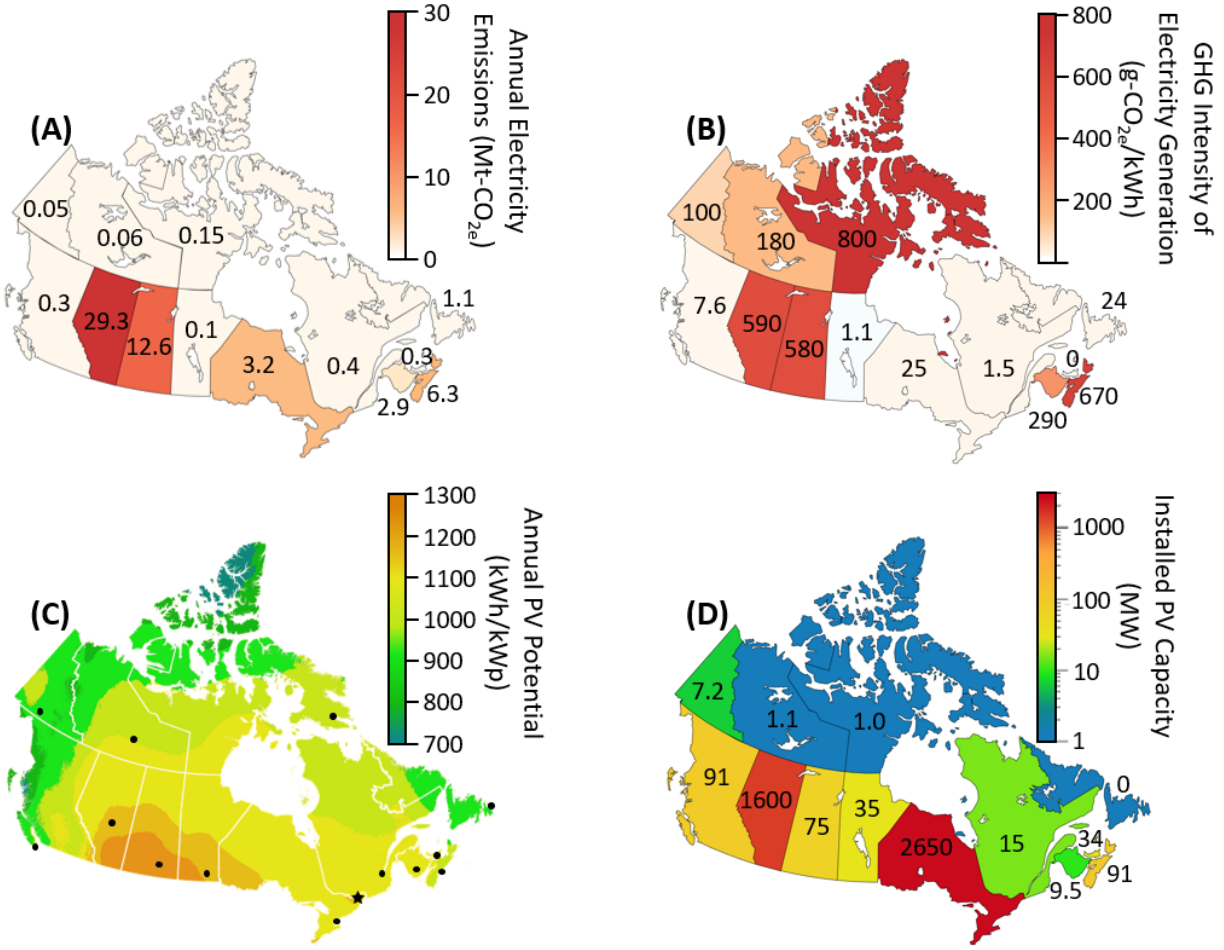

Figure 1.4: (A) Annual electricity emissions, and (B) the intensity of electricity generation greenhouse gas emissions across Canada. Reported numbers are for 2020 from the Canada Energy Regulator [51]. (C) The calculated annual PV potential for latitude-tilt fixed-tilt PV across Canada, adapted from Natural Resources Canada [52]. Dots correspond to capital cities, while the star is Ottawa, the nation's capital. (D) Installed PV capacity in Canada as of 2022, according to the Canadian Renewable Energy Association [53].

of PV in the northern territories of Canada is also underway, particularly in the Yukon where 7.2 MW of PV capacity is installed with at least 5.5 MW of further development in the planning and proposal stage. The main objective of this thesis is to help support further PV development in cold climates by modelling, analyzing, and characterizing PV performance under the high latitude operating conditions found throughout Canada and beyond.

1.1 Thesis outline

This thesis is composed of seven chapters and has been written in a 'thesis-by-papers' style. All figures in all chapters of this thesis have been made by the author of this thesis. Chapters 2 and 3 provide background information supporting this thesis work, with Chapter 2 presenting background information relevant to photovoltaic cells and Chapter 3 presenting background information relevant to photovoltaic systems. Chapter 4 analyzes high latitude environmental conditions and summarizes their impact on system design, while Chapter 5 and Chapter 6 introduce and reproduce the journal articles of this thesis. Six lead-author journal articles are included in this thesis. The contributions of each co-author are stated at the beginning of each publication. The novelties of each publication are summarized before their placement in this thesis.

The methodologies used throughout this thesis differ, depending on the approach of the publication. Generally, the scientific method has been used and statistical analysis has been conducted on modelled and measured data. The models used in this thesis have been validated against measurements conducted using calibrated equipment. Field data in test-sites have been well-instrumented and documented, and any short-comings in data quality have been discussed in their associated publications. The work presented in this thesis has been done in collaboration with other research institutes well established in the PV community - Arizona State University, NREL, and the Alaska Center for Energy and Power (ACEP).

Chapter 2 walks through the background physics necessary to understand the research presented in this thesis, covering semiconducting material principles, the photovoltaic effect, solar resource on Earth, and drift-diffusion cell-level modelling.

Chapter 3 introduces bifacial photovoltaic solar cells, modules, and systems. This chapter also introduces common sky, optical, and electrical models for predicting the performance of PV systems. The PV system-level modelling platforms used in journal articles (Section 5.2, Section 6.1, Section 6.2, Section 6.3, Section 6.4) are presented and compared.

Chapter 4 provides a deeper overview of the physical environmental conditions present in high latitude locations, presenting original analysis on annual and seasonal trends in solar

resource, ambient temperature, and snowfall. Sections 4.1, 4.2, and 4.3 are the first-draft contribution to a greater review paper covering the perspective of PV in high latitudes. This section was written by myself, the author of this thesis. However, future versions of this section will be reviewed by paper collaborators and incorporated into a collaborative paper. As our manuscript is still in the early draft stages, the author-list and title is still pending. Section 4.4 summarizes some key technical take-aways for PV in high latitudes, and links these take-aways to the research articles presented in the subsequent chapters.

Chapter 5 presents two published journal articles on the characterization of bifacial PV devices. Section 5.1 presents an article published in *Solar Energy Materials and Solar Cells* on the effect of air mass on carrier transport in bifacial SHJ solar cells. Section 5.2 presents a commentary published in *Joule*, speculating on an extension to indoor bifacial solar cell measurement method standards which incorporates the effects of albedo.

Chapter 6 presents two published journal articles and two submitted manuscripts on PV system-level trends with latitude. Section 6.1 presents an article published in *Solar Energy* on the optimization of row spacing and tilt for bifacial PV systems as a function of latitude. Section 6.2 presents an article published in *Progress in Photovoltaics: Research and Applications* on spectral mismatch factors for bifacial PV systems in high latitudes. Section 6.3 presents a submitted manuscript (July 2024) on validating bifacial PV system models for vertical systems and in a high latitude location. This work was completed during a 6-month internship to NREL. Section 6.4 presents the final manuscript of this thesis, submitted for publication in August of 2024. This manuscript analyzes and reviews degradation rates of PV systems located in cold, snowy climates.

Chapter 7 summarizes the thesis as a whole and discusses the future outlook of PV in northern environments.

Chapter 2

Physics of semiconductors & solar cells

Solar power arises
From the photovoltaic effect.
With sufficient photon-energy sizes
One finds excited electrons to collect!

❄ ❄ ❄

Photovoltaic devices operate on the photovoltaic effect, where photons absorbed into semiconducting materials result in the excitation of electrons to higher energy states. This charge separation results in an increase in electric potential, or voltage, which can then be used to do work when connected in an electrical circuit. This effect was first discovered in 1839 by Edmond Becquerel, with observations of an electrochemical cell increasing in voltage when exposed to sunlight [55]. The first photovoltaic cell was produced in 1883 using molten selenium and a thin layer of gold [56], but it wasn't until 1954 that the first photovoltaic cell with an efficiency $>1\%$ was produced by Daryl Chapin, Calvin Fuller, and Gerald Pearson of Bell Laboratories [57].

In order to understand the underlying properties of photovoltaic devices that lead to efficiencies $>20\%$ today, it is first necessary to understand the underlying atomic properties of the materials which give rise to the photovoltaic effect. To do this, we must understand the nature of semiconducting materials. As silicon-based devices are the focus of this thesis work, emphasis will be given to silicon semiconductors and photovoltaic devices. Silicon is the most commonly used semiconductor on Earth due to its natural abundance, low cost, and stability.

2.1 Semiconductor materials

Semiconducting materials are a class of materials with properties between that of conductors and insulators. The conductive properties of semiconductors are highly tunable, making them attractive materials for electronic and photonic device applications.

The distinction between semiconductors, conductors, and insulators lies in their electronic band structure. In solid materials, atoms are arranged in dense crystalline structures with single-atom electronic energy levels overlapping and hybridizing into large-scale continuous bands of energy levels. In this band structure, conduction band states refer to the collection of delocalized states that allow for flow of electrons throughout the material. Valence band states are the collection of highly localized states around atomic nuclei, which inhibits valence electronic movement. The bandgap of a material is defined as the difference in energy between the highest valence band energy level and the lowest conduction band energy level, and the Fermi level of the material is defined as the energy level where electrons have a 50% probability of occupation.

In conductors, the conduction band state is populated with free electrons without external excitation, resulting in a Fermi level occurring within or at the conduction band edge. These materials are sometimes described as having a zero or negative bandgap.

Semiconductors, on the other hand, have a positive, non-zero bandgap of usually $<$3 eV. When electrons are excited, for example by photon absorption, they may be excited from the occupied valence band into unoccupied conduction band states, allowing for electron flow throughout the material. The density of electrons in the conduction band of a semiconductor is usually less than 10^{20} cm^{-3}, whereas conductive materials have electron densities on the order of 10^{23} cm^{-3} [58].

Like semiconductors, insulators have zones of forbidden energy states defined by the bandgap of the material. However, for insulators the bandgaps are so large ($>$3 eV) that this energy barrier is improbable to be overcome under normal operating conditions. Thus, insulators have a negligible density of charge carriers in the conduction band. Insulators can become semiconducting if sufficient excitation conditions are present, and common semiconducting materials can exhibit insulating properties when insufficient excitation conditions are present [58].

In the following subsections, some physical properties of semiconducting materials relevant to photovoltaic devices are described. Much of this work is adapted and inspired by Jenny Nelson's *The Physics of Solar Cells* [59] and the PhD thesis of Meghan Beattie [60].

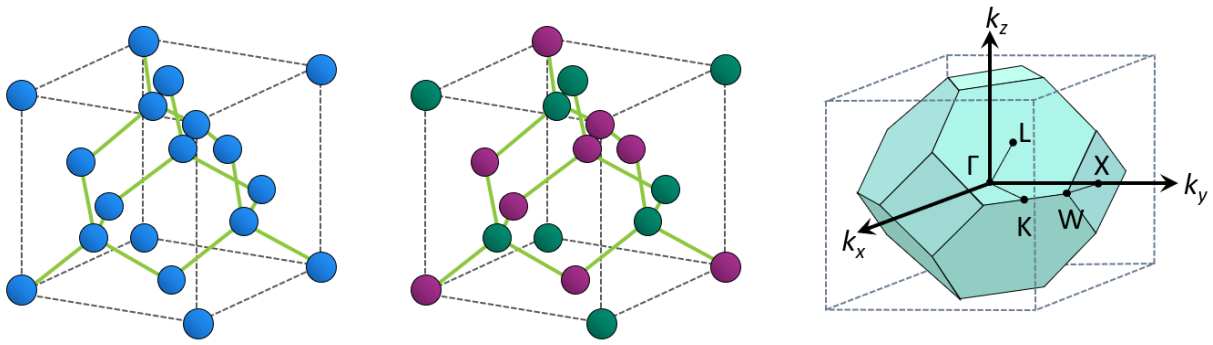

(A) Diamond lattice **(B)** Zincblende lattice **(C)** First Brillouin zone

Figure 2.1: (A) Real-space diamond cubic lattice structure, (B) real-space zincblende cubic lattice structure, and (C) the first Brillouin zone in k-space for both FCC lattices.

2.1.1 Crystal and energy band structure

Semiconductor materials are comprised of atoms held together in crystalline structures with covalent bonds. In a perfect crystal, the atomic lattice is highly uniform and periodic over long-range distances. Sub-optimal growing conditions can result in multi-crystalline or amorphous semiconductors, exhibiting crystalline order on medium to short-range scales.

The most common method for crystal growth of silicon is the Czochralski process [61]. In the Czochralski process a silicon seed crystal is dipped into a crucible of hot, molten silicon and then slowly withdrawn and rotated to the surface. Liquid silicon crystallizes to the seed and gradually forms a large, cylindrical crystal. Dopants, such as boron or phosphorus, may be added to the crucible during growth to alter the electrical properties of the silicon crystal [61]. The large silicon crystal is then typically sliced into flat, thin sheets and polished to remove defects and surface impurities.

Figure 2.1 demonstrates two common crystalline structures found in semiconducting materials. Group IV semiconductors such as silicon (Si) and germanium (Ge) form diamond cubic lattice structures with each atom bonded covalently to its four nearest neighbours, as provided in Fig. 2.1A. Semiconductors made from elements in group III and group V of the periodic table (or, III-V semiconductors), instead form into zincblende cubic lattices, as depicted in Fig. 2.1B. The same underlying intersecting face-centered cubic (FCC) lattice is present in both structures, but with the two FCC lattices being either the same atoms (as in the case of silicon) or distinct atoms (for III-V materials).

The periodic nature of the underlying atomic structure of semiconductor crystals (Fig. 2.1A/B) can be described in momentum space (k-space) by taking the Fourier transform of

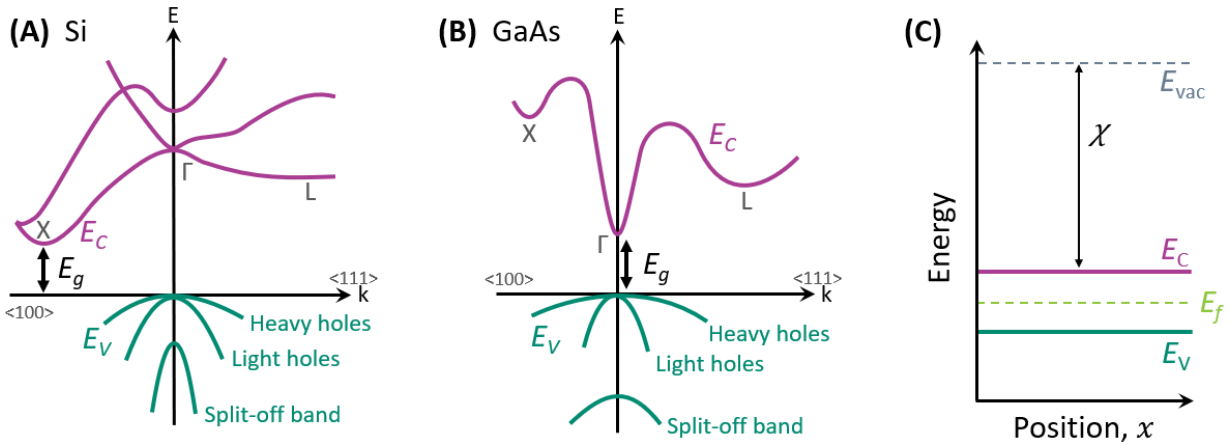

Figure 2.2: Energy band structure of (A) silicon and (B) gallium arsenide (GaAs). Band structures are modified from [62]. (C) Simplified energy band structure as a function of position, showing the conduction band edge, E_c, the valence band edge, E_v, the bandgap, E_g, and the electron affinity, χ.

the crystal lattice in real space. The primitive unit cell of this reciprocal lattice containing a single central lattice point, is called the first Brillouin zone. The first Brillouin zone for an FCC lattice is provided in Fig. 2.1C. Points of high symmetry are labelled. Given that optical transitions must conserve both energy and momentum, it is useful to have a k-space framework for describing and analyzing the band structure.

The high symmetry points labelled in Fig. 2.1C correspond to features in the energy band structures of semiconducting materials. Figure 2.2 shows the energy band structure of silicon and GaAs as function of energy and momentum. Some high symmetry points are labelled on the diagrams, corresponding to those labelled in the first Brillouin zone in Fig. 2.1C. The conduction bands, E_c, are drawn in purple while the valence bands, E_v, are drawn in teal. The bandgap, E_g, is labelled for each diagram.

Silicon is an indirect bandgap semiconductor, meaning that the minimum bandgap energy, E_g, does not occur at the k=0 Γ-point. An appropriate change in momentum is required to promote an electron from the valence to conduction band. This momentum is usually supplied by a phonon, or lattice vibration. Thus, band-to-band electron promotion at the fundamental bandgap can only happen in silicon if there are a sufficient number of phonons with sufficient momentum. As a consequence, indirect bandgap semiconductors tend to have lower optical absorption than direct bandgap semiconductors, such as GaAs.

To show the energy band structure as a function of position within a device, a simplified diagram is used, presented in Fig. 2.2C. It is assumed that a continuum of states exists in each

E_c and E_v band. The electron affinity, χ, defines the minimum required energy to remove an electron from the semiconductor. The energy of a free electron outside of the semiconducting material is defined by the vacuum level, E_{vac}.

2.1.2 Density of states

The density of states (DOS) of a semiconductor describes the number of available quantized states between $(E, E + dE)$ in a particular energy continuum band. Near the conduction or valence band edge, the bands can be approximated as parabolic in k-space. Thus, the energy, E, corresponds to the band edge with an expansion about this of dE.

With the parabolic band approximation, the DOS, $g(E)$, near a band edge can be approximated as:

$$g(E) = \frac{2}{(2\pi)^3}\, 4\pi k^2\, \frac{dk}{dE} \tag{2.1}$$

with $2/(2\pi)^3$ k-states per unit crystal volume.

For the conduction band, the DOS under the parabolic approximation for an energy, E, within the conduction band, E_c, works out to be:

$$g_c(E) = \frac{1}{2\pi^2}\left(\frac{2m_c^*}{\hbar^2}\right)^{\frac{3}{2}} \sqrt{E - E_c} \tag{2.2}$$

Similarly, the DOS in the valence band E_v is:

$$g_v(E) = \frac{1}{2\pi^2}\left(\frac{2m_v^*}{\hbar^2}\right)^{\frac{3}{2}} \sqrt{E_v - E} \tag{2.3}$$

where $\hbar$ is the reduced Plank's constant and the symbol m^* denotes the effective mass of a carrier in either the conduction or valence band. The effective mass is a parameter defined by the band structure, often assumed to be constant near a band valley.

The effective mass is given by:

$$m^* = \hbar^2\, \frac{\partial^2 E}{\partial k^2} \tag{2.4}$$

where E is either the valence band, E_v, or conduction band E_c, for holes and electrons, respectively.

The parabolic band approximation only holds for limited ranges near the bottom of band valleys, as eventually these valleys connect into a continuum as in Fig. 2.2A/B. Spin-orbit interactions may also perturb the parabolic band approximation [58].

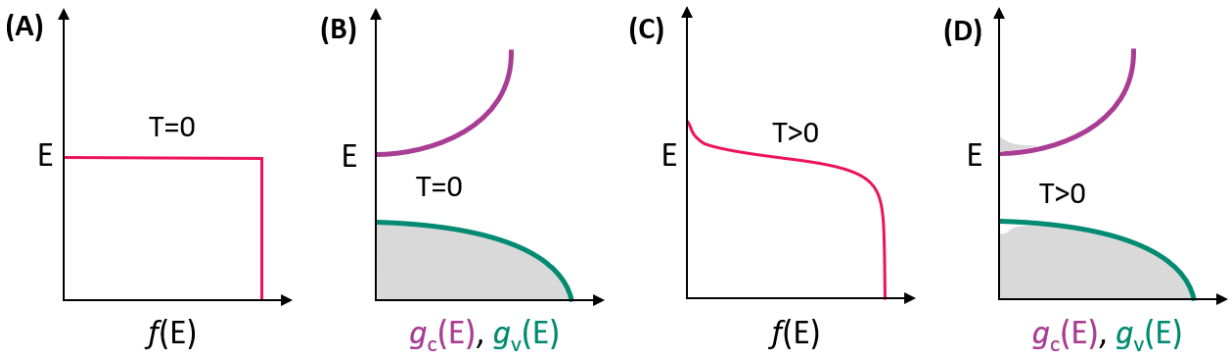

Figure 2.3: (A) The Fermi-Dirac distribution and (B) the density of states functions for $g_c(E)$ and $g_v(E)$ at $T = 0$. (C) The Fermi-Dirac distribution and (D) the density of states functions at $T > 0$. The shaded grey background in (B) and (D) correspond to the concentration of electrons.

2.1.3 Carrier concentration

Above, the DOS described the distribution of band states in energy and momentum space. In order to calculate the number of electrons and holes in an energy band, we must first characterize the occupation probability of the states. The occupation probability of an energy level can be determined by the Fermi-Dirac distribution, $f(E)$:

$$f(E) = \frac{1}{1 + e^{\frac{E - E_f}{k_B T}}} \tag{2.5}$$

where E_f is the Fermi-level, k_B is the Boltzmann constant, and T is the temperature. At absolute zero, every state below the Fermi-level, E_f, is occupied and every state above is unoccupied. For $T > 0$, the thermal kinetic energy of electrons results in some excitation to states above the Fermi-level and into the conduction band. Figure 2.3 provides a visualization of $f(E)$ and $g(E)$ for $T = 0$ and $T > 0$.

Thus, the concentration of electrons in the conduction band, n, can be calculated from the integration of $g(E)$ and $f(E)$ from the conduction band edge E_c to infinity:

$$n = \int_{E_c}^{\infty} n(E)\, dE = \int_{E_c}^{\infty} g_c(E) f(E)\, dE \tag{2.6}$$

The corresponding expression for the number density of holes, p, or vacancies of electrons left behind in the valence band, is thus:

$$p = \int_{-\infty}^{E_v} p(E)\, dE = \int_{-\infty}^{E_v} g_v(E)[1 - f(E)]\, dE \tag{2.7}$$

In the case where the Fermi level, E_f, is sufficiently far from either of the band edges, the Boltzmann approximation can be used. For $E >> E_f$ the Fermi-Dirac function simplifies:

$$f(E) \approx e^{\frac{E_f - E}{k_B T}} \tag{2.8}$$

This allows for the evaluation of 2.6 and 2.7 using $f(E)$ from 2.8:

$$n = N_c \, e^{\frac{E_f - E_c}{k_B T}}, \quad p = N_v \, e^{\frac{E_v - E_f}{k_B T}} \tag{2.9}$$

The constants N_c and N_v describe the effective conduction and valence band density of states, respectively:

$$N_c = 2 \left(\frac{m_c^* k_B T}{2\pi\hbar^2} \right)^{\frac{3}{2}}, \quad N_v = 2 \left(\frac{m_v^* k_B T}{2\pi\hbar^2} \right)^{\frac{3}{2}} \tag{2.10}$$

In an intrinsic semiconductor, the product of np is a constant with the carrier concentrations of electrons and holes equal:

$$n_i^2 = np = N_c \, N_v \, e^{-\frac{E_g}{k_B T}} \tag{2.11}$$

where n_i is referred to as the intrinsic carrier density of the semiconductor.

This leads to the Fermi level of the intrinsic semiconductor, E_i, to be near the center of the bandgap:

$$E_i = \frac{E_c - E_v}{2} - \frac{k_B T}{2} \ln \left(\frac{N_c}{N_v} \right) \tag{2.12}$$

The intrinsic electron concentration ($n = n_i$) at 300 K in silicon is 1.7x10^{13} cm^{-3} [63].

Effect of doping

An intrinsic semiconductor describes a perfect crystal with minimal impurities. Dopants introduce impurities which change the local distribution of electronic energy structure and may be used to tune the properties of semiconducting materials.

Dopants can be classified as either donors or acceptors, depending on their valence electron count compared to the bulk crystal structure. For silicon semiconductors, the underlying crystal lattice is composed of four nearest neighbour tetrahedral bonds. A donor impurity, such as phosphorus with five valence electrons, can introduce energy levels above E_i and donate

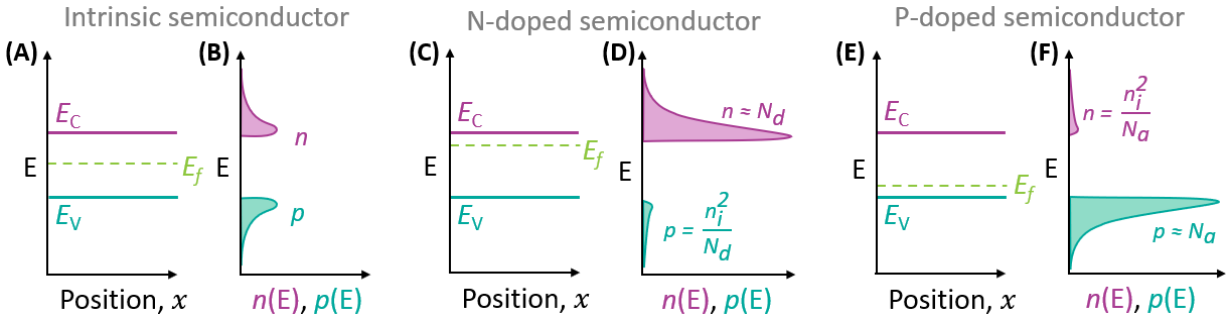

Figure 2.4: The energy band diagrams and number densities for electron and holes for (A-B) an intrinsic semiconductor, (C-D) an n-doped semiconductor, and (E-F) a p-doped semiconductor. These subplots have been adapted from [60].

extra valence electrons to the conduction band via ionization. This results in an increase in electrons and a shift of the Fermi level towards the conduction band. An n-type semiconductor describes a semiconductor which has been doped to have higher relative concentration of electrons compared to holes.

An acceptor impurity, such as boron with three valence electrons, can introduce unoccupied energy levels below E_i that may then be filled by other electrons within the valence band. This ionizes the dopant atom, increases the hole concentration in the valence band, and shifts the Fermi level towards the valence band. A p-type semiconductor describes a semiconductor which has been doped to have lower relative concentration of electrons compared to holes.

Figure 2.4 displays the energy band structure and electron and hole number densities for an intrinsic semiconductor, an n-doped semiconductor, and a p-doped semiconductor. If the density of donor dopants, N_d, is significantly larger than n_i, then $n \approx N_d$ and $p = n_i^2/N_d$. If the density of acceptor dopants, N_a, is significantly larger than n_i, then $p \approx N_a$ and $n = n_i^2/N_a$.

Effect of an external bias

The properties described so far for semiconducting materials have been under equilibrium, without any net current flow. The populations of electrons and holes in a semiconductor can be varied from equilibrium by exposure to light, or by an external applied bias. For an applied bias, V, electron and hole populations relax to quasi thermal equilibrium. The Fermi level splits by $\Delta\mu$ (related to the intensity of the external bias) into separate quasi-Fermi levels for electrons, E_{fn}, and holes, E_{fp}:

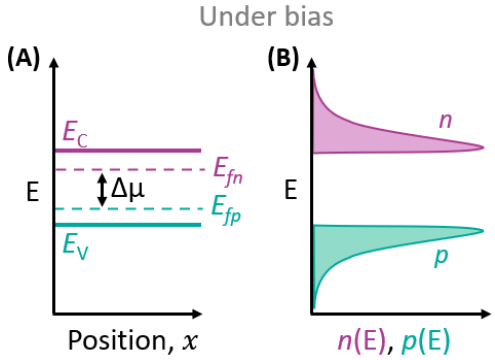

Figure 2.5: (A) The energy band diagram showing the splitting of the Fermi level and (B) the number densities for electrons and holes for an intrinsic semiconductor under a voltage bias.

$$\Delta\mu = E_{fn} - E_{fp} \tag{2.13}$$

This approximation may be used since relaxation times within each band is much quicker than relaxation between bands, resulting in the electron and hole populations having distinct quasi-Fermi levels and temperatures.

Under a bias, the electron and hole densities are simply Equation 2.9 with E_{fn} and E_{fp} in place of E_f:

$$n = N_c\, e^{\frac{E_{fn}-E_c}{k_B T}}, \quad p = N_v\, e^{\frac{E_v-E_{fp}}{k_B T}} \tag{2.14}$$

A depiction of quasi-Fermi level splitting under an external bias is provided in Figure 2.5.

2.1.4 Conductivity and mobility

Semiconductor conductivity is directly related to the free carrier densities, n and p, as well as the carrier mobilities, μ_n and μ_p:

$$\sigma = q(\mu_n n + \mu_p p) \tag{2.15}$$

where q is the elementary electric charge.

Thus, the material conductivity can be tuned by introducing additional electron or hole carriers via doping, described in Section 2.1.3.

The electrical mobility of a carrier is the magnitude of the drift velocity per unit electric field, $\mathbf{E}$:

$$\mu = \frac{|v|}{\mathbf{E}} \tag{2.16}$$

The mobility is defined as positive for both electrons and holes, but the drift velocities, v, will be in different directions with the electric field for the carriers.

The mobility is composed of a variety of contributions from various scattering processes. These processes can be reciprocally summed:

$$\frac{1}{\mu} = \frac{1}{\mu_{phonon}} + \frac{1}{\mu_{doping}} + \frac{1}{\mu_{carrier}} + \frac{1}{\mu_{defect}} \tag{2.17}$$

where μ_{phonon} is the phonon scattering mobility, μ_{doping} is ionized impurity scattering mobility from dopants, $\mu_{carrier}$ is carrier-carrier scattering mobility, and μ_{defect} is defect scattering mobility.

Phonon interband scattering tends to decrease the mobility of holes in particular compared to electrons due to band degeneracy at the valence band edge. This increases the probability of interband scattering, which reduces hole mobility [63].

2.1.5 Drift and diffusion

The current density, J, in a semiconductor can be described as the sum of two terms: a drift current density, J_{drift}, and a diffusion current density, $J_{diffusion}$:

$$J = J_{drift} + J_{diffusion} \tag{2.18}$$

The drift current describes the motion of the charge carriers driven by an electric field, whereas the diffusion current describes the motion of charge carriers driven by a concentration gradient.

In an electrostatic field, $\mathbf{E}$, the drift current density is described by $J_{drift} = \sigma\mathbf{E}$ and can be separated into electron and hole terms:

$$J_{drift} = J_{drift,n} + J_{drift,p} = q(\mu_n n + \mu_p p)\mathbf{E} \tag{2.19}$$

Free charge carriers are driven to move in the electrostatic field to reduce their electrostatic potential energy. The electrostatic field causes a gradient in the vacuum level, conduction band,

and valence band. Electrons drift down the conduction band, while holes drift up the valence band, travelling in opposite directions and producing current in the direction of the electric field.

The diffusion current density is instead driven by carrier concentration gradients, ∇p and ∇n:

$$J_{diffusion} = J_{diffusion,n} + J_{diffusion,p} = q(D_n \nabla n - D_p \nabla p) \tag{2.20}$$

where D_n and D_p are the diffusion coefficients of electrons and holes, respectively. The diffusion coefficients are proportional to the carrier mobilities, μ_n and μ_p [59]:

$$D_n = \frac{\mu_n k_B T}{q} \ , \quad D_p = \frac{\mu_p k_B T}{q} \tag{2.21}$$

In the presence of a concentration gradient, free charge carriers are driven to minimize their statistical potential energy by migrating from areas of high carrier concentration to low carrier concentration.

2.1.6 Generation and recombination

The generation of an excited electron can happen from thermal excitation, but, more importantly for solar cells, the energy required to transition an electron in the valence band to the conduction band can be supplied by the absorption of a photon with energy above the bandgap. Electronic excitation events which promote an carrier from a lower energy state to a higher energy state are called generation events. Generation events which take place as a result of photon absorption are referred to as photogeneration.

For photogeneration with photon energy $E > E_g$, excess carrier energy is lost to lattice interactions until the excited carrier relaxes to the band edge in a process called thermalization. A schematic of photogeneration and thermalization is provided in Figure 2.6.

Generation events which excite electrons to the conduction band perturb the equilibrium carrier concentrations:

$$n = n_0 + \Delta n, \quad p = p_0 + \Delta p \tag{2.22}$$

where n_0 and p_0 are electron and hole concentrations in equilibrium.

Recombination is the loss of electronic excitation through the decay of a carrier from a higher energy state to a lower energy state. The released energy from this process may be given up with photon emission, as heat with phonon emission, or as kinetic energy to another carrier. Both generation and recombination processes can occur from band-to-band, or may occur with localized states. A few common recombination mechanisms are outlined below.

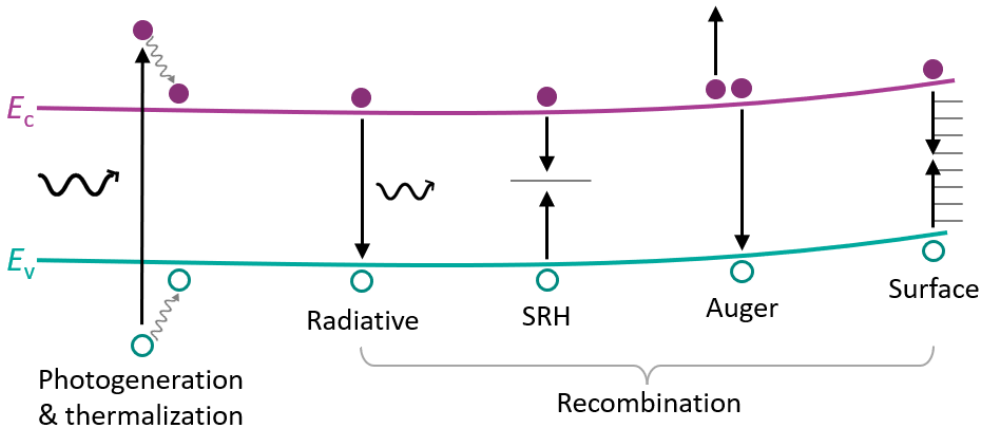

Figure 2.6: A schematic of photogeneration and thermalization alongside recombination mechanisms of radiative, SRH, Auger, and surface recombination.

Radiative recombination

Radiative recombination is the process by which an excited electron moves to a lower energy state and combines with a hole via the emission of a photon (see Fig. 2.6). Radiative recombination, R_{rad}, may be calculated using:

$$R_{rad}(n,p) = B_{rad}(np - n_i^2) \tag{2.23}$$

where B_{rad} is a carrier density-independent property called the radiative recombination coefficient.

For a doped semiconductor, R_{rad} is proportional to excess minority carrier density. The minority carrier radiative lifetime for a p-doped semiconductor, $\tau_{rad,n}$, is given by:

$$\tau_{rad,n} = \frac{1}{B_{rad}N_a} \tag{2.24}$$

The minority carrier radiative lifetime for a n-doped semiconductor, $\tau_{rad,p}$, is given by:

$$\tau_{rad,p} = \frac{1}{B_{rad}N_d} \tag{2.25}$$

Radiative recombination tends to be suppressed in indirect bandgap materials like silicon, since this recombination process requires additional momentum transfer.

Auger recombination

In Auger recombination, band-to-band or trap-assisted recombination is accompanied with a carrier-carrier interaction resulting in the transfer of kinetic energy from one carrier to another. Two similar carriers collide, causing one carrier to excite to a higher energy level and the other to recombine across the bandgap (Fig. 2.6). The carrier with increased kinetic energy decays in time back to the band edge via thermalization.

The rate of Auger recombination, R_{aug}, is a three carrier process, leading to n^2p and np^2 carrier concentration dependency:

$$R_{aug}(n,p) = \left(C_{aug,n}\ n + C_{aug,p}\ p\right)\left(np - n_i^2\right) \tag{2.26}$$

where C_{aug} are Auger recombination coefficients for electrons and holes.

The minority carrier Auger lifetimes for doped semiconductors are given by:

$$\tau_{aug,n} = \frac{1}{C_{aug,n}\ N_a^2}, \quad \tau_{aug,p} = \frac{1}{C_{aug,p}\ N_d^2} \tag{2.27}$$

Auger recombination events conserve energy and momentum and involve the transfer of momentum between carriers in the process. As a result, Auger recombination is often the dominant recombination process in high quality indirect bandgap materials such as silicon.

Shockley-Read-Hall recombination

Shockley-Read-Hall (SRH) recombination is a non-radiative recombination process that involves localized defect or trap states. Carriers can thermalize into localized trap states to recombine (Fig. 2.6). These trap states can be a result of dopant impurities, or may be related to other defects such as lattice vacancies.

The rate of SRH recombination, R_{SRH}, through a single trap state can be calculated from:

$$R_{SRH}(n,p) = \frac{np - n_i^2}{\tau_{SRH,p}(n + n_t) + \tau_{SRH,n}(p + p_t)} \tag{2.28}$$

where τ_{SRH} terms are the minority carrier SRH lifetimes, and n_t is the electron density and p_t is the hole density when the electron Fermi level is equal to the trap energy, E_t.

SRH minority carrier lifetimes can be empirically modelled as doping dependent by using the Scharfetter relationship [64]:

$$\tau_{SRH}(N_d, N_a) = \tau_{min} + \frac{\tau_{max} - \tau_{min}}{1 + \left(\frac{N_a + N_d}{N_{ref}}\right)^{\gamma}} \tag{2.29}$$

where τ_{min}, τ_{max}, γ, and N_{ref} are fitting parameters for the material.

SRH recombination is not intrinsic to semiconductor crystals like radiative and Auger recombination processes, and can be reduced by having very pure semiconducting crystals. However, in any realistic environment, some amount of defects will be introduced into crystal lattices during fabrication and end-use. Highly doped regions of devices will also have higher SRH recombination rates due to the addition of recombination centers and trap states. When the defect and impurity densities are sufficiently high, SRH recombination can dominate over the dominant intrinsic material recombination process (either radiative or Auger recombination).

The above mentioned recombination processes are processes associated with the bulk of a semconducting material. The effective minority carrier lifetime of the bulk is the inverse combination of all bulk minority carrier recombination lifetimes:

$$\frac{1}{\tau} = \frac{1}{\tau_{rad}} + \frac{1}{\tau_{aug}} + \frac{1}{\tau_{SRH}} \tag{2.30}$$

The average length a carrier travels before recombination is characterized by the diffusion length, L_n or L_p, and relates to the minority carrier lifetime:

$$L_n = \sqrt{D_n \tau_n}\ , \quad L_p = \sqrt{D_p \tau_p} \tag{2.31}$$

where D_n and D_p are the diffusion coefficients for the minority carriers given by Eq. (2.21).

Surface recombination

Recombination processes are also associated with the surfaces and interfaces of materials. At the surface of a material, there tend to be dangling bonds, which result in localized surface states within the bandgap that can act as recombination centers for electron-hole pairs (see Fig. 2.6). Surface recombination is characterized by a surface recombination velocity, S, in units of cm/s:

$$S = v_T \Omega N_s \tag{2.32}$$

where v_T is the thermal velocity, Ω is the surface area capture cross-section, and N_s is the density of surface traps.

The surface recombination rate, R_{surf}, is a form of surface SRH recombination, and can be calculated in a similar manner:

$$R_{surface} = \frac{n_s p_s - n_i^2}{(n_s + n_t)/S_p + (p_s + p_t)/S_n} \tag{2.33}$$

where n_s and p_s are the electron and hole densities at the surface of the material.

2.1.7 The transport equations

The movement of charge carriers within a semiconductor is determined by light absorption, current generation, and charge recombination. In order to calculate semiconductor transport equations, two main principles must be met: the number of electrons and the number of holes must each individually be conserved, and the electrostatic potential caused by the charge carriers must follow Poisson's equation.

The conservation of electron number requires that:

$$\frac{\partial n}{\partial t} = \frac{1}{q}\nabla J_n + G_n - R_n \tag{2.34}$$

where t is time, J_n is the total electron current density, G_n is the generation rate of electrons, and R_n is the total recombination rate of electrons. The conservation of hole number takes a similar form, but with negative elementary charge:

$$\frac{\partial p}{\partial t} = -\frac{1}{q}\nabla J_p + G_p - R_p \tag{2.35}$$

Equations 2.34 and 2.35 are referred to as the continuity equations.

Poisson's equation relates the electric field, $\mathbf{E}$, to the density of charge carriers in the material:

$$\nabla \cdot \mathbf{E} = -\nabla^2 \phi = \frac{q}{\epsilon_s}(N_a - N_d + n - p) \tag{2.36}$$

where ϵ_s is the static dielectric constant and ϕ is the electrostatic potential.

2.1.8 Optical properties

The topic of photon absorption is a rich field, covering band-to-band transitions, excitonic transitions, inter-band transitions, impurity-band transitions, free carrier transitions, and resonant transitions with vibrational lattice states. Here, we review briefly some basic equations for determining optical properties of reflection, transmission, and absorption relevant for silicon solar cells.

The complex index of refraction, $\tilde{n}$, describes the refraction and absorption properties of a material:

$$\tilde{n} = n_r + i\kappa \tag{2.37}$$

where n_r is the real component and κ is the extinction coefficient. In general, these values depend on wavelength.

The extinction coefficient determines the absorption of the material, α:

$$\alpha = \frac{4\pi\kappa}{\lambda} \tag{2.38}$$

where λ is the wavelength of light.

The reflection and transmission of light from one medium to another is determined by the complex index of refraction. The reflectivity, R, at a plane interface between two materials at normal incidence can be calculated using the complex index of refraction for each medium:

$$R = \left| \frac{\tilde{n}_1 - \tilde{n}_2}{\tilde{n}_1 + \tilde{n}_2} \right|^2 \tag{2.39}$$

For solar cells, this calculation is often done between the index of refraction of air ($n = 1$) and the top surface material of the solar cell ($n \sim 3-4$), giving a reflectivity of around 30-40%. Generally, net reflectivity increases as incident angles become more oblique. Further discussion on the design of solar cells for reduced light refection is discussed in Section 2.3.

2.2 Photovoltaic energy conversion

So far, we have discussed the generation and transportation of charge carriers in a semiconducting material. In order to successfully have photovoltaic energy conversion, charge separation must also occur. The most common method for charge separation in PV devices is via a p-n junction.

2.2.1 p-n junctions

p-n junctions are formed by the physical contact of two semiconducting materials, one n-doped and the other p-doped. Their physical contact results in the alignment of the Fermi levels between the two materials and a shift in the vacuum level. This causes a built-in potential which is driven by the difference in material work functions, Φ:

$$\Phi = \frac{1}{q}(E_{vac} - E_f) \tag{2.40}$$

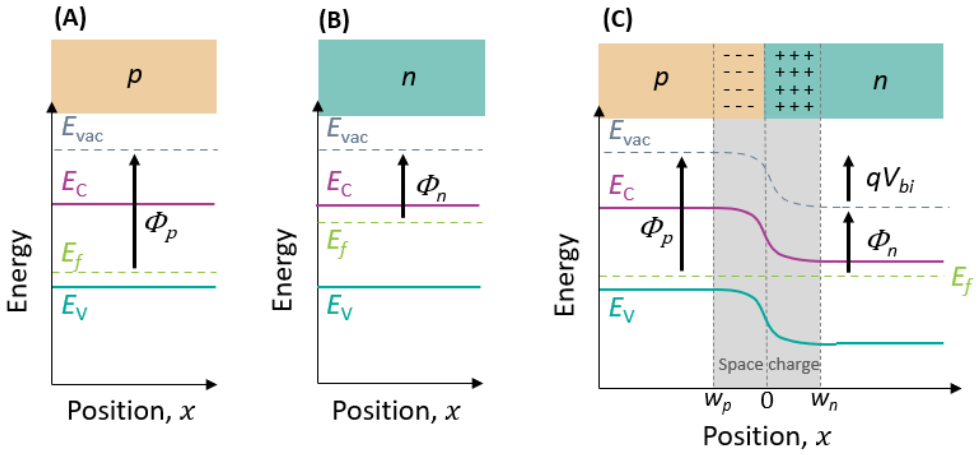

Figure 2.7: (A) A p-doped material, (B) an n-doped material, and (C) a p-n junction.

$$V_{bi} = q(\Phi_p - \Phi_n) \tag{2.41}$$

A depiction of the Fermi level alignment and band structure of a p-n junction is provided in Figure 2.7. In terms of carrier motion, when a p-doped material is placed in contact with an n-doped material, their carrier concentration differences result in a diffusion current. Electrons from the n-doped material diffuse towards the p-doped material, leaving behind positive ions. Holes similarly diffuse from the p-doped material to the n-doped material, leaving behind negative ions. These ions create an internal electric field near the interface which induces a minority carrier drift current to balance the majority carrier diffusion current under equilibrium.

The built-in bias resulting from a p-n junction can be calculated from carrier concentrations N_a and N_d with:

$$V_{bi} = \frac{k_B T}{q} \ln\left(\frac{N_a N_d}{n_i^2}\right) \tag{2.42}$$

In the depletion approximation, it is assumed that there are no majority carriers located over a region of $\omega_p + \omega_n$ around the interface. This region is called the depletion region, or the space charge region, as labelled in Fig. 2.7. The width of the space charge region can be found using Poisson's equation and assuming that the potential outside of this region is constant [59]:

$$\omega_p = \frac{1}{N_a}\sqrt{\frac{2\epsilon_s V_{bi}}{q(\frac{1}{N_a} + \frac{1}{N_d})}}, \quad \omega_n = \frac{1}{N_d}\sqrt{\frac{2\epsilon_s V_{bi}}{q(\frac{1}{N_a} + \frac{1}{N_d})}} \tag{2.43}$$

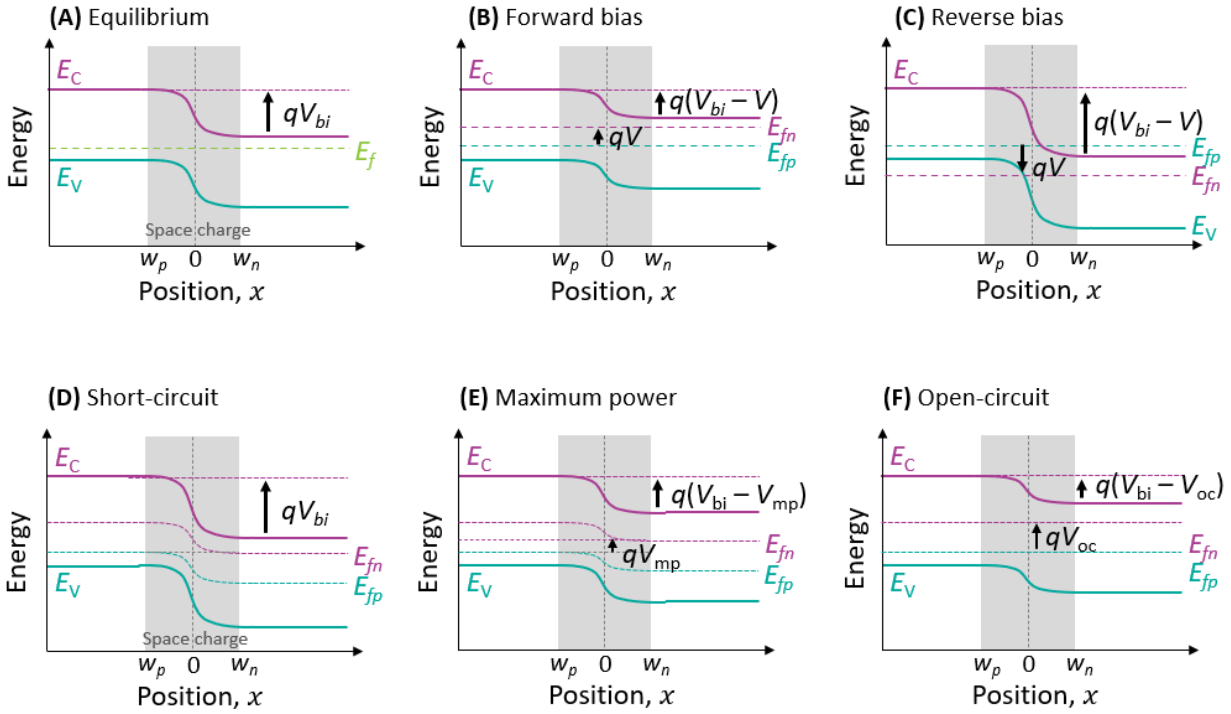

Figure 2.8: Schematics of a p-n junction at (A) equilibrium, (B) forward bias, (C) reverse bias, (D) short-circuit, (E) maximum power, and (F) open-circuit.

Thus, the total width of the space charge region, ω_{scr}, becomes:

$$\omega_{scr} = \omega_p + \omega_n = \sqrt{\frac{2\epsilon_s}{q}\left(\frac{1}{N_a}+\frac{1}{N_d}\right)V_{bi}} \tag{2.44}$$

with ϵ_s the static dielectric constant, q the elementary charge, N_a the density of ionized acceptors in the p-doped material, N_d the density of ionized donors in the n-doped material, and V_{bi} the built-in bias.

Wide depletion regions aid in carrier collection, while high doping levels aid in cell voltage. If doping increases on either the p or the n side, the depletion region shrinks. This is one of the fundamental compromises in solar cell design.

Another depletion region requirement is that E_{fn} - $E_{fp} = qV$ = constant in the space-charge region, leading to:

$$pn = n_i^2 \, e^{\frac{qV}{k_B T}} \quad \text{for} \quad -\omega_p < x < \omega_n \tag{2.45}$$

This holds true under an external bias, V, which splits the Fermi level into E_{fn} and E_{fp}. The total junction bias is given by $V_j = V_{bi} - V$. When $V_j < V_{bi}$ the device is under forward bias, the depleted region is reduced in width, and the barrier to majority carrier diffusion decreases. When $V_j > V_{bi}$ the device is under reverse bias, the depleted region increases in width, and the barrier to majority carrier diffusion increases. This is visualized in Figure 2.8B/C.

2.2.2 Current-voltage characteristics

Under illumination

Under illumination, electron and hole populations increase above their equilibrium values and reach quasi-thermal equilibrium populations described by Fermi level splitting. Increased minority carrier concentrations in the depletion region result in a drift current referred to commonly as the short-circuit current, J_{sc}, which is related to the intensity of the illumination light. Fig. 2.8D shows the band structure under short-circuit illumination.

The short-circuit current of a solar cell is determined by the incident photon flux, $\Phi_p(E)$, and the external quantum efficiency (EQE) of the cell. The EQE characterizes the ability of the material to convert photons of wavelength λ into carriers that are collected by an external circuit. It is the ratio between collected carriers to incident photons. An example EQE curve is shown in Figure 2.9 for a silicon solar cell. EQE is reduced from an ideal value of $EQE = 1$ for energies above the bandgap ($< 1100\ nm$ in wavelength for silicon) due to reflection off the surfaces of the solar cell and transmission through the solar cell.

The photocurrent, or J_{sc}, can be calculated from:

$$J_{sc} = q \int_0^\infty \Phi_p(E)\ EQE(E)\ dE \tag{2.46}$$

To examine the collection efficiency of absorbed photons, reflection and transmission losses can be removed from the EQE. This is referred to as the internal quantum efficiency (IQE):

$$IQE(\lambda) = \frac{EQE(\lambda)}{1 - \mathcal{R}(\lambda) - \mathcal{T}(\lambda)} \tag{2.47}$$

where $\mathcal{R}$ is the reflectivity and $\mathcal{T}$ is the transmittance of the solar cell.

The spectral response, SR, describes the relationship between the photocurrent and the incident spectrum power:

$$SR(\lambda) = \frac{q\lambda}{hc} EQE(\lambda) \tag{2.48}$$

The EQE, IQE, and SR of an example silicon solar cell is provided in Figure 2.9.

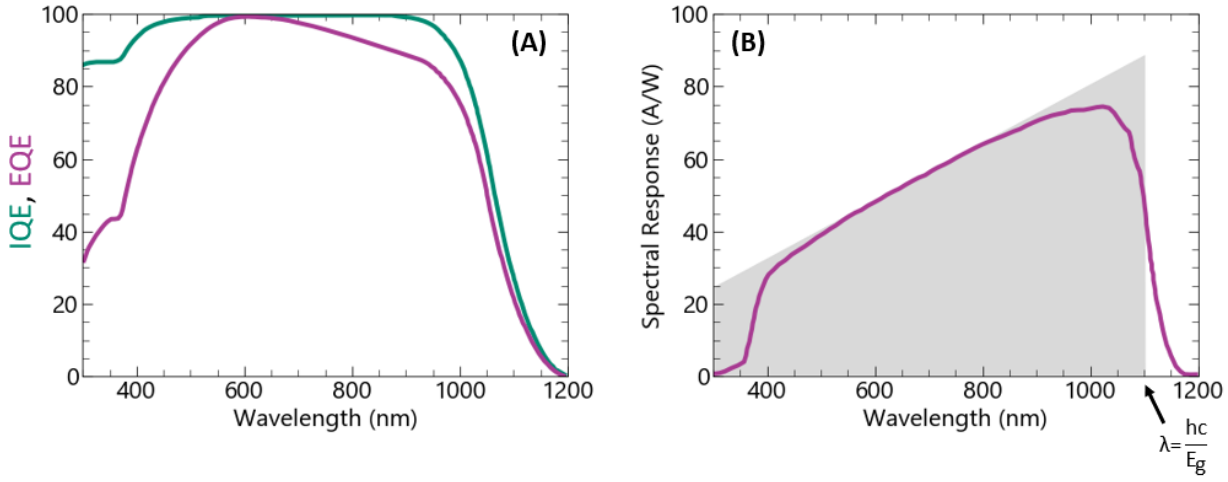

Figure 2.9: (A) IQE and EQE, (B) spectral responsitivity. The shaded grey background corresponds to an ideal cell.

Under an external bias

Under an external forward bias, the potential barrier across a p-n junction is reduced (Fig. 2.8B). Consequently, the majority carrier diffusion current increases, injecting minority carriers into opposite polarity sides of the p-n junction and opposing any generated photocurrent. In the dark, solar cells behave like diodes, with significantly higher current under forward bias than reverse bias. The non-ideal diode equation describes the net current flow in the absence of illumination:

$$J_{dark} = J_0 \left(e^{\frac{qV}{mk_BT}} - 1 \right) \tag{2.49}$$

where J_0 is the dark saturation current density, and m is the ideality factor. In an ideal diode, $m = 1$ and there is little recombination in the depletion region and the dark current is diffusion-dominated. If significant recombination occurs in the depletion region, m can reach a value of $m = 2$.

Under illumination and an external bias

The total current under illumination and external forward bias can be calculated by $J_{sc} + J_{dark}$. Since the dark current flows in the opposite direction as J_{sc}, the equation becomes:

$$J(V) = J_{sc} - J_{dark}(V) = J_{sc} - J_0 \left(e^{\frac{qV}{mk_BT}} - 1 \right) \tag{2.50}$$

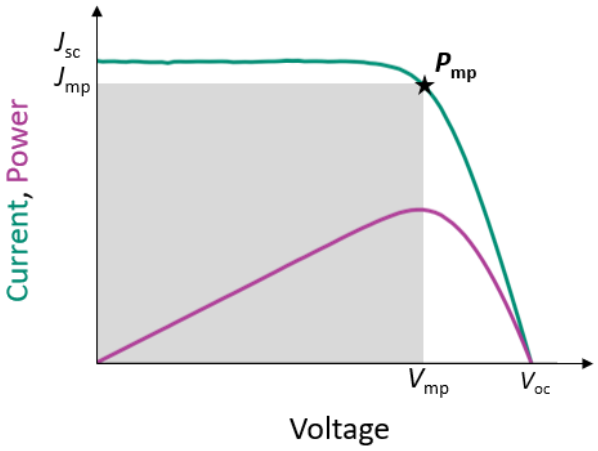

Figure 2.10: An example I-V curve for a PV device under illumination. Power is provided by the purple curve, while current is given in teal. Key I-V curve parameters are labelled.

Figure 2.10 shows an example current-voltage (J-V) curve for a PV device under illumination and varied forward bias.

The open-circuit voltage, V_{oc}, is the voltage where light and dark currents cancel, providing a net current flow of zero. This is visualized in Fig. 2.8F and can be calculated from the ideal diode equation (Eq. 2.50) to be:

$$V_{oc} = \frac{k_B T}{q} \ln\left(\frac{J_{sc}}{J_0} + 1\right) \tag{2.51}$$

Open-circuit voltage increases logarithmically with illumination intensity and cannot be larger than the bandgap of the semiconductor.

The device power density, P, depicted in purple in Fig. 2.10, can be simply calculated by $P = JV$. The maximum power point describes the peak in PV power production and is denoted by P_{mp} for a current of J_{mp} and a voltage of V_{mp} ($P_{mp} = J_{mp}V_{mp}$). Fill factor (FF) measures the squareness of the J-V curve (shaded area in Fig. 2.10) and can be calculated from the maximum power point:

$$FF = \frac{J_{mp}V_{mp}}{J_{sc}V_{oc}} \tag{2.52}$$

Finally, the power conversion efficiency, η of the device is calculated by dividing the output maximum power by the input illumination power:

$$\eta = \frac{P_{mp}}{P_{inc}} = \frac{J_{mp}V_{mp}}{P_{inc}} = \frac{J_{sc}V_{oc}FF}{P_{inc}} \tag{2.53}$$

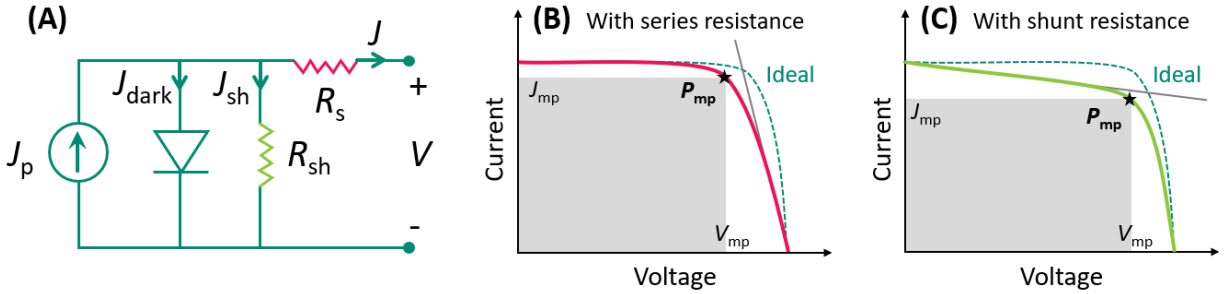

Figure 2.11: (A) Simplified equivalent circuit of a solar cell with parasitic resistances. Current-voltage curves of a solar cell with (B) series resistance and (C) shunt resistance.

where P_{inc} is the power of the incident light.

Solar cell efficiency can be reduced by the presence of series resistance, R_s, and shunt resistance, R_{sh}. These extra resistances can be added into Equation 2.50:

$$J(V) = J_{sc} - J_{dark}(V) = J_{sc} - J_0\left(e^{\frac{q(V+JAR_s)}{mk_BT}} - 1\right) - \frac{V + JAR_s}{R_{sh}} \tag{2.54}$$

where A is the active area of the solar cell. The effect of series and shunt resistances on J-V curve behaviour is visualized in Figure 2.11. Fig. 2.11A shows a simplified equivalent circuit model of a solar cell with parasitic resistances as labelled.

Effect of illumination intensity and temperature

Figure 2.12A displays the effect of illumination intensity on current-voltage behaviour. As mentioned previously, short-circuit current scales linearly over the range of non-concentrating illumination intensity, while open-circuit voltage scales logarithmically. This tends to result in an increase in cell efficiency with increasing illumination intensity, however series resistance effects under high light concentration will eventually limit the efficiency of PV devices [59].

Increasing temperature, on the other hand, largely impacts the open-circuit voltage of solar cells. As temperature increases, the population of intrinsic carriers increases. Dark saturation current, J_{dark}, increases as a result, which reduces open-circuit voltage. To a smaller effect, increasing temperature shifts the band-edge towards narrower bandgaps, resulting in an increase in photocurrent. However, the loss in V_{oc} out-weighs this photocurrent increase. The effect of temperature on current-voltage curves and EQE is visualized in Fig. 2.12B&C.

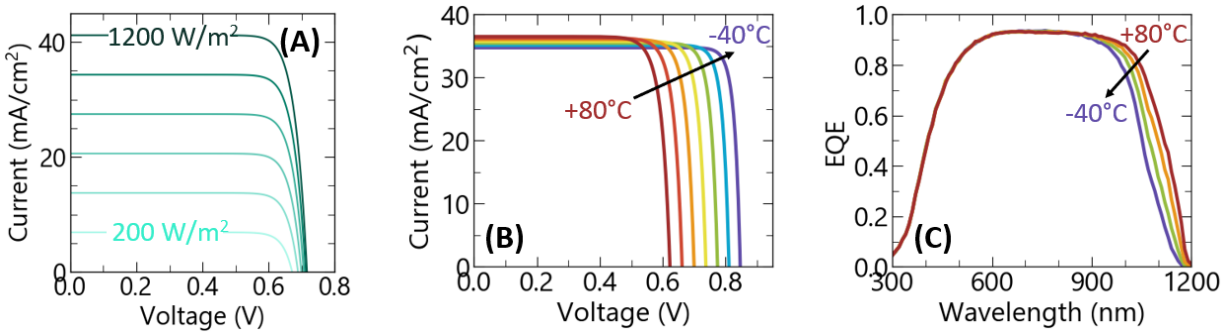

Figure 2.12: Example effect of (A) varied illumination intensity and (B) varied temperature on current-voltage curves of a silicon solar cell. (C) Effect of temperature on the absorption band-edge.

2.3 Light trapping

As mentioned in Section 2.1.8, for the interface between two planar materials of air and a semiconducting surface, the reflectivity in the visible wavelength regime is high, typically around 30-40% [59]. For solar cells, where the short-circuit current is linearly related to the amount of absorbed incident light, minimizing reflection to maximize semiconductor absorption is critical to achieving a high efficiency device.

Two main techniques are used in non-concentrating silicon solar cells for increasing semiconductor light absorption: the application of anti-reflection coatings (ARCs) and surface texturing.

ARCs consist of thin-film deposited dielectric layers on the front (and rear) surfaces of the semiconductor with index of refraction between that of air and the semiconductor. Depending on the thickness of the deposited layer, the surface reflection can be tuned to minimize at an optimal point for the solar spectrum. Multiple layers of ARCs can be used to further reduce reflection over a broader range of wavelengths. The implementation of ARCs in silicon solar cell designs, can be seen in Section 3.1.

Texturing of the front and rear surfaces of silicon solar cells reduces the net reflection of light over the silicon absorption range and increases the optical path length of photons travelling inside the PV device. This increases the probability of photon absorption by causing reflection and scattering at angles wider than the surface normal.

For light travelling within a semiconductor towards an air-boundary and for any angles greater than the critical angle, θ_c, the light will be internally reflected:

$$\theta_c = \sin^{-1}\left(\frac{\tilde{n}_{air}}{\tilde{n}_{semi}}\right) \tag{2.55}$$

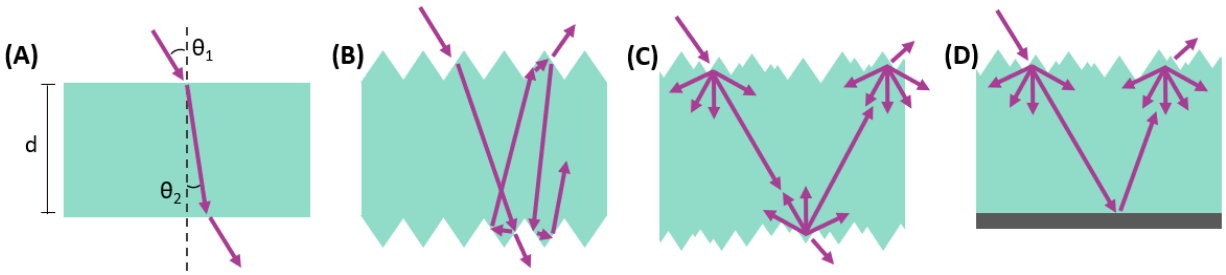

Figure 2.13: A schematic showing light trapping effects for various surface textures: (A) flat surfaces, (B) regular pyramids, (C) random pyramids, and (D) random pyramids with a rear reflector. Note: texturing is not to scale and arrows trace example ray trajectories. Adapted from [65].

Figure 2.13 shows a schematic of the path of light rays in various textured structures. For surface texture structures $d_{texture} \gg \lambda$ on a semiconducting substrate with $d_{substrate} \gg d_{texture}$, light can be treated with ray tracing techniques.

In a perfectly randomizing surface, reflected light rays are scattered equally across all possible hemisphere angles. This is referred to as a Lambertian surface. In a perfect Lambertian surface, the ideal path length enhancement is around 50× in silicon [59]. In practice, regular and random pyramidal textured surfaces are often used in place of Lambertian reflectors due to their relative fabrication ease. Silicon PV devices are most commonly textured with random pyramids during fabrication using selective etching acidic baths. The random pyramids introduced by selective etching typically achieve path length enhancements closer to 10× that of a planar structure [59].

2.4 Efficiency limits

PV devices have limited maximum efficiencies based off fundamental thermodynamic limits between the emitted solar spectrum of the sun and the solar cell temperature. In 1961, Shockley and Queisser developed a methodology for determining the ultimate limiting efficiency of a single junction solar cell on Earth [66]. Here, we briefly outline the modified single-junction efficiency limit which incorporates the standard solar spectrum, AM1.5G[1], and radiative recombination [59]. This limit is known as the Shockley-Queisser limit, or the detailed balance limit. The main assumptions of this limit are:

- The sun radiates at a spectrum of AM1.5G with 1000 W/m^2.

[1]The standard solar spectrum of AM1.5G is discussed further in the next section, Section 2.5

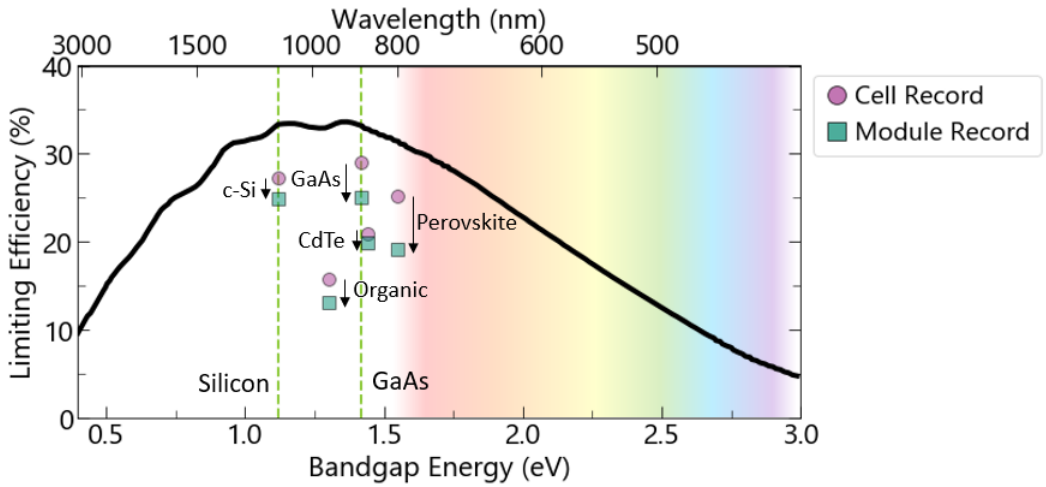

Figure 2.14: The single-junction solar cell detailed balance efficiency limit as a function of bandgap and wavelength for AM1.5G. A selection of record-breaking efficiency cells and modules as published in Version 64 of the Martin Green efficiency tables are provided, given by circles and squares [67]. The bandgap of silicon and GaAs are given by vertical dashed lines.

- The solar cell has a perfect step-wise absorption where all light with $E > E_g$ is absorbed.
- One photon with $E > E_g$ generates one electron-hole pair.
- Charges are perfectly separated within the solar cell, with only radiative recombination losses.
- No potential is lost through external resistances in the circuit, with collected electrons providing $\Delta\mu = qV$ of work to the external circuit.

Given these assumptions, the maximum efficiency limit is dependent on the cell temperature, T, and the bandgap, E_g, according to the following equation from Ref. [59]:

$$\eta = \frac{JV}{P_{inc}} \approx \frac{V}{P_{inc}}\Big[J_{sc} - J_0(e^{qV/k_BT} - 1)\Big] \tag{2.56}$$

where both the J_{sc} and J_0 terms are dependent on the bandgap energy. The net current generated by the solar cell is the result of the difference in absorbed photon flux and the emitted photon flux. A peak in the maximum efficiency limit as a function of E_g can be found, demonstrating the fundamental trade-off between absorbed current density and maximum power operating voltage.

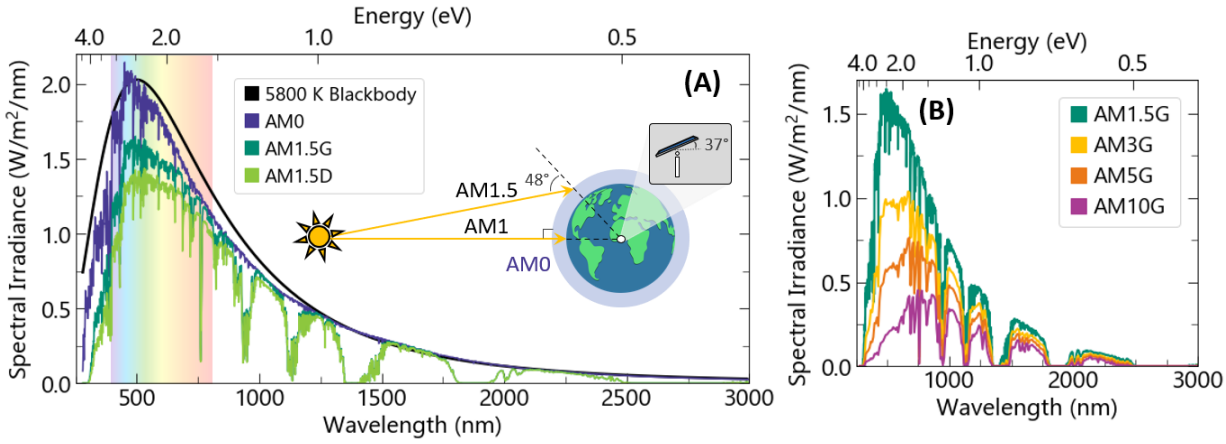

Figure 2.15: (A) The spectral irradiance emitted from a 5800 K blackbody radiator, the extraterrestrial solar spectrum, AM0, the standard solar spectrum AM1.5G, and the direct-beam component of AM1.5. An inset schematic demonstrates the definition of various AM spectra. (B) The spectral irradiance of the sun under various AMs. Plotted spectra have been generated using SMARTS [68].

Figure 2.14 shows a plot of the limiting efficiency of a single-junction, non-concentrating solar cell as a function of device bandgap energy. Vertical dashed lines show the bandgaps of silicon and GaAs. Current record breaking efficiencies for a few select technologies are displayed for both record breaking cells (circles), and recording breaking modules (squares).

2.5 Solar resource

In order to have a better understanding of the capabilities of solar cells to generate current, we must consider the source of illumination - our neighbourhood Sun.

The sun radiates energy primarily from the ultraviolet (UV) to the infrared (IR), peaking in the visible wavelength region. The emitted spectrum of the sun can be modelled as a blackbody radiator with a characteristic temperature $T_s \approx 5800\ K$. A blackbody radiation spectrum is displayed in Figure 2.15A with an example extraterrestrial spectrum of the sun given by AM0. The blackbody radiation spectrum is reduced by the subtended angle of the sun on Earth. The sun deviates from an idealized blackbody model due to photon absorption within the sun from atoms, ions, and in rare cases molecules. The chemical species present in the sun (primarily hydrogen, helium, with small amounts of carbon, nitrogen, oxygen, calcium, silicon, and iron) result in specific absorption features, indicating electronic transitions.

Given the angle the sun subtends in Earth's sky, the amount of radiation received just outside the Earth's atmosphere (AM0) is relatively constant, around 1360 W/m^2 [69, 70]. Further attenuation occurs as sunlight passes through the Earth's atmosphere and scatters and absorbs. The amount of attenuation depends on a variety of factors: the season of the year and time of day, the location latitude, and variations in atmospheric constituents, and sky conditions (clouds, aerosols, water vapour).

Air mass (AM) quantifies the path length of sunlight through the atmosphere normalized to the path length when the sun is at a zenith angle of 0° (directly overhead). Standard solar spectra have been defined based off AM to facilitate comparisons between PV devices. For terrestrial applications, the standard solar spectrum is AM1.5G, where the 'G' refers to global radiation, including both direct and diffuse components. AM1.5D, on the other hand, is the standard solar spectrum for only direct radiation. AM0 is the standard solar spectrum for extraterrestrial applications without atmospheric attenuation from the Earth [70]. These solar spectra are plotted in Fig. 2.15A. Some of the main absorption features of the Earth's atmosphere can be seen in the solar spectra for AM1.5G and AM1.5D. Water and CO_2 in the atmosphere cause significant absorption features in the near IR from 900 nm to 2600 nm.

AM1.5G is defined by when the sun is at a zenith angle of 48° with the receiving surface at a tilt of 37°, and scaled to an irradiance of 1000 W/m^2. These values were chosen to represent an average location in continental USA [70]. However, the AM of the sun varies throughout the year, depending on location, time of day, and season. Fig. 2.15B shows the solar spectra for higher AMs, corresponding to lower solar elevation angles. Higher AM leads to significant attenuation in the solar spectra and a shift in spectral content towards the near IR. This means that though PV devices are optimized, tested, and rated at AM1.5G, in practice device efficiencies can vary quite significantly depending on the illumination conditions of the deployment location.

2.5.1 Irradiance components

The electromagnetic radiation emitted from the Sun and incident on Earth's surface is often measured and quantified by three common metrics in the PV field: direct normal irradiance (DNI), diffuse horizontal irradiance (DHI), and global horizontal irradiance (GHI). A schematic of these irradiance components is presented in Figure 2.16. DNI quantifies the amount of solar radiation received per unit area by a surface perpendicular to the sun's position in the sky. This value typically includes circumsolar radiation, defined often as a 2.5° radius circle centred on the sun [71]. DHI, on the other hand, characterizes the amount of radiation arriving on a flat-plane surface that does not come directly from the sun and has been scattered by particles

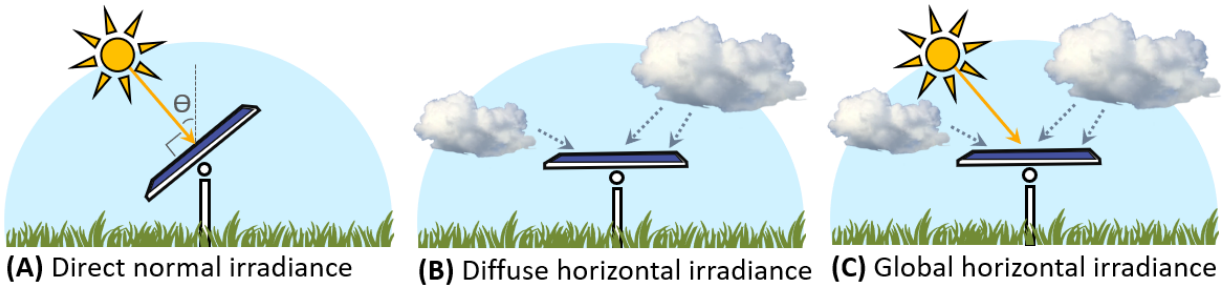

Figure 2.16: Components of solar irradiance: (A) DNI, (B) DHI, (C) GHI.

and molecules in the atmosphere. These two quantities together form the GHI, with the GHI being defined for a surface horizontal on the Earth's surface, as pictured in Figure 2.16C.

Thus, the GHI is calculated from the following equation, accounting for varied solar position for the measurement of DNI:

$$GHI = DHI + DNI \cos\theta \tag{2.57}$$

In this equation θ is the solar zenith angle, the angle subtended by the sun's position in the sky and a vertical line normal to the Earth's surface, as labelled in Figure 2.16A.

2.5.2 Albedo

Ground-reflected irradiance can also compose a significant portion of incident irradiance on PV systems, particularly for bifacial PV systems [72]. In the photovoltaic world, albedo quantifies the reflectance of the ground over all possible solar angles by comparing upwelling to downwelling irradiance [73]. This is typically done by measuring broadband solar radiance with two pyranometers, one facing up towards the sky (as is done to measure GHI) and the other facing towards the ground. Albedo, a, is then calculated as the ratio between these two values, with values expected to fall between 0 (totally absorptive ground) and 1 (totally reflective ground):

$$a = GUI/GHI \tag{2.58}$$

where GUI refers to global upwelling irradiance measured by the pyranometer facing towards the ground [73]. Figure 2.17 shows an example measurement set-up for determining albedo[2].

[2]Sky-facing pyranometers are recommended to be heated with sufficient power to melt any potential snow accumulation, as can be seen in Fig. 2.17B. This meteorological station contains a separate heated GHI sensor, not depicted, which is used for calculating albedo.

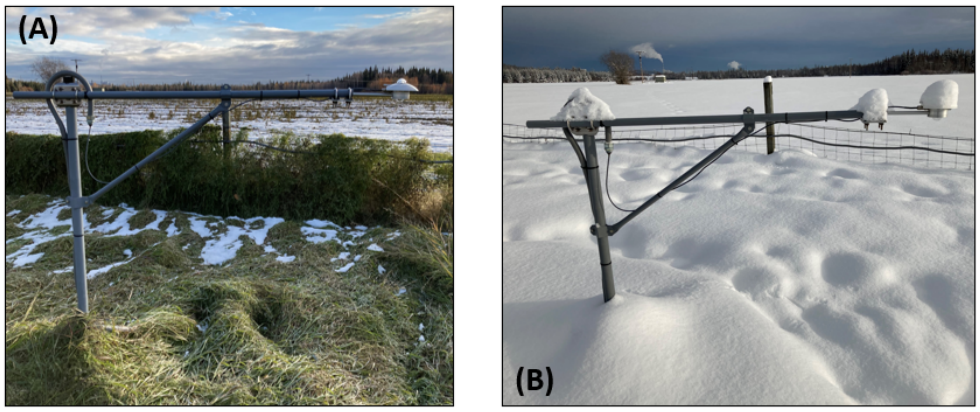

Figure 2.17: The albedometer set-up at the E-W vertical test-site in Fairbanks, Alaska, maintained by the Alaska Center for Energy and Power. Photo credit: William Fisher.

Albedo is commonly measured as a broadband value over the solar spectrum, but may also be measured per wavelength to get a spectral albedo. Broadband albedo, a_{bb}, can be calculated by integrating the measured spectral albedo, $A(\lambda)$, by the standard solar spectrum of AM1.5G over all available wavelengths, λ:

$$a_{bb} = \frac{\int A(\lambda)\ AM1.5G(\lambda)\ d\lambda}{\int AM1.5G(\lambda)\ d\lambda} \tag{2.59}$$

Figure 2.18 below shows the spectral and broadband albedos for fresh snow, green grass, dry grass, and soil, given by solid and dashed lines, respectively. The albedo of soil is plotted using data from the Simple Model of the Atmospheric Radiative Transfer of Sunshine (SMARTS) database [68] and the remaining albedos are digitized from Ref. [74]. As we will see in later chapters, the effect of albedo can be substantial for bifacial PV performance.

2.6 Drift-diffusion modelling

To model the performance of practical photovoltaic devices with non-radiative recombination, surface texture, multiple layers, doping gradients, and 2D or 3D structure, optoelectronic drift-diffusion models for semiconducting materials may be used. Here, we provide a basic outline of drift-diffusion modelling via Synopsis Sentaurus technology computer-aided design (TCAD), necessary to understand the background of the device physics modelling done in Chapter 5.

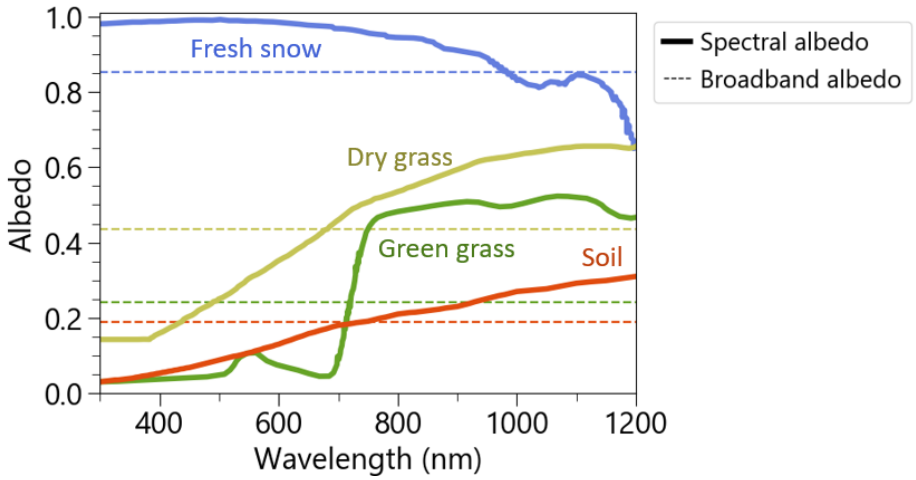

Figure 2.18: Spectral and broadband albedos of fresh snow, dry grass, green grass, and soil [68, 74].

Sentaurus is a modelling package for simulating optoelectronic semiconductor devices using finite element and finite difference methods.

Sentaurus relies on a number of packages to perform various tasks in a device simulation. A typical tool flow is depicted in Figure 2.19, indicating the flow of input and output files.

The Epi tool generates an epitaxially layered device by assigning materials, layer thicknesses, and doping concentrations. The MatPar tool assigns remaining material parameters according to detailed material parameter files, including parameters such as doping-dependent mobility, recombination coefficients, and density of states. The Structure Editor tool creates contacts on the material stack and generates a mesh, discretizing the regions according to user commands. The mesh density is typically non-uniform throughout a simulation to optimize solution time and ensure accuracy in regions with strong potential gradients and optical generation. The Sentaurus Device tool performs the main analysis, using input files describing the device structure, material properties, and simulation mesh.

Sentaurus Device solves for J-V curves by first computing Poisson's equation (Eq. 2.36) to determine carrier density under equilibrium. Optical generation given a defined input spectrum is then calculated, followed by steady state electrostatic potential and carrier concentrations using Poisson's equation and electron and hole continuity coupled partial differential equations (Eq. 2.34, 2.35, 2.36). These equations are solved numerically over the mesh while stepping through a voltage sweep. EQE can also be calculated in this tool by solving the drift-diffusion equations as a function of wavelength [76].

Results of the simulations done in Sentaurus Device can then be plotted and exported using

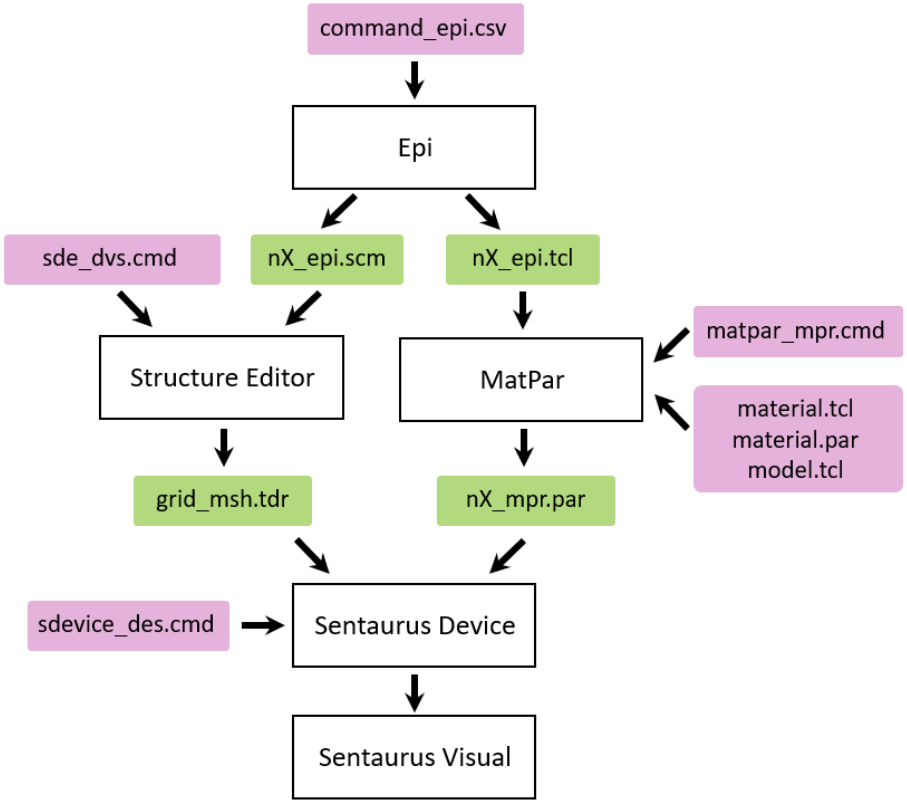

Figure 2.19: Workflow of Sentaurus tools and input and output files, adapted from Ref. [75].

Sentaurus Visual.

For a detailed example of simulating a simple p-n junction silicon solar cell in 1D in Sentaurus, please refer to Chapter 3 of of Ref. [75].

In this thesis, the workflow for simulating solar cells in Sentaurus is more complicated than the picture provided in Figure 2.19. Figure 2.20 outlines the simulation workflow used in this thesis. In order to accurately model bifacial solar cells, which have dual-sided textured surfaces, the computation of optical generation must be calculated first in 3D. This 3D computation involves using a Monte Carlo ray tracing approach with thin-film transfer matrix method (TMM) boundary conditions to handle micron-scale surface textured structures with nanometer-scale conformal thin films. Optical generation must be calculated for both front illumination and rear illumination conditions, and are considered to be linearly additive for when the solar cell is simultaneously illuminated from both sides.

The optical calculation is computed on the smallest repeating unit cell to reduce computational time. A process for converting the resulting 3D generation profile into a 1D profile that can be used for lower-dimensional electrical simulations is described in detail in Refs. [77, 78]. The example Sentaurus project for a monofacial single-sided textured silicon solar cell in Ref. [77] was modified by the author of this thesis to function for bifacial dual-sided textured solar cells.

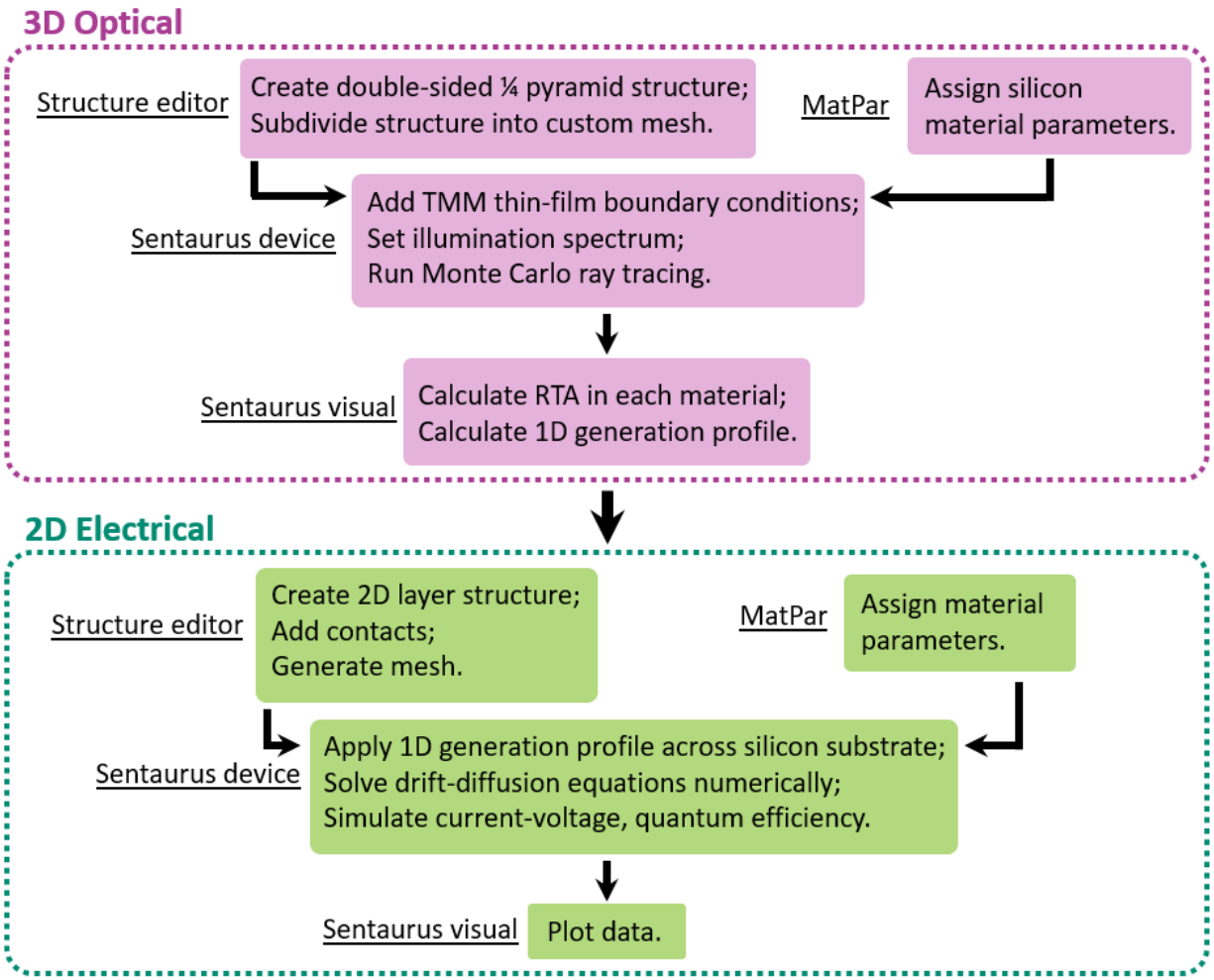

Figure 2.20: A schematic workflow of Sentaurus drift-diffusion modelling for textured bifacial solar cells.

Chapter 3

Fundamentals of bifacial photovoltaics

Bifacial PV collects light on both faces
To enhance energy yields.
There are gains in many places
Especially snow-covered fields.
.
Modifications to traditional designs
Are minimal but required.
New modelling guidelines
Are under-development and desired.

❄ ❄ ❄

Beyond the semiconductor and solar cell physics presented in Chapter 2, additional cell and system-level design considerations must be understood for a broader understanding of their practical application. For this thesis in particular, bifacial photovoltaic designs are discussed.

Bifacial photovoltaics collect light on both front and rear faces by exposing rear-side semiconducting material to light absorption. The first bifacial solar cell design was filed for patent by Hiroshi Mori in 1961 [79]. In the decades following, bifacial solar cells were investigated for use in both terrestrial and space applications [80, 81], with researchers noting the potential cost-benefits of this additional rear-side absorption [81]. Mass commercialization of bifacial modules has now been underway since the 2010s, with bifacial module manufacturing exceeding monofacial manufacturing capacity in recent years to now compose between 80-90% of the world solar cell market share [41].

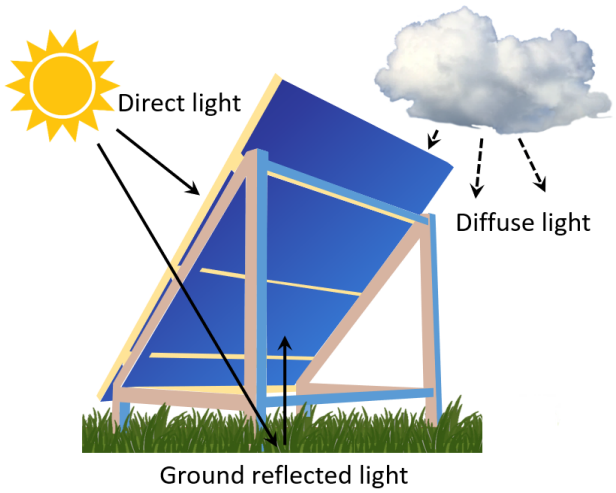

Figure 3.1: Irradiance sources for bifacial PV systems.

Figure 3.1 shows a sketch of a bifacial module, as viewed from the rear. Direct-beam, diffuse, and ground-reflected light can be absorbed on both front and rear faces. This additional absorption results in a bifacial gain, $\mathcal{B}$:

$$\mathcal{B} = \frac{EY_{bi} - EY_{mo}}{EY_{mo}} \tag{3.1}$$

where EY_{bi} is the energy yield of a bifacial module or array and EY_{mo} is the energy yield of an equivalent monofacial module or array. Bifacial gain is often also reported and calculated optically, using incident plane-of-array irradiance [82].

The energy yield bifacial gain of a PV system is fundamentally limited by the bifaciality of the underlying solar cell design. The International Electrotechnical Commission (IEC) Technical Specification 60904-1-2:2019 defines the measurement procedure for bifaciality coefficients φ_{Jsc}, φ_{Voc}, and φ_{Pmp} [83]. Bifaciality coefficients are determined by measuring front-illuminated and rear-illumination current-voltage curves under Standard Test Conditions (STC) (1000 W/m^2, AM1.5, normal incidence, and 25°C):

$$\varphi_{Jsc} = \frac{J_{sc,r}}{J_{sc,f}} \tag{3.2}$$

$$\varphi_{Voc} = \frac{V_{oc,r}}{V_{oc,f}} \tag{3.3}$$

$$\varphi_{Pmp} = \frac{P_{mp,r}}{P_{mp,f}} \tag{3.4}$$

where subscripts r and f refer to rear-illumination and front-illumination, respectively. On module manufacturing sheets often only φ_{Pmp} is reported.

Bifaciality coefficients typically fall between 60-90% due to semiconductor device properties, differences in rear-side metallization patterns, and, in the case of full modules, other rear-side obstructions such as junction boxes [84]. High bifaciality factors may be achieved through the use of high quality c-Si substrates and high-symmetry device design, however, solar cells are designed for optimal performance under front-side illumination, where most light is incident. This often leads to bifaciality factors $<$1.

Including the solar cell design and associated bifaciality coefficients, the bifacial gain of a PV system also depends on a number of system-design and environmental factors. These include the mounting geometry (height, tilt, row-to-row separation, frames), rear-side mounting structure (racking, torque tubes), ground albedo and spatial homogeniety, array design and size, sky conditions, near-by obstructions, and geographical location [85]. Given the wide range of factors that can influence bifacial gain, typical reported values fall in the range of 5-30% [74, 86–88], but may be $>$50% in some cases [80, 89].

In the following sections, the design of common bifacial solar cells, modules, and systems are discussed followed by an introduction to system-level bifacial modelling.

3.1 Solar cell design

The basic components of 1-junction silicon solar cells are a bulk n-doped or p-doped silicon substrate, emitter, back surface field, ARC, and metallization in the form of busbars and fingers. Bifacial solar cells enable the collection of rear-side light by using a metallization pattern of fingers and busbars on the rear-face, in place of the full-surface rear-side metal contact used in monofacial cells. Some common present and historic bifacial silicon solar cell designs are provided in Figure 3.2.

For many decades, Al-BSF technologies dominated the silicon solar cell market, using mc-Si p-doped substrates with aluminium doping by the rear-side metal contacts to form a back surface field [91]. Bifacial versions of these cells were developed as early as the 1980s [92]. With the dropping cost of high-quality c-Si wafers, PERC technologies entered the market, including bifacial PERC technologies in 2017 [86]. PERC structures have been explored on both p-doped and n-doped substrates [93].

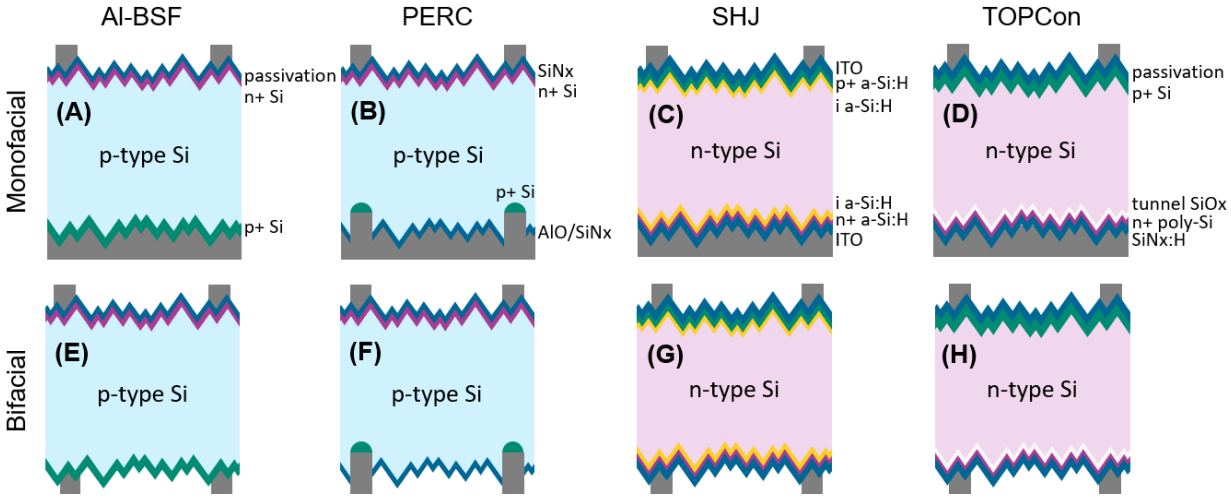

Figure 3.2: A schematic of common monofacial (A-D) and bifacial (E-H) silicon solar cell designs: (A,E) Al-BSF, (B,F) PERC, (C,G) SHJ, and (D,H) TOPCon. Rear-side morphology is shown as textured in all cases, but monofacial designs may be polished flat [90].

	p-type PERC	n-type PERC	SHJ	TOPCon
Bifaciality (%)	60-75	85-90	90-95+	80-90

Table 3.1: Bifaciality of select modern silicon solar cell technologies.

Figure 3.2 also displays some emerging high-efficiency n-type substrate designs, namely SHJ and TOPCon. SHJ designs (also commonly referred to as heterojunction with intrinsic thin-layer (HIT)), were first introduced in 1997, with the patent opening to the public in 2010, resulting in recent adoption [94]. SHJ cells consist of a c-Si substrate with thin-film doped hydrogenated amorphous silicon (a-Si:H), thin-film intrinsic a-Si:H, and transparent conducting oxide (TCO) layers on both front and rear faces [95]. Similar to how SHJ cell designs improve bifacial solar cell efficiencies via surface passivation with a-Si:H, TOPCon cells improve rear surface recombination by introducing contact passivation with an ultra-thin layer of silicon dioxide and a thin layer of doped poly-silicon [96]. SHJ and TOPCon solar cell technologies have achieved record monofacial efficiencies between 26-27% to date [97, 98]. With better quality c-Si substrates and new techniques for passivating surfaces, bifacial cell efficiencies have approached that of monofacial cell efficiencies.

The typical range of bifacialities of modern bifacial solar cell structures is provided in Table 3.1, with values based off Ref. [94] and Ref. [86].

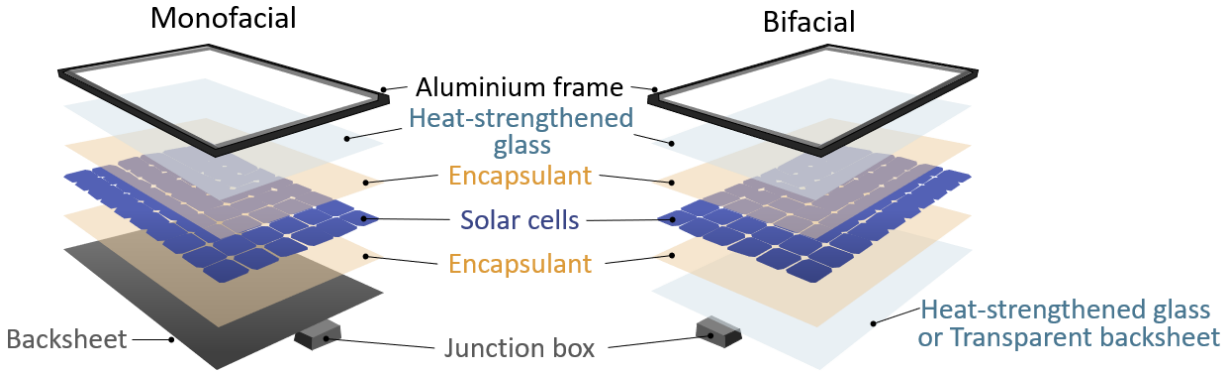

Figure 3.3: Module components and layers for monofacial and bifacial modules.

3.2 Module design

Solar cells are electrically connected in series and parallel and then packaged to make PV modules. Modules typically consist of three strings of cells, each containing a bypass diode, as visualized above the module in Figure 3.4. Bypass diodes protect individual solar cells from entering reverse bias breakdown. Current is able to flow through a bypass route in the diode in the scenarios where module shading would otherwise cause high reverse biasing.

After electrical connection, solar cells must be encapsulated using an encapsulant such as ethylene-vinyl acetate (EVA) or a polyolefin elastomer (POE), and then structural support and rigidity is supplied by application of heat-strengthened or tempered glass. For monofacial modules, an opaque rear-side backsheet is used to seal the module within an aluminium frame. In the case of bifacial modules, this opaque backsheet is replaced with either a transparent backsheet or another layer of heat-strengthened glass (referred to as glass-transparent backsheet, or glass-glass modules, respectively). Figure 3.3 shows the main layers and components of monofacial and bifacial PV modules. A junction box contains the electrical wiring connections for the module, and is often placed on the rear-side of modules. The optimum design and placement of junction boxes for bifacial PV is an active area of research [99, 100].

Modules with half-cut cells are being adopted by industry, where solar cells are diced and connected in series. This reduces resistive losses in the module string, and can create a module which is more tolerant to non-uniform illumination [101]. However, unpassivated raw cell edges can also result in power loss if the edge-to-area ratio becomes too high [101].

Frameless modules have also been explored in recent years, as these modules reduce self-shading. Frameless modules, however, can come with mechanical and durability challenges [102].

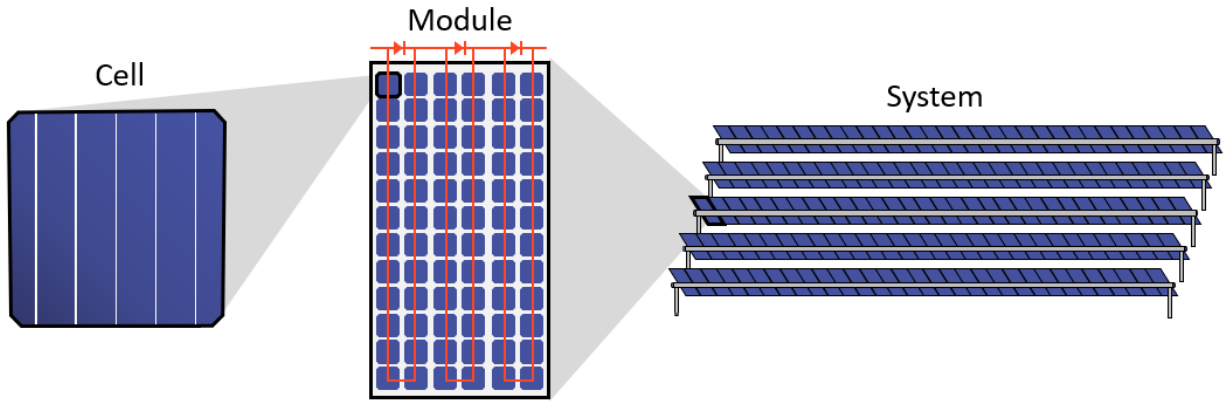

Figure 3.4: Diagram showing how PV cells get packaged into modules which then become deployed PV systems. Bypass diodes are shown above the module for illustrative purposes.

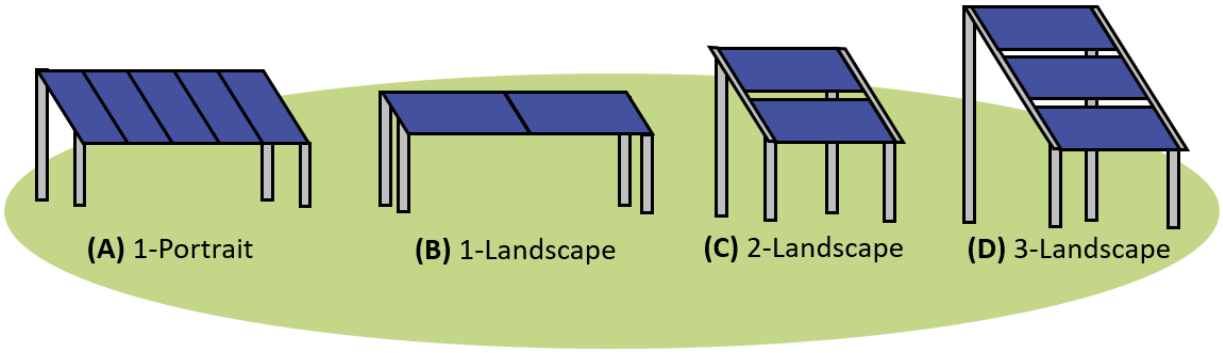

Figure 3.5: Schematic diagram of various portrait and landscape PV mounting architectures, with varying tier number.

3.3 System design

PV systems are composed of a series of electrically connected modules, with the modules composed of electrically connected PV cells. This is visualized in Figure 3.4.

Modules are commonly mounted in PV systems in a few different configurations: "in portrait", "in landscape", and with or without multiple tiers. Some example configurations are shown in Figure 3.5. For example, a "1-in-portrait" or 1-P PV system refers to a single level of modules mounted with their short-side closer to the ground. A "2-in-landscape" or 2-P system refers to two tiers of modules mounted in the same row with their long-side closer to the ground.

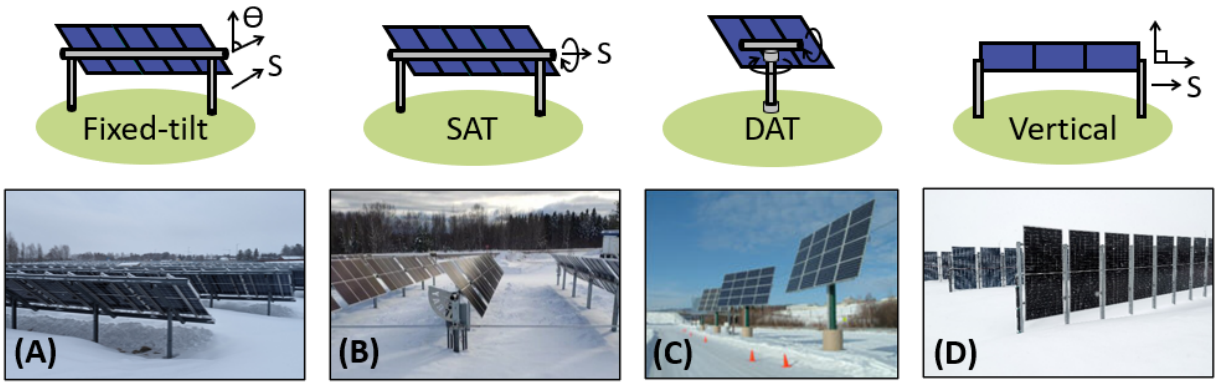

Figure 3.6: Common PV system configurations. (A) A south-facing fixed-tilt site located in Luleå, Sweden, photographed by the author. (B) A SAT site located at Michigan Technological University [103]. (C) A DAT site located in Fairbanks, USA [104]. (D) A east-west vertical bifacial site located in Luleå, Sweden, photographed by the author.

PV systems may either be mounted at a fixed-tilt, or in a configuration that allows for sun-tracking, depending on factors such as the projected levelized cost of electricity, available land, and reliability concerns. Some common PV configurations with example site photographs is provided in Figure 3.6.

Fixed-tilt systems are commonly deployed facing the equator (south-facing in the northern hemisphere, north-facing in the southern hemisphere) at a tilt from horizontal around the location latitude. This leads to a peak in PV production at solar noon. Fixed-tilt systems may also be deployed in various other configurations, including being mounted at low tilt on roof-tops, against the façades of buildings, or even vertically like a fence. East-west oriented bifacial vertical fixed-tilt PV systems have been deployed in recent years in small-scale arrays of $<$1 MW. E-W vertical systems offer some potential advantages compared to traditional equator facing fixed-tilt designs, discussed further in Section 4.4 and Chapter 6.

For tracked PV systems, modules must be mounted on rotating racking structures. In the case of horizontal single-axis trackers (SATs), modules commonly rotate from the east to the west along a torque tube, resulting in a horizontal tilt at solar noon. Double-axis tracker (DAT) systems introduce an additional degree of freedom to track the sun similar to a sunflower.

Example PV production curves throughout a day for these system configurations is modelled and plotted for reference in Figure 3.7 for a clear-sky day in June in Whitehorse, Yukon. Energy yield is modelled in Dual-sided Energy Tracer (DUET) [105] for a central module in a utility-scale array using typical meteorological year (TMY) data from the Canadian Weather-year for Energy Calculation (CWEC) database. All modules are bifacial with a bifaciality of 75%.

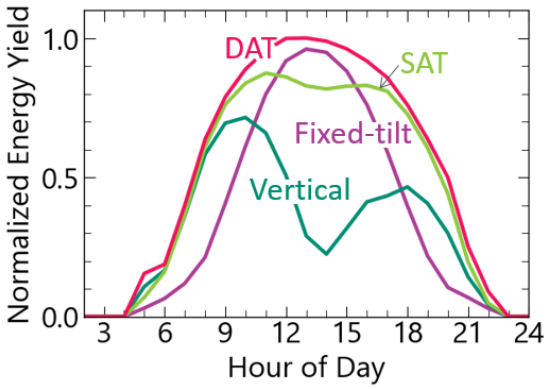

Figure 3.7: Clear-sky day PV module production curves for a south-facing latitude-tilt fixed-tilt system, E-W vertical system, SAT system, and DAT system for June 15th in Whitehorse, Yukon. Energy yield is normalized to peak with the DAT production peak. All systems are modelled as bifacial.

The DAT PV production curve acts as a rough envelope for the maximum possible energy yield due to tracking. In practice, rotation limits and sub-optimal tracking practices on non-flat terrain or during cloudy days can reduce this modelled envelope [106]. Due to reaching a horizontal tilt at solar noon, which increases cosine losses, the SAT energy yield slightly decreases at solar noon. Both the DAT and fixed-tilt systems experience an energy yield peak at solar noon. E-W vertical systems, as a contrast, experience two peaks during daily clear-sky operation: one in the morning associated with sunrise in the east, and one in the evening associated with sunset in the west. SAT system production similarly remains high in the morning and afternoon due to east-west rotation capabilities. As a final note, vertical PV production reaches a minimum at solar noon due to grazing angles-of-incidence on the vertical modules leading to large reflection losses.

3.4 System modelling

Modelling of PV systems is critical for the design, financial analysis, and monitoring of PV deployments. The modelling of bifacial PV is particularly challenging due to the need for robust methodologies for capturing the optical and electrical effects of rear-side irradiance. This is a complex problem due to the inhomogeneous spread of irradiance over module surfaces, which is particularly prevalent for the rear-face in tilted or tracked systems [85]. Rear-side electricity production is not simply proportional to optical gain either, it is reduced by the bifaciality factor

of the module (described by Eqs. 3.2, 3.4, and 3.3) and can further incur electrical mismatch losses in the system [107]. Rear-side shading and irradiance will change over the course of a day, season, and depending on location and surrounding environment.

3.4.1 Sky models

In order to calculate the amount of incidence plane-of-array irradiance on the front and rear faces of bifacial modules, a method for translating measured GHI, DNI, and DHI is required. If measurements of DNI and DHI are not available, decomposition models using measured GHI may be used [108, 109].

The modelling of diffuse-sky contributions to plane-of-array irradiance is particularly complex due to the wide range of sky conditions that can occur to generate a measured value of DHI, and diffuse radiation is, by nature, not well-defined to a specific location. Thus, diffuse sky models are required to simulate the distribution of DHI across the sky-dome.

Many models exist for simulating the distribution of diffuse irradiance across the sky [110], however, by far the most common sky models employed by PV modelling platforms are either the 1993 Perez sky model [111] or the 1990 Perez sky model [112]. In both models, the diffuse sky is separated into three main components: a circumsolar region, a horizon region, and the remainder of the sky dome. These irradiance components are visualized in Figure 3.8. The total irradiance of the diffuse sky, when summed, is equal to the DHI.

In the more recent version of the Perez model (1993), cloudy conditions are accounted for by adjusting five empirical coefficients describing the luminance distribution for different sky clearness indexes [111]. The coefficients adjust the relative intensity and shape of the horizon-zenith gradient, the circumsolar region, and the effect of backscattered light off the surface of the Earth. These coefficients were determined using measured sky scans in Berkeley, California. It has been shown that locally-optimizing the Perez model coefficients can significantly improve model accuracy [110].

3.4.2 Irradiance transposition models

Techniques for calculating irradiance transposition given a diffuse sky model and measurements of GHI, DNI, DHI, fall into three main categories: empirical models, view factor (VF) models, and ray tracing models. As we will see in Section 3.4.4 for the DUET model, there may be other techniques outside of these three main categories as well, though they are less common.

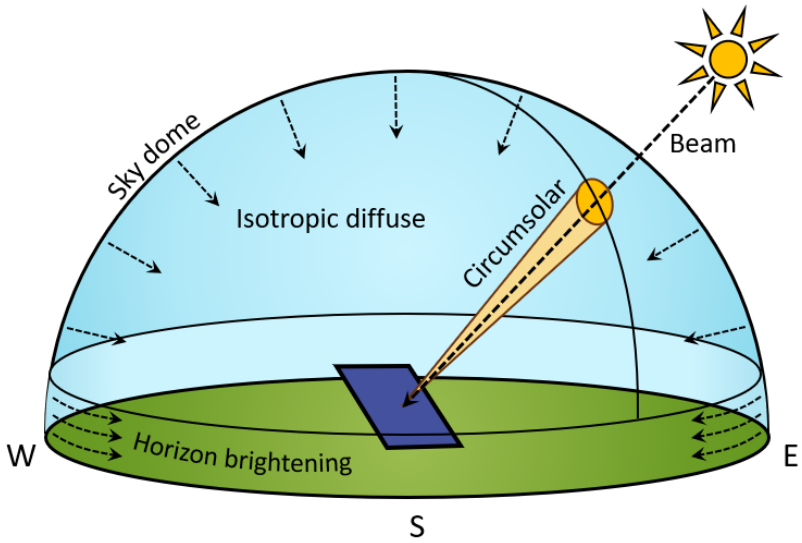

Figure 3.8: A schematic of the Perez sky model with beam irradiance, circumsolar irradiance, isotropic diffuse irradiance, and horizon brightening effects labelled.

Empirical models

Empirical models may be used to calculate PV plane-of-array irradiance by relating measured irradiance components (GHI, etc.) to incident module irradiance using experimental data. Some empirical PV models exist for predicting bifacial gain, requiring a simplified set of inputs such as only albedo, clearance height, module tilt, and ground coverage ratio [84]. While useful for their simplicity, empirical models cannot compete with the accuracy of models which require more thorough inputs and model the specific geometry, electrical parameters, and locations of PV deployments.

View factor models

View factor models calculate the radiation transfer between two surfaces, with the "view factor" being the fraction of emitted energy from one surface which is incident on the other [113, 114]. This is visualized in Figure 3.9A. In a 2D view factor model, the radiation transfer is calculated in a reduced dimension by assuming rows of modules are of infinite extent. This allows for fast computation time and is suitable for studying the performance of central PV modules within utility-scale arrays. Several PV modelling platforms make use of 2D view factor models for calculating bifacial PV performance, including PVSyst [115], the System Advisor Model

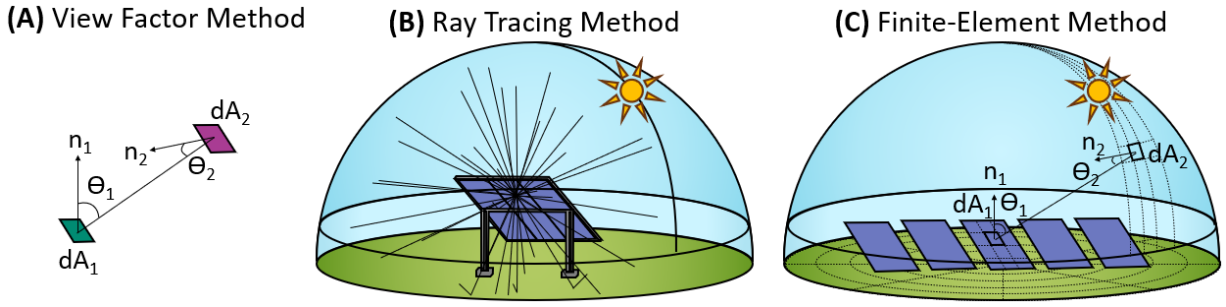

Figure 3.9: Visualization of (A) view factor methodology, (B) ray tracing methodology, and (C) finite-element methodology for irradiance transposition.

(SAM) [116], and bifacialVF [117]. 3D view factors, on the other hand, solve numerically the radiation transfer between surfaces to capture the effects of finite array size, demonstrated in Ref. [118] and Ref. [119].

Examples of view factor calculations for some example simple surfaces may be found in Ref. [84] and Ref. [120].

Ray tracing models

Ray tracing algorithms rely on the concept of light 'rays' where individual light ray reflection, transmission, and absorption properties are traced within a 3D scene. The geometry of the 3D scene must be constructed given user inputs, and material properties governing reflection, transmission, and absorption are assigned to each object within the scene. Backwards ray tracing algorithms may be used to map the irradiance transfer outward from objects of interest. This method decreases computation time by focusing on sampling ray paths relevant to the object of interest [121]. A simple visualization of backward ray tracing is shown in Fig. 3.9B for a PV system. The 3D nature of ray tracing techniques allows for modelling edge effects and the effects of complex shading structures, particularly relevant for rear-side irradiance calculations with racking.

Ray tracing models have been implemented for the PV field in, for example, bifacial_radiance [122] and SunSolve Yield [123]. Due to computational complexity, ray tracing simulations require the use of high performance computers or cloud computing capabilities.

3.4.3 Electrical models

In addition to the plane-of-array irradiance calculated using irradiance transposition models, another critical input parameter for modelling PV system energy yield is the solar cell operating temperature.

A variety of PV thermal models exist in the PV field. A few common empirical temperature models are the nominal operating temperature (NOCT) model [124], the Faiman model [125], and the Sandia model [126]. In the NOCT model, operating cell temperature, T_{cell}, is calculated to linearly increase with incident irradiance, G, given the module manufacturer reference temperature, T_{NOCT}:

$$T_{cell} = T_{amb} + \frac{(T_{NOCT} - 20)}{800} G \tag{3.5}$$

where T_{amb} is the ambient temperature of the outdoor PV deployment, and T_{NOCT} is measured under 800 W/m^2 with ambient temperature 20°C and wind speed of 1 m/s.

In the Sandia model, a distinction is created between the module operating temperature, T_{mod}, as measured from the module glass, and the underlying solar cell temperature. The cell operating temperature is then calculated as a function of plane-of-array irradiance, ambient temperature, wind speed, v_w, and two empirical coefficients, a and b. Coefficients a and b correspond to either open-rack or roof-mounted systems, and either glass-glass or glass-backsheet packaging [126]. The equation for determining cell temperature with the Sandia model is:

$$T_{cell} = T_{amb} + G(e^{a+bv_w}) + \frac{G}{1000} \Delta T \tag{3.6}$$

where ΔT=3°C for bifacial modules.

The Faiman model also relies on two coefficients, U_0 and U_1, corresponding to a constant heat transfer coefficient and a convective heat transfer coefficient, respectively [125]. Cell temperature is calculated as:

$$T_{cell} = T_{amb} + \frac{G}{U_0 + U_1 v_w} \tag{3.7}$$

where values of U_0 and U_1 are available for seven different types of glass-backsheet modules [125].

A few simple models for computing the electrical output of PV models given plane-of-array irradiance and operating temperature exist. In the approach applied by PVSyst [113, 114], a single-diode model is used to determine maximum power where the current is determined simply by the product of the incident plane-of-array irradiance and a solar cell technology responsivity.

Additional loss factors, such as electrical mismatch and soiling, must be applied following this calculation.

In PVWatts [127], the DC power of the PV array is calculated given the module nameplate power rating, P_{rated}, and efficiency temperature coefficient, γ:

$$P_{dc} = \frac{G}{1000} P_{rated} [1 + \gamma(T_{cell} - 25)] \tag{3.8}$$

where P_{rated} is measured at STC with 1000 W/m^2 and 25°C. Similar to PVSyst, loss mechanisms, such as shading, soiling, snow accumulation, mismatch, and degradation, are applied given default or user-defined values [127].

PV module current-voltage behaviour can instead be determined more accurately by calculating individual IV curves for the module cells and following Kirchoff's Laws. For example, PVMismatch is a python package which computes module IV curves from cell IV curves by appropriately summing cell IV curves in parallel and series, based on PV equivalent circuit theory [128, 129]. Cell current-voltage behaviour is modelled using either a 1-diode model (Eq. 2.50 or Eq. 2.54), or a 2-diode model. In the 2-diode approach, recombination is accounted for by having two 1-diode terms, one with an ideality factor of 1 and the other with an ideality factor of 2. In this model, bypass diodes are treated as perfect conductors in the case when the cell substring voltage is less than the bypass diode trigger voltage and perfect insulators otherwise. Modelling approaches, such as that employed by PVMismatch, can account for effects of shading and irradiance non-uniformity and thus, do not rely on user-estimates or default values.

In this thesis, modelling is completed on individual modules situated within larger PV arrays. For modelling the power output of multiple strings of modules or full arrays, further calculations can be done to combine module IV curves and account for effects such as maximum power point tracking algorithms and DC-to-AC conversion.

3.4.4 Select bifacial photovoltaic models

The bifacial PV models employed in this thesis are briefly described below. Table 3.2 summarizes some key capabilities of the models, including versions used throughout thesis simulations and a comparison of computation time. With the exception of DUET, models have been used solely for their optical capabilities.

PVSyst

PVSyst is a commercial PV software package used commonly in the PV industry to model system performance and determine system sizing for stand-alone and grid-connected systems [115].

	PVSyst	bifacialVF	SAM	bifacial_radiance	DUET
Main algorithm	2D VF	2D VF	2D VF	Ray tracing	3D finite-element
Spectral albedo	✗	✗	✗	✓	✗
Specular reflections	✗	✗	✗	✓	✗
Rear-irradiance non-uniformity	✗	✓	✓	✓	✓
Rack shading	✓[1]	✗	✗	✓	✓
Edge effects	✗	✗	✗	✓	✓
Data resolution	Hourly	Sub-hourly	Sub-hourly	Sub-hourly	Sub-hourly
Albedo resolution	Monthly	Sub-hourly	Sub-hourly	Sub-hourly	Sub-hourly
Speed (time/timestamp)[2]	<1 s	3 s	<1 s	6 s	6 s
Version used	v7.4.8	v0.1.8.1	v4.2.0	v0.4.2	v0-research

Table 3.2: Bifacial photovoltaic models.

PVSyst uses a 2D VF approach coupled with a single-diode module model to calculate PV system performance. Loss factors, such as electrical mismatch, soiling, and rear-irradiance non-uniformity, are applied in the model using user-defined or default correction factors.

bifacialVF

BifacialVF is an open-source python-based bifacial PV software developed by NREL for calculating optical properties of PV systems under infinite row length assumptions [117]. The model uses a 2D view factor approach for solving 1D linescans of front and rear plane-of-array irradiance per timestamp, based off user-input geometry and weather files. Some electrical modelling abilities are possible using a bilinear interpolation code add-on [130, 131], available on the bifacialVF GitHub.

[1] Speed test was completed on a Windows 10.0 Dell OptiPlex 7020 computer with an Intel Core i5-4690 processor (4 cores) and 16GB of RAM.

[2] Rack shading is not calculated by the program, but can be implemented by defining a structure shading factor.

The System Advisor Model

SAM is a performance and financial model developed by NREL used to simulate a variety of energy systems, including PV, wind, geothermal, battery, and hybrid systems [116]. PV modelling is completed using a 2D view factor model. Grid-tied electrical modelling is then carried out using PVWatts [127] based off user or library-defined module and inverter specifications.

bifacial_radiance

Bifacial_radiance is an open-source python wrapper using the ray tracing software RADIANCE which calculates non-uniform 2D irradiance profiles on the front and rear sides of PV modules within a 3D scene [122]. Developed by NREL, bifacial_radiance can evaluate the 2D irradiance profiles of any select module within a user-created PV array, including effects such as rack shading, nearby obstructions, and edge-effects. The RADIANCE ray tracing algorithm uses a backwards ray tracing approach with rays generated stocastically using a Monte Carlo algorithm. Bifacial_radiance uses PVMismatch software for computing power output and electrical mismatch [128, 129].

DUET

DUET, developed internally by the University of Ottawa with lead development by A. Russell [105], is a 3D PV performance model which uses a numerical finite-element method to solve 3D view factor algebra. Irradiance transposition is calculated by segmenting the 3D scene, including the sky, ground, and PV array, into a mesh of elements, as visualized in 3.9C. Radiation transfer is calculated between, for example, the ground and the rear-side of a bifacial module by calculating the summation of partial view factors from all ground elements to all rear-module surface elements. Details on these calculations can be found in Ref. [120].

3D shading calculations are completed in the model using a ray-intersection algorithm, which verifies whether the path between emitting radiation elements and non-emitting elements in the scene are blocked by shading objects, such as the module frame or racking [105]. The emitted ray can be completely or partially blocked by the shade object, depending on the material transparency.

Electrical behaviour is solved using an approach similar to the 1-diode IV summation approach described for PVMismatch in Section 3.4.3. STC short-circuit current is solved by multiplying the total incident power on the module by the module bifaciality and responsivity. Correction factors which account for variations in spectrum can be applied at this stage. The

current is then adjusted according to the current temperature coefficient of the module and the operating cell temperature. Operating cell temperature can be calculated in DUET using the NOCT, Faiman, or Sandia models described in Section 3.4.3. Current-voltage curves are then calculated using a 1-diode model as in Eq. 2.54, and cell IV curves are combined using equivalent circuit theory to determine module IV curves.

DUET can model the effects of half-cut cells as well as varying internal electrical wiring schemes on output module power. Dynamic optical and module IV curves are computed for each timestamp given user-input weather and solar resource files. Typically, calculations of energy yield are computed using TMY data. Annualized and per timestamp PV performance metrics, such as calculated plane-of-array irradiance, bifacial gain, electrical mismatch, and energy yield, are output into data files. Figure 3.10 summarizes the main simulation workflow in DUET.

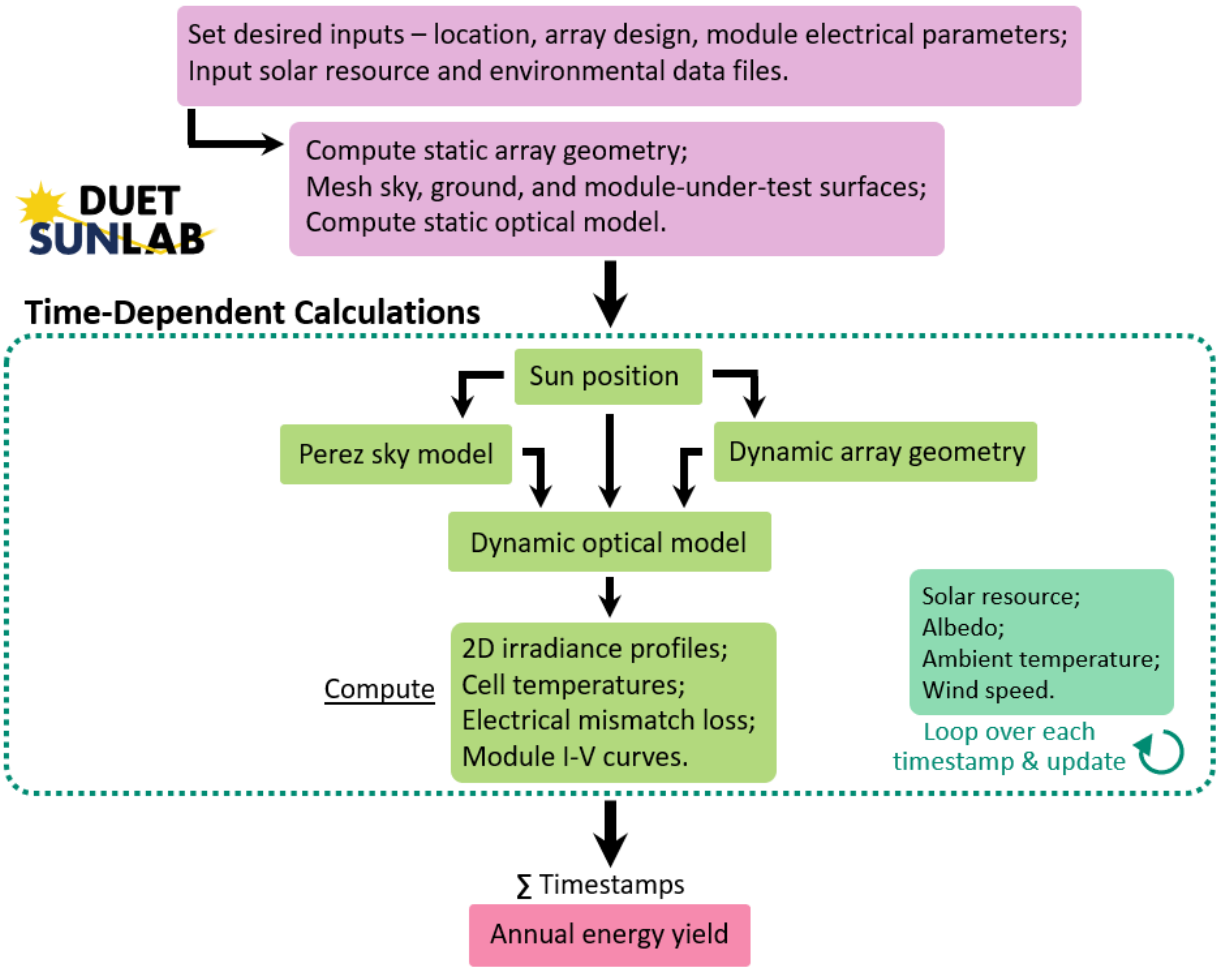

Figure 3.10: Schematic workflow of DUET, adapted from [105].

Chapter 4

High latitude environmental conditions

Northern environmental conditions
Include strong variation with season,
Significant snowfall traditions,
And temperatures that are freezin'.

❄ ❄ ❄

With the emergence of PV systems in northern high latitudes, it is crucial to understand the impact of unique northern environmental conditions on PV system performance, data collection, modelling, and reliability. The potential for solar PV in high latitude regions benefits from and is challenged by the unique physical characteristics of these regions. In contrast to lower latitudes, high latitude regions are characterized by:

- Dramatic seasonal variation
- Low solar elevation and large range of solar azimuth
- Higher diffuse fractions and less UV light
- High albedo from snowfall
- Lower average ambient temperatures

Key high latitude environmental physical characteristics are presented in the following subsections: available solar resource, ambient temperature, and snowfall.[1]

[1]Note: Sections 4.1, 4.2, and 4.3 are the first draft contribution to an international collaborative review paper on the opportunities and challenges associated with high latitude photovoltaics, led by Erin Whitney, Director of the Arctic Energy Office in the US Department of Energy.

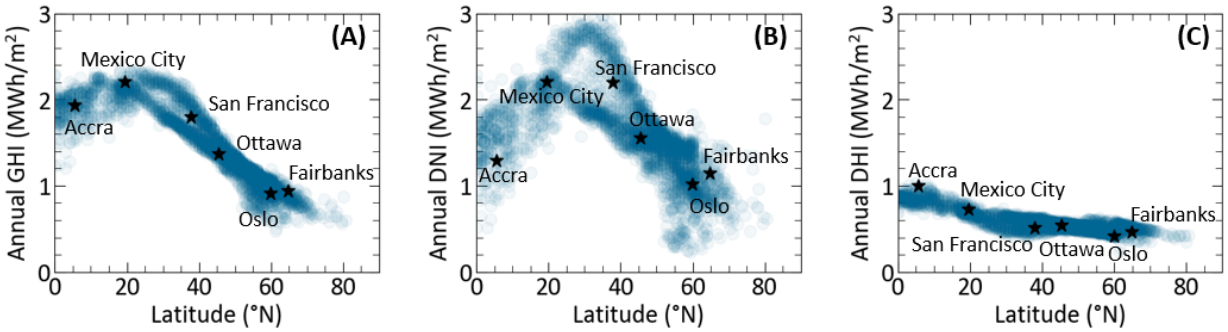

Figure 4.1: Annual (A) GHI, (B) DNI, and (C) DHI as a function of latitude for ∼3000 locations. Labeled stars indicate example locations of Accra (Ghana), Mexico City (Mexico), San Francisco (USA), Ottawa (Canada), Oslo (Norway), and Fairbanks (USA).

4.1 Available solar resource

Annual solar irradiance components of GHI, DNI, and DHI are presented in Figure 4.1 for ∼3000 locations using hourly TMY files from the National Solar Radiation Database (NSRDB) [132]. A few example locations are indicated in the subplots by labeled black stars. On an annual basis, the total amount of terrestrial solar insolation decreases as a function of latitude for GHI, DNI, and DHI. This is largely driven by a decrease in solar resource during winter months caused by the axial tilt of the Earth relative to our orbit around the sun. Figure 4.2A demonstrates the cumulative GHI in three locations of differing latitudes (25°N, 45°N, and 65°N) on a monthly basis. Seasonal effects are much more extreme for high latitudes, with the sun staying below the horizon at winter solstice for latitudes at and above the Arctic Circle (66.56°N).

The seasonal effects of solar resource is shown in Figure 4.3A-D with monthly average solar insolation plotted for March, June, September, and December of 2023. The geographical data for making these plots was downloaded from the NASA Earth Observations website [133]. These subplots show the effect the length of daylight has on insolation patterns. Near the summer solstice (June), high latitude regions are bathed in a large amount of solar irradiance. In contrast, during the winter near the winter solstice (December) little to no insolation occurs.

The relative position of the sun in the sky over time follows a significantly different pattern in high latitudes than at lower latitudes. To further characterize the effects of solar position, the function *get_solarposition* in pvlib was used [134]. Figure 4.4 shows latitude trends for solar resource and sun path during the summer solstice, spring or fall equinox, and winter solstice. Fig. 4.4A-E shows the solar elevation angle and solar azimuth traced by each day for locations between 20-80°N. The length of daylight, maximum solar elevation angle, and range in solar

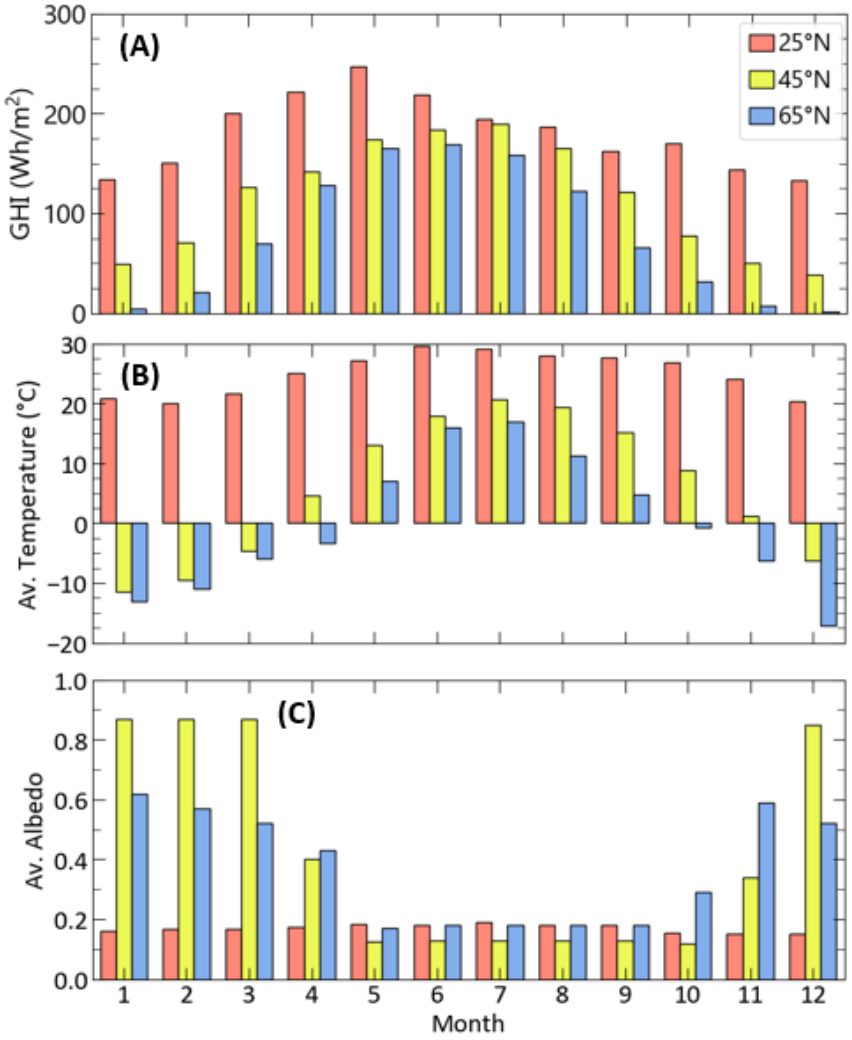

Figure 4.2: Monthly (A) GHI, (B) average ambient temperature, and (C) average albedo for three example locations: Culiacán, Mexico (25°N), Ottawa, Canada (45°N), and Fairbanks, USA (65°N).

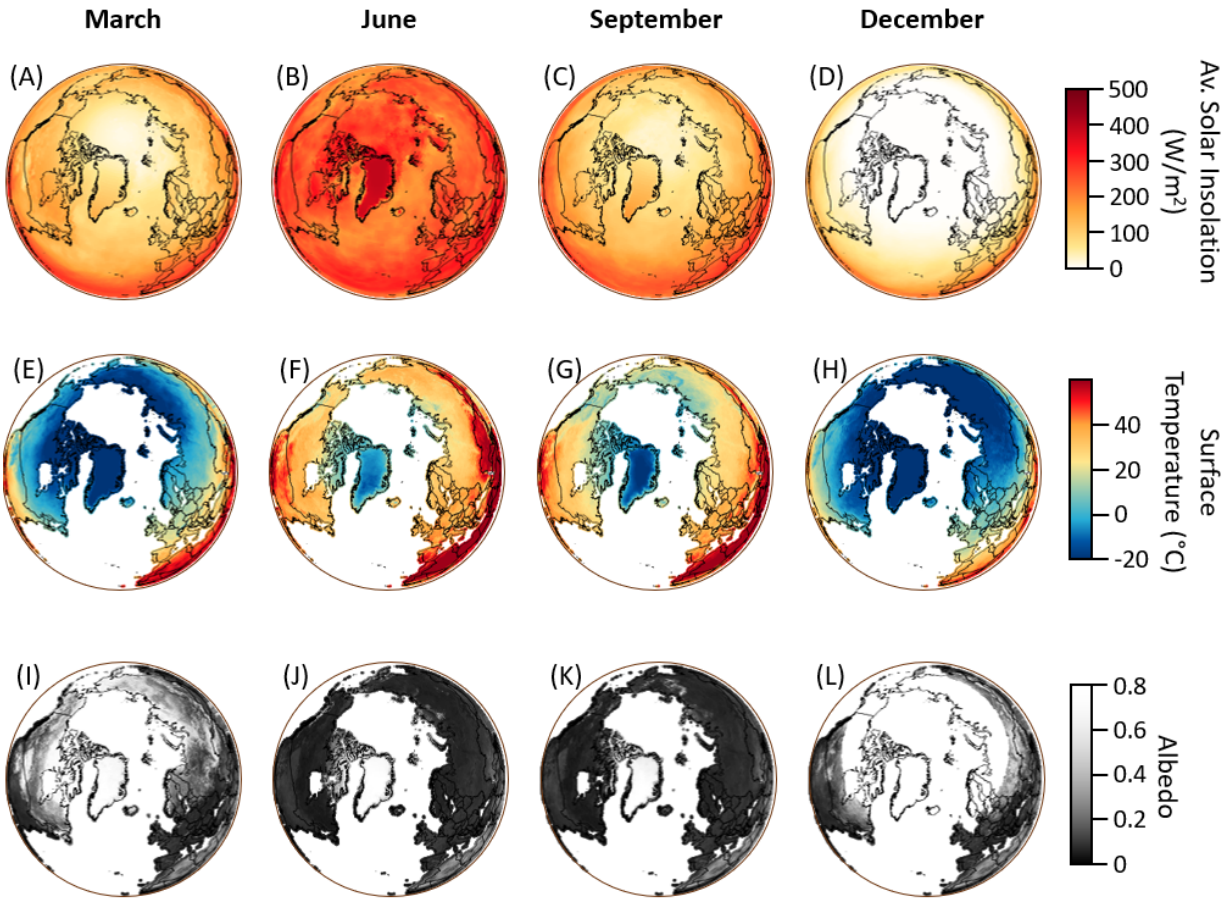

Figure 4.3: Average monthly map of the northern hemisphere for (A-D) solar insolation, (E-H) surface temperature, and (I-L) albedo for March, June, September, and December. Data for creating these plots was retrieved from Ref. [133].

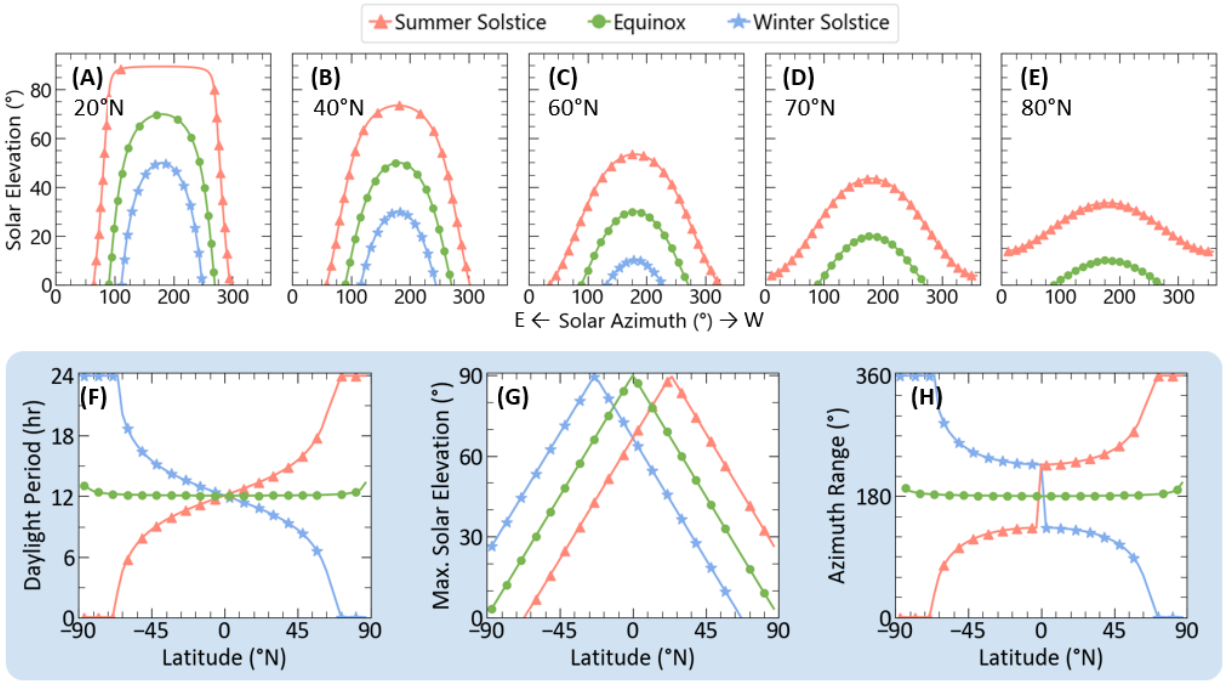

Figure 4.4: The solar elevation angle and solar azimuth for (A) 20°N, (B) 40°N, (C) 60°N, (D) 70°N, and (E) 80°N locations during the summer solstice, spring or fall equinox, and winter solstice. (F) The length of daylight, (G) maximum solar elevation, and (H) range of azimuth angle traversed by the sun for each day as a function of latitude.

azimuths for the solstices and equinox are provided as a function of latitude in Fig. 4.4F-H. Above 60°N, there is an extreme difference in day length at the solstices, very low solar elevations, and very large solar azimuth ranges.

Not only does the total amount of annual and seasonal solar insolation change as a function of latitude corresponding to differences in sun path, the spectral contents of the solar insolation tend to change as well. Figure 4.5A demonstrates the annual GHI-weighted average diffuse fraction as a function of latitude for several locations. Diffuse fraction is calculated as a ratio between the DHI and GHI, and tends to increase as a function of latitude, though a wide range of diffuse fractions are observed for locations at similar latitudes. Increasing diffuse fraction is an indicator of frequent cloudy conditions. An example measured cloudy spectrum is provided in Figure 4.5C with a clear-sky spectrum, both normalized at 500 nm. The cloudy spectrum demonstrates a shift in spectral content compared to clear-sky atmospheric absorption.

Figure 4.5B shows the GHI-weighted annual average clear-sky AM for these same locations.

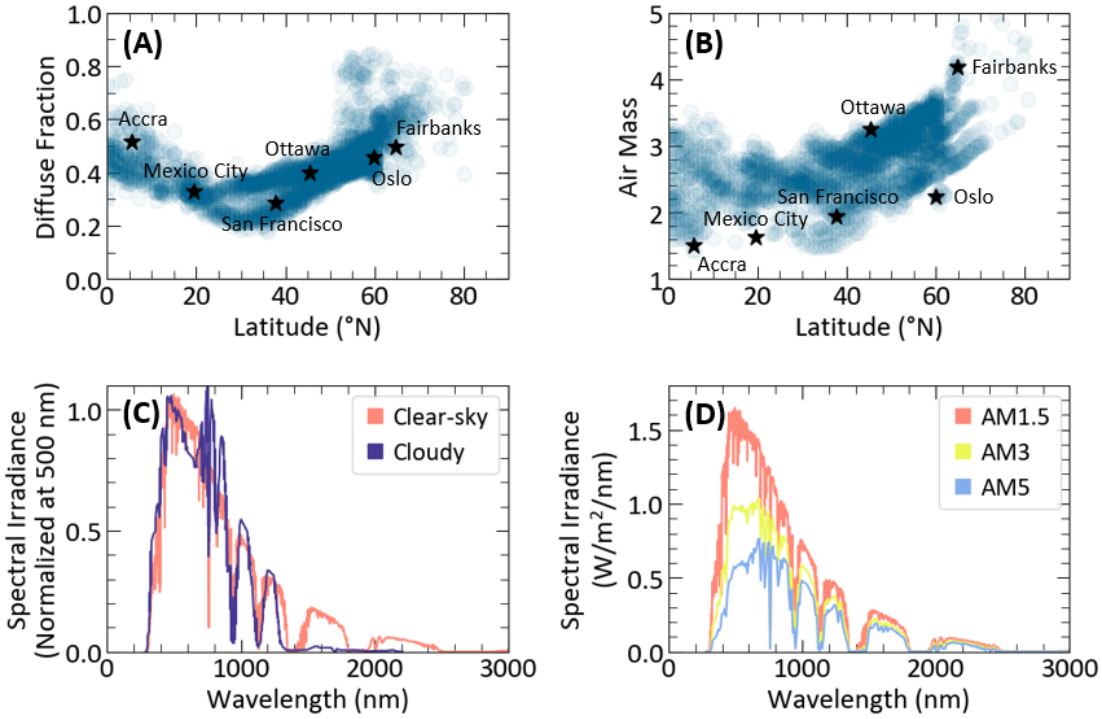

Figure 4.5: Latitude trends for annual GHI-weighted average (A) diffuse fraction and (B) air mass. (C) Example solar spectra for clear-sky and cloudy days. (D) Example solar spectra for AM1.5, AM3, and AM5. The cloudy spectrum is digitized from Ref. [135].

GHI-weighted AM was calculated using pvlib's *get_relative_airmass* function for all hours in a year in each location [134]. Some example air masses are provided in Fig. 4.5D. More annual solar irradiation tends to occur at higher AM for high latitudes, a consequence of lower solar elevation angles. Higher AM shifts the spectral contents of solar irradiation away from the UV and into the IR.

4.2 Ambient temperature

Ambient surface temperature on the Earth tends to decrease as one moves away from the equator and towards the poles. Figure 4.6A shows the annual average ambient temperature for ∼3000 locations using NSRDB TMY files. The 98th percentile TMY measured annual high and low ambient temperatures are provided in subplots Fig. 4.6B/C. Since each month in a TMY dataset may be taken from a different year of historic data to represent a 'typical' year,

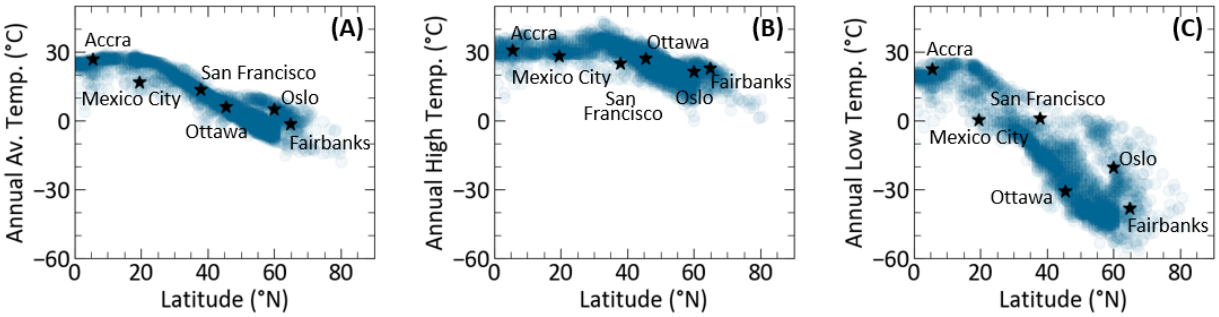

Figure 4.6: (A) Annual average ambient temperature as a function of latitude. The 98th percentile annual temperature (B) high and (C) low in each location's TMY dataset.

these 98th percentile high and low ambient temperatures do not capture extreme or anomalous fluctuations in temperature, which are becoming more common [136].

Surface temperatures are nearly always lower at high latitudes when compared to lower latitude regions regardless of season. Figure 4.2B shows the average ambient temperature for three locations of varied latitude using TMY data. Ambient temperature varies seasonally in all locations, but experiences the most dramatic fluctuations for higher latitude locations. This can also be observed in Fig.4.6, by comparing the annual high and low temperatures to the average temperature. For lower latitude regions, locations tend to have high and low temperatures more similar to their annual average. Higher latitude locations tend to experience more dramatic temperature swings, particularly towards colder temperatures during the winter season when sunlight is scarce. In Fig.4.2B, the monthly average temperature fluctuates by 10°C in Culiacán (25°N) throughout the year while higher latitude locations of Ottawa (45°N) and Fairbanks (65°N) fluctuate by nearly 35°C.

The seasonal effects of ambient surface temperature are shown for the northern hemisphere in Figure 4.3E-H with monthly average temperatures plotted for March, June, September, and December of 2023 using data from Ref. [133]. Near the summer solstice (June), high latitude regions experience their warmest average temperatures due to an abundance of sunlight, compared to the winter solstice month of December. Seasonal differences between equinox months of March and September can be seen, with March experiencing significantly lower temperatures than September due to Earth's seasonal lag caused by the high latent heat of water.

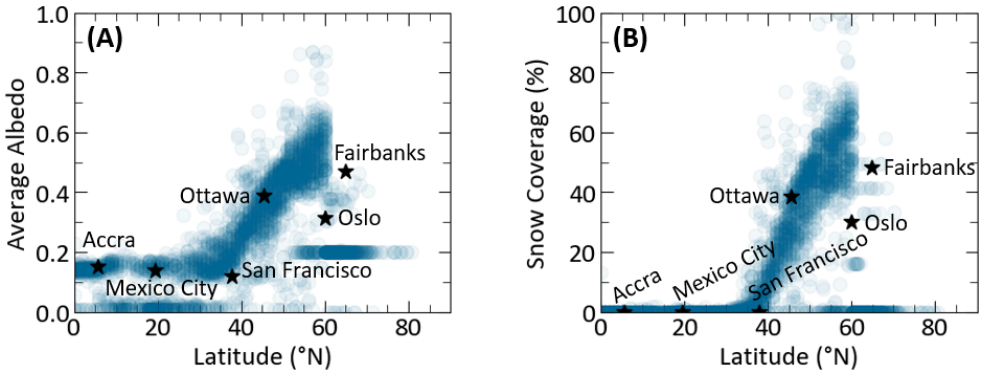

Figure 4.7: (A) Average annual albedo as a function of latitude and (B) percentage of the year with snow coverage.

4.3 Snow

Ice crystals may form in our atmosphere, grow, and eventually tumble to the Earth's surface as snow. Snowfall tends to occur primarily in the northern half of the northern hemisphere, Antarctica, and in high altitude mountainous regions with sufficiently cool temperatures and humidity. Albedo is widely used to characterize the reflectance of the Earth's surface and can be used as a measure for quantifying the presence of snow (see Section 2.5.2).

The annual average albedo and percentage of the year with snow cover for TMY locations is provided in Figure 4.7. Snow coverage is calculated by assuming any timestamp with an albedo >0.5 is due to the presence of snow on the ground. All hours of the year are considered in this calculation, including timestamps with no sunlight. This figure gives an approximate idea of how annual average albedo tends to increase with latitude, driven by periods of snow accumulation during the year. However, the albedo timeseries data provided in TMY files are limited in many cases, particularly for high latitude locations where data availability is low and high quality ground-station or satellite measurements of albedo is sparse. In many cases, albedo is simply assumed to always be 0.2 or 0, leading to a series of locations with average albedos at 0 and 0.2 in Fig.4.7A. This results in erroneously low snow coverage in Fig.4.7B, shown by the data points at 0% for many high latitude locations. A dashed line that continues lower latitude trends into high latitude regions is provided as a guide for the eye in Fig.4.7.

In some cases, a simple binary between fresh snow (albedo=0.85) and non-snow (albedo=0.2) ground cover is also assumed in the datasets [137]. This can lead to an over-estimation of ground albedo [11], as the albedo of snow tends to decay in time due to changes in chemical composition and soiling [138]. The intial albedo of fresh snow may also be different due to

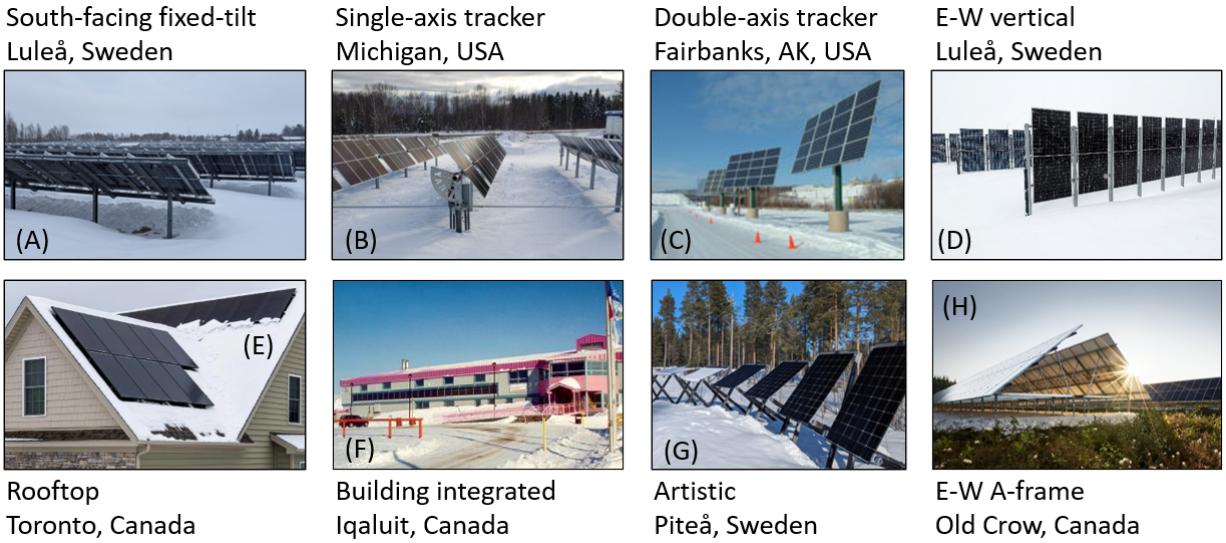

Figure 4.8: A diverse array of photovoltaic system configurations can be found in high latitude regions. (A) A south-facing fixed-tilt PV plant owned and operated by Luleå Energy, photographed by the author. (B) A SAT test-site in Michigan [103]. (C) A DAT test-site in Fairbanks, Alaska [104]. (D) A 100-kW E-W vertical bifacial PV pilot plant installed by the Sunna Group in Luleå, Sweden, photographed by the author. (E) A rooftop PV installation installed by SILFAB Solar in Toronto [140]. (F) PV modules integrated into the façade of the Nunavut Arctic College [32]. (G) An art installation of PV panels called Piteå Solvåg, photographed by the author. (H) The Old Crow solar project, using an E-W A-frame design [141].

variations in temperature, humidity, grain size, and impurity content [68,138,139]. Figure 4.2C shows the average monthly albedo for three locations of varied latitude. For Ottawa at 45°N, a binary albedo assumption can be seen, while the albedo for Fairbanks at 65°N is likely based off ground-station measurements, leading to lower average winter time albedo. In Culiacán, Mexico, the albedo does not vary dramatically with the seasons due to having no snowfall.

Figure 4.3I-L shows the same monthly average map of the northern hemisphere for surface albedo, as measured by Ref. [133]. Close to the North Pole, snow is present on the ground continuously throughout the year, but at more moderate latitudes albedo tends to dramatically fluctuate with the seasons.

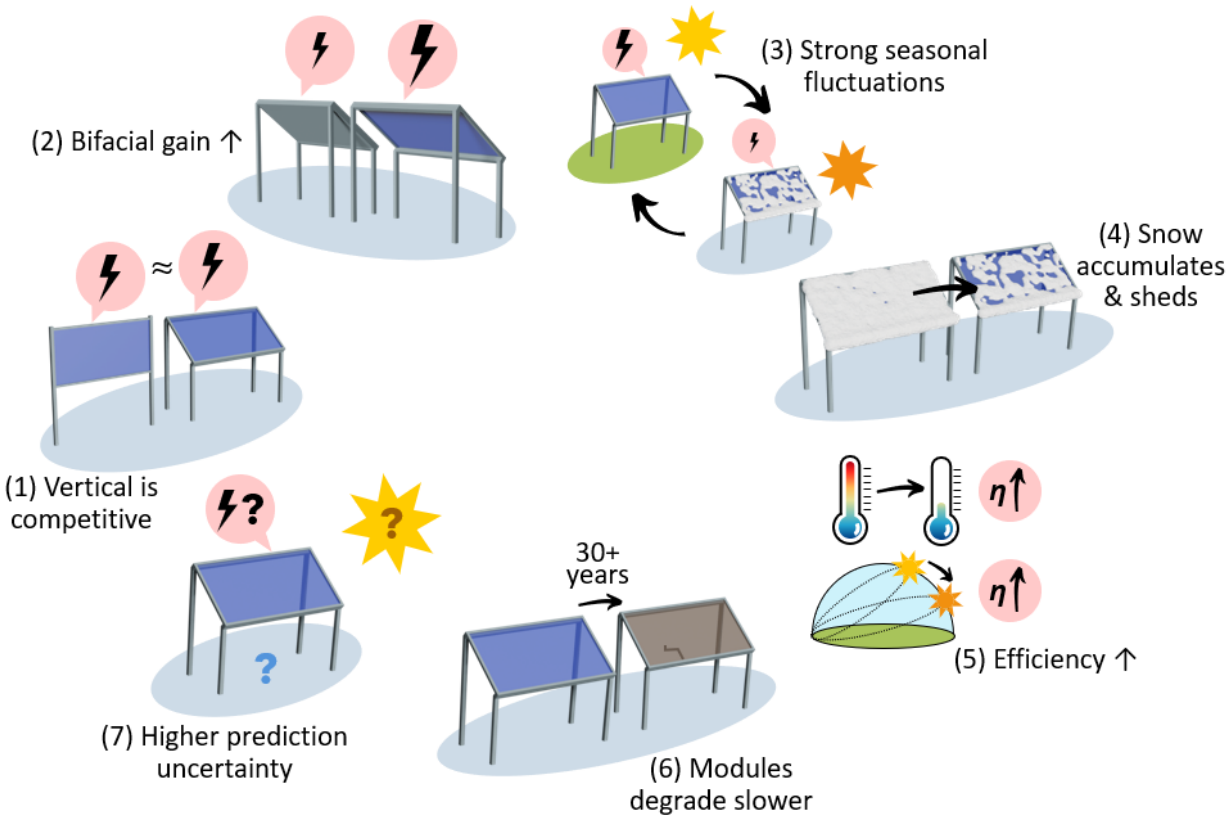

Figure 4.9: Visualization of key technical northern PV performance outcomes, summarized in this chapter.

4.4 Impact on system design & performance

The unique physical characteristics of high latitude regions lead to the use of unique and diverse photovoltaic systems. Figure 4.8 demonstrates eight example PV sites found in snowy climates.

Some key generalized technical impacts of northern PV systems are introduced below and tied into the results of this thesis' journal articles and submitted manuscripts. Figure 4.9 summarizes the discussed impacts visually.

1. Vertical PV systems are competitive

In northern latitudes vertically oriented PV systems, such as that in Fig. 4.8D, become competitive on an annual insolation and energy yield basis compared to traditional south-facing

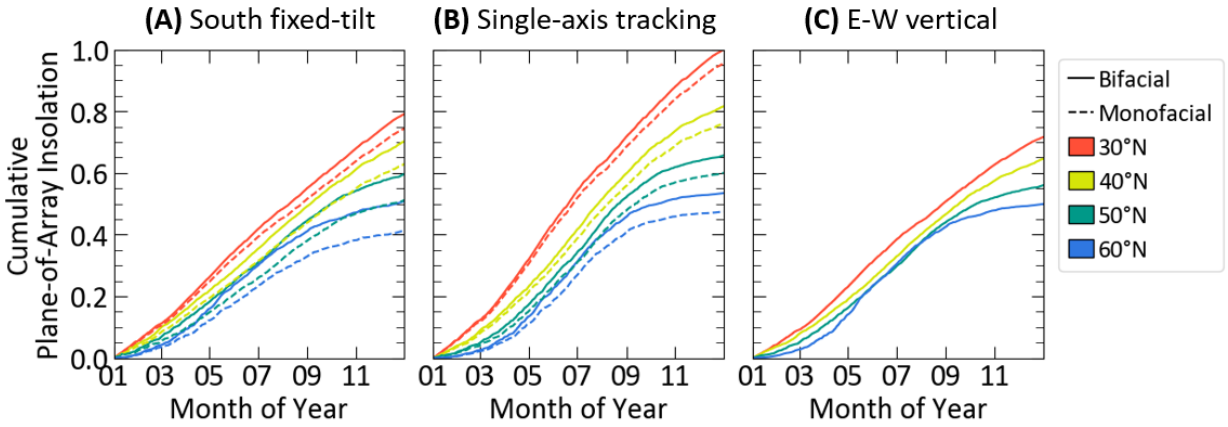

Figure 4.10: Annual cumulative plane-of-array insolation for (A) south-facing fixed-tilt, (B) SAT, and (C) E-W vertical PV modules at different latitudes.

fixed-tilt PV [142–145]. This is driven by the increase in albedo, low solar elevation angles, and tendency to have an increased portion of diffuse light [145]. Vertical systems are additionally being explored in northern environments due to their ability to better load-match and improve building self-consumption in the case of building-integrated façades or low-profile rooftop arrays [143, 146–148].

In addition to competitive annual insolation, vertical arrays have the added benefit in northern environments of substantially reducing snow accumulation effects. Soiling effects from snow and dust have been shown to be low or near zero for vertical PV in recent studies [147, 149]. This effect is additionally observed in the manuscript presented in Section 6.3 of this thesis.

Figure 4.10 shows the cumulative plane-of-array insolation received on south-facing fixed-tilt, SAT, and E-W vertical PV modules in different locations (Hermosillo - 30°N, Golden - 40°N, Regina - 50°N, and Churchill - 60°N). These results were modelled using TMY data in SAM (for a description of SAM, see Section 3.4.4) and neglects the effects of potential snow accumulation on PV modules. Cumulative plane-of-array insolation is normalized to peak for the lowest latitude location with the SAT PV module. E-W vertical insolation is similar to that found for south-facing fixed-tilt systems in both Regina and Churchill.

Figure 4.11 shows the annual plane-of-array insolation for SAT, E-W vertical, and N-S vertical modules relative to south-facing latitude-tilt fixed-tilt modules across the northern hemisphere for ∼400 locations modelled in SAM without snow loss. There is a clear trend towards more similar annual insolation values for different configurations, allowing for greater opportunity to diversify PV systems in high latitudes. Including snow loss effects for tilted and tracked PV systems will further enhance the relative performance of vertical PV systems in

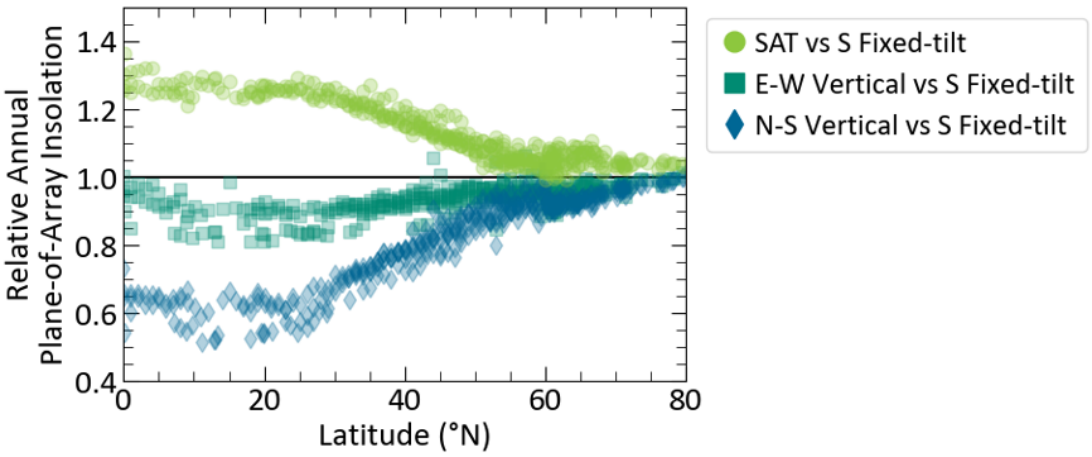

Figure 4.11: Annual plane-of-array insolation relative to south-facing fixed-tilt PV systems as a function of deployment latitude.

locations with significant annual snowfall.

In this thesis, E-W vertical PV systems are included in the analysis of row spacing latitude trends in the journal article presented in Section 6.1 [150]. In Section 6.3, the bifacial PV models introduced in Section 3.4.4 are validated against E-W and N-S vertical irradiance data collected in two test-sites. Finally, in Section 6.4, vertical site data for a system in Fairbanks, Alaska is analyzed and discussed in the context of cold climate PV degradation.

2. Bifacial gain increases

Bifacial gain (Eq. 3.1) is well understood to increase with latitude due to long-lasting and seasonal snowfall in northern latitudes [45–48]. Bifacial systems may also be able to shed snow faster due to increased heating potential from the acceptance rear-side irradiance when the front-side is covered by snow [151–153].

In this thesis the effect of snowfall on output PV performance motivates the work presented in Section 5.2 [154]. The proportion of total insolation which is ground-reflected on the surfaces of bifacial PV systems is shown to significantly increase with latitude in the publication presented in Section 6.2 [72].

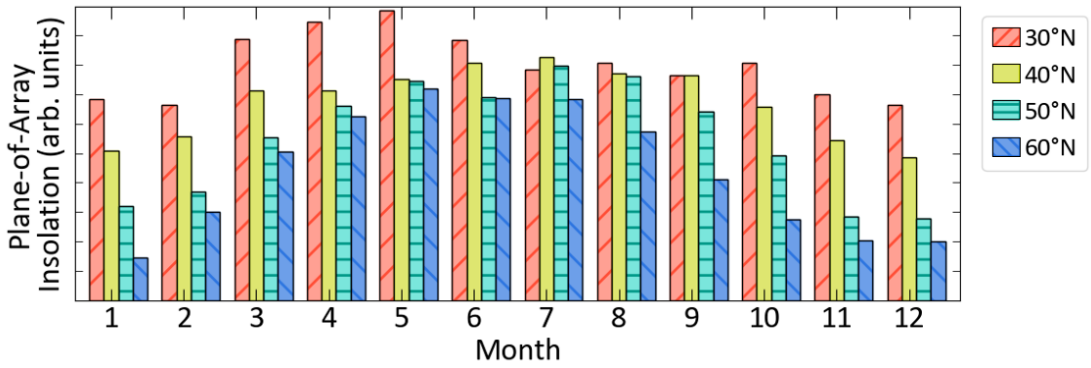

Figure 4.12: Monthly plane-of-array insolation trends for a monofacial fixed-tilt PV module in Hermosillo - 30°N, Golden - 40°N, Regina - 50°N, and Churchill - 60°N.

3. Strong seasonal variation in solar resource directly translates to strong seasonal swings in PV production

Due to the intrinsic tie between available solar resource and PV production, the large seasonal differences in GHI seen in Fig. 4.2A directly correspond to large seasonal swings in PV production. The monthly plane-of-array insolation of a equator-facing fixed-tilt PV module at a few different latitudes is shown in Figure 4.12, to illustrate. Insolation was modelled using TMY data in SAM. The energy yield of PV modules in northern latitudes have been measured to dramatically change seasonally [143].

4. Snow accumulation can hault PV production

The presence of snow ground cover can greatly enhance the bifacial gain of systems in northern latitudes, however, snow can also accumulate on the top surfaces of modules and block PV production, resulting in a snow loss [155, 156]. Snowdrifts accumulating around PV arrays can also build up to the point of blocking sunlight [157]. Snow will tend to shed from the surface of PV models during sunny conditions. Figure 4.13 shows some example photos taken by the author of snow that is in the process of shedding from PV modules. In Fig. 4.13A, the effect of tilt can be directly seen on the speed of the snow shedding. In this case, the modules are frameless, and the snow slid evenly off the surfaces, with higher tilt modules clearing the snow quicker. In Fig. 4.13B and 4.13C the same PV array can been seen with images taken about 30 minute apart as the sun broke through the clouds. In this case, the snow shedding is uneven. Predicting the snow accumulation and shedding characteristics of PV arrays in snowy climates

Figure 4.13: Images of snow shedding patterns on bifacial PV modules. Photos taken by the author for (A) Piteå Solvåg and (B-C) a Luleå Energy PV plant.

is an active field of research [9,10,158]. The sudden shedding of snow off PV modules can also pose a hazard in rooftop applications [159,160].

In this thesis, the effect of snow accumulation was found to have an impact on model validation of a south-tilted fixed-tilt system in Alaska, presented in Section 6.3.

5. Photovoltaic conversion efficiency increases

Maximum power temperature coefficients of c-Si solar cells typically lie in the range of -0.25%/°C to -0.40%/°C [161], with both maximum power and photovoltaic energy conversion efficiencies increasing for the colder temperatures found in higher latitude locations. This is due to increasing voltage with lower temperatures, discussed previously in Section 2.2.2. Figure 4.14 shows the measured module temperature over multiple years at 15-minute resolution for a SHJ bifacial south fixed-tilt module deployed in Fairbanks, Alaska, described further in Ref. [143] and with further site results given in this thesis in Sections 6.3 and 6.4. The median operating temperature of the module is 15°C. In Fig. 4.14B, the output efficiency of a modelled bifacial SHJ solar cell is shown using the dual-sided textured cell model developed in Sentaurus (see Section 2.6) with an efficiency temperature coefficient of -0.07% abs. per °C. In low-to-mid latitudes, PV operating temperatures typically fall between 20-50°C, while in tropical environments temperature can be as high as 50-60°C [162]. Given a -0.07% abs. per °C temperature coefficient, a temperature change from 40°C to 15°C would result in an efficiency increase of 1.7% abs.

In this thesis, photovoltaic conversion efficiency is additionally shown to be improved for higher air masses in Section 5.1 [163] and in the presence of fresh snow in Section 6.2 [72].

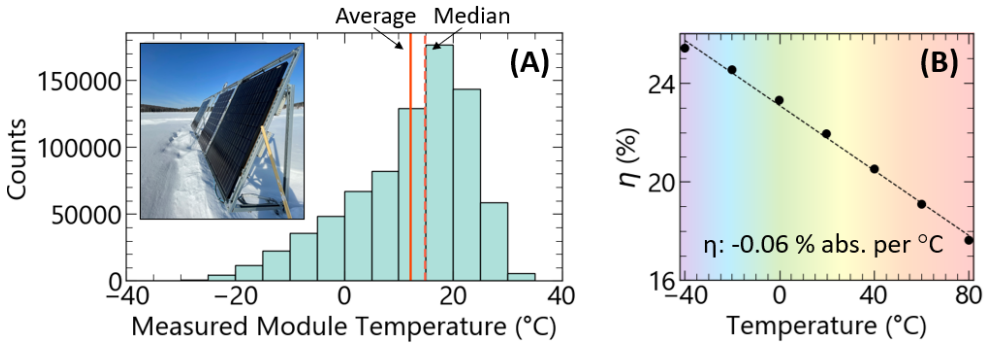

Figure 4.14: (A) Example distribution of measured module temperature for a south-facing fixed-tilt PV module in Fairbanks, Alaska. (B) Example photovoltaic conversion efficiency gain with lower operating temperatures, as simulated in Sentaurus for a SHJ cell.

6. PV systems tend to degrade slower

The effect of climate on PV degradation has been studied in a number of scientific articles [164–166]. A few such studies include cooler climates that can be found in northern countries like Canada [33, 167, 168]. These studies have found indications that cooler climates tend to result in slower PV performance degradation than warmer climates.

This thesis presents a manuscript which provides a to-date comprehensive review of the effect of cold climates on PV degradation and performance loss rates, discussed in detail in Section 6.4.

7. Uncertainty associated with energy yield modelling increases

High latitude environmental conditions lead to increased uncertainty in PV models. The causes for this uncertainty is multi-fold: modelling uncertainty increases with cloudy conditions and under high albedo conditions, PV models are not often validated in high latitudes, diffuse sky models have been optimized in California, and, moreover, these uncertainties are exacerbated by lower data availability and quality in northern latitudes. The effect of high latitude environmental conditions on modelling uncertainty is discussed in detail in the journal article presented in Section 6.3. Modelling error resulting specifically from spectral effects of albedo is discussed in Section 6.2 [72]. Further research on the sparsity of irradiance stations and data quality issues at high latitudes can be found in, for example, Refs. [169–171].

Chapter 5

Bifacial photovoltaic cell characterization & measurement

This chapter details my work on the characterization of bifacial solar cells under varying illumination conditions. Two papers are presented in this chapter, one which emphasizes the impact of changes in front-incident solar spectrum as air mass increases (for a description of air mass, see Section 2.5), and the other which develops a measurement technique for including effects of the rear-side incidence solar spectrum caused by albedo (albedo - Section 2.5.2). This research seeks to enhance the understanding of how emerging high-bifaciality designs respond to variations in the spectral content of incidence light from both the front and rear, providing pathways for improved modelling and measurement accuracy of bifacial structures under varied illumination conditions.

5.1 Effect of air mass on current losses in bifacial silicon heterojunction solar cells

In this paper the effect of spectra was investigated
Into high bifaciality cells.
A drift-diffusion model was created
For simulating carrier transport well.
.
Efficiency was found to peak
At an air mass of five point oh.
These results critique

AM1.5 assumption status-quo.

❄ ❄ ❄

Scope and impact

Bifacial SHJ solar cells are characterized under high air mass operating conditions using the optoelectronic drift-diffusion model developed in Sentaurus and introduced in Section 2.6. In most PV system-level models, module performance is estimated by assuming nameplate efficiency and power output, determined under the standard solar spectrum of AM1.5G. Deviations from AM1.5G can enhance or diminish photovoltaic conversion efficiency, resulting in modelling uncertainty up to a few percent. Air mass modifiers can be applied into PV system models, however, estimates of these modifiers must first be calculated.

In this work, performance deviations from the standard solar spectrum of AM1.5G are quantified for emerging SHJ solar cells.

This article has the following novelties:

1. A dual-sided textured bifacial solar cell model is developed and validated in Sentaurus, capable of simulating various operating conditions on bifacial SHJ solar cell performance. Measurements of the complex index of refraction for a-Si:H and indium tin oxide (ITO) layers are provided, alongside a parameterization of the density of states in a-Si:H layers.

2. Current loss mechanisms are quantified as both a function of wavelength and voltage for varied solar spectrum incident on the front and rear.

3. *I-V* parameters, including short-circuit current, maximum power, and efficiency, are provided as a function of air mass, and may be incorporated as air mass modifiers into PV system models.

4. Cell efficiency is found to peak at an air mass of AM5, rising by 0.5% abs. from AM1.5G to AM5G, due to decreased parasitic absorption in passivating surface layers.

Overall, we find that changes in spectral content are especially important for cell structures with high bifaciality, for locations with large portions of diffuse light, and in mid-to-high latitude locations where solar elevation tends to be lower throughout the year. Our results may inform future bifacial SHJ solar cell designs, SHJ system-level modelling, and provide motivation towards region-specific cell optimization.

Author contributions

Erin M. Tonita As the lead author of this work, I developed the bifacial silicon heterojunction model in Sentaurus described in this work and introduced in Section 2.6 of this thesis. Alongside Christopher Valdivia and Karin Hinzer, I developed the study's investigation into the effects of air mass on solar cell carrier transportation. I ran and analyzed all simulation results and led model validation efforts, which included taking measurements of solar cell EQE at the University of Ottawa. I wrote the original manuscript draft.

Christopher E. Valdivia provided regular supervision and guidance over the course of this study, in addition to reviewing and editing the manuscript.

Michael Martinez-Szewczyk was responsible for fabricating the SHJ devices used in this study at Arizona State University. He also provided Suns-Voc measurements for publication in this manuscript.

Mandy R. Lewis provided measurements of the complex index of refraction and extinction coefficients for a-Si:H and ITO layers, which were used in the Sentaurus model.

Mariana I. Bertoni supervised the fabrication of silicon heterojunction cells at Arizona State University and the shipment of samples to the University of Ottawa. Mariana Bertoni also revised and edited the manuscript.

Karin Hinzer supervised this research project, provided valuable guidance and research direction, funded the project, and edited the manuscript.

Copyright

E. M. Tonita, C. E. Valdivia, M. Martinez-Szewczyk, M. R. Lewis, M. I. Bertoni, and K. Hinzer, "Effect of air mass on current losses in bifacial silicon heterojunction solar cells," *Solar Energy Materials and Solar Cells*, 230, 111293 (2021). https://doi.org/10.1016/j.solmat.2021.111293

Solar Energy Materials & Solar Cells 230 (2021) 111293

Contents lists available at ScienceDirect

Solar Energy Materials and Solar Cells

journal homepage: www.elsevier.com/locate/solmat

Effect of air mass on carrier losses in bifacial silicon heterojunction solar cells

Erin M. Tonita [a,*], Christopher E. Valdivia [a], Michael Martinez-Szewczyk [b], Mandy R. Lewis [a], Mariana I. Bertoni [b], Karin Hinzer [a]

[a] SUNLAB, Centre for Research in Photonics, University of Ottawa, Ottawa, Ontario, Canada
[b] DEfECT Lab, Arizona State University, Tempe, AZ, USA

ARTICLE INFO

Keywords:
Bifacial photovoltaics
Carrier transport
Recombination
Spectral albedo
Solar spectrum
Optoelectronic modelling

ABSTRACT

We investigate the effect of incident spectra on current loss as a function of depth and voltage into high efficiency textured bifacial silicon heterojunction solar cells. We integrate thin-film ellipsometry measurements with a 3D optical model and a 2D electronic model and validate our model with measurements of external quantum efficiency and Suns-Voc. For front illumination at normal incidence, an increasing air mass of AM1.5 to 10 reduces current density loss due to parasitic absorption in ITO and a-Si:H from 8.1% to 4.0%, and increases recombination loss at maximum power from 4.2% to 4.7%, resulting in an overall increase in collected current (88.2% to 90.5%). Cell performance metrics are summarized as a function of air mass, with efficiency peaking at AM5.0 for front illuminated and rear illuminated cells with an albedo of unity. We further demonstrate the impact of spectra on bifacial efficiency by calculating rear-side performance with the spectral albedo of dry grass. Overall, current-collection and efficiency trends emphasize the importance of considering spectral effects in energy yield models. These results are of particular importance for cell structures with high bifaciality and significant spectral albedo contributions, locations with large proportions of diffuse light, and high air mass locations as in mid-to-high latitudes.

1. Introduction

Silicon heterojunction (SHJ) solar cell technology is rapidly increasing in global market share, with industrial production lines able to reliably produce cells with efficiencies as high as 24% using streamlined low-temperature deposition techniques [1]. At the same time, the global market-share of *bifacial* photovoltaics (PV) is growing at a 15% compound annual growth rate and is predicted to overtake monofacial PV within the next decade [2] as a consequence of their enhanced energy yield potential and diminishing cost premiums. SHJ is an excellent candidate for use in bifacial panels, demonstrating the highest bifacialities (>95%) of all silicon technology thus far [3]. Understanding the nature of carrier transport in SHJ solar cells that gives rise to such high efficiencies has been a topic of much discussion [4]. The interfaces, discontinuities, and band-offsets present in such structures influence and often dominate carrier movement. Previous studies have shed light on potential mechanisms for carrier transport in SHJ cells in different bias regimes, including diffusion processes, thermionic emission, barrier tunneling, and multistep tunneling through mid-gap defect states [4–7]. Recombination pathways through mid-gap defect states in crystalline silicon, mid-gap states in amorphous silicon, and interface defects contribute to carrier loss, and can change the primary mechanism of, or even dominate over, carrier transport. Within these studies some consensus has been found, suggesting that high forward-bias regimes around the cell maximum power point operation in high-efficiency SHJ cells are diffusion dominated [6]. Carrier diffusion is limited by barrier heights at hetero-interfaces, and recombination events throughout the structure resulting from crystal lattice dislocations, impurity atoms, and surface defects [8,9]. To identify avenues for further efficiency enhancements in bifacial operation, quantification of recombination mechanisms throughout bifacial SHJ cells is required. While others have explored the impact of bifacial illumination on overall cell and module performance [10–12], detailed investigations of cell-level phenomena can provide further insight.

In this paper, we have developed and employed an optoelectronic model to quantify generation and recombination rate trends throughout

* Corresponding author. 25 Templeton Street, Ottawa, ON, K1N 6N5, Canada.
E-mail address: etoni044@uottawa.ca (E.M. Tonita).

https://doi.org/10.1016/j.solmat.2021.111293
Received 26 March 2021; Received in revised form 23 June 2021; Accepted 19 July 2021
Available online 6 August 2021

bifacial SHJ solar cells for both front and rear illumination as a function of spectra for the first time, to the authors knowledge. We use our model to investigate individual Auger, Shockley-Read-Hall (SRH), and radiative recombination mechanisms as a function of depth from the front-face of a bifacial SHJ device. Additionally, we study the effect of variations in incident spectra to elucidate their influence on generation, recombination, current density loss, and cell efficiency. We take a particular interest in investigating incident spectra outside of standard test conditions (STC) and explore high air mass (AM) conditions and the influence of spectrally resolved albedo, as real-world operating conditions rarely occur at STC [12]. Our high AM results are relevant for mid-to-high latitude locations, where GHI-weighted average AMs are above 1.5 [13]. Furthermore, we support our simulated results with measurements of bifacial SHJ solar cell external quantum efficiency and Suns-Voc.

2. Materials and methods

2.1. Fabrication

Hydrogenated amorphous silicon (a-Si:H) layers and indium tin oxide (ITO) layers were deposited on substrates of c-Si for optical characterization of each material. Substrates first underwent a 10 min RCA-B (6:1:1 H_2O:H_2O_2:HCl) ionic clean at 75°C, followed by a 10 min piranha (8:1 H_2O:H_2SO_4) organic clean at 110°C, and a 10 min buffered oxide etch at 25°C prior to thin film deposition. An Applied Materials P5000 Plasma-Enhanced Chemical Vapor Deposition (PECVD) tool was used for deposition of doped and intrinsic a-Si:H at 250°C, alongside combinations of silane (SiH_4), hydrogen (H_2), phosphine (PH_3), and diborane (B_2H_6) gases. Indium tin oxide (ITO) was sputtered to a thickness of 70 nm at 1 kW with 3% oxygen gas flow at a pressure of 5.5 mTorr onto glass substrates that had been cleaned for 5 min with sonication in acetone, isopropanol, and distilled water. ITO samples were then annealed for half an hour at 280°C.

A J. A. Woollam M-2000 ellipsometer was used to obtain optical constants of deposited thin films with Tauc-Lorentz and Lorentz-Drude models for a-Si:H and ITO layers, respectively. Fig. 1 displays the complex index of refraction results for our thin films. These same materials were deposited on full 156 × 156 mm^2 bifacial SHJ cells using similar processing steps. Cells were completed with silver metal paste screen printed on front and rear faces. Additional measurements of optical constants, including as-deposited ITO and varied film thicknesses, have been reported in Ref. [14].

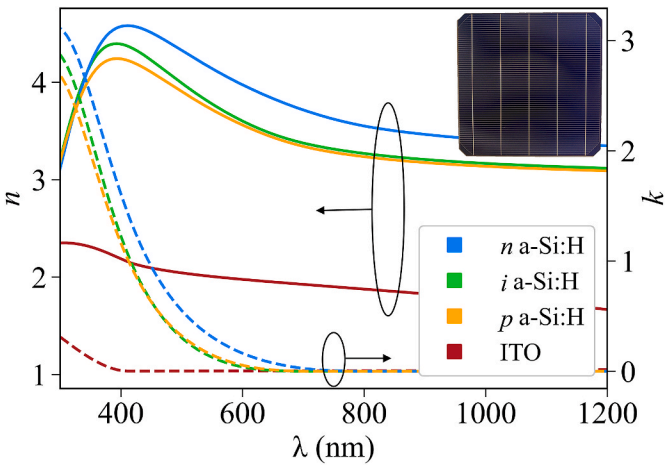

Fig. 1. Measured complex index of refraction for a-Si:H layers and ITO with ellipsometry.

2.2. Optoelectronic model

We model bifacial SHJ solar cells in Synopsys TCAD Sentaurus. To model front and rear regular inverted pyramidal texturing, optical calculations are completed on the unit cell of a 3D quarter inverted pyramid (side-wall angle 54.7°, height 7 μm) with reflective boundary conditions, shown in Fig. 2. Measured complex index of refraction of ITO and a-Si:H thin films (Fig. 1) are used as optical model inputs. The thin film effects of ITO and a-Si layers are computed using the transfer matrix method, then applied as boundary conditions within a Monte Carlo ray tracing algorithm on the front and rear faces of the c-Si substrate. Complex reflection and transmission coefficients are used to compute the probability of a ray being reflected or transmitted when impinging on an interface, including the rear facet, with incident, reflected, and transmitted angles governed by Snell's Law. Rays are initialized in air propagating along the z-axis towards either the front or rear, resulting in a 3D wavelength-dependent profile of the carrier generation rate. As described in Ref. [15], we collapse this 3D profile to 1D by averaging over x- and y-dimensions while transforming z-coordinates (depth) according to the light-travel distance into the structure. We model a total effective thickness of 180 μm, which includes the front and rear surface texture. ITO and a-Si:H layers on the front and rear of the SHJ structure are modelled as parasitic absorbers, with all generated carriers in these layers considered lost, a reasonable assumption given their low collection efficiencies (0–30%) reported in literature [16,17]. This assumption will result in slightly over-estimating parasitic absorption loss. We run simulations for both front-only illumination and rear-only illumination.

For electrical calculations, a 2D cell structure spanning 1100 μm (the half-width between fabricated grid lines) is simulated by solving Poisson's equation coupled with electron and hole continuity equations to generate depth-resolved recombination rate profiles [18]. The previously calculated 1D optical carrier generation profile is applied uniformly across the cell, except for the regions under the contacts (70 μm half-width, 6.4% shading) which are left dark. Fig. 2 outlines a schematic of the simulation workflow for front-illumination.

For accurate modelling of a-Si:H layers, the density of states (DOS) localized within the a-Si:H bandgap must be defined [19–21]. We model

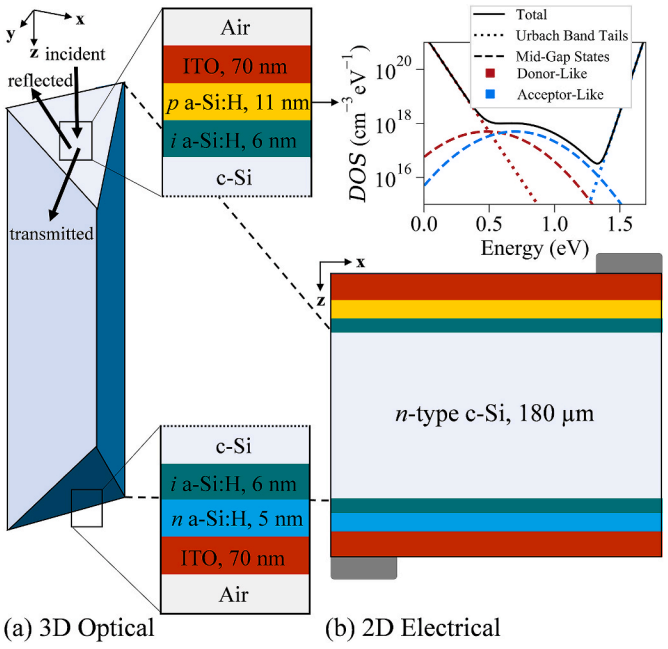

Fig. 2. Model schematic based on fabricated bifacial SHJ cell design, with (a) optical calculations computed on a 3D quarter inverted pyramid structure, and (b) electrical calculations computed on a 2D cell. Rays are labelled for z-propagating front illumination. Inset: DOS for doped a-Si:H layers.

Table 1
Input parameters.

Parameter		*p* a-Si:H	*i* a-Si:H	*n* a-Si:H	*n* c-Si
Thickness (nm)		11	6	5	180,000
Bandgap (eV) [37]		1.7	1.7	1.7	1.12
Electron affinity (eV) [37]		3.9	3.9	3.9	4.07
Permittivity (F/m) [37]		11.9	11.9	11.9	11.7
Electron mobility (cm^2/Vs) [40]		5	20	5	1417
Hole mobility (cm^2/Vs) [40]		1	5	1	470
Doping concentration (cm^{-3})		1×10^{19}	1×10^{14}	1×10^{19}	2×10^{16}
SRH electron lifetime (s)		1×10^{-7}	1×10^{-7}	1×10^{-7}	2×10^{-3}
SRH hole lifetime (s)		1×10^{-7}	1×10^{-7}	1×10^{-7}	2×10^{-3}
Effective electron band density of states (cm^{-3}) [41]		2.5×10^{20}	2.5×10^{20}	2.5×10^{20}	2.9×10^{19}
Effective hole band density of states (cm^{-3}) [41]		2.5×10^{20}	2.5×10^{20}	2.5×10^{20}	1.8×10^{19}
Exponential band tails	Density of states (cm^{-3} eV^{-1}) [21]	2×10^{21}	2×10^{21}	2×10^{21}	–
	Donor characteristic energy (eV) [21]	0.06	0.06	0.06	–
	Acceptor characteristic energy (eV) [21]	0.03	0.03	0.03	–
	Donor state capture cross section: *e*, *h* (cm^2) [40]	1×10^{-14}, 1×10^{-16}	1×10^{-14}, 1×10^{-16}	1×10^{-14}, 1×10^{-16}	–
	Acceptor state capture cross section: *e*, *h* (cm^2) [40]	1×10^{-16}, 1×10^{-14}	1×10^{-16}, 1×10^{-14}	1×10^{-16}, 1×10^{-14}	–
Gaussian mid-gap states	Density of states (cm^{-3} eV^{-1}) [21]	5×10^{17}	1×10^{14}	5×10^{17}	–
	Donor peak energy (eV) [21]	0.48	0.48	0.48	–
	Acceptor peak energy (eV) [21]	0.70	0.70	0.70	–
	Standard energy deviation (eV) [21]	0.23	0.23	0.23	–
	Donor state capture cross section: *e*, *h* (cm^2) [40]	1×10^{-14}, 1×10^{-16}	1×10^{-14}, 1×10^{-16}	1×10^{-14}, 1×10^{-16}	–
	Acceptor state capture cross section: *e*, *h* (cm^2) [40]	1×10^{-16}, 1×10^{-14}	1×10^{-16}, 1×10^{-14}	1×10^{-16}, 1×10^{-14}	–

exponential Urbach band tails and Gaussian mid-gap states with both donor-like states and acceptor-like states, as presented in Fig. 2b. The equations below describe the distribution of Urbach band tails (g_{DT} and g_{AT}) and mid-gap states associated with dangling bond defects (g_{DM} and g_{AM}) for donor and acceptor states, respectively:

$$g_{DT}(E) = N_{DT} \exp\left(- \left| \frac{E - E_V}{E_D} \right| \right) \quad (1)$$

$$g_{AT}(E) = N_{AT} \exp\left(- \left| \frac{E - E_C}{E_A} \right| \right) \quad (2)$$

$$g_{DM}(E) = N_{DM} exp\left(- \frac{1}{2} \frac{(E - E_{Dp})^2}{\sigma^2} \right) \quad (3)$$

$$g_{AM}(E) = N_{AM} exp\left(- \frac{1}{2} \frac{(E - E_{Ap})^2}{\sigma^2} \right) \quad (4)$$

where N_{DT} and N_{AT} are the effective density of states for donor and acceptor states in the band tail near the conduction band edge (E_C) and valence band edge (E_V), respectively; and characteristic energies are given by E_D and E_A for donors and acceptors. Similarly, for the mid-gap states, N_{DM} and N_{AM} correspond to the effective density of states, while E_{Dp} and E_{Ap} select the energies where the peak density of donor and acceptor states occur, relative to the band edges. Finally, σ characterizes the width of the distribution of states in the bandgap. Parameters governing the distribution of defect states in a-Si:H are adapted from Ref. [22], and are based upon previous experimental and theoretical studies of a-Si:H [23–25].

Conventionally, the loss of modelled surface area when collapsing a 3D textured optical model to an equivalent flat 2D electrical model is incorporated into simulations through an Auger and SRV texture multiplier, typically 1.7 for random pyramid texturing [26,27]. Accordingly, we assume a multiplier of 1.7 for Auger recombination. While typical SRVs are around 1 cm/s for similar structures [28,29], our model is insensitive to SRVs of 10 cm/s and lower as other loss mechanisms dominate. We therefore assume a SRV of 10 cm/s at a-Si:H interfaces to account for non-ideal passivation quality and the effect of surface area loss. Additionally, thermionic emission and band-to-band tunneling models are active at hetero-interfaces.

An ohmic contact is modelled between ITO/a-Si:H layers, assuming a well-aligned work function [30,31] and an ITO bulk resistivity of 1×10^{-3} Ω cm (150 Ω/□) for test-cells and 2×10^{-4} Ω cm (30 Ω/□) for cells with optimized ITO layers [32–34]. Test cells fabricated for model validation have estimated ITO sheet resistances of 150 Ω/□, but 30 Ω/□ is achievable for optimized fabrication processes that balance optical and electrical losses [35,36]. This includes free carrier absorption, resistivity, and reflectance. Due to lack of measured values and low current densities, we simplify our model by using the same measured refractive index for both resistances.

Electrical simulation input parameters, including those governing a-Si:H defect states, are summarized in Table 1. We have assumed an input SRH lifetime of 2 ms, corresponding to the lower bound of our c-Si wafer rated quality. All results presented in this paper are for a temperature of 300 K with Fermi statistics enabled.

Finally, to demonstrate the impact of albedo on rear-side performance, we consider two rear-side scenarios: an albedo of unity and a spectrally-resolved albedo for dry grass provided in Ref. [37]. Air mass spectra used in this work are generated from SMARTS by varying the air mass of AM1.5G parameters [38,39]. The irradiance (280–4000 nm) and total incidence current (280–1200 nm) for each AM are provided in Table 2.

3. Results and discussion

3.1. Experimental results and model validation

To validate our model parameterization and elucidate collection efficiency behavior as a function of wavelength, we measured the external quantum efficiency (EQE) of a fabricated bifacial SHJ solar cell with random upright pyramid texturing. We performed measurements on a reflective chuck, and thus for direct comparison, a back-reflector was added to the model. To best match the light-trapping effect of random pyramid texturing while working with a repeating structure, we

Table 2
Incident air mass power.

AM	Irradiance (W/m^2)	J_{inc} (mA/cm^2)
1.1	1075	49.6
1.5	1000	46.4
2	862	40.3
3	673	31.8
4	553	26.3
5	469	22.4
7	356	17.1
10	255	12.2

simulate periodic inverted pyramid texturing, which has been shown to provide J_{sc} to within 1% of random texturing [14,46]. Fig. 3a/b demonstrates excellent agreement between experimental measurements and simulations, with computed J_{sc} within ~0.1% and ~1% of the experimentally extracted J_{sc} for front and rear AM1.5 illumination, respectively. Our fabricated cell has a high measured bifaciality of 97.3% at AM1.5 and agrees well with simulated 96.5% bifaciality.

Further, Suns-Voc measurements were completed on a fabricated bifacial SHJ test cell using a Sinton Instruments WTC-120, and are compared to simulated front-face current-voltage (*I–V*) behavior in Fig. 3c. Input J_{sc} is taken to be the same as modelled results, in line with <0.1% disagreement found for front-illuminated EQE. Pseudo cell performance metrics derived from the Suns-Voc measurement are provided in the inset of Fig. 3c, corresponding to *I–V* behavior in the absence of series resistance. Our modelled curve deviates, as expected, from the pseudo curve vertical slope near V_{oc} due to simulated non-zero series resistance, and presents a small 0.4% discrepancy in V_{oc}. Measured *FF* and η both differ by 0.1% abs. compared to simulation, demonstrating close performance predictability for fabricated cells with optimized resistances. Future optimization of ITO deposition parameters for improved conductivity will increase fabricated cell efficiency. All following results assume an ITO resistivity of 2×10^{-4} Ω•cm.

3.2. Recombination and generation

Using our validated model, we calculate the generation and recombination rates of the bifacial SHJ structure of Fig. 2 as a function of depth measured from the front air/ITO surface. Fig. 4 outlines important physical phenomena under cell operation at maximum power (P_{max}). Our model assumes purely parasitic absorption in films of ITO and a-Si:H, resulting in zero carrier generation in these layers [16,17].

The electronic band structure of our SHJ cell is provided in Fig. 4a, and demonstrates good a-Si:H front and rear-surface fields for the case where the cell is front-illuminated with standard global-irradiance reference spectrum, AM1.5G. The large valence band-offset of 0.45 eV at the rear c-Si/a-Si interface prevents minority carriers (holes) in the c-Si wafer from recombining at the rear surface. Likewise, a barrier of 0.15 eV in the conduction band in addition to a continued rise of 0.3 eV in front a-Si:H films prevents majority carriers (electrons) from reaching the front surface. These simulated band-offsets are equivalent to previously measured offsets for SHJ cells [9].

Electron and hole carrier densities are calculated as a function of depth into the solar cell from the front air/ITO interface for air masses of 1.5, 3.0, and 5.0, and plotted in Fig. 4b. We calculate a minority carrier density of $<10^{13}$ cm^{-3} in the a-Si:H layers, indicative of front-side conduction and rear-side valence band-offsets at hetero-interfaces creating effective barriers against electron and hole carrier transport, respectively. Our simulated decrease in minority carrier density in these layers results in negligible recombination of c-Si-generated carriers in these thin front and rear surface films.

In Fig. 4c we plot the effect of varying AM on generation and recombination rates for front-illumination. Due to our choice of analyzing at P_{max} voltages, all recombination rates are mostly flat throughout the c-Si depth; for other voltages, recombination rates vary as a function of depth. At P_{max} for all AM, Auger recombination reaches a local minimum while SRH recombination reaches a local maximum just beyond the depletion region, with the depletion region spanning 0.08–0.13 μm depths. As Auger recombination is known to have a small impact for low carrier density [42–44], the dip in Auger recombination around the depletion region is expected as carriers are being swept away from this area. Similarly, Shockley-Read-Hall recombination exhibits expected behavior, peaking where carrier concentrations are equal [8,

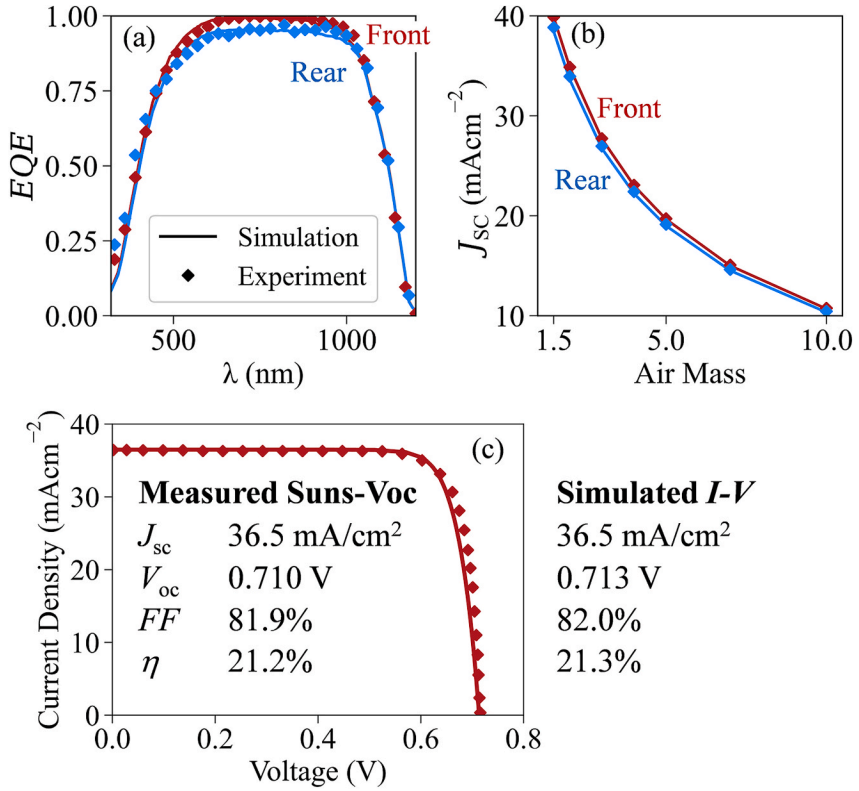

Fig. 3. Measured (data points) and simulated (lines) performance: (a) *EQE* of a bifacial SHJ solar cell; (b) extracted J_{sc} behavior as a function of AM; and (c) *I–V* behavior with measured Suns-Voc.

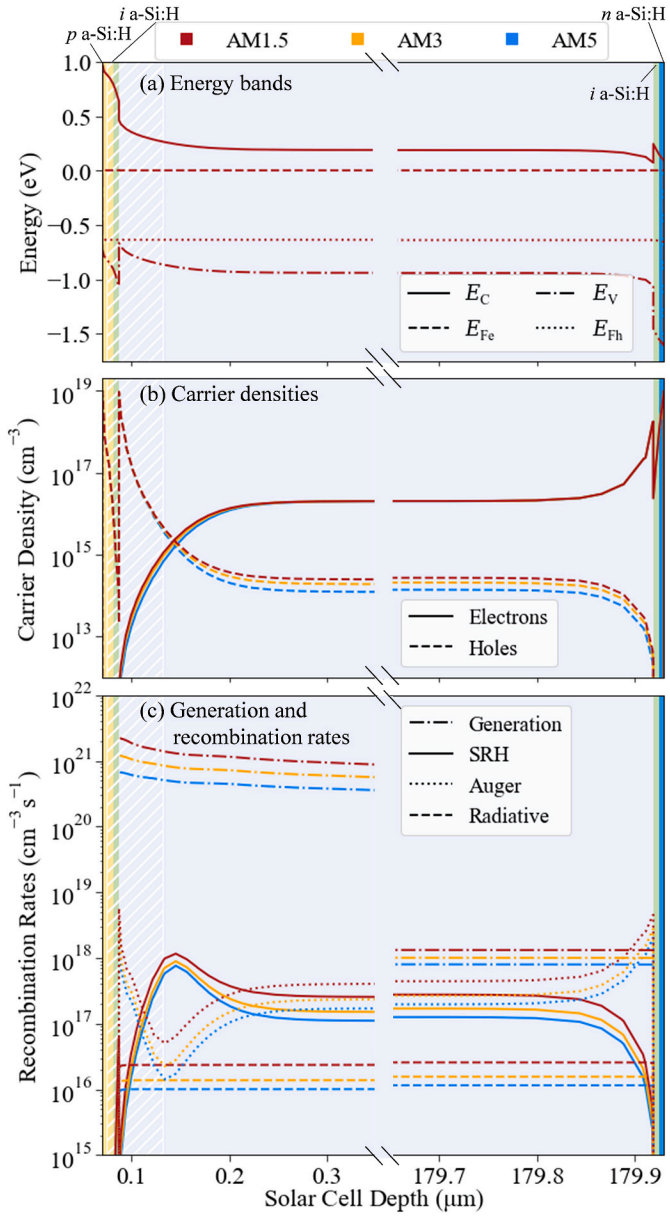

Fig. 4. P_{max} cell operation for front illumination as a function of depth and AM. The white dashed region is the depletion region.

45]. Radiative recombination remains low, between 1–3 × 10^{16} $cm^{-3}s^{-1}$. We calculate minimal changes in recombination rates in the depletion region for varying AM due to the effectiveness of the electric field at clearing away carriers from this region, regardless of changes in carrier generation rate [8]. Fig. 4b additionally shows this behavior, with hole and electron densities remaining the same in the depletion region as AM varies. Thus, variations in incident spectra predominately affect the recombination rates outside the depletion region, in the bulk of the c-Si.

In our structure, intrinsic recombination limits device efficiency with Auger recombination dominant at P_{max} operation and SRH closely following. Though not shown here, we compute similar recombination rate behavior for rear illumination, both with and without spectral albedo applied. For the rear, all recombination rates are higher by one order of magnitude throughout the c-Si due to the overall increased diffusion lengths required by carriers to reach the p-n junction.

As AM increases, the optical carrier generation rate decreases due to an overall loss in incident light intensity and shifts in shape with more carriers generated deeper into the c-Si. While generation and recombination behavior changes with AM and albedo, the overall effect of spectral variations becomes clearer when we consider current loss and current collection, ultimately leading to cell performance metrics, like P_{max} and efficiency (η).

3.3. Cell performance

Current collection and losses via parasitic absorption and recombination are presented in Fig. 5 for front and rear illumination under two AM spectra, 1.5 and 5.0. We selected AM5 as it displays the largest efficiency discrepancy compared to AM1.5 over the AM range of 1–10. In each sub-plot, current is normalized to its own total photogenerated current, J_{ph}, and voltage is normalized to its own open-circuit voltage, V_{oc}. Overlaid text describes J_{ph}, J_{sc}, current density at maximum power (J_{mp}), V_{oc}, fill factor (*FF*), and η. For both front and rear illumination, as

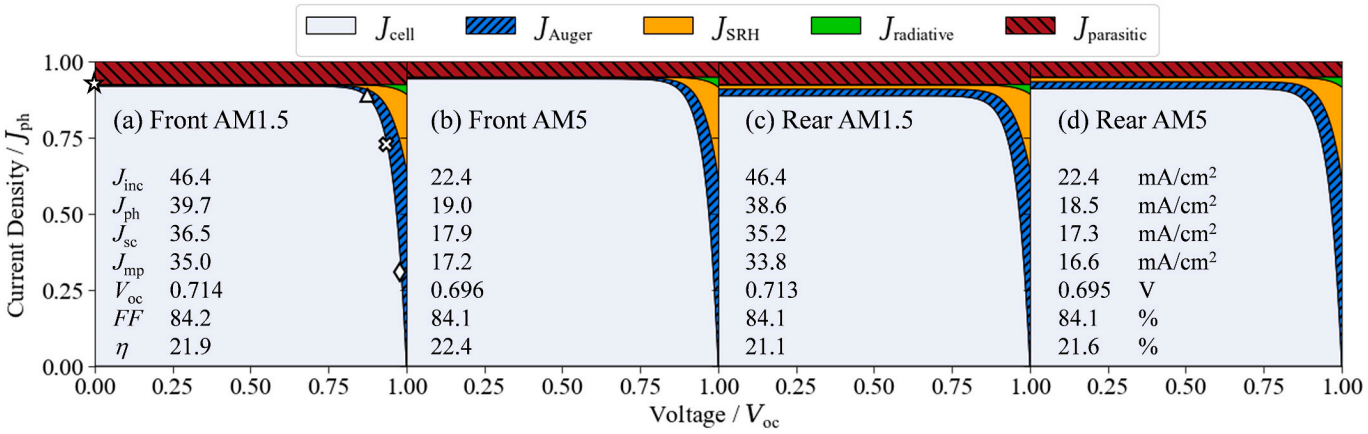

Fig. 5. Current-voltage behavior for front and rear illumination with AM1.5 and AM5. Y- and x-axis limits for each subplot are set, respectively, to the total absorbed current density and open-circuit voltage for each incident spectra. Total incident current from 0.3 to 1.2 μm, J_{inc}, is provided. Symbols in (a) correspond to voltages plotted in Fig. 6.

AM increases, proportionally fewer carriers are lost to parasitic absorption in ITO and a-Si:H. This is expected due to reduced ultraviolet (UV) light content leading to proportionally fewer carriers being generated in surface films. As voltage increases, recombination in c-Si dominates over parasitic absorption losses, with Auger and SRH contributions similar at P_{max}, as anticipated from Fig. 4c. For front AM1.5 illumination, 88.2% of the total carriers absorbed in the cell are collected at P_{max}. This collection increases to 90.5% for AM5.0. Likewise, for the rear, total current collection increases from 87.6% to 89.7% from AM1.5 to AM5.0. As a result, efficiency follows similar trends.

We anticipate that incident spectra containing proportionally more photon energies in regions of high EQE (~500–1000 nm, see Fig. 3a) will have higher overall collection efficiencies. This effect is shown in Fig. 6, with wavelength-resolved current losses provided as a function of applied bias for front (a-d) and rear (e-h) illumination. Symbols in panels a–d reference voltages in Fig. 5a. We plot the current loss mechanisms for front-surface film and rear-surface film parasitic recombination ($J_{parasitic,\ front}$, $J_{parasitic,\ rear}$), transmittance (J_T), reflectance (J_R), and total recombination (J_{rec}). For these simulations, we have removed the effect of a reflective chuck as well as finger-shading losses. The voltage given in Fig. 6b represents the P_{max} voltage for AM1.5 illumination, and, in overlay, shows the normalized spectral irradiance of AM1.5 and AM5. Proportionally more incident current (J_{inc}) is available for collection by the cell (J_{cell}) when higher AM are considered due to the spectral shift away from the UV and towards the near-infrared. This shifted spectrum is better matched with the c-Si spectral response and its band-edge. As applied bias increases beyond P_{max}, the proportion of current lost to c-Si recombination rapidly increases, particularly between 400 and 1000 nm. For rear-side performance most parasitic absorption occurs in the rear ITO and a-Si:H layers. Rear-side c-Si recombination loss is also increased compared to front-side, consistent with Fig. 5, and occurs primarily between 400 and 1000 nm wavelengths. This increase is seen

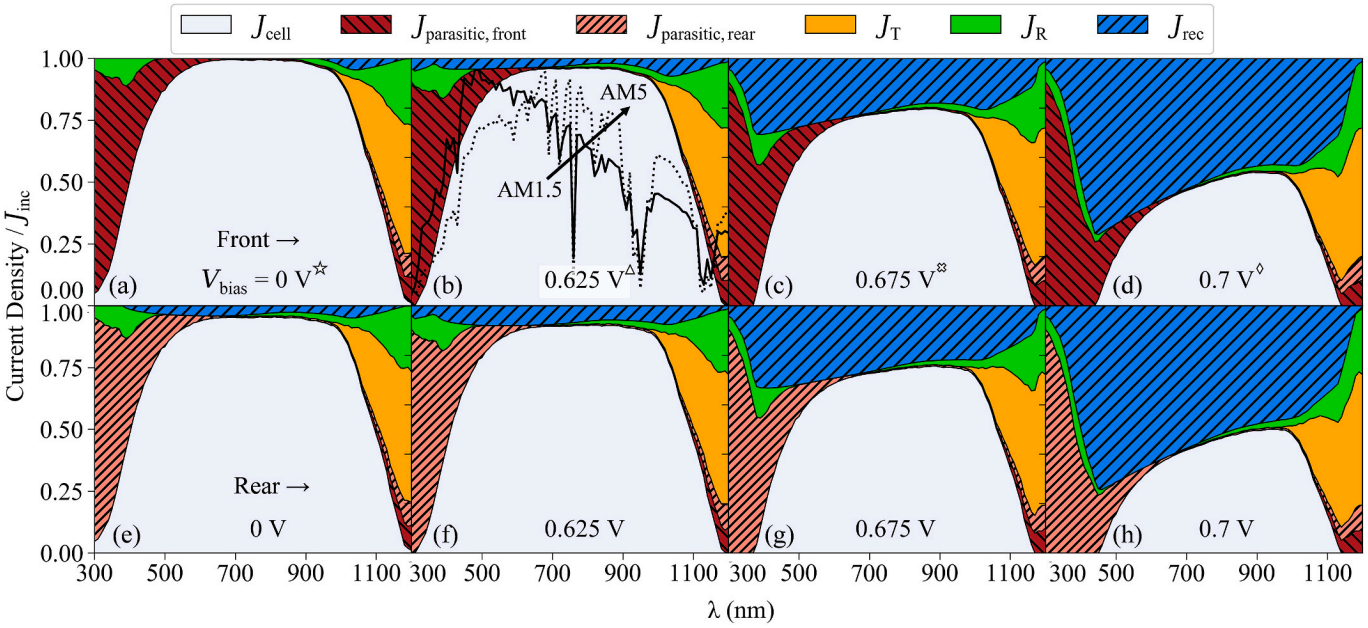

Fig. 6. Current losses as a function of wavelength for front illumination (a–d) and rear illumination (e–h) under 0 V, 0.625 V, 0.675 V, and 0.7 V. Panel (b) represents P_{max} biasing for AM1.5 illumination and includes superimposed AM of 1.5 and 5. AM5 is normalized to have the same total power as AM1.5. Colors correspond to proportion of current collected in the cell and lost to parasitic absorption, transmission, reflection, and recombination. Symbols in (a–d) correspond to voltages plotted in Fig. 5a. (For interpretation of the references to colour in this figure legend, the reader is referred to the Web version of this article.)

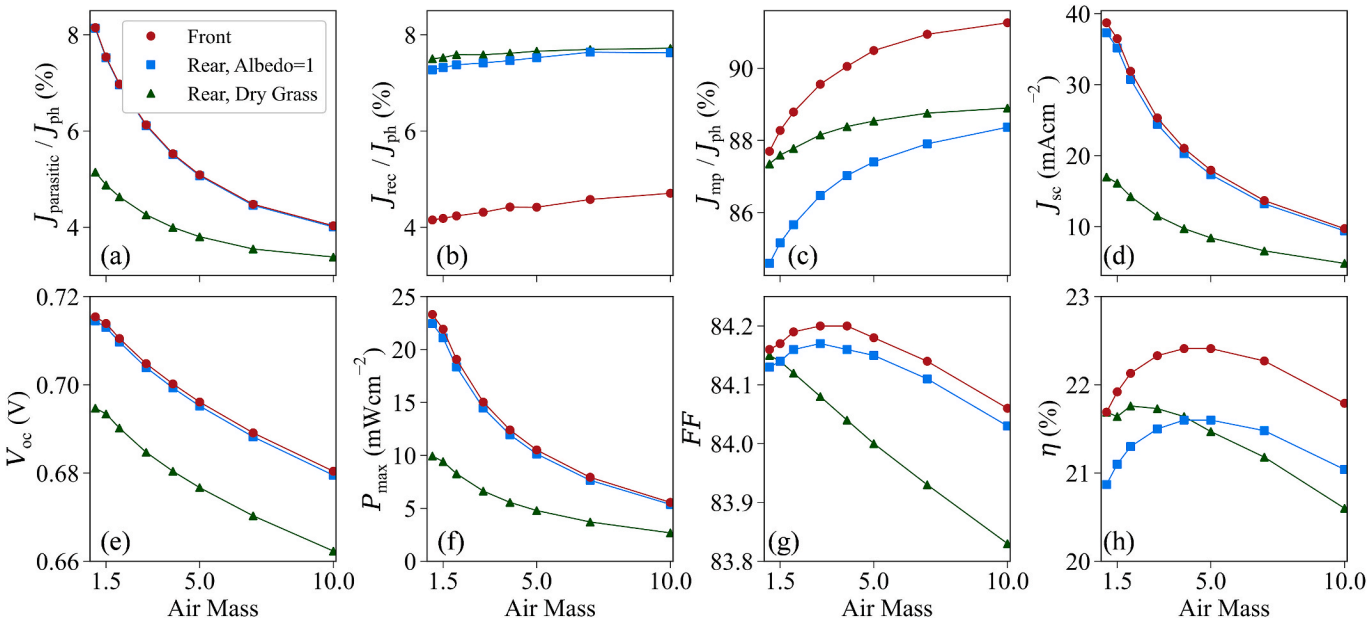

Fig. 7. Simulated influence of AM for a bifacial SHJ regular inverted pyramid-textured cell on (a) parasitic absorption current loss, (b) recombination current loss at P_{max}, (c) current collection at P_{max}, (d) J_{sc}, (e) V_{oc}, (f) P_{max}, (g) FF, and finally (h) η for front illumination and rear illumination with different ground-cover.

in Fig. 6e compared to Fig. 6a for zero applied bias, but is present across all voltages.

Fig. 7 summarizes the effect of AM up to AM10 on cell performance metrics – parasitic absorption loss, recombination loss, J_{mp}, J_{sc}, P_{max}, V_{oc}, FF, and η – for front illumination, rear illumination with unity albedo, and rear illumination with dry grass spectral albedo. As previously discussed, increased AM results in a dramatic decrease in parasitic absorption (Fig. 7a) for all considered scenarios. This is particularly the case for front illumination and rear illumination with unity albedo where parasitic absorption halves from AM1.5 to AM10. While parasitic absorption decreases with higher AM, we instead observe that the proportion of current lost to recombination (Auger, SRH, and radiative in c-Si) increases by 0.5% abs. from AM1.5-10 (Fig. 7b) when operated at P_{max}. As relatively more carriers are generated in c-Si, c-Si recombination dominates current loss. For example, for rear AM5 illumination with an albedo of unity, the proportion of current lost to c-Si recombination is 7.5% compared to 5.2% lost to parasitic absorption. For higher AM operation, as in mid-to-high latitudes, efficiency enhancements focused on thinning surface films may not be necessary, thus widening the available design space. Overall, the combined effect of reduced parasitic absorption and only slightly increased recombination results in enhanced current collection probability with AM (Fig. 7c).

Due to reduced overall incident light intensity J_{sc} (Fig. 7d), V_{oc} (Fig. 7e), P_{max} (Fig. 7f), and FF (Fig. 7g) tend to drop with AM. In Fig. 7h, simulations show a rise in efficiency with AM that peaks near AM5 for front illumination and rear illumination with perfectly reflective albedo. Up to AM5, spectral shifts result in greater overlap with regions of high c-Si EQE, with transmission losses increasing in importance beyond this air mass. As a contrast, dry grass preferentially reflects light beyond the bandgap of silicon while absorbing visible light, resulting in a decline in efficiency for all higher AM [37]. In this case, the loss of light above the bandgap of c-Si out-weights the enhanced current collection simulated in Fig. 7c.

Thus, while it is well understood that total available power decreases with AM, we have demonstrated that for front illumination the spectral shifts resulting from these conditions result in enhanced cell efficiency. These enhancements will influence energy yield, with panels operating with higher AM, producing more power over the course of a year than otherwise expected.

3.4. Effect of encapsulation

This same analysis has been repeated for cells encapsulated on both front and rear faces with 0.45 mm of ethylene vinyl acetate (EVA) and 3 mm of borosilicate glass. EVA and glass optical constants are taken from Ref. [47]. The addition of encapsulation increases the proportion of absorbed current density lost to parasitic absorption by 4.3% abs. and 3.9% abs. compared to bare cells at AM1 and AM10, respectively. The detrimental effects of UV absorption in EVA and glass layers are less significant with higher AM due to red-shifting of the spectra. Though the absorptivity and reflectivity of encapsulating materials are wavelength-dependent, efficiency trends as a function of AM are found to be the same as bare cells, with efficiency decreased by 1.40 ± 0.02% abs. from AM1-10. Further details on this analysis are presented in Ref. [48].

3.5. Oblique incidence angles

All results presented in this work are for normal incidence. However, during normal operation a wide range of angles will be incident on both front and rear faces, particularly for higher air masses. Higher angles-of-incidence (AOI) will result in decreased light-coupling into the device primarily due to cosine losses, but also due to decreased EQE [14]. Consequently, for the rear-side and for non-tracked systems the efficiency will be lower than presented in this work. In the case of EVA-based encapsulated silicon cells, higher AOI results in a more-significant drop in performance compared to bare cells [49]. These effects will be explored in more detail in future work.

4. Conclusion

In this study, we investigated recombination losses in high-efficiency bifacial SHJ solar cells as a function of depth, voltage, and wavelength. We demonstrated a decrease in parasitic absorption of up to 50% rel. with AM increasing from 1.5 to 10 and a slight rise (~0.5% abs.) in c-Si recombination, resulting in overall improved cell efficiency up to AM5

for front illumination and rear illumination with unity albedo. Our simulated cell collects proportionally more photogenerated current when AM increases from 1.5 to 5.0, with 2.3% and 2.1% more current density collected under front-face and rear-face illumination at P_{max}, respectively. Consequently, efficiency rises by 0.5% abs. Additionally, we investigate the influence of spectrally-resolved dry grass albedo on rear-side cell performance, demonstrating a sharp decrease in efficiency with increased AM, unlike the case of unity albedo. As efficiency tends to rise with AM, we expect such benefits to enhance energy yield in locations with significant power contributions at high AM. Thus, the spectral influence of AM and albedo is most impactful for high bifaciality cells, locations with a high proportion of diffuse-to-direct light, and mid-to-high latitudes where GHI-weighted AM exceeds 1.5.

CRediT authorship contribution statement

Erin M. Tonita: Investigation, Methodology, Writing – original draft, Visualization, Software, Validation. **Christopher E. Valdivia:** Writing – review & editing, Supervision, Conceptualization. **Michael Martinez-Szewczyk:** Validation, Investigation. **Mandy R. Lewis:** Validation, Investigation. **Mariana I. Bertoni:** Writing – review & editing, Resources, Supervision, Conceptualization. **Karin Hinzer:** Writing – review & editing, Resources, Supervision, Conceptualization, Funding acquisition.

Declaration of competing interest

The authors declare that they have no known competing financial interests or personal relationships that could have appeared to influence the work reported in this paper.

Acknowledgements

The authors gratefully acknowledge the support of CMC Microsystems and the Natural Sciences and Engineering Research Council of Canada [NSERC CREATE 497981, NSERC STPGP 521894, NSERC CGS-D]. Work at ASU was supported by the Engineering Research Center Program of the National Science Foundation and the Office of Energy Efficiency and Renewable Energy of the Department of Energy under NSF Cooperative Agreement [No. EEC1041895].

References

[1] C. Ballif, M. Boccard, A. Descoeudres, C. Allebé, A. Faes, O. Dupré, J. Haschke, P. J. Ribeyron, M. Despeisse, Solving all bottlenecks for silicon heterojunction technology, Photo Interpret. 42 (2019) 85–97.
[2] C. Deline, S.A. Pelaez, B. Marion, B. Sekulic, M. Woodhouse, J. Stein, Bifacial PV System Performance: Separating Fact from Fiction, 46th IEEE Photovoltaic Specialists Conference, Chicago, IL, 2019.
[3] T.S. Liang, M. Pravettoni, C. Deline, J.S. Stein, R. Kopecek, J.P. Singh, W. Luo, Y. Wang, A.G. Aberle, Y.S. Khoo, A review of crystalline silicon bifacial photovoltaic performance characterisation and simulation, Energy Environ. Sci. 12 (2019) 116–148.
[4] N. Jensen, U. Rau, R.M. Hausner, S. Uppal, L. Oberbeck, R.B. Bergmann, J. H. Werner, Recombination mechanisms in amorphous silicon/crystalline silicon heterojunction solar cells, J. Appl. Phys. 87 (5) (2000) 2639.
[5] M. Taguchi, E. Maruyama, M. Tanaka, Temperature dependence of amorphous/crystalline silicon heterojunction solar cells, Jpn. J. Appl. Phys. 47 (2) (2008) 814–818.
[6] T.F. Schulze, L. Korte, E. Conrad, M. Schmidt, B. Rech, Electrical transport mechanisms in a-Si:H/c-Si heterojunction solar cells, J. Appl. Phys. 107 (2010), 023711.
[7] Y.J. Song, M.R. Park, E. Guliants, W.A. Anderson, Influence of defects and band offsets on carrier transport mechanisms in amorphous silicon/crystalline silicon heterojunction solar cells, Sol. Energy Mater. Sol. Cells 64 (2000) 225–240.
[8] C.-T. Sah, R.N. Noyce, W. Shockley, Carrier generation and recombination in p-n junctions and p-n junction characteristics, Proc. IRE 45 (1957) 1228.
[9] A. Descoeudres, Z.C. Holman, L. Barraud, S. Morel, S. De Wolf, C. Ballif, 21% efficient silicon heterojunction solar cells on n- and p-type wafers compared, IEEE J. of Photovolt. 3 (1) (2013) 83–89.
[10] N. Wohrle, A.A. Sabater, J. Greulich, Genuine Bifacial Simulation and Optimization of an MC-Silicon PERC Solar Cell. 32nd European PV Solar Energy Conference And Exhibition, Munich, Germany, 2016.
[11] F. Fertig, N. Wohrle, J. Greulich, K. Krauss, E. Lohmuller, S. Meier, A. Wolf, S. Rein, Bifacial potential of single and double-sided collecting silicon solar cells, Prog. Photovoltaics Res. Appl. 24 (2016) 818–829.
[12] J. Cattin, O. Dupré, B. Aissa, J. Haschke, C. Ballif, M. Boccard, Optimized design of silicon heterojunction cells for field operating conditions, IEEE J. of Photovolt. 9 (6) (2019).
[13] M. Yandt, K. Hinzer, H. Schriemer, Representative atmospheric parameters in multijunction solar cell design, IEEE J. of Photovolt. 8 (3) (2018) 895–901.
[14] M. Lewis, E.M. Tonita, C.E. Valdivia, R.J.K. Obhi, M.I. Bertoni, K. Hinzer, Angular dependence of textured bifacial silicon heterojunction solar cells for high latitudes. 46th IEEE Photovoltaics Specialists Conference Proceedings, Chicago IL, 2019.
[15] S.C. Baker-Finch, K.R. McIntosh, One-dimensional photogeneration profiles in silicon solar cells with pyramidal texture, Prog. Photovoltaics Res. Appl. 20 (2012) 51–61.
[16] Z.C. Holman, A. Descoeudres, L. Barraud, F.Z. Fernandez, J.P. Seif, S. De Wolf, C. Ballif, Current losses at the front of the silicon heterojunction solar cells, IEEE J. of Photovolt. 2 (2012) 7–15.
[17] J. Shi, Z.J. Yu, A. Leilaeioun, K. Fisher, Z.C. Holman, Effects of Amorphous Silicon Thickness Variation on Infrared-Tuned Silicon Heterojunction Bottom Cells, *46th IEEE PVSC Conference Proceeding*, 2019.
[18] M. Wilkins, K. Hinzer, Chapter 40, "Multi-junction solar cells", in: J. Piprek (Ed.), Handbook of Optoelectronic Device Modeling and Simulation – Volume Two, CRC Press, 2017.
[19] S. Olibet, E. Vallat-Sauvain, C. Ballif, Model for a-Si/c-Si interface recombination based on the amphoteric nature of silicon dangling bonds, Phys. Rev. B 76 (2007) 1–14, 35326.
[20] R.A. Street, Trapping parameters of dangling bonds in hydrogenated amorphous silicon, Appl. Phys. Lett. 41 (1982) 1060.
[21] K. Winer, I. Hirabayashi, L. Ley, Distribution of occupied near-surface band-gap states in a-Si:H,, Phys. Rev. B 38 (11) (1988) 7680–7693.
[22] N. Hernandez-Como, A. Morales-Acevedo, Simulation of hetero-junction silicon solar cells with AMPS-1D, Sol. Energy Mater. Sol. Cells 94 (2010) 62–67.
[23] D.V. Lang, D. Cohen, J.P. Harbison, Measurement of the density of gap states in hydrogenated amorphous silicon by space charge spectroscopy, Phys. Rev. B 25 (8) (1982) 5285–5320.
[24] H. Plagwitz, B. Terheiden, R. Brendel, Staebler-Wronski-like formation of defects at the amorphous-silicon-crystalline silicon interface during illumination, J. Appl. Phys. 103 (2008), 094506.
[25] R. Varache, J.P. Kleider, W. Favre, L. Korte, Band bending and determination of band offsets in amorphous/crystalline silicon heterostructures from planar conductance measurements, J. Appl. Phys. 112 (2012) 123717.
[26] A. Fell, K.R. McIntosh, P.P. Altermatt, G.J.M. Janssen, R. Stangl, A. Ho-Baillie, H. Steinkemper, J. Greulich, M. Müller, B. Min, K.C. Fong, M. Hermle, I.G. Romijn, M.D. Abbott, Input parameters for the simulation of silicon solar cells in 2014, IEEE J. of Photovolt. 5 (4) (2015) 1250–2363.
[27] S.C. Baker-Finch, K.R. McIntosh, M.L. Terry, Y. Wan, Isotextured silicon solar cell analysis and modeling 2: recombination and device modeling, IEEE J. Photovolt. 2 (4) (2012) 465–472.
[28] S. Bernardini, T.U. Nærland, A.L. Blum, G. Coletti, M.I. Bertoni, Unravelling bulk defects in high-quality c-Si material via TIDLS, Prog. Photovoltaics Res. Appl. 25 (2017) 209–217.
[29] S.Y. Herasimenka, C.J. Tracy, V. Sharma, N. Vulic, W.J. Dauksher, S.G. Bowden, Surface passivation of n-type c-Si wafers by a-Si/SiO2/SiNx stack with <1cm/s effective surface recombination velocity, Appl. Phys. Lett. 103 (2013) 183903.
[30] B. Halliop, Interface Properties of the A-Si/c-Si Heterojunction Photovoltaic Cell, University of Toronto, PhD, 2015.
[31] R. Lachaume, W. Favre, P. Scheiblin, X. Garros, N. Nguyen, J. Coignus, D. Munoz, G. Reimbold, Influence of a-Si/ITO interface properties on performance of heterojunction solar cells, En. Proc. 38 (2013) 770–779.
[32] H. Kim, C.M. Gilmore, Electrical, optical, and structural properties of indium-tin-oxide thin films for organic light-emitting devices, J. Appl. Phys. 86 (11) (1999) 6451–6461.
[33] S. Ishibashi, Y. Higuchi, Y. Ota, K. Nakamura, Low resistivity indium-tin-oxide transparent conductive films, effect of sputtering voltage on electrical properties of films, J. Vac. Sci. Technol. 8 (1990) 1403.
[34] L. Zhao, Z. Zhou, H. Peng, R. Cui, Indium tin oxide thin films by bias magnetron rf sputtering for heterojunction solar cells application, Appl. Surf. Sci. 252 (2005) 385–392.
[35] M. Leilaeioun, Fill Factor Loss Mechanisms: Analysis and Basic Understanding in Silicon Hetero-Junction Solar Cells, " Ph.D dissertation, Arizona State University, Tempe, 2018.
[36] M. Leilaeioun, Z.J. Yu, Z. Holman, Optimization of front TCO layer of silicon heterojunction solar cells for tandem applications. 43rd IEEE Photovoltaics Specialists Conference Proceedings, Portland OR, 2016.
[37] T.C.R. Russell, R. Saive, A. Augusto, S.G. Bowden, H.A. Atwater, The influence of spectral albedo on bifacial solar cells: a theoretical and experimental study, IEEE. J. of Photovolt. 7 (6) (2017) 1611–1618.
[38] SMARTS–Simple Model of the Atmospheric Radiative Transfer of Sunshine, Christian A. Gueymard, Solar Consulting Services, USA, 2006. https://www.nrel.gov/grid/solar-resource/smarts.html.
[39] C.A. Gueymard, D. Myers, K. Emery, Proposed reference irradiance spectra for solar energy systems testing, Sol. Energy 73 (6) (2002) 443–467.
[40] J. Lin, C. Lai, C. Lee, Y. Hu, K. Ho, S. Haga, A high-efficiency HIT solar cell with pillar texturing, IEEE J. of Photovolt. 8 (3) (2018) 669–675.

[41] S. Geiffendorder, J. Lacome, G. Letay, K. Von Maydell, C. Agert, Simulation of Amorphous and Microcrystalline Thin Film Silicon Solar Cells with Sentaurus TCAD, 25th European Photovoltaic Solar Energy Conference And Exhibition, 2010.
[42] P. Campbell, M.A. Green, The limiting efficiency of silicon solar cells under concentrated sunlight, IEEE Trans. Electron. Dev. 33 (2) (1986) 234–239.
[43] M. Kerr, A. Cuevas, P. Campbell, Limiting efficiency of crystalline silicon solar cells due to Coulomb-enhanced Auger recombination, Prog. Photovoltaics Res. Appl. 11 (2003) 97–104.
[44] A. Richter, S.W. Glunz, Improved quantitative description of Auger recombination in crystalline silicon, Phys. Rev. B 86 (2012) 165202.
[45] R. Corkish, M.A. Green, Junction recombination current in abrupt junction diodes under forward bias, J. Appl. Phys. 80 (5) (1996) 3083–3090.
[46] S.C. Baker-Finch, K.R. McIntosh, Reflection of normally incident light from silicon cells with pyramidal texture, Prog. Photovoltaics Res. Appl. 19 (2011) 406–416.
[47] K.R. McIntosh, J.N. Cotsell, J.S. Cumpston, A.W. Norris, N.E. Powell, B.M. Ketola, An optical comparison of silicone and EVA encapsulants for conventional silicon PV modules: a ray-tracing study, in 34th IEEE Photovoltaic Specialists Conference (2009) 544–549.
[48] E.M. Tonita, C.E. Valdivia, M.I. Bertoni, K. Hinzer, The role of spectrum in encapsulated bifacial silicon heterojunction solar cells. 48th IEEE Photovoltaics Specialists Conference, Virtual, 2021.
[49] J.L. Balenzategui, F. Chenlo, Measurement and analysis of angular response of bare and encapsulated silicon solar cells, Sol. Energy Mater. Sol. Cells 86 (2005) 53–83.

5.2 A bifacial photovoltaic device measurement method incorporating albedo

Bifacial standards that have been composed
Lack albedo to their detriment.
A new method is proposed
For adding rear light to measurement.
.
Rear illumination is weighted
For common systems you might come-by.
Thus, rear light is calibrated
To not be excessively high.

❄ ❄ ❄

Scope and impact

Over 50% of solar panels deployed in 2022 have used bifacial technology [41]. However, indoor measurements of bifacial photovoltaic devices often have limited applicability to field operation due to neglecting the effects of albedo on the rear, or significantly overestimating rear incident irradiance. In our article, we propose a bifacial illumination method that includes albedo and appropriately scales the rear-side illumination to include loss mechanisms which occur in the field. We evaluate the ability of this method to represent real-world illumination conditions and align with system-level energy yield. This method is compared to bifacial measurement standards published in IEC 60904-1-2 in 2019.

This article has the following novelties:

1. An extension to the recent IEC bifacial measurement standard IEC 60904-1-2 is proposed, incorporating the effects of albedo.

This new method, referred to as the Scaled Rear Irradiance (SRI) method in the article, assigns rear illumination values to specific ground covers and makes a distinction between equator-facing fixed-tilt PV systems and SAT systems. Rear illumination values are calibrated using system-level modelling in Boulder, Colorado. The SRI method is designed and calibrated such that test illumination conditions of bifacial PV devices better represent illumination conditions in the field. This method may be used in place of previous implementations of albedo into

bifacial PV studies, where AM1.5G was simply reduced by the spectral or broadband albedo of the ground, resulting in erroneously high estimates of bifacial gain and spectral effects.

The measurement method described in this article has received discussion by committee members of IEC 60904-1-2. Further standardization of the SRI method by, for example, calibrating the method for fielded modules under a single instance of normal-incidence AM1.5G illumination, may be pursued in the future for implementation into measurement standard text. Nonetheless, the method developed in this work may be used by bifacial PV researchers to test the effects of albedo indoors under operating conditions which are more representative of outdoor conditions in the interm. Further development of this model could open pathways for bifacial module manufacture ratings to include power ratings under a few example ground conditions such as snow, grass, and soil.

Author contributions

Erin M. Tonita As the lead author of this work, I led the conceptualization of the study, developed the measurement methodology described in the paper, and ran all PV device and system-level simulations in Sentaurus and DUET. I wrote the original manuscript and generated all figures.

Christopher E. Valdivia refined and developed the methodology presented in this paper. He provided supervision and edited the manuscript.

Annie C. J. Russell provided training and guidance on the utilization of the PV system-level software DUET. She reviewed and edited the manuscript.

Michael Martinez-Szewczyk fabricated SHJ solar cells at Arizona State University, used for validating the bifacial PV device model in Sentaurus. He provided text describing the fabrication of the solar cells in the Supplemental Information and edited the manuscript text.

Mariana I. Bertoni supervised the fabrication of SHJ mini-modules at Arizona State University. She edited and reviewed the manuscript.

Karin Hinzer supervised the project as a whole, aided in project conceptualization, and provided funding. She reviewed and edited versions of this manuscript.

Copyright

E. M. Tonita, C. E. Valdivia, A. C. J. Russell, M. Martinez-Szewczyk, M. I. Bertoni, and K. Hinzer, "A general bifacial photovoltaic method to predict system performance," *Joule*, 7(1), 5-12 (2023). https://doi.org/10.1016/j.joule.2022.12.005

Joule
Commentary

CellPress

A general illumination method to predict bifacial photovoltaic system performance

Erin M. Tonita,[1,*] Christopher E. Valdivia,[1] Annie C.J. Russell,[1] Michael Martinez-Szewczyk,[2] Mariana I. Bertoni,[2] and Karin Hinzer[1]

Erin Tonita is currently a PhD candidate in physics at the University of Ottawa under the supervision of Dr. Karin Hinzer of the SUNLAB. Her research activities focus on the modeling and characterization of bifacial photovoltaic technologies for diesel displacement in the Arctic. Her hobbies include biking, interpretive dance, and astrophotonics.

Christopher Valdivia is a senior research scientist in the University of Ottawa's SUNLAB, with more than 20 years of research in photonics. He holds a PhD from the Optoelectronics Research Centre, University of Southampton, UK (2007). His research focus is renewable solar energy generation and photonic power, with activities spanning novel photonic device design to systems energy yield modeling.

Annie Russell is a PhD candidate at the University of Ottawa SUNLAB where she develops the bifacial PV performance software, DUET. She works from unceded territory of the Musqueam, Squamish, and Tsleil-Waututh Nations.

Michael Martinez-Szewczyk is currently a PhD student at Arizona State University under the supervision of Dr. Mariana Bertoni. His research activities focus on novel low-resistance silver metallization for low-temperature applications and their use in next-generation photovoltaic devices by way of dispense printing.

Mariana I. Bertoni is a professor at Arizona State University. She received her PhD in 2007 from Northwestern University, followed by a postdoctoral fellowship at the Massachusetts Institute of Technology. Her group focuses on defect engineering and advanced characterization of solar cells and modules.

Karin Hinzer is vice-dean of research of the Faculty of Engineering and a professor at the School of Electrical Engineering and Computer Science with a cross-appointment in the Department of Physics at the University of Ottawa and is the university research chair in photonic devices for energy. She has published over 190 refereed papers and trained over 170 highly qualified personnel, and her laboratory has spun-off three Canadian companies in the energy sector. Her research interests include new materials, high-efficiency light sources and light detectors, photovoltaics, solar modules, new electrical grid architectures, and power converters.

Introduction

The International Energy Agency has outlined a roadmap to achieving net-zero greenhouse gas emissions by 2050, requiring a rapid transformation of the global energy sector toward renewable technologies.[1] While the cumulative total deployed photovoltaic (PV) capacity exceeded 1 TW in 2022, annual PV deployments on the scale of several terawatts by the mid-2030s are anticipated.[2] By 2050, PV technologies are projected to supply 20% of global energy and >70% of global electricity.[1] Of these PV devices, bifacial technologies are expected to dominate the market share by >80%[3] due to the bifacial benefits of increased power production per area, increased module lifetime, and cost-competitive manufacturing.[4] Planning of system deployments to meet global energy demand requires accurate and standardized measurements of bifacial PV devices. Standard measurements are quoted on commercial module datasheets and used to plan system performance needs, which impacts system cost, technology choice, material consumption, land use, and grid stability.

In recent years, progress has been made on standardizing bifacial measurement procedures.[5–8] In 2019, the International Electrotechnical Commission (IEC) published a technical specification, IEC 60904-1-2,[5] which defines two standard methods of characterizing bifacial PV devices where the front face is illuminated with 1,000 W/m^2, while the rear face is illuminated in the range of 100–250 W/m^2. Work is underway to

[1]SUNLAB, Centre for Research in Photonics, University of Ottawa, Ottawa, ON K1N6N5, Canada

[2]DEfECT Lab, Arizona State University, Tempe, AZ 85287-9709, USA

*Correspondence: etoni044@uottawa.ca

https://doi.org/10.1016/j.joule.2022.12.005

evaluate the merits and drawbacks of these two measurement methods.[6,8]

Rear-side incident irradiance contributions can vary widely from 0 to 700 W/m^2 depending on the albedo of the surrounding environment, orientation of the module, shading, angle of the sun, atmospheric conditions, and temporal fluctuations.[7,9] In a recent systems-level study, Onno et al.[9] evaluated incident photon-flux on bifacial modules, finding rear irradiances from 0 to 400 W/m^2 under typical operating conditions, with the two most important factors governing irradiance variation being tracking type and the ground albedo. Ground albedo changes naturally across diverse global environments and can be engineered to increase energy yield. An irradiance of 200 W/m^2 is the value selected by IEC to represent a typical rear-side contribution for bifacial testing methods in IEC 60904-1-2. However, this rear irradiance is not attributed to any particular ground condition nor does it account for spectral variation on the rear face, as it applies the standard air mass (AM) spectrum of AM1.5G to both faces. In the field, rear incident light has a unique spectral shape determined by the physical properties of the ground cover, which previous research demonstrates in some cases to yield device power variation of >5%.[10,11]

In this paper, we propose a method to complement IEC measurement procedures that accommodates the effects of spectral albedo and realistic rear-front irradiance ratios. We model the performance of a typical bifacial silicon heterojunction (SHJ) solar cell under three bifacial illumination techniques: the two standard methods outlined by IEC and our new spectral albedo approach, the scaled rear irradiance (SRI) method. Finally, we demonstrate at the cell/module level the ability of our proposed method to represent and predict energy yield by comparison to a detailed system-level optical and electrical performance model.

Bifacial illumination methods

IEC 60904-1-2

In the IEC bifacial method, the 1-sun (1,000 W/m^2) AM1.5G spectrum illuminates the front side, while the same spectrum is scaled to a value between 0.1 and 0.25 suns (100–250 W/m^2) on the rear side. In the IEC equivalent irradiance (EQI) method, 1-sun front-side irradiance, $G_{f,\mathrm{EQI}}(\lambda)$, is increased according to the device's bifaciality, φ. For example, for a rear irradiance of 0.2 suns, the applied spectrum is

$$G_{f,EQI}(\lambda) = AM1.5G(\lambda) + [0.2\,\varphi\,AM1.5G(\lambda)] \quad \text{(Equation 1)}$$

with wavelength given by λ. For the SHJ device examined in this paper, the bifaciality factor is 0.96 but can range from 0.6 to 1 depending on the cell and module technology. Technologies with lower bifaciality will have lower bifacial gain than what is presented in this paper but will exhibit similar trends. For example, in our device, to mimic bifacial illumination with a rear incident contribution of 200 W/m^2, the equivalent front-side illumination is 1,192 W/m^2. The EQI method is intended to provide a simpler measurement procedure, eliminating the need for customized device mounting or additional lamps and optics.

The SRI method

In our proposed SRI method, the rear-side irradiance is determined by the spectral albedo of the ground. The rear incident spectrum, $G_{r,\mathrm{SRI}}$, is:

$$G_{r,\mathrm{SRI}}(\lambda) = AM1.5G(\lambda)\,R_{SRI}(x,\tau) \quad \text{(Equation 2)}$$

where R_{SRI} represents a system-level ratio of rear-to-front module plane of array irradiance (PoA) for spectral albedo, x, and system tracking type, τ. In this paper, x represents the ground types studied: snow, white sand, dry grass, light sand, concrete, roof shingle, green grass, red brick, and soil. Spectral albedo data is retrieved from Russell et al.,[11] with light sand and soil provided by the SMARTS database.[12] Data spanning the wavelength range of 280–3,000 nm is digitized and reproduced in Figure 1A. We consider tracking types of horizontal single-axis tracked (HSAT) and latitude fixed-tilt. Values of R_{SRI} are given in Table 1, while their calibration is discussed in the following sections.

The SERI method

Analogous to the IEC equivalent irradiance method, in the scaled equivalent rear irradiance (SERI) method, the rear-side irradiance is added to the front:

$$G_{f,\mathrm{SERI}}(\lambda) = AM1.5G(\lambda) + [R_{SRI}\,\varphi\,AM1.5G(\lambda)] \quad \text{(Equation 3)}$$

Due to the equivalency of this method and the SRI method for optically linear device technologies, as is the case for most PV technologies, all results presented in this work are under illumination on both front and rear faces.

Calibration of the SRI method

As the two most important factors governing rear-side irradiance are albedo and tracking type,[9] calibration must occur for each system configuration of interest. We exemplify our approach using a bifacial horizontal single-axis tracked array located in Boulder, Colorado. Results for a latitude fixed-tilt system are additionally summarized in Table 1 and Figure 1.

Calibration of the SRI method requires a bifacial PV performance model that inputs broadband albedo and outputs front and rear insolation. Broadband albedo, a_{bb}, is calculated by weighting

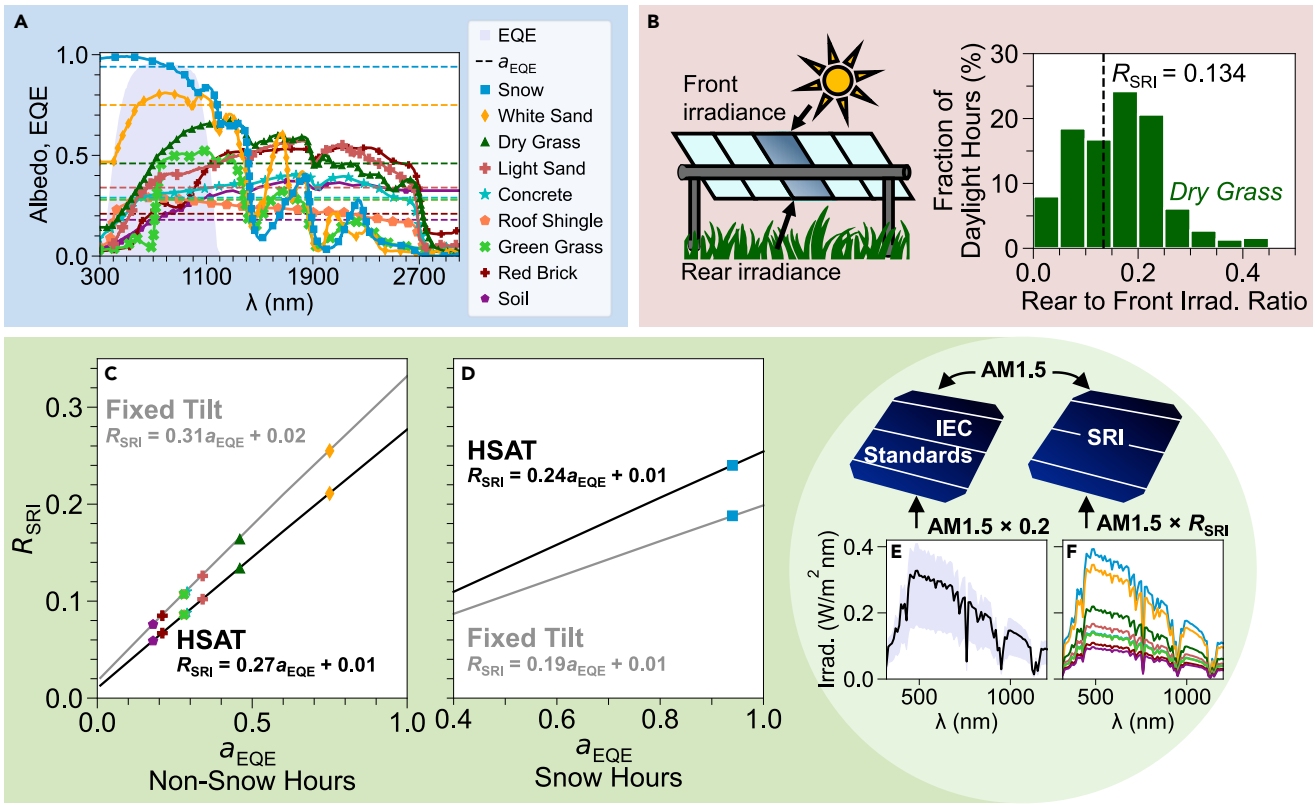

Figure 1. The scaled rear irradiance method

(A) Spectral albedos considered in this work, digitized from Russell et al.[11] and Gueymard et al.[12] Rear-side EQE, as measured by the authors for our SHJ device, is provided in the background. Dashed lines indicate the EQE-weighted albedo, as defined by Equation 5.

(B) Depiction of the SRI method calibration for dry grass. The histogram displays the fraction of daylight hours, which occur at a particular ratio of rear-to-front plane-of-array irradiance on a module in an HSAT array.

(C and D) The relationship between systems-input spectrally weighted albedo and R_{SRI} for fixed-tilt and HSAT tracking types during (C) non-snow hours and (D) snow hours.

(E and F) Illustration of the irradiance applied under (E) the IEC bifacial method compared to (F) the spectral-albedo-determined irradiance of the SRI method.

the spectral albedo, $A_x(\lambda)$, by the AM1.5G spectrum[13]

$$a_{bb} = \frac{\int A_x(\lambda)\, AM1.5G(\lambda)\, d\lambda}{\int AM1.5G(\lambda)\, d\lambda} \quad \text{(Equation 4)}$$

Integration bounds are determined by the pyranometer sensitivity, in our case 280–3,000 nm. We performed this calibration using the detailed system-level 3D view factor model, DUET.[14] DUET applies system array configurations and environmental conditions to calculate hourly front and rear irradiance profiles and I-V curves, among other outputs. This model has been validated against field data and other software.[14]

Typical meteorological year (TMY) input data were obtained from NREL's National Solar Radiation Database (NSRDB).[15] The chosen representative bifacial PV array consists of 72-cell modules with a 1-in-portrait configuration and a 1.22 m ground clearance. Input single-diode model parameters are taken from our optoelectronic cell model for the encapsulated bifacial SHJ structure detailed in Tonita et al.[16] For a summary of all system inputs, see Table S2.

System performance models typically apply broadband albedo value(s) to reduce computational cost, so the effects of spectrally resolved albedo are introduced by the application of an external quantum efficiency (EQE)-weighted albedo, a_{EQE}:

$$a_{EQE} = \frac{\int A_x(\lambda)\, EQE(\lambda)\, AM1.5G(\lambda)\, \lambda\, d\lambda}{\int EQE(\lambda)\, AM1.5G(\lambda)\, \lambda\, d\lambda} \quad \text{(Equation 5)}$$

This approach reduces output electrical power discrepancy caused by spectral versus broadband albedo use, as it weighs the spectral albedo according to the responsivity of the specific technology.[13] These EQE-weighted albedos are provided in Table 1 and visualized in Figure 1A. Broadband albedo values are provided in Table 1 for comparison.

Finally, to determine the representative rear-to-front incident irradiance ratio for

Table 1. Summary of albedo and SRI method parameters

Ground cover, x	Soil	Red brick	Green grass	Roof shingle	Concrete	Light sand	Dry grass	White sand	Snow
Broadband albedo, a_{bb}	0.19	0.23	0.24	0.26	0.29	0.33	0.44	0.67	0.85
EQE-weighted albedo, a_{EQE}	0.18	0.21	0.28	0.28	0.29	0.34	0.46	0.75	0.94
Horizontal single-axis tracked irradiance ratio, R_{SRI}	0.059	0.067	0.086	0.086	0.088	0.102	0.134	0.211	0.240
Fixed-tilt irradiance ratio, R_{SRI}	0.076	0.085	0.107	0.107	0.110	0.126	0.164	0.255	0.188

each spectral albedo (R_{SRI} in Equations 2 and 3), we calculate hourly 2D front and rear irradiance profiles on a representative module in the bi-HSAT array over the course of a year. Hourly albedo data are categorized into two datasets: hours with snow and hours without snow. To identify the representative ratio for snowy albedo, the albedo of snow is applied to only snowy hours (83 days). For all other albedos, they are applied to non-snowy hours (282 days).

The ratio of rear (r) to front (f) module plane of array (PoA) insolation across all timesteps t with albedo x determines R_{SRI}:

$$R_{SRI} = \frac{\sum_t PoA_r(t)}{\sum_t PoA_f(t)} \quad \text{(Equation 6)}$$

The distribution of R_{SRI} across timesteps for dry grass is provided as an example in Figure 1B, while all identified irradiance ratios are provided in Figures 1C and 1D and summarized in Table 1. Figure 1C depicts the relationship between system-input albedo, a_{EQE}, and R_{SRI} for fixed tilt and HSAT array configurations during non-snowy hours, while the relationship for snowy hours is given in Figure 1D. It is possible to extract from these subplots the appropriate R_{SRI} value for any albedo of interest.

Figure 1E depicts the rear-side irradiance applied during the IEC bifacial method, while Figure 1F shows the irradiance used in the SRI method using calibrated R_{SRI}.

Results

Device-level performance

We simulated simultaneous front and rear illumination in Synopsys TCAD Sentaurus using an optoelectronic model for textured crystalline silicon (c-Si) based encapsulated bifacial SHJ solar cells.[16] A schematic of our cell structure under bifacial illumination scenarios is shown in Figure S1.

To align with standard test conditions, cells were maintained at 25°C, and incoming light was normally incident for all calculations. For a detailed description of our model and model validation see the supplemental information and Tonita et al.[16]

The maximum power and efficiency output under the SRI method are provided in Figures 2A and 2B, with IEC standards given by dotted and solid lines for comparison. Front-only illumination is represented by an open circle at 0 W/m^2 rear irradiance. For the IEC methods, we extend the recommended testing range of rear-side irradiances of 100–250 W/m^2 to 0–400 W/m^2 and indicate the recommended testing regime by the shaded backgrounds throughout Figure 2.

The conventional monofacial definition of efficiency (η) is a ratio between total electrical output power, P_{mp}, and total incident power, P_{tot}. As the definition of efficiency under bifacial illumination is not yet clearly defined,[7] we consider the total incident power to be the sum of front, $P_{inc,f}$, and rear, $P_{inc,r}$, incident power contributions. Thus, bifacial efficiency becomes:

$$\eta = \frac{P_{mp}}{P_{tot}} = \frac{P_{mp}}{P_{inc,f} + P_{inc,r}} \quad \text{(Equation 7)}$$

To include the effects of spectral shape on efficiency in the SRI method, $P_{inc,r}$ must be set to:

$$P_{inc,r} = 1000\frac{W}{m^2} R_{SRI} \frac{a_{bb}}{a_{EQE}} \quad \text{(Equation 8)}$$

This accounts for the scaling of the AM1.5G rear irradiance according to the spectral shape of the ground albedo. For example, relatively more photons are present in the c-Si absorption range when the spectral albedo is snow compared to AM1.5G, resulting in $a_{EQE} > a_{bb}$. To achieve the same P_{mp} using a spectrum modified by the ground spectral albedo, less total irradiance must be applied to the rear, given by Equation 8 above. This definition is equivalent to integrating the rear incident spectrum reflected off the ground, which emphasizes the power conversion efficiency of all light incident on the device and is necessary for calculations of thermalization and heating.

Figures 2A and 2B show significant variation in P_{mp} and efficiency depending on the applied rear irradiance. The two IEC methods have near-overlapping lines in all subplots, demonstrating a negligible difference between the equivalent irradiance method and the bifacial method, as designed. In Figure 2B, their efficiencies decrease with increased rear contribution as rear-injected carriers require on-average longer diffusion lengths to reach the front p-n junction, resulting in higher recombination loss. The efficiency becomes a weighted average of the front and rear efficiency, with the weight determined by their relative irradiance contributions.

The SRI method is intended to provide a method to test the effects of spectral albedo on device performance. The rear irradiances resulting from R_{SRI} for each

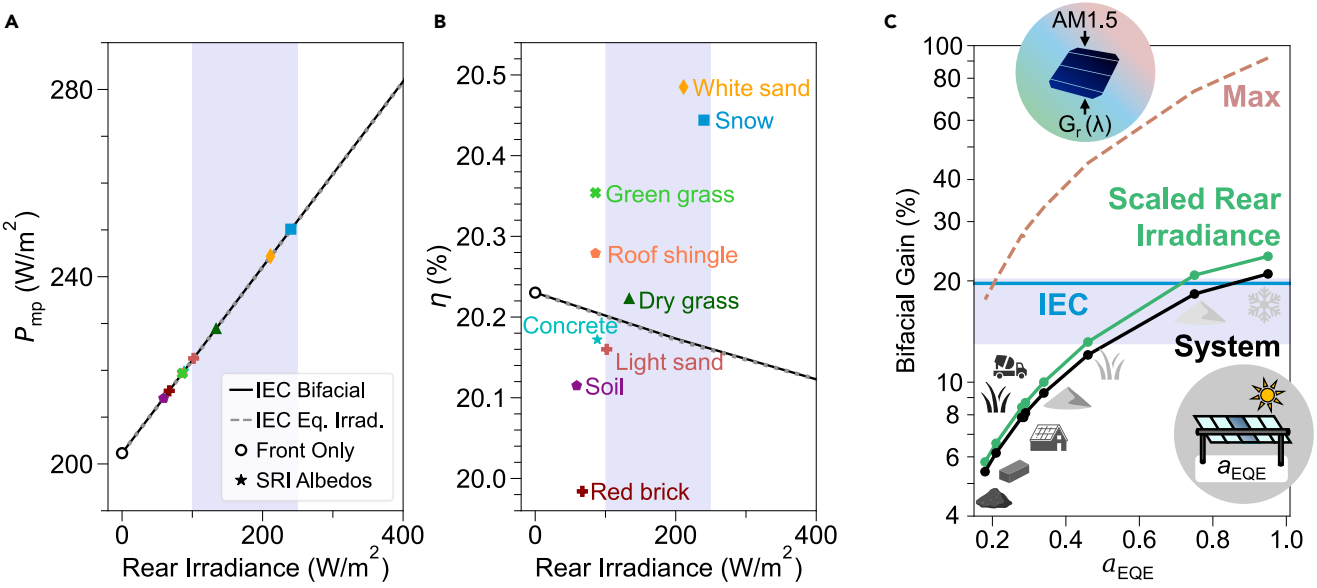

Figure 2. Performance of bifacial illumination methods on a device and system level

(A) The maximum power produced by an SHJ cell using the IEC and SRI methods. Front-only results are given by the white circles, while the shaded background corresponds to the recommended IEC testing range.

(B) The device bifacial efficiency for these methods. SRI efficiency is calculated using Equations 7 and 8, resulting in the deviation from the AM1.5G IEC lines.

(C) Bifacial gain calculated using two methods. In black, the bifacial energy yield gain of a bi-HSAT module using a validated system-level 3D view factor model, DUET. The remaining lines are calculated as the gain in device power under bifacial illumination conditions compared to front-only illumination for device measurement methods. The shaded background around the IEC 60904-1-2 line corresponds to the rear irradiance range of 100–250 W/m^2. The "Max" line represents the maximum theoretical gain due to ground-reflected light in the ideal case devoid of any ground shading. Data are spaced according to the EQE-weighted broadband albedo (a_{EQE}) input into DUET, with icons depicting the ground condition associated with each data point.

ground cover fall within the typical rear-irradiance operating range reported at the system level,[9] with input incident AM1.5G rear irradiance between 59 and 240 W/m^2 on the x axes of Figures 2A and 2B. The maximum and minimum output power using the SRI method for the considered albedo dataset covers a range of values spanning 36 W/m^2.

As efficiency includes the effects of spectral shape through Equation 8, we calculate efficiency differences between +0.33% abs. to −0.20% abs. compared to IEC methods that assume AM1.5G on both faces. For example, snow reflects >90% of light in the c-Si absorption range, leading to an efficiency 0.30% abs. higher than what is given by the IEC methods. Thus, the efficiency of a device at absorbing incident radiation under varying ground conditions cannot be accurately characterized without considering changes in spectral shape.

Energy yield prediction

The SRI method provides illumination conditions that match operating conditions for a given combination of ground cover and system design, more closely representing bifacial system-level performance than 200 W/m^2 IEC rear irradiance. To illustrate, we calculate the energy yield for a module in the bi-HSAT array located in Boulder, Colorado using DUET. The black line of Figure 2C displays its bifacial gain, defined as the percentage increase in energy yield compared to an equivalent monofacial module. Different ground conditions are plotted on the x axis, with spacing determined by the EQE-weighted albedo applied within DUET.

For comparison, device-level characterization methods are plotted using bifacial P_{mp} gain, defined as the gain in power under bifacial illumination conditions compared to front-only AM1.5G illumination. This is calculated for the IEC bifacial and SRI methods. As an additional comparison point, the maximum bifacial P_{mp} gain due to ground-reflected light is plotted in red, for the case where $R_{SRI} = a_{EQE}$ in Equation 2.

Since the system-level ratio of rear-to-front total annual irradiance dictates the rear irradiance applied in the SRI method, the resulting bifacial gain tracks the full system-level analysis well, with only a 1.7% abs. discrepancy with DUET on average across varied ground conditions. The agreement between bifacial P_{mp} gain and DUET energy yield gain confirm that in-lab device characterization using the SRI method is sufficient to capture the main sources of energy yield variation—namely albedo and tracking type. While R_{SRI} was calibrated for Boulder, Colorado (40°N, diffuse fraction 0.36), energy yield gains predicted using R_{SRI} are within 2.0% and 0.7%

abs. on average in Phoenix, Arizona (33°N, diffuse fraction 0.27) and Ottawa, Canada (45°N, diffuse fraction 0.43), respectively. Thus, it is possible to use the values presented in this paper for other locations, with an R_{SRI} error of <7%. Further details on the impact of geography are provided in the supplemental information and Table S1.

As a contrast, IEC standards do not provide a pathway for adjusting rear irradiance given system configuration and ground cover and thus produce a flat bifacial gain in Figure 2C. For a rear irradiance of 200 W/m^2, the IEC method over-estimates bifacial gain by between +14% abs. to +1.4% abs for all ground covers except snow. This discrepancy reinforces the need for the SRI method to realistically represent a range of operating conditions.

Discussion

The SRI method as a full spectrum calculation

With the development of LED solar simulator technologies and the possibility for use of custom spectral filters, bifacial measurements with unique front and rear spectra could be implemented in the future. Although the SRI method utilizes AM1.5G on the front and the rear of cells or modules, it is possible to implement this method with rear-side spectral shape given by the spectral albedo, $A_x(\lambda)$.

Rather than a scaling of AM1.5G, the rear spectrum, $G_{r,SRI}(\lambda)$, is applied as given:

$$G_{r,SRI}(\lambda) = AM1.5G(\lambda)\ \frac{A_x(\lambda)}{a_{bb}}\ R_{SRI}(x,\tau) \quad \text{(Equation 9)}$$

The device power output by Equation 9 is closely matched by the SRI method depicted in Figure 2A, as the effect of spectral shape is included in the calibration of the SRI method through a_{EQE}. This method can additionally be applied to any solar spectrum of interest, not just AM1.5G, such as spectra with varying air mass, precipitable water, or aerosol optical depth. Further details are provided in supplemental information.

Impact and significance

In this work, the SRI method was described and shown to be an improved method for measuring and modeling bifacial devices that is representative of annual performance, particularly due to its ability to represent different surface albedos. Incorporating this new method into future bifacial standards would provide a consistent methodology for testing bifacial devices with spectral or broadband albedo, corresponding to globally varying illumination conditions. This is of particular importance as renewable energy penetration increases toward a net-zero world, with bifacial PV projected to contribute ~16% of the global energy supply by 2050, around 30,000 TWh annually.[1,3]

Early implementation of this method into IEC standards can do the following:

1. Enable comparisons between existing and emerging bifacial technologies

For example, the SRI method can provide a consistent approach for future experimental studies of emerging tandem solar devices, which have a strong spectral dependence due to their design of segmenting absorption into series-connected top and bottom cells. Tandem devices are anticipated to be among the next-generation of silicon solar cell technologies due to their ability to exceed the single-junction efficiency limit.[9]

2. Enable application-specific optimization

With the SRI method, it is possible to optimize rear-side passivation and anti-reflection coatings for specific illumination conditions. For example, in the case of silicon heterojunction cells with UV-absorptive ground conditions such as green grass, tolerances on rear-side ITO properties are broadened and thicker layers can be fabricated.

3. Increase PV deployments in non-traditional markets

This method also highlights the favorable conditions of snow accumulation present in high-latitude locations by enabling in-lab device characterization under snowy ground conditions.

4. Improve system deployment sizing

Adopting this method can also reduce investment risk in PV deployments and impact system planning. For example, a 1% rel. increase in efficiency of the bi-HSAT system located in Boulder, Colorado results in a 1.1% increase in annual energy yield. More-accurate measurement capabilities can affect future terawatt deployments on the several gigawatt scale, therefore changing system cost, material consumption, and land use. Accurate system predictions and planning can also potentially reduce system inefficiencies caused by mismatch in PV generation and grid load or impact the sizing of storage technologies.

5. Support bifacial power ratings

Furthermore, as instantaneous front-only AM1.5G illumination power ratings are currently used for monofacial and bifacial modules alike, this method can inform future bifacial power ratings. We suggest manufacturers provide bifacial power ratings for different common ground conditions and tracking types, such as snow, sand, grass, and soil for single-axis tracked and fixed tilt configurations.

Estimates of the bifacial power produced under the SRI method from existing 1-sun front-only module power

ratings can be done given the linear short-circuit current (J_{sc}) and logarithmic open-circuit voltage (V_{oc}) relationship with irradiance. For instance, assuming a negligible change in fill factor, the maximum power produced under bifacial illumination with the SRI method, $P_{mp,SRI}$, can be calculated as follows:

$$P_{mp,SRI} = P_{mp,1-sun} X \left(1 + \frac{0.2569\ \mathrm{V}}{V_{oc}} \ln(X)\right) \quad \text{(Equation 10)}$$

where X is the effective increase in incident irradiance for a particular albedo:

$$X = 1 + R_{SRI}\,\varphi \quad \text{(Equation 11)}$$

The use of bifacial power ratings defined with the SRI method will highlight the benefit of bifacial technologies, while facilitating PV technology choice that is best suited for the needs of individual projects.

Conclusion

In this study, we described a general bifacial illumination method, the SRI method, which can predict outdoor system performance under varying ground conditions by appropriate scaling of the standard AM1.5G spectrum. We outline how the SRI method can be used as an extension to IEC 60904-1-2 bifacial measurement standards to (1) capture efficiency differences under varied spectral albedo and (2) represent system-specific illumination levels through in-lab bifacial device measurements. Implementation of this approach in IEC standards would provide commercial bifacial module manufacturers with a power ratings methodology for common ground covers, such as snow, sand, grass, and soil. This additional rating would allow for technology comparisons and design optimizations specific to the planned PV deployment, while potentially hastening bifacial PV adoption. As bifacial PV deployments are already exponentially rising each year[2] and module lifetimes exceed 25 years, improvements to bifacial measurement standards must happen rapidly to keep pace with increasingly varied installation conditions, reduce financial risk, maximize system energy yields, and limit greenhouse gas emissions.

DATA AND CODE AVAILABILITY

The data supporting the findings of this study are available in the main text and supplemental information and are additionally available upon request from the corresponding author. Details regarding the code used in this paper are published in Russell et al.[14] and Tonita et al.[16]

SUPPLEMENTAL INFORMATION

Supplemental information can be found online at https://doi.org/10.1016/j.joule.2022.12.005.

ACKNOWLEDGMENTS

The authors thank CMC Microsystems and the Natural Sciences and Engineering Research Council of Canada (NSERC CREATE 497981, NSERC STPGP 521894, NSERC CGS-D, NSERC RGPIN-2015-04782) for their funding support. M.I.B. and M.M.-S. acknowledge funding from the Department of Energy (DOE) under contract no. DE-EE0008166. Any opinions, findings, and conclusions or recommendations expressed in this material are those of the author(s) and do not necessarily reflect the views of the Department of Energy. The University of Ottawa is on the unceded territory of the Anishinaabe Algonquin Nation.

AUTHOR CONTRIBUTIONS

Conceptualization, E.M.T., C.E.V., M.I.B, and K.H.; methodology, E.M.T.; software, E.M.T. and A.C.J.R.; validation, E.M.T. and M.M.-S.; investigation, E.M.T. and M.M.-S.; writing – original draft, E.M.T.; writing – review & editing, E.M.T., C.E.V., A.C.J.R., M.M.-S., M.I.B, and K.H.; visualization, E.M.T.; supervision, C.E.V., M.I.B., and K.H.

REFERENCES

1. IEA (2021). Net Zero by 2050. https://www.iea.org/reports/net-zero-by-2050.
2. Haegel, N.M., Atwater, H., Jr., Barnes, T., Breyer, C., Burrell, A., Chiang, Y.M., De Wolf, S., Dimmler, B., Feldman, D., Glunz, S., et al. (2019). Terawatt-scale photovoltaics: transform global energy. Science *364*, 836–838. https://doi.org/10.1126/science.aaw1845.
3. VDMA (2022). International Technology Roadmap for Photovoltaic (ITRPV), 2021 Results. https://www.vdma.org/international-technology-roadmap-photovoltaic.
4. Kopecek, R., and Libal, J. (2021). Bifacial photovoltaics 2021: Status, opportunities and challenges. Energies *14*, 2076. https://doi.org/10.3390/en14082076.
5. IEC (2019). IEC 60904-1-2: Photovoltaic Devices – Part 1-2: Measurement of Current-Voltage Characteristics of Bifacial PV Devices. https://standards.iteh.ai/catalog/standards/iec/e785e8f8-4662-4726-99c3-5a0649327f50/iec-ts-60904-1-2-2019.
6. Rauer, M., Schmid, A., Guo, F., Neuberger, F., Gebhardt, P., and Hohl-Ebinger, J. (2020). Comprehensive Evaluation of IEC Measurement Procedures for Bifacial Solar Cells and Modules. In 37th European PV Solar Energy Conference and Exhibition (EU PVSEC). https://doi.org/10.4229/EUPVSEC20202020-4CO.2.1.
7. Deline, C., MacAlpine, S., Marion, B., Toor, F., Asgharzadeh, A., and Stein, J.S. (2017). Assessment of bifacial photovoltaic module power rating methodologies – inside and out. IEEE J. Photovoltaics *7*, 575–580. https://doi.org/10.1109/JPHOTOV.2017.2650565.
8. Rauer, M., Guo, F., and Hohl-Ebinger, J. (2019). Accurate measurement of bifacial solar cells with single- and both-sided illumination. In Proccedings of the 36th Euro. Photovolt. Sol. Energy Conference Exhibition (EU PVSEC). https://doi.org/10.4229/EUPVSEC20192019-2CO.12.1.
9. Onno, A., Rodkey, N., Asgharzadeh, A., Manzoor, S., Yu, Z.J., Toor, F., and Holman, Z.C. (2020). Predicted power output of silicon-based bifacial tandem photovoltaic systems. Joule *4*, 580–596. https://doi.org/10.1016/j.joule.2019.12.017.
10. Brennan, M.P., Abramase, A., Andrews, R.W., and Pearce, J.M. (2014). Effects of spectral albedo on solar photovoltaic devices. Sol. Energy Mater. Sol. Cell. *124*, 111–116. https://doi.org/10.1016/j.solmat.2014.01.046.
11. Russell, T.C.R., Saive, R., Augusto, A., Bowden, S.G., and Atwater, H.A. (2017). The influence of spectral albedo on bifacial

solar cells: a theoretical and experimental study. IEEE J. Photovoltaics *7*, 1611–1618. https://doi.org/10.1109/JPHOTOV.2017.2756068.

12. Gueymard, C.A., Myers, D., and Emery, K. (2002). Proposed reference irradiance spectra for solar energy systems testing. Sol. Energy *73*, 443–467. https://doi.org/10.1016/S0038-092X(03)00005-7.

13. Vogt, M.R., Gewohn, T., Bothe, K., Schinke, C., and Brendel, R. (2018). Impact of using spectrally resolved ground albedo data for performance simulations of bifacial modules. In Proceedings of the 35th Euro. Photovolt. Sol. Energy Conference Exhibition (EU PVSEC). https://doi.org/10.4229/35thEUPVSEC20182018-5BO.9.5.

14. Russell, A.C.J., Valdivia, C.E., Bohémier, C., Haysom, J.E., and Hinzer, K. (2022). DUET: A novel energy yield model with 3D shading for bifacial photovoltaic systems. IEEE J. Photovoltaics *12*, 1576–1585. https://doi.org/10.1109/JPHOTOV.2022.3185546.

15. Sengupta, M., Xie, Y., Lopez, A., Habte, A., Maclaurin, G., and Shelby, J. (2018). The National Solar Radiation Data Base (NSRDB). Renew. Sustain. Energy Rev. *89*, 51–60. https://doi.org/10.1016/j.rser.2018.03.003.

16. Tonita, E.M., Valdivia, C.E., Martinez-Szewczyk, M., Lewis, M.R., Bertoni, M.I., and Hinzer, K. (2021). Effect of air mass on carrier losses in bifacial silicon heterojunction solar cells. Sol. Energy Mater. Sol. Cell. *230*, 111293. https://doi.org/10.1016/j.solmat.2021.111293.

Joule, Volume 7

Supplemental information

A general illumination method to predict bifacial photovoltaic system performance

Erin M. Tonita, Christopher E. Valdivia, Annie C.J. Russell, Michael Martinez-Szewczyk, Mariana I. Bertoni, and Karin Hinzer

SUPPLEMENTAL INFORMATION

Cell-Level Model and Validation

We simulated simultaneous front and rear illumination in Synopsys TCAD Sentaurus using an optoelectronic model for crystalline silicon (c-Si) based encapsulated bifacial SHJ solar cells [S1], depicted in Figure S1. In our model, we use regular inverted pyramid texturing to emulate random pyramidal light-trapping. Optical calculations use Monte Carlo 3D ray tracing, with subwavelength hydrogenated amorphous silicon (a-Si:H) and indium tin oxide (ITO) thin films accommodated via transfer matrix method boundary conditions between the c-Si substrate and air. On both faces, we apply a 6.4% shading loss corresponding to the finger width and metallization coverage of the fabricated cells. Electrical calculations are solved using Poisson's equation and electron and hole continuity equations with the finite volume method in 2D. We apply surface recombination velocities between a-Si:H and c-Si layers of 2 cm/s [S2] and an ITO sheet resistance of 99.2 Ω/□, corresponding to our fabrication process [S3][S4]. The c-Si wafers used have a manufacturer-rated SRH lifetime of 2 ms, which we assume for our simulations. For a detailed description of our model and all other chosen parameters, see Ref. [S1].

We fabricated bare bifacial SHJ cells at Arizona State University for model validation. Crystalline silicon wafers were textured in a KOH bath before being cleaned in three 10-minute baths: a RCA-B (6:1:1 H_2O:H_2O_2:HCl) 74°C bath, a piranha (8:1 H_2O:H_2SO_4) 110°C bath, and a buffered oxide etch 25°C bath. Layers of doped and intrinsic hydrogenated amorphous silicon (a-Si:H) were deposited on cleaned 156×156 mm^2 c-Si wafers with an Octopus II (INDEOtec) plasma-enhanced chemical vapor deposition (PECVD) tool at 250°C. Indium tin oxide (ITO) was sputtered with a 2% oxygen gas flow to a thickness ~70 nm in an MRC 944 sputtering tool. Silver metallization was applied via screen printing on front and rear faces and cured/annealed for around half an hour at 200 °C.

Measurements of external quantum efficiency (EQE) and Suns-Voc under front-only and rear-only illumination were conducted to evaluate model performance as a function of wavelength and voltage, as given in Figure S1B and S1C. Measurements of EQE were conducted with an Oriel 300 W calibrated xenon lamp and Oriel Cornerstone 130 1/8 m Monochromator, while Suns-Voc measurements were conducted on a Sinton Instruments WTC-120.

Since EQE and Suns-Voc measurements were conducted on reflective chucks, a back-reflector was added to the simulations for this comparison, but it is not present for any other data analysis presented in this work. Under a spectrum of AM1.5G, modelled short-circuit current density (J_{sc}) has a discrepancy of 0.1 mA/cm^2 under front illumination and 0.3 mA/cm^2 in comparison to measured EQE-extracted J_{sc}. Thus, as inputs into Suns-Voc measurements, we apply pseudo short-circuit current densities equal to our simulation output. We provide these J_{sc} input values in the first row of the table inset in Figure S1C. As Suns-Voc is an open-circuit voltage (V_{oc}) measurement technique, effects of series resistance are eliminated, resulting in the *pseudo J-V* curve presented in S1C by experimental dots. Modelled *J-V* behavior, including resistances, is given by solid lines for comparison.

Measured and modelled V_{oc} shows excellent agreement, with a <5 mV discrepancy for both front and rear illumination. Pseudo-efficiency (p-η) output by Suns-Voc differs from our modelled efficiency (η) by 0.2% abs. and 0.1% abs for front and rear illumination, respectively. Rear side η is lower than front-side η primarily due to lower J_{sc},

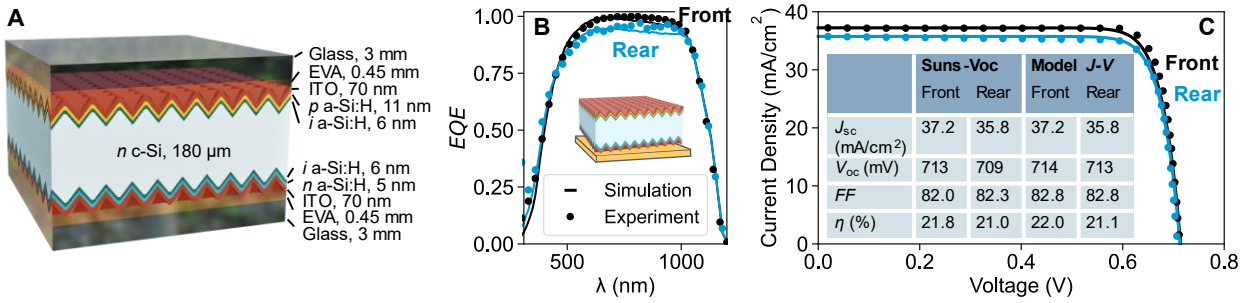

Figure S1. Silicon Heterojunction Cell Model Validation

(A) Encapsulated bifacial silicon heterojunction cell structure, as simulated in this work. Layer thicknesses are as labelled and align with cell fabrication. (B) Measured and simulated EQE for front-only and rear-only illumination of a bare cell on a reflective chuck. (C) Measured Suns-Voc with modelled *J-V*. Parameters extrapolated from Suns-Voc and modelled *J-V* curves are inset.

as depicted in S1B, caused by SRH recombination in the c-Si bulk. With higher c-Si wafer quality, reduced contamination during wafer cleaning, and optimized contacts, efficiencies around 24% are achievable [S5].

The Scaled Rear Irradiance Method in Multiple Locations

The same analysis presented in the main paper has been repeated in Phoenix, USA and Ottawa, Canada to demonstrate variations in the calibration for other mid-latitude locations with different diffuse irradiance fractions. The results are summarized in Table S1 for the bifacial HSAT described in the main text. Ottawa, having a higher GHI-weighted ratio of diffuse light, has R_{SRI} on average 3% higher than in Boulder. Phoenix, with more direct light, has on average 7% lower R_{SRI}. For either location, use of the calibrated values as given by Boulder results in similar energy yield deviations from full system-level analysis with DUET.

Table S1. Calibration and Performance of the SRI Method in Multiple Locations

		Phoenix	Boulder	Ottawa
Latitude		33.45°N	40.01°N	45.42°N
Annual DHI/GHI ratio		0.27	0.36	0.43
$R_{\mathrm{SRI}}(x, \tau = HSAT)$	Snow	-	0.240	0.254
	White sand	0.199	0.211	0.214
	Dry grass	0.125	0.134	0.136
	Light sand	0.095	0.102	0.104
	Concrete	0.092	0.088	0.091
	Roof shingle	0.080	0.086	0.088
	Green grass	0.080	0.086	0.088
	Red brick	0.062	0.067	0.070
	Soil	0.054	0.059	0.062
Annual predicted bifacial gain discrepancy with DUET using Boulder calibration values (% abs.)	IEC	10	8	8
	Max	27	33	32
	Scaled	2	1.7	0.7

The Spectral Scaled Rear Irradiance Method

As described in the main text, the scaled rear irradiance (SRI) method can be adapted to include the effects of spectral albedo via Equation 9 rather than a scaling of AM1.5G. We refer to this form of the SRI method as the spectral scaled rear irradiance (S-SRI) method. This method instead changes the applied front and rear spectra based on the spectral shape of the ground cover. Using the SRI method, output power of the full spectral, S-SRI calculation is predicted to within 0.2 W/m^2 on average. Efficiency for the SRI method accounts for the effect of spectral shape via Equation 7 and 8. Thus, efficiency calculated with S-SRI and SRI methods agree to within 0.03% abs. on average for the dataset of considered albedos.

Additional Variations in Incident Spectra

Additional factors, such as atmospheric conditions and sun position, shift the incident spectrum received on bifacial cells and modules. This analysis could also be decomposed into direct and diffuse irradiance components. To keep calculations as simple as possible, and for ease of comparison with IEC 60904-1-2 standards, all calculations presented in the main text of this article have used the standard AM1.5G spectrum which assumes a particular ratio of direct-to-diffuse light and set values for atmospheric conditions. Under real-world conditions, this ratio depends on location, time of day, day of the year, system design, and other environmental factors [S6]. As diffuse light tends to have a higher UV content than direct light, locations with more diffuse light will have higher spectral-albedo enhancements for ground coverings that are UV-reflective, such as snow. For example, if the diffuse irradiance fraction increases by 10%, the ratio of EQE-weighted albedo to broadband albedo of snow will rise by around 1%.

Summary of 3D View Factor System-Level Model Inputs

In Table S2 we summarize the environmental, cell, and system inputs into the 3D view factor model, DUET, for a bifacial horizontal single-axis tracked array. For fixed tilt array configurations, modules are South-facing at latitude-tilt. The performance of DUET has been compared to other software in Ref. [S7].

Table S2. Summary of DUET Inputs

Environment	City	Boulder, Colorado, USA
	Latitude, longitude	40.01°N, 105.26°W
	Sky model	Perez sky luminance distribution model
	Environmental data	NREL NSRDB
Cell geometry	Cell size	M2 (156.75 mm)
	Cell area (cm^2)	238.84
	Metallization shading fraction (%)	7%
	Irradiance sample points per cell	16
Cell *I-V*	Bifaciality (%)	96
	Short-circuit current (A/cell)	8.19
	Responsivity (A/W)	0.343
	Open-circuit voltage (V)	0.712
	Ideality factor	1.08
	Saturation current (nA/cell)	0.35
	Shunt resistance (Ω)	12.6
	Series resistance (Ω)	0.00018
	Temp. coef. short-circuit current (K^{-1})	0.035
	Temp. coef. open-circuit voltage (K^{-1})	-0.00235
	Nominal operating cell temp. (°C)	42
	Incidence angle modifier model	ASHRAE
Module geometry	Number of cells	72
	Module orientation	Portrait
	Frame?	Included
Array geometry	Row alignment	North-South
	Number of rows	5
	Row pitch (m)	4.84
	Number of tables per row	1
	Number of modules per table	31
	Module spacing (m)	0.03
	Number of tiers	1
	Ground clearance	1.22
	Racking?	Includes purlins and torque tube
Tracker	Type	East-West single-axis tracking
	Backtracking?	Included
Torque tube	Shape	Round
	Radius (m)	0.05

REFERENCES

[S1]. E. M. Tonita, C. E. Valdivia, M. Martinez-Szewczyk, M. R. Lewis, M. I. Bertoni, and K. Hinzer, "Effect of air mass on carrier losses in bifacial silicon heterojunction solar cells," *Solar Energy Materials & Solar Cells*, 230, 111293(2021). https://doi.org/10.1016/j.solmat.2021.111293

[S2]. S. Y. Herasimenka, C. J. Tracy, V. Sharma, N. Vulic, W. J. Dauksher, and S. G. Bowden, "Surface passivation of n-type c-Si wafers by a-Si/SiO2/SiNx stack with <1cm/s effective surface recombination velocity," *Appl. Phys. Lett*., 103, 183903 (2013). https://doi.org/10.1063/1.4827821

[S3]. Z. C. Holman, A. Descoeudres, L. Barraud, F. Z. Fernandez, J. P. Seif, S. De Wold, and C. Ballif, "Current losses at the front of silicon heterojunction solar cells," *IEEE J. of Photovolt*., 2, 7-15 (2012).

[S4]. Z. C. Holman, M. Filipic, A. Descoeudres, S. De Wolf. F. Smole, M. Topic, and C. Ballif, "Infrared light management in high-effiency silicon heterojunction and rear-passivated solar cells," *J. Appl. Phys*, 113, 013107 (2013). https://doi.org/10.1109/JPHOTOV.2011.2174967

[S5]. C. Ballif, M. Boccard, A. Descoeudres, C. Allebé, A. Faes, O. Dupré, J. Haschke, P. J. Ribeyron, M. Despeisse, "Solving all bottlenecks for silicon heterojunction technology," *Photo. Interpret*., 42, 85-97 (2019).

[S6]. J. L. Torres, M. De Blas, A. Garcia, and A. de Francisco, "Comparative study of various models in estimating hourly diffuse solar irradiance," *Renewable Energy*, 35, 1325-1332 (2010). https://doi.org/10.1016/j.renene.2009.11.025

[S7]. J. Stein, C. Reise, G. Friesen, G. Maugeri, E. Urrejola, and S. Ranta, "Bifacial Photovoltaic Modules and Systems: Experience and Results from International Research and Pilot Applications," IEA-PVPS T13-14:2021, Apr. 2021. doi: 10.2172/1779379

Chapter 6

Latitude trends for bifacial photovoltaic systems

In this chapter, latitude trends of bifacial PV systems are explored. Four journal articles are presented spanning row spacing and tilt optimization, spectral albedo, model validation, and degradation rates under varying latitudes. This research aims to advance the knowledge of PV modelling uncertainty in high latitudes; parameterize appropriate row spacing for fixed-tilt, SAT, and vertical PV systems as a function of latitude; and review long-term performance of existing northern PV sites.

6.1 Ground coverage ratios for tracked and fixed-tilt photovoltaic systems for latitudes up to 75°N

Guidelines for row spacing
Have been historically made for low latitude.
Here, northern PV placing
With modern systems is pursued.

.

Formulae are given
For calculating spacing up to 75 degrees.
Rows should be driven
Further apart in locations that freeze.

❄ ❄ ❄

Scope and impact

The PV market is globally shifting towards single-axis tracking and bifacial technologies, while also expanding to higher latitudes [42]. However, general guidelines for PV system design that are often employed today were historically developed for monofacial fixed-tilt systems at low-to-moderate latitudes. Existing row spacing trendlines have not been shown beyond latitudes of 55°N [172]. In this work, we provide empirical equations for calculating appropriate row spacing depending on the PV deployment latitude and configuration for a few shading tolerance scenarios up to 75°N. We generalize the appropriate row spacing for any module size by presenting results in terms of ground coverage ratio (GCR) – the ratio between PV collector length and row pitch.

This article has the following novelties:

1. Empirical equations are provided for calculating appropriate row spacing for fixed-tilt, SAT, and vertical PV deployments as a function of latitude under three shading loss scenarios.

2. The tilt of equator-facing fixed-tilt PV systems is optimized for varying latitudes and GCR. For the 5% shading loss scenario, annual optimum tilt is calculated to be latitude-tilt minus 10°.

3. We show that bifacial PV arrays require GCRs 11% lower on average than monofacial GCRs, regardless of tracking type.

4. We demonstrate that tracked and fixed-tilt PV arrays have similar optimal GCRs around and above 55°N, but that <55°N tracked systems are significantly more sensitive to shading losses caused by reducing the spacing between rows.

5. Energy yield density is found to peak for equator-facing fixed-tilt systems for GCR between 0.5 and 0.7. Increasing the number of modules in the same land area will eventually result in an overall loss to the energy yield produced on the land due to high shading loss. SAT and vertical PV systems are found to be more tolerant to high packing density across all latitudes.

Overall, the formulae presented in this paper for calculating optimum PV system GCR using the location latitude can be directly used by system developers and researchers to aid in system design. Our results can inform future PV deployment for any location >15°N by providing updated guidelines that represent the progression of solar energy development.

Author contributions

Erin M. Tonita As the lead author of this work, I led the design of experiment, ran all simulations, analyzed and fit results, and wrote the original manuscript.

Annie C. J. Russell helped to conceptualize this research, provided guidance on the running of DUET simulations, and guided the selection of appropriate system-level parameters. She revised and edited the manuscript.

Christopher E. Valdivia supervised the simulations and provided guidance on system-level parameters. He revised and edited the manuscript.

Karin Hinzer supervised the project, provided funding, and revised and edited the manuscript.

Copyright

E. M. Tonita, A. C. J. Russell, C. E. Valdivia, and K. Hinzer, "Optimal ground coverage ratios for tracked and fixed-tilt photovoltaic systems for latitudes up to 75°N," *Solar Energy*, 258, 8-15 (2023). https://doi.org/10.1016/j.solener.2023.04.038

Solar Energy 258 (2023) 8–15

Contents lists available at ScienceDirect

Solar Energy

journal homepage: www.elsevier.com/locate/solener

Optimal ground coverage ratios for tracked, fixed-tilt, and vertical photovoltaic systems for latitudes up to 75°N

Erin M. Tonita *, Annie C.J. Russell, Christopher E. Valdivia, Karin Hinzer

SUNLAB, University of Ottawa, Ottawa, Ontario, Canada

ARTICLE INFO

Keywords:
Fixed tilt
Single axis
Vertical
Row spacing
Ground coverage ratio
Bifacial

ABSTRACT

General guidelines for determining the layout of photovoltaic (PV) arrays were historically developed for monofacial fixed-tilt systems at low-to-moderate latitudes. As the PV market progresses toward bifacial technologies, tracked systems, higher latitudes, and land-constrained areas, updated flexible and representational guidelines are required. Using our 3D view-factor PV system model, DUET, we provide formulae for ground coverage ratios (GCRs –i.e., the ratio between PV collector length and row pitch) providing 5%, 10%, and 15% shading loss as a function of mounting type and module type (bifacial vs monofacial) between 17-75°N. Fixed-tilt arrays span a wide range of GCR (0.15–0.68, 5% loss) compared to single-axis tracked arrays (0.17–0.32) and vertical east–west arrays (0.11–0.16). We additionally optimize fixed-tilt module tilt, finding that the optimum tilt can vary from 7° above latitude-tilt to 60° below latitude-tilt in certain cases. We demonstrate that tracked and fixed-tilt PV arrays should have similar GCRs >55°N, but tracked systems are more sensitive to row-to-row shading losses <55°N. The GCR of fixed-tilt arrays at lower latitudes can reach 0.55 without introducing >2.5% shading loss, whereas tracked and vertical arrays reach 2.5% shading loss by GCRs <0.22 and <0.10, respectively. We additionally find that bifacial PV arrays require GCRs up to 0.03 lower than monofacial GCRs. These results can inform future deployment designs for latitudes >15°N.

1. Introduction

The inter-row spacing of photovoltaic (PV) arrays is a major design parameter that impacts both a system's energy yield and land-use, thus affecting the economics of solar deployment. Adjacent rows in a PV array introduce energy yield loss via direct beam shading and diffuse-sky masking (Appelbaum and Aronescu, 2022; Van Schalkwijk et al., 1997) and contribute to greater irradiance inhomogeneity and current mismatch losses. These negative effects of neighbouring PV rows can be reduced by increasing the spacing between rows and by moving tracked PV off-sun during morning and afternoon hours in a loss-minimizing practice known as *backtracking*. However, as PV deployment continues to accelerate with decarbonization plans predicting unprecedented renewable sector expansion (International Technology Roadmap for Photovoltaic (ITRPV), 2021; The International Energy Agency, 2021), PV land-use may become more limited and costly (Bolinger and Bolinger, 2022; Kafka and Miller, 2020; Tawalbeh et al., 2021). Optimization of PV array configuration within a constrained field is required, and previous guidelines for PV row spacing which focus on eliminating shading may not be adequate.

A commonly cited approach for determining inter-row spacing in fixed-tilt systems is the "winter solstice rule", where spacing is determined by the shadow length cast on the winter solstice at solar noon. Some versions of this rule call for even wider row spacing by instead constraining the time with no direct shading to between the hours of 9:00 AM and 3:00 PM on the winter solstice. The winter solstice rule is not a practical method for determining row spacing when the economics of land-use, cabling cost, and associated voltage power losses must be considered (Appelbaum and Aronescu, 2022; Sanchez-Carbajal and Rodrigo, 2019).

Similarly, the general guideline for traditionally deployed equator-facing fixed-tilt system module inclination is to set the module tilt to a value between 5-15° less than the latitude (Calabro, 2013; Lewis, 1987; Qiu and Ruiffat, 2003), which is particularly important for higher latitudes (Armstrong and Hurley, 2010; Schroder, 2011; International Renewable Energy Agency, 2014). The interplay of array tilt and row spacing must also be considered (Rehman et al., 2020), as the incorrect coupling of tilt and row spacing can lead to unnecessary production loss.

* Corresponding author.
E-mail address: etoni044@uottawa.ca (E.M. Tonita).

https://doi.org/10.1016/j.solener.2023.04.038
Received 6 March 2023; Received in revised form 14 April 2023; Accepted 18 April 2023
Available online 29 April 2023

For example, a PV plant located in Qatar has reported a 4% annual loss in energy yield due to a non-ideal coupling of tilt and row spacing, described by Shah et al. (2019).

While these general guidelines provide a simple methodology for preliminary system design, greater flexibility on row spacing requirements and characterization of associated shading loss is needed to minimize the levelized cost of electricity as available land becomes more scarce and costly. Moreover, these approaches were initially developed for monofacial equator-facing fixed-tilt systems at low-to-moderate latitudes. Now that the PV market is globally shifting towards single-axis tracking and bifacial technologies (The International Energy Agency, 2021), while also expanding to higher latitudes (Frimannslund et al., 2021; Pike et al., 2021), an investigation into optimal row spacing – or *ground coverage ratio* (GCR) (i.e., the ratio between PV collector length and row pitch) – for a wider range of technologies and locations is warranted.

Among a growing configuration of PV technologies is the use of vertical fixed-tilt arrays. East-west vertical bifacial fixed-tilt PV arrays have competitive performance with south-facing panels in at high latitudes (Jouttijarvi et al., 2022; Pike et al., 2021), and are also being explored for agrivoltaic and building-integrated applications (Reker et al., 2022; Tahir and Butt, 2022).

It is generally acknowledged that horizontal single-axis tracked (HSAT) arrays require larger row spacing – or smaller GCRs – than fixed-tilt counterparts. For example, Berrian *et al.* cites GCRs of around 35% are typical for HSAT deployments whereas south-facing fixed-tilt GCRs are often >50% (Berrian et al., 2019). However, there is little existing literature which indicates how selection of the appropriate GCR varies with latitude, nor directly compares the performance of HSAT, south-facing fixed-tilt, and east–west vertical fixed-tilt arrays.

Many studies on row spacing and system design are limited to moderate latitudes around 15-40° either North or South of the equator, with few studies up to latitudes around 50°. For example, Baloch *et al.* examined the interplay of row spacing and mounting height on bifacial fixed-tilt and vertical PV arrays at 25°N, finding fixed-tilt arrays are more sensitive to mounting height than vertical arrays (Baloch et al., 2020). On the other hand, vertical arrays have been found to be more sensitive to shading loss due to row spacing compared to fixed-tilt arrays in a 32°N location (Appelbaum, 2016). Verissimo *et al.* compared how favorable PV array system designs vary with GCR for Brazil (Verissimo et al., 2020), Narvarte *et al.* compared tracking gain in Spain at 38°N (Narvarte and Lorenzo, 2008), and Al-Quraan *et al.* explored the interplay of PV array tilt and row spacing in Saudi Arabia (24°N) and Yemen (15°N) (Al-Quraan et al., 2022) .

Few studies have examined row spacing and system optimization in higher latitudes. Jacobson *et al.* conducted an extensive study on the effects of tracking type around the globe, considering cities with latitudes between 37°S and 64°N, and extrapolating to ±80° of the equator (Jacobson and Jadhav, 2018). However, this study was limited to monofacial systems and did not discuss how row spacing and land-use must vary by location. Khan *et al.* compared bifacial vertical arrays to monofacial equator-facing fixed-tilt arrays across the globe using a clear-sky model, and asserted that a 2 m row spacing should be used in practice (Khan et al., 2017). Pike *et al.* performed a seasonal comparison of monofacial and bifacial fixed-tilt and vertical PV module performance in Alaska, considering only single-module arrays (Pike et al., 2021). Frimannslund *et al.* compared the PV potential in the Arctic and Antarctic and discussed in a 78°N case study how the tilt of fixed-tilt arrays can be adjusted to better suit lower row spacing (Frimannslund et al., 2021).

On the bifacial side, research regarding bifacial system design configuration and challenges is becoming more common, however there has been little direct comparison between row spacing for bifacial vs monofacial technologies and still many recent publications on PV system design focus solely on monofacial systems (Bolinger and Bolinger, 2022; Jacobson and Jadhav, 2018).

In this paper we demonstrate how row spacing affects system performance for both monofacial and bifacial arrays, comparing south-facing fixed-tilt, HSAT, and east–west vertical configurations for North American locations at latitudes of 17°N up to 75°N. For each configuration and location, we quantify the inter-row shading and resulting system energy yield losses for GCRs between 0 and 1. We then provide latitude-optimal GCRs – and tilts, in the fixed-tilt case – for 5%, 10%, and 15% allowable annual energy yield loss due to inter-row shading.

2. Methodology

We selected 31 locations from across North American countries of Mexico, the United States, and Canada for PV row spacing characterization and optimization. Locations were selected to include a wide distribution in latitude (17°N to 75°N). Where possible, the locations represent multiple diffuse fractions within a given latitude range, with diffuse fraction defined as the annually-averaged ratio of diffuse horizontal irradiance (DHI) to global horizontal irradiance (GHI). Fig. 1 displays a map of diffuse fraction across the continent with our selected locations indicated by open circles. Environmental data was retrieved from the US National Solar Radiation Database (Sengupta et al., 2018) with the exception of latitudes >60°N, which were obtained from the Canadian Weather Energy Calculation database (Environment and Climate Change Canada, 2022). Typical Meteorological Year data was used for each location at an hourly resolution, including hourly-updating albedo values. A summary of pertinent environmental conditions for each location can be found in Table S1 of the Supplemental Information section.

We modelled the performance of the PV arrays depicted in Fig. 2 using our PV performance prediction software, DUET (Russell et al., 2022). DUET generates a detailed 3D model of the PV system including supportive structures and multiple rows. Optical calculations are then completed considering direct beam radiation, anisotropic diffuse sky radiation, and ground-reflected radiation by segmenting the modules, ground, and diffuse sky-dome into patches. A shading algorithm is implemented using a deterministic ray intersection method (Moller and Haines, 2002; Williams et al., 2005) to capture the effect of objects in the 3D scene. These shading results are combined with a 3D view-factor model to calculate two-dimensional front and rear irradiance profiles for each timestep (Coathup et al., 2023; Russell et al., 2022). Using environmental conditions and module electrical parameters, DUET translates these irradiance profiles into per-timestep cell current–voltage (*I-V*) curves through a temperature and irradiance-dependent single-diode model. Cell temperature is computed using the Sandia glass-cell-glass temperature model (King et al., 2004). Module *I-V* curves are constructed assuming the wiring diagram depicted in Fig. 2C, with 72-cells connected in series and parallel with three bypass diodes. The instantaneous module power is then scaled by the timestep (hour) to arrive at the module energy yield. Yearly total module energy yield, as analyzed in this work, is given by the summation of energy yield over all hourly timestamps. DUET has been validated against hourly field data from fixed-tilt and tracked bifacial PV systems to within a mean absolute error of <0.02 W/Wp (Russell et al., 2022; Stein et al., 2021).

To emulate utility-scale systems (Berrian et al., 2019), we calculated the energy yield of 1 central module in a 5-row array where each row contains 31 modules, as provided in Fig. 2A. To align with common deployment configurations, fixed-tilt and HSAT arrays are arranged in a 1-in-portrait (1P) configuration with module frames, purlins, and torque tubes as in Fig. 2B. Torque tube and purlin dimensions were chosen to align with the range of dimensions used in literature (Coathup et al., 2023; Deline et al., 2020). Vertical arrays are instead modelled in a 1-in-landscape (1L) configuration, as this is commonly used to reduce rear-side irradiance inhomogeneity (Valdivia et al., 2017; Wang et al., 2020). Modules were composed of either monofacial or bifacial silicon heterojunction (SHJ) solar cells with 20.2% efficiency and bifaciality of 96%. Module SHJ parameters, summarized in Table S2, were extracted

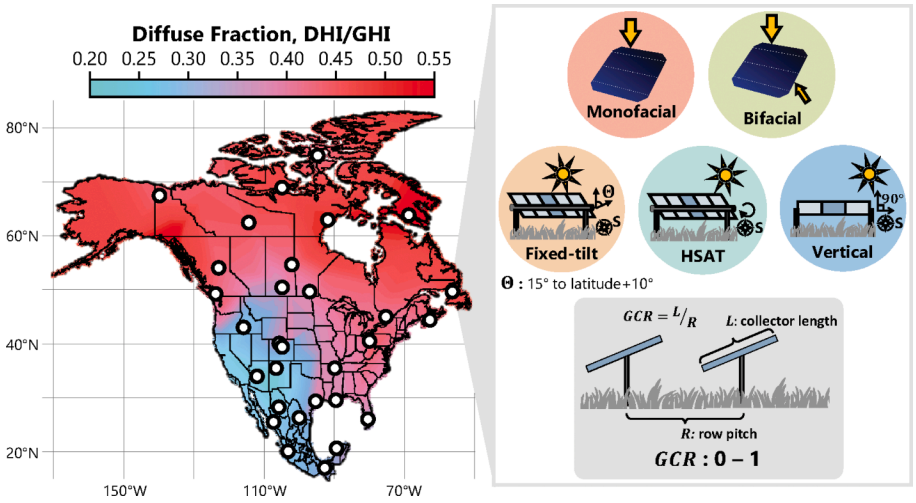

Fig. 1. A map of diffuse fraction across North American countries of Mexico, the United States, and Canada. White circles indicate the 31 locations studied. South-facing fixed-tilt systems are studied with tilts from latitude-tilt + 10° to a minimum tilt of 15°, in 5° increments. East-west HSAT systems studied have a range of motion covering ± 60°. Ground coverage ratios (GCRs) between 0 and 1 are studied for all illumination and mounting types, for both monofacial and bifacial modules. Depicted fixed-tilt, HSAT, and vertical arrays are simplified to show only 1 row containing 3–5 modules.

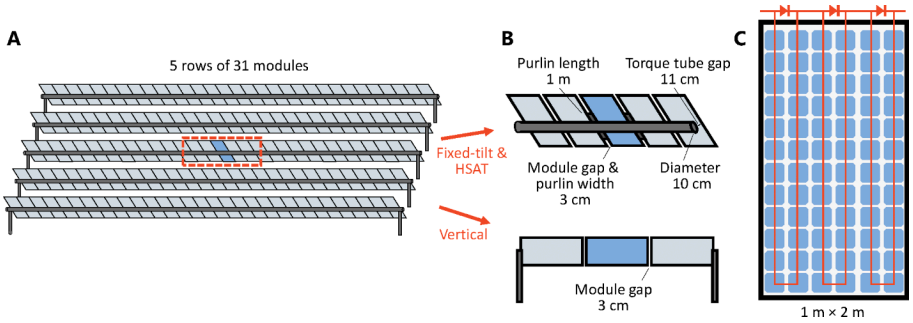

Fig. 2. (A) The full simulated PV array scene viewed from the rear-side for fixed-tilt, HSAT, and vertical arrays. Vertical modules are not tilted, as depicted. (B) Supportive structure dimensions. Purlins are simulated only around the central array module to reduce computation time in the case of fixed-tilt and HSAT arrays. (C) Framed-module layout and internal module wiring structure with bypass diodes indicated above the module.

using a validated drift–diffusion model for dual-sided textured photovoltaic devices described in Tonita et al. (2021). This model has been validated against measurements of SHJ devices (Tonita et al., 2021).

For this study, we calculated the effect of ground coverage ratios between 0 and 1 on monofacial and bifacial fixed-tilt and HSAT arrays, as visualized in Fig. 1. Vertical array GCR is only analyzed for the bifacial case, as the primary appeal of vertical PV arrays is for electricity generation in both morning and afternoon hours. GCR is defined by Equation (1) below:

$$GCR = \frac{L}{R} \tag{1}$$

where L is the collector length perpendicular to the row length and R is the row pitch. A GCR of 1 corresponds to the inter-row spacing where the horizontal gap between modules becomes zero if the module was to be rotated to horizontal tilt. A GCR of 0 corresponds to the case where only a single row in the array is considered, or the inter-row spacing between modules approaches infinity.

This study investigates full cell 1P arrays where L is the length of a single module (2.0 m) and 1L arrays where L is the instead the width of a single module (1.0 m), but results provided in terms of GCR will be generally applicable to other collector lengths, tier-number, and half-cut modules. For example, in Boulder, USA at 40°N, a bifacial full-cell 2-in-portrait (2P) fixed-tilt system with a tier gap above the torque tube of 0.2 m should have a GCR higher by 0.04 compared to the 1P case. Of a similar scale, a bifacial half-cut 1P fixed-tilt system should have a GCR higher by 0.03 compared to a full-cell system. Placing multiple electrically separated modules across the collector length, through either adding additional tiers or half-cutting cells, results in proportionally lower electrical mismatch loss and allows for marginally higher GCR. Due to comparably reduced irradiance inhomogeneity between tracked and fixed-tilt modules, the difference between 2P and 1P for HSAT system GCR need only be 0.01. Similarly, the difference between half-cut and full-cell HSAT system GCR is <0.01. Thus, calculated behaviour with GCR will apply to other collector lengths and half-cut cells.

For fixed-tilt arrays, we additionally varied the tilt angle, θ, from 10° greater than the latitude to a minimum tilt of 15° (in 5° increments) for all locations and all GCRs. A minimum limit of 15° is recommended in practice to reduce accumulation of dust and dirt, and to facilitate rain-based cleaning (Figgis et al., 2017; International Renewable Energy Agency, 2014). For the tilt, θ, we introduce a *latitude-tilt adjustment factor*, φ, for latitude, α, defined as:

$$\theta = \alpha + \varphi;\ \theta \geq 15^{\circ} \tag{2}$$

This latitude-tilt adjustment factor is introduced to emphasize the displacement from latitude-tilt during analysis. The ground clearance from the middle of modules to the ground, H, in meters was then adjusted according to the module tilt, θ:

$$H = \frac{L}{2}\sin\theta + 0.25 \tag{3}$$

We model our arrays with a modest minimum module ground clearance of 25 cm to align with tolerances of HSAT systems in the field, where H typically varies between 0.8 and 1.5 m (Ayala Pelaez et al., 2019; Berrian et al., 2019). Increasing this minimum ground clearance to 1.0 m for fixed-tilt, HSAT, and vertical arrays decreases the optimal GCR in Boulder by 0.01, 0.02, and 0.01, respectively. For the HSAT systems modelled in this work, H is set to 1.12 m where θ in Eq. (3)

equates to the tracking bounds of ± 60° tilt. In addition, a conventional backtracking algorithm is employed for all HSAT arrays (Lorenzo et al., 2011). In this algorithm, HSAT module tilt is adjusted away from direct-beam normal incidence to eliminate direct shading between adjacent rows. For further information, a summary of all system inputs is provided in Table S2.

3. Results

3.1. Influence of ground coverage ratio on optimal tilt in a fixed-tilt system

The interplay of GCR and tilt of fixed-tilt modules is an optimization problem. As GCR increases (or inter-row spacing decreases), energy yield loss due to shading for a given module tilt becomes more and more substantial. For higher GCR values, a lower tilt enhances energy yield by reducing row-to-row shading loss, despite additional cosine losses (Al-Quraan et al., 2022; Rehman et al., 2020; Van Schalkwijk et al., 1997). Fig. 3A displays how changing the tilt of a fixed-tilt array away from latitude-tilt by φ affects the bifacial energy yield of a central module located in a 5-row array in Boulder, USA. For a given GCR, the tilt adjustment factor providing the highest energy yield, φ_{opt}, is displayed by a star. To the right of the star shading losses dominate, while to the left of the star cosine losses dominate. As GCR increases from 0 to 1.0, the optimal tilt of the module moves from latitude + 5° to the minimum allowed tilt of 15°, or tilt adjustment factor of −25° for Boulder, Colorado. One can also observe on this plot the substantial influence GCR has on module energy yield, particularly for GCRs > 0.5. From a GCR of 0 to 0.5 the energy yield drops by 9%. From a GCR of 0.5 to 1.0, the energy yield drops by 50%.

The latitude of the fixed-tilt array also affects the optimal tilt adjustment factor. Here, we combine the effect of GCR, latitude, and module tilt for latitudes between 20 and 75°N. Fig. 3B and 3C display the optimal tilt adjustment factors as a function of GCR for different latitude bins for monofacial and bifacial modules, respectively. Locations are binned and averaged by latitude within the error bounds indicated in the legend, with 2–4 locations per bin. As a contrast to previous findings which suggest using tilt adjustment factors between −5° to −15° (Calabro, 2013; Lewis, 1987; Qiu and Ruiffat, 2003), we find that the appropriate latitude-tilt adjustment factors vary between +7° to −60° when a wide range of latitudes and GCRs are considered. At all latitudes, shifting towards higher GCR favours shallower tilt angles in order to limit inter-row shading loss, as seen in Boulder in Fig. 3A. For GCR >0.7, the minimum tilt of 15° should be used at all latitudes. In higher latitude locations, the tilt adjustment factor is significantly more sensitive to GCR due to lower average solar elevation. For example, when changing GCR from 0.3 to 0.4, the optimum tilt adjustment factor for a monofacial fixed-tilt module at 17°N decreases by 0.4°, while the optimum tilt for this same module located at 75°N decreases by 14°.

Additionally, whether the modules are monofacial or bifacial can have a slight impact on the choice of optimal module tilt. For GCRs >0.5 bifacial and monofacial optimal tilts are about the same since the irradiance contribution from rear-incident light is proportionally small. However, when GCR decreases below 0.5, there is more opportunity for diffuse, reflected, and occasionally direct-beam radiation to reach the rear-side, increasing the relative contribution of row shading on the front side. The balance between these two effects leads to higher optimal tilt angles for bifacial arrays than for monofacial arrays at lower GCRs. For the scenario of no neighbouring rows (GCR = 0), bifacial module tilts should be on average 3° steeper than monofacial tilts for all locations. For a moderate GCR of 0.35, bifacial modules optimum tilts are between 0 and 3° steeper than monofacial tilts, and 1° steeper on average. However, this difference depends on the bifaciality of the technology used and will be smaller for modules with bifaciality <96%; thus, in most cases, the optimum tilt of monofacial and bifacial fixed-tilt arrays can be assumed to be about the same.

All fixed-tilt results that follow are with the tilt set to the appropriate optimum value.

3.2. Influence of ground coverage ratio on inter-row losses

Next, we quantified the sensitivity of annual module energy yield to changes in GCR for fixed-tilt, HSAT, and vertical arrays. Fig. 4 displays the results for a bifacial module in a fixed-tilt array (4A), HSAT array (4B), and vertical array (4C). The inter-row energy yield loss, or the amount of energy yield that is lost in comparison to an infinite row spacing case (GCR = 0), is plotted on the y-axis. Thus, this inter-row energy yield loss includes losses associated with direct-beam inter-row shading, diffuse-sky masking from adjacent rows, and, in the case of HSAT modules, the cosine losses associated with backtracking to minimize shading.

There is a substantial difference in the impact of GCR on fixed-tilt, HSAT, and vertical arrays for low-to-moderate latitudes. For example, at our lowest latitude case of Tuxtla Gutiérrez, Mexico at 17°N, 5% inter-row shading loss occurs at a GCR of 0.68 for fixed-tilt arrays compared to a GCR of 0.32 for HSAT arrays and 0.16 for vertical arrays. Lower latitude locations with fixed-tilt arrays have a wide range of GCRs with inter-row energy yield loss <5%. At our highest latitude location in Resolute Bay, Canada at 75°N, the difference between fixed-tilt and HSAT array GCR causing 5% loss is only 0.02. As a contrast, the energy yield lost to inter-row shading effects steeply increases with GCR for vertical arrays, with less sensitivity to latitude than fixed-tilt and HSAT cases. To achieve 5% shading loss, vertical array GCR must be <0.20 for all locations.

Monofacial module trends are similar to the bifacial trends plotted, only shifted by 11% on average towards higher GCR for equivalent

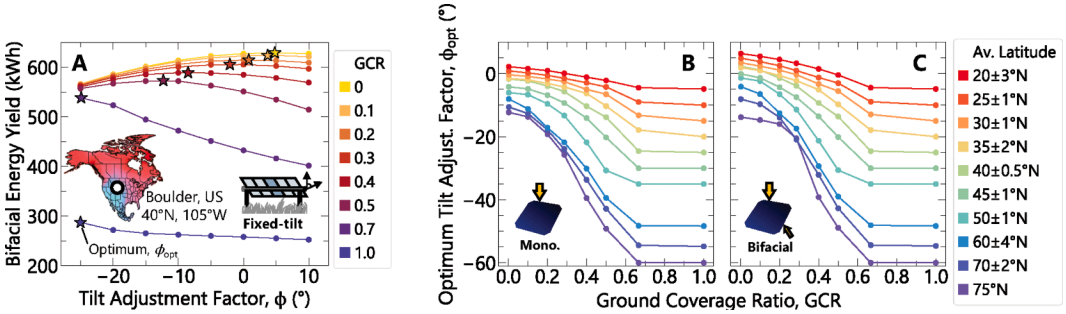

Fig. 3. (A) The bifacial energy yield of a central fixed-tilt module in a 5-row PV array as the tilt adjustment factor, ϕ, is varied from −25° to + 10° for Boulder, USA. A tilt-adjustment factor of zero corresponds to latitude-tilt. Stars indicate the interpolated point of highest energy yield, corresponding to the optimal tilt-adjustment factor for a given GCR. The optimum tilt-adjustment factors for different GCRs and latitudes is plotted in (B) for monofacial and (C) bifacial south-facing fixed-tilt systems. Data for the latitudes provided is an average of 2–4 locations, located within the given latitude-bin. The constraint of a minimum tilt of 15° causes plateaus in the adjustment-factor for GCRs > 0.7.

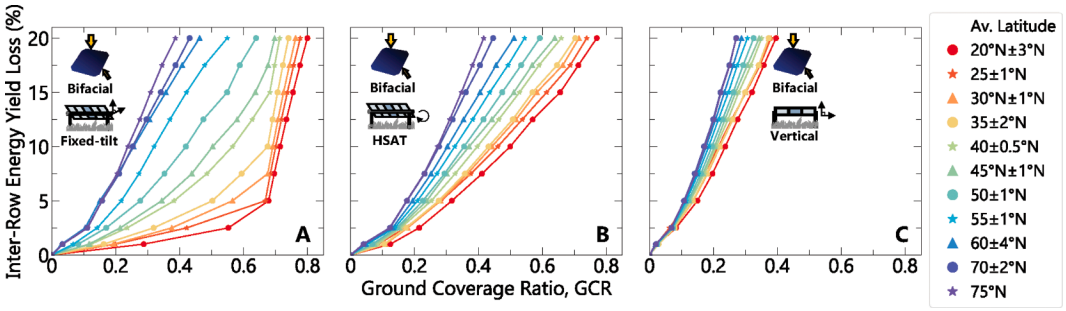

Fig. 4. The impact of GCR on the total amount of energy yield lost to inter-row effects of direct-beam shading and diffuse-sky radiation masking for all 31 North American locations for bifacial (A) fixed-tilt systems, (B) HSAT systems, and (C) vertical systems.

annual relative inter-row losses. Further comparison between bifacial and monofacial results is presented and discussed in the following section.

3.3. Latitude trends

To further elucidate GCR trends between 17 and 75°N, we consider the requirements for each system configuration to perform with an accepted inter-row energy yield loss of 5%. Fig. 5 displays the GCR for each of our 31 locations that results in 5% inter-row losses parsed by latitude and diffuse fraction for fixed-tilt arrays (5A), HSAT arrays (5B), and vertical arrays (5C). Inset in each of these plots is a linearly-interpolated geographical map displaying the GCRs.

While there is a correlation between diffuse fraction and latitude, with a Pearson correlation coefficient of r = 0.71, we find that GCRs are more strongly influenced by latitude than diffuse fraction. This can be seen by the dominating shift of GCR from low to high latitude. Locations at similar latitudes but different diffuse fractions have an average standard deviation in GCR of just ±0.02.

Fixed-tilt GCRs achieving only 5% inter-row energy yield loss span between 0.14 and 0.68 from 75°N to 17°N for bifacial modules, while HSAT GCRs range between 0.18-0.32 and vertical GCRs between 0.10-0.16. To achieve a given relative inter-row energy yield loss, HSAT arrays generally require lower GCR values than fixed-tilt arrays, especially for lower latitude locations. However, in Canada and Alaska, spacing requirements are similar for the two configurations, and HSAT arrays even allow narrower row spacing than fixed-tilt arrays for latitudes >55°N. This is more easily seen in Fig. 6, which shows the latitude-trends of GCRs achieving inter-row energy yield losses of (A) 5%, (B) 10%, and (C) 15%. These higher inter-row loss scenarios would apply for PV deployments where land is limited and modules must be spaced closer together to achieve desired yields.

Trendlines for monofacial and bifacial modules in fixed-tilt, HSAT, and vertical arrays are plotted in Fig. 6. Fixed-tilt behaviour is fit to an S-curve, with the following equation:

$$GCR = \frac{P}{1 + e^{-k(\alpha - \alpha_0)}} + GCR_0 \tag{4}$$

where P, k, α_0, and GCR_0 are fitting parameters and α is the latitude. All fitting parameters for the subplots in Fig. 6 are provided in Table 1, allowing for the computation of appropriate GCR for any latitude between 15-75°N. For the HSAT and vertical array linear regression parameters, m is the slope, while b represents the y-intercept. The standard deviation between the fitting functions and calculated data points is ±0.03 for fixed-tilt arrays and ±0.01 for HSAT and vertical arrays.

Fixed-tilt array GCR exhibits S-curve behaviour, with low-latitude GCR plateauing due to a minimum tilt of 15° and high-latitudes experiencing diminishing returns on further increases in row spacing. HSAT and vertical array behaviour is fit by a linear regression, with GCR decreasing linearly towards higher latitudes. Vertical arrays only show a marginal dependence on latitude, leading to a simple linear fit. While HSAT behaviour is more sensitive to latitude, HSAT trends are different than south-facing fixed-tilt arrays due to shade-reduction via back-tracking. For a given GCR, HSAT arrays at higher latitudes will back-track more often than lower latitude arrays, resulting in higher cosine losses. Therefore, higher latitude systems require lower GCR to maintain a specific inter-row loss.

For all depicted inter-row shading loss scenarios, HSAT GCRs and fixed-tilt GCRs are comparable for latitudes >55°N. This means that land requirements for deployments in the North will be similar for HSAT and fixed-tilt arrays. Land-usage should not dictate whether single-axis

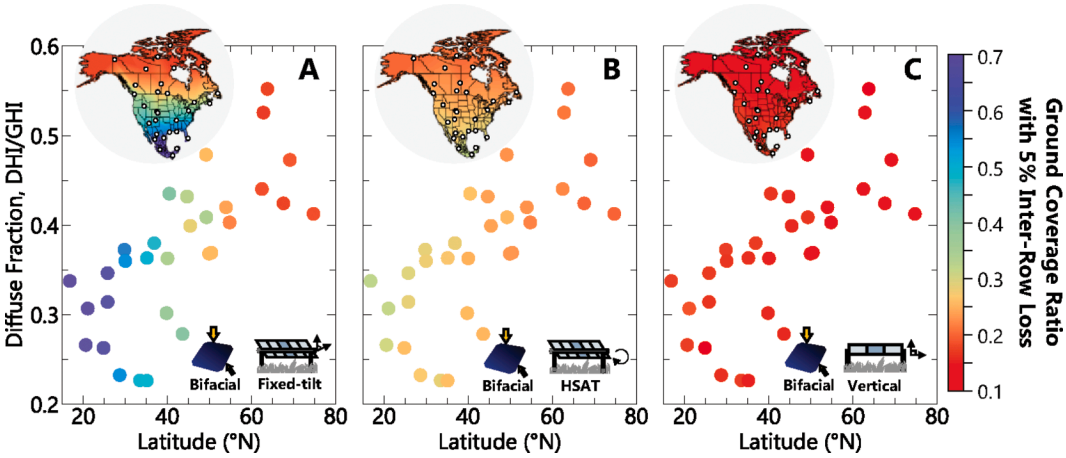

Fig. 5. The GCR giving a 5% inter-row spacing energy yield loss for all 31 locations as a function of latitude and diffuse fraction for (A) bifacial fixed-tilt systems, (B) bifacial HSAT systems, and (C) bifacial vertical systems. Inset maps show the GCR linearly interpolated across Mexico, the United States, and Canada.

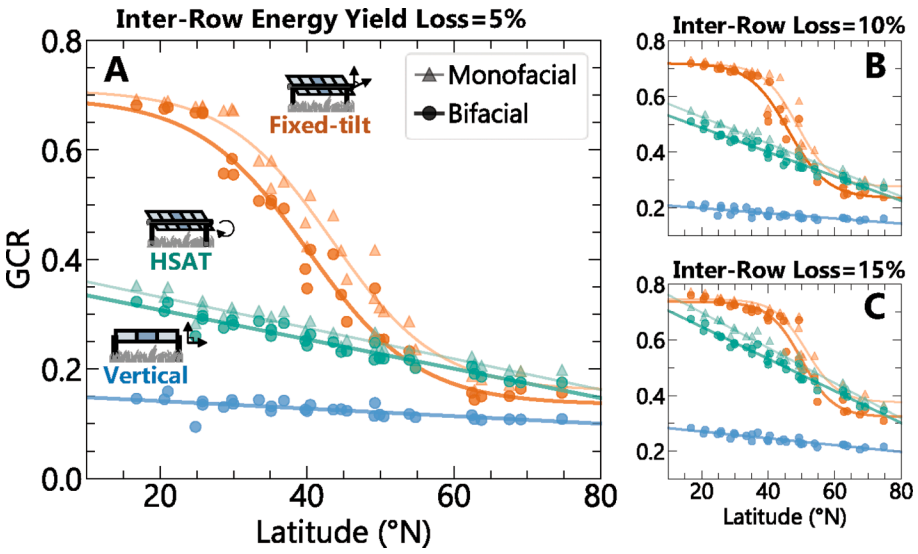

Fig. 6. GCR latitude-trends for (A) inter-row energy yield shading loss ('inter-row loss') of 5%, (B) 10%, and (C) 15%. Fixed-tilt data is given in orange, while HSAT data is given in teal and vertical data in blue. Monofacial and bifacial system results are additionally provided by lighter triangles and darker circles, respectively, with deviations between bifacial and monofacial performance emphasized by the high module bifaciality of 96%. The appropriate GCR for any latitude > 15°N can be extracted from these plots, with fit parameters summarized in Table 1. (For interpretation of the references to colour in this figure legend, the reader is referred to the web version of this article.)

Table 1
Fitting Parameters for Calculating Ground Coverage Ratio.

		Fixed-tilt				HSAT		Vertical	
		P	k (1/°)	α_0 (°)	GCR_0	m (1/°)	b	m (1/°)	b
Inter-row energy yield loss 5%	Bifacial	−0.560	0.133	40.2	0.70	-2.68×10^{-3}	0.361	-6.87×10^{-4}	0.155
	Monofacial	−0.550	0.138	43.4	0.71	-2.82×10^{-3}	0.388	–	–
Inter-row energy yield loss 10%	Bifacial	−0.485	0.171	46.2	0.72	-4.37×10^{-3}	0.575	-1.23×10^{-3}	0.257
	Monofacial	−0.441	0.198	48.7	0.72	-4.76×10^{-3}	0.621	–	–
Inter-row energy yield loss 15%	Bifacial	−0.414	0.207	49.9	0.74	-5.76×10^{-3}	0.762	-1.93×10^{-3}	0.357
	Monofacial	−0.371	0.208	51.5	0.75	-6.33×10^{-3}	0.825	–	–

trackers are deployed in the North, instead decision-makers can focus on other relevant factors such as tracking cost, feasibility, and energy yield gain.

For low-to-moderate latitudes, HSAT array inter-row shading loss is more sensitive to changes in GCR than fixed-tilt systems. For example, in Miami, USA at 26°N, the GCR for bifacial HSAT arrays is lower than fixed-tilt arrays by 0.13 under the 15% loss scenario, but this discrepancy nearly triples to 0.37 under the 5% loss scenario. Contrary to the high-latitude case, low latitude decision-makers who wish to minimize inter-row shading losses must consider land-use as a key factor when choosing between tracking and fixed-tilt systems. Vertical system GCR may reach up to 0.29 when shading loss is more tolerable at low latitudes, as in the 15% shading loss scenario in Fig. 6C. However, low GCRs <0.20 are necessary for all latitudes when limiting shading loss to 5%. This suggests that vertical PV arrays may need to tolerate higher shading losses to be more feasible in practice compared to south-facing fixed-tilt and HSAT arrays.

Whether the array is bifacial or monofacial additionally affects the latitude-optimal GCRs. As shown in Fig. 6, the trends between bifacial and monofacial modules for fixed-tilt and HSAT arrays follow the same behaviour, with bifacial module GCRs shifted lower on average by 0.03 than monofacial, since larger row spaces leads to higher rear irradiance. The appropriate GCR for any configuration at any latitude >15°N can be extracted from these plots or calculated using the fitting parameters provided in Table 1.

4. Discussion

While this paper discusses the interplay of inter-row energy yield loss on GCR for tracking/fixed-tilt/vertical systems and bifacial/monofacial modules, the appropriate selection of system configuration is a complex economic objective function, and further design optimizations should be considered. For example, PV arrays can be further optimized by accounting for non-flat terrain (Al-Quraan et al., 2022), considering the effects of wind-based module cooling caused by array layout (Glick et al., 2020), alternating panel inclination between neighboring rows (Kafka and Miller, 2020), varying mounting height (Baloch et al., 2020), and using row-specific tracking algorithms for HSAT arrays (Daly and Abbaraju, 2018). In addition, other non-conventional array mounting configurations may be of benefit. For example, high density, shallow ground-mounted array layouts with little spacing between array rows have been recently emerging onto the market, claiming land-use reductions ~30% (Carroll, 2021; GameChange Solar, 2023; Jurchen Technology, 2023).

Here, we presented the sensitivity of inter-row energy yield shading loss to GCR by comparing to the energy yield of a module with no neighbouring rows (GCR = 0). In some cases, it might be more beneficial to instead consider energy density, as suggested by Verissimo et al. (2020). This could be of more use when, for example, available land for PV is limited and module costs are low. Figure S1 in the supplemental information shows a plot of energy yield density as a function of GCR for the 31 locations considered in this work. For HSAT arrays, energy yield density continues to increase towards GCRs of 1.0, despite increased shading losses. If the sole objective is to maximize the energy yield of a given plot of land regardless of module cost, HSAT rows can be placed with little to no gap between rows, since losses associated with near constant backtracking are offset by the sheer number of modules on site. However, this is not a practical site layout in most circumstances as space must be left for operation and management practices, and modules spend most of the year backtracking to tilts < 15°. Fixed-tilt energy density, on the other hand, peaks for GCRs between 0.5 and 0.7 for latitudes between 17°N to 75°N. Even with negligible module cost, GCRs beyond these peaks are unlikely to be economically feasible, as reducing row spacing further results in an overall loss to energy yield; the benefit

gained by fitting more modules into a given space is very literally overshadowed by shading losses if a minimum 15° tilt is maintained to avoid soiling. Eliminating the minimum tilt requirement of 15° can allow for non-conventional shallow-tilt array layouts with high energy yield density at GCRs of 1 (Carroll, 2021; GameChange Solar, 2023; Jurchen Technology, 2023). Unlike their equator-facing fixed-tilt counterparts, east–west facing vertical panels do not experience an energy yield density peak for GCRs up to 1; it is possible to have GCRs >1 to increase the energy yield density of the PV array (Khan et al., 2017; Riaz et al., 2021; Tahir and Butt, 2022). In agrivoltaic applications, the effect of vertical PV row spacing on crop yield must also be considered, with certain crops being more shade-tolerant or shade-sensitive (Riaz et al., 2021; Tahir and Butt, 2022). In all cases, incorporating the effect of GCR on both module energy yield and energy yield density will be necessary to help inform PV array design.

PV arrays were composed of full-cell silicon technology for the presented GCR and energy yield analysis. The power output of a module is generally proportional to the amount of incident irradiance, however, some technologies may be more shade-tolerant. For example, both half-cut cells and cadmium telluride (CdTe) technologies have demonstrated a lower sensitivity to shading than full-cell silicon modules, resulting in tracking schemes that reduce or even eliminate backtracking hours for overall improved performance (Cheein et al., 2021; Ngan et al., 2013). In this case, restrictions on appropriate GCR values as a function of latitude will be lessened, and closer row spacing could be used.

The analysis we have presented has been conducted for North American locations, but covers a wide range of operating conditions, including diffuse fractions between 0.23 and 0.55, average GHI-weighted ambient temperatures of −4°C to 31°C, average GHI-weighted albedos between 0.10 and 0.65, and city elevations between 1 and 1600 m. These location parameters are summarized in Table S1. Including locations across other continents and in the southern hemisphere in this analysis would further the range of operating conditions and contribute to more scatter in the presented trends. Since latitude was the dominating factor effecting inter-row energy yield loss, our results should provide an estimate of the performance of equivalent PV arrays across the globe.

5. Conclusion

Traditional guidelines for determining PV array layouts were developed for monofacial fixed-tilt equator-facing systems at low-to-moderate latitudes, and no longer suit well the expanding PV market, which has been progressing toward bifacial technologies, tracked systems, higher latitudes, and land-constrained areas. Old approaches, like the winter solstice rule, are insufficient to capture the nuance of deployment planning, where practical and economical constraints vary widely both geographically and temporally. In this work, we have quantified the row spacing for tracked, fixed-tilt, and vertical arrays with both bifacial and monofacial technologies in 31 locations from 17–75°N with acceptable inter-row shading losses of 5–15%. We generalize our results to an arbitrary collector area by presenting results in terms of ground coverage ratio. GCR varies widely between 0.15–0.68 for fixed-tilt systems compared to 0.17–0.32 for HSAT systems, both with a strong latitude-dependence. Similarly, the optimal tilt of fixed-tilt arrays varies widely from 7° above latitude-tilt to 60° below latitude-tilt, depending on the latitude and GCR. Vertical systems are less sensitive to latitude, with GCR varying from 0.10 to 0.16 between 17-75°N. We also find that it is reasonable to approximate the row spacing of bifacial arrays as equivalent to monofacial arrays, with bifacial modules of 96% bifaciality requiring GCRs lower by 0.03 on average than monofacial modules. We demonstrate that latitude is a stronger driver of inter-row energy yield shading losses than diffuse fraction, and present formulae for calculating the appropriate row spacing of a PV array for any latitude between 15–75°N. Our results provide updated guidelines for PV deployment system design that better suit the expanding PV sector.

6. Data and code availability

The data supporting the findings of this study are available in the main text and supplemental information and are additionally available upon request from the corresponding author. Details regarding the code used in this paper are published in Russell et al. (2022).

CRediT authorship contribution statement

Erin M. Tonita: Conceptualization, Methodology, Investigation, Data curation, Writing – original draft, Writing – review & editing, Visualization. **Annie C.J. Russell:** Conceptualization, Methodology, Software, Validation, Investigation, Writing – review & editing. **Christopher E. Valdivia:** Conceptualization, Writing – review & editing, Supervision. **Karin Hinzer:** Conceptualization, Writing – review & editing, Supervision.

Declaration of Competing Interest

The authors declare that they have no known competing financial interests or personal relationships that could have appeared to influence the work reported in this paper.

Acknowledgements

The authors gratefully acknowledge the support of CMC Microsystems Canada and the Natural Sciences and Engineering Research Council of Canada [NSERC CREATE 497981, NSERC STPGP 521894, NSERC CGS-D].

The University of Ottawa is located on the unceded territory of the Anishinaabe Algonquin Nation.

Appendix A. Supplementary data

Supplementary data to this article can be found online at https://doi.org/10.1016/j.solener.2023.04.038.

References

Al-Quraan, A., Al-Mahmodi, M., Alzaareer, K., El-Bayeh, C., Eicker, U., 2022. Minimizing the utilized area of PV systems by generating the optimal inter-row spacing factor. Sustainability 14, 6077.

Appelbaum, J., 2016. Bifacial photovoltaic panels field. Renew. Energy 85, 338–343.

Appelbaum, J., Aronescu, A., 2022. Inter-row spacing calculation in photovoltaic fields – a new approach. Renew. Energy 387–394.

Armstrong, S., Hurley, W.G., 2010. A new methodology to optimise solar energy extraction under cloudy conditions. Renew. Energy 35 (4), 780–787.

Ayala Pelaez, S., Deline, C., Greenberg, P., Stein, J.S., Kostuk, R.K., 2019. Model and validation of single-axis tracking with bifacial PV. IEEE J. Photovolt. 9 (3), 715–721.

Baloch, A.A.B., Hammat, S., Figgis, B., Alharbi, F.H., Tabet, N., 2020. In-field characterization of key performance parameters for bifacial photovoltaic installation in a desert climate. Renew. Energy 50–63.

Berrian, D., Libal, J., Klenk, M., Nussbaumer, H., Kopecek, R., 2019. Performance of bifacial PV arrays with fixed tilt and horizontal single-axis tracking: comparison of simulated and measured data. IEEE J. of Photovolt. 9 (6), 1583–1589.

Bolinger, M., Bolinger, G., 2022. Land requirements for utility-scale PV: an empirical update on power and energy density. IEEE J. of Photovolt. 12 (2), 589–594.

Calabro, E., 2013. An algorithm to determine the optimum tilt angle of a solar panel from global horizontal solar radiation. J. Renew. Energy 307547.

Carroll, D., 2021. "5B backs bigger is better with new generation of modular solar solution," *PV Magazine*. Online: https://5b.co/news/2021/media-release-new-5b-maverick-offers-improved-performance-and-safety.

Cheein, F., Dolan, D.S.L., Patrick, S.H., 2021. "Effective backtracking algorithm for half-cut cell solar panels", *The 9th Renewable Power Generation Conference*. Dublin Online 355–358.

Coathup, T., Lewis, M.R., Russell, A.C.J., Haysom, J.E., Valdivia, C.E., Hinzer, K., 2023. Impact of torque tube reflection on bifacial photovoltaic single axis tracked system performance. Opt. Express 31 (4), 6155.

Daly, A., Abbaraju, V., 2018. Optimizing your energy yield: TrueCapture smart control technology boosts energy production and financial returns. NEXTracker, Fremont, CA USA.

Deline, C., Ayala Pelaez, S., MacAlpine, S., Olalla, C., 2020. Estimating and parameterizing mismatch power loss in bifacial photovoltaic systems. Prog. Photovolt. Res. Appl. 28 (7), 691–703.

Environment and Climate Change Canada, 2022. "Engineering climate datasets," Online. Available: https://climate.weather.gc.ca/prods_servs/engineering_e.html.
Figgis, B., Ennaoui, A., Ahzi, S., Remond, Y., 2017. Review of PV soiling particle mechanisms in desert environments. Renew. Sustain. Energy Rev. 76, 872–881.
Frimannslund, I., Thiis, T., Aalberg, A., Thorud, B., 2021. Polar solar power plants – investigating the potential and the design challenges. Sol. Energy 224, 35–42.
Glick, A., Ali, N., Bossuyt, J., Calaf, M., Cal, R.B., 2020. Utility-scale solar PV performance enhancements through system-level modifications. Sci. Rep. 10, 10505.
International Renewable Energy Agency, 2014. "IRENA global atlas: spatial planning techniques, session 2b" Online. Available: https://www.irena.org/-/media/Files/IRENA/Agency/Events/2014/Jul/15/10_Solar_power_spatial_planning_techniques_Cairo_Egypt.pdf.
International Technology Roadmap for Photovoltaic (ITRPV), 2021 Results, Ed. 13, Frankfurt, Germany (2022).
Jacobson, M.Z., Jadhav, V., 2018. World estimates of PV optimal tilt angles and ratios of sunlight incident upon tilted and tracked PV panels relative to horizontal panels. Sol. Energy 169, 55–66.
Jouttijarvi, S., Lobaccaro, G., Kamppinen, A., Miettunen, K., 2022. Benefits of bifacial solar cells combined with low voltage power grids at high latitudes. Renew. Sustain. Energy Rev. 161, 112354.
Kafka, J., Miller, M.A., 2020. The dual angle solar harvest (DASH) method: An alternative method for organizing large solar panel arrays that optimizes incident solar energy in conjunction with land use. Renew. Energy 155, 531–546.
Khan, M.R., Hanna, A., Sun, X., Alam, M.A., 2017. Vertical bifacial solar farms: physics, design, and global optimization. Appl. Energy 206, 240–248.
King, D.L., Kratochvil, J.A., Boyson, W.E., 2004. Photovoltaic array performance model. Sandia Report – SAND2004-3535 8, 1–19.
Lewis, G., 1987. Optimum tilt of a solar collector. Sol. Wind Technol. 4 (3), 407–410.
Lorenzo, E., Narvarte, L., Munoz, J., 2011. Tracking and back-tracking. Prog. Photovolt. Res. Appl. 19 (6), 747–753.
Moller, T., Haines, E., 2002. Ray/box intersection – intersection test methods. In: Real-Time Rendering, 2nd ed.,. AK Peters/CRC Press, Natick, MA, USA, pp. 572–1278.
Narvarte, L., Lorenzo, E., 2008. Tracking and ground cover ratio. Prog. Photovolt: Res. Appl. 16, 703–714.
Ngan, L., Jepson, C., Blekicki, A., Panchula, A., 2013. "Increased energy yield production of First Solar horiztonal single-axis tracking PV systems without backtracking", *IEEE 39th Photovoltaic Specialists Conference*, Tampa. FL, USA, pp. 792–796.
Pike, C., Whitney, E., Wilber, M., Stein, J.S., 2021. Field performance of south-facing and east-west facing bifacial modules in the Arctic. Energies 14, 1210.
Qiu, G., Ruiffat, S.B., 2003. Optimum tilt angle of solar collectors and its impact on performance. Int. J. Ambient Energy 24 (1), 13–20.
Rehman, N.U., Uzair, M., Allauddin, U., 2020. An optical-energy model for optimizing the geometrical layout of solar photovoltaic arrays in a constrained field. Renew. Energy 149, 55–65.
Reker, S., Schneider, J., Gerhards, C., 2022. Integration of vertical solar power plants into a future German energy system. Smart Energy 7, 100083.
Riaz, M.H., Imran, H., Younas, R., Butt, N.Z., 2021. The optimization of vertical bifacial photovoltaic farms for efficient agrivoltaic systems. Sol. Energy 230, 1004–1012.
Russell, A.C.J., Valdivia, C.E., Bohémier, C., Haysom, J.E., Hinzer, K., 2022. DUET: A novel energy yield model with 3D shading for bifacial photovoltaic systems. IEEE J. of Photovolt. 12 (6), 1576–1585.
Sanchez-Carbajal, S., Rodrigo, P.M., 2019. Optimum array spacing in grid-connected photovoltaic systems considering technical and economic factors. Int. J. Photoenergy 1489749.
Schroder, A., 2011. Determination of annual optimum altitude and azimuth angles of fixed tilt solar collectors in the continental United States using the National Solar Radiation Database. Proceedings of the ASES National Solar Conference.
Sengupta, M., Xie, Y., Lopez, A., Habte, A., Maclaurin, G., Shelby, J., 2018. The National Solar Radiation Data Base (NSRDB). Renew. Sustain. Energy Rev. 89, 51–60.
Shah, S.F.A., Khan, I.A., Khan, H.A., 2019. Performance evaluation of two similar 100 MW solar PV plants located in environmentally homogeneous conditions. IEEE Access 7, 161697.
GameChange Solar, "MaxDensity East West System," accessed 2023. Online: https://gamechangesolar.com/maxdensity.
Stein, J., Reise, C., Castro, J.B., Friesen, G., Maugeri, G., Urrejola, E., Ranta, S., 2021. Bifacial photovoltaic modules and systems: experience and results from international research and pilot applications. Int. Energy Agency Photovolt. Power Syst. Programme T13–14, 2021.
Tahir, Z., Butt, N.Z., 2022. Implications of spatial-temporal shading in agrivoltaics under fixed tilt & tracking bifacial photovoltaic panels. Renew. Energy 190, 167–176.
Tawalbeh, M., Al-Othman, A., Kafiah, F., Abedlsalam, E., Almomani, F., Alkasrawi, M., 2021. Environmental impacts of solar photovoltaic systems: a critical review of recent progress and future outlook. Sci. Total Environ. 759, 143528.
Jurchen Technology, "PEG design: The revolution in the field of PV substructure," accessed 2023. Online: https://www.jurchen-technology.com/products/solar-mounting/peg/peg-design/.
The International Energy Agency, Net Zero by 2050, Paris, France (2021). https://www.iea.org/reports/net-zero-by-2050.
Tonita, E.M., Valdivia, C.E., Martinez-Szewczyk, M., Lewis, M.R., Bertoni, M.I., Hinzer, K., 2021. Effect of air mass on carrier losses in bifacial silicon heterojunction solar cells. Sol. Energy Mater. Sol. Cells 230 (15), 111293.
Valdivia, C.E., Li, C.T., Russell, A., Haysom, J.E., Li, R., Lekx, D., Sepeher, M.M., Henes, D., Hinzer, K., Schriemer, H.P., 2017. "Bifacial photovoltaic module energy yield calculation and analysis", *44th IEEE Photovoltaic Specialists Conference*, Washington. DC, USA, pp. 1094–1099.
Van Schalkwijk, M., Kil, A.J., Van Der Weiden, T.C.J., 1997. Dependence of diffuse light blocking on the ground cover ratio for stationary PV arrays. Sol. Energy 61 (1), 381–387.
Verissimo, P.H.A., Campos, R.A., Guarnieri, M.V., Verissimo, J.P.A., Rafael do Nascimento, L., Ruther, R., 2020. Area and LCOE considerations in utility-scaled, single-axis tracking PV power plant topology optimization. Sol. Energy 211, 433–445.
Wang, L., Liu, F., Yu, S., Quan, P., Zhang, Z., 2020. The study on micromismatch losses of the bifacial PV modules due to the irradiance non-uniformity on its backside surface. IEEE J. Photovolt. 10 (1), 135–143.
Williams, A., Barrus, S., Morley, R.K., Shirley, P., 2005. An efficient and robust ray-box intersection algorithm. J. Graph Tools 10 (1), 49–54.

Supplemental Information

E. M. Tonita, A. C. J. Russell, C. E. Valdivia, and K. Hinzer, "Optimal ground coverage ratios for tracked, fixed-tilt, and vertical photovoltaic systems for latitudes up to 75°N".

I. Optimized Locations

We selected 31 locations from across North American countries of Mexico, the United States, and Canada for photovoltaic (PV) row spacing characterization and optimization. A summary of pertinent parameters for these locations is given in Table S1 below. Environmental Typical Meteorological Year data was retrieved from the National Solar Radiation Database (NSRDB) [S1] for locations <60°N. For locations >60°N, the Canadian Weather Energy Calculation Database (CWEC) was used [S2]. Environmental data was used at an hourly resolution, however yearly average insolation, ambient temperature, and albedo are provided in Table S1. A range of elevation from 1-1636 m above sea level occurs in our dataset. High elevation tends to increase PV performance due to decreased average temperatures [S3-4]. Since our analysis considers relative changes in energy yield on a location-by-location basis, the effects of elevation should have a negligible contribution to the results presented in the main text.

Table S1. Summary of Location Environmental Data

City	Latitude (°N)	Longitude (°W)	Diffuse Fraction	Av. Insolation (kWh/m^2/day)	Av. Annual Temp. (°C)*	Av. Annual Albedo*	Elevation (m)
Tuxtla Gutiérrez	16.8	93.1	0.34	5.8	26.9	0.16	699
Guadalajara	20.6	103.4	0.27	6.3	25.1	0.18	1590
Mérida	21.1	89.7	0.31	5.8	28.5	0.16	4
Culiacán	24.8	107.5	0.26	5.9	30.2	0.17	30
Monterrey	25.8	100.3	0.31	5.4	28.8	0.15	716
Miami	25.8	80.2	0.35	5.2	25.8	0.16	5
Chihuahua	28.7	106.1	0.23	6.1	25.4	0.18	1462
Houston	29.8	95.4	0.37	4.8	25.6	0.15	15
New Orleans	30.0	90.1	0.36	4.9	23.5	0.15	1
Phoenix	33.5	112.1	0.23	5.8	30.5	0.17	321
Albuquerque	35.1	106.7	0.23	5.6	22.3	0.17	1496
Memphis	35.1	90.0	0.36	4.6	22.5	0.14	85
Virginia Beach	36.9	76.0	0.38	4.5	18.5	0.10	3
Denver	39.8	105.0	0.30	4.9	19.1	0.23	1587
Boulder	40.0	105.3	0.36	4.5	18.5	0.26	1636
Pittsburgh	40.5	80.0	0.44	3.9	17.5	0.17	257
Boise	43.6	116.2	0.28	4.6	20.3	0.17	847
Halifax	44.7	63.6	0.43	3.6	11.5	0.22	1
Ottawa	45.4	75.7	0.40	3.8	13.2	0.32	62
Deer Lake	49.2	57.4	0.48	3.2	10.4	0.35	58
Vancouver	49.3	123.1	0.41	3.2	15.9	0.13	45
Regina	50.5	104.6	0.37	3.7	14.0	0.30	570
Winnipeg	49.9	97.4	0.37	3.7	13.0	0.31	228
Prince George	53.9	122.8	0.42	3.3	12.2	0.28	599
Flin-Flon	54.8	101.9	0.40	3.3	9.1	0.36	312
Yellowknife	62.5	114.4	0.44	2.9	8.2	0.36	206
Rankin Inlet	62.8	92.1	0.53	2.7	-0.3	0.52	32
Iqaluit	63.8	68.6	0.55	2.5	-0.3	0.51	34
Old Crow	67.6	139.8	0.43	2.7	6.7	0.38	251
Cambridge Bay	69.1	105.1	0.47	2.4	-2.4	0.56	31
Resolute Bay	74.7	95.0	0.41	2.4	-4.3	0.65	68

*GHI-weighted averages

II. SYSTEM DESIGN

In Table S2 we summarize the input parameters used in the 3D view factor PV system simulator, DUET [S5]. System parameters presented are for a bifacial horizontal single axis tracked (HSAT) array. For south-facing fixed-tilt systems, the tracking type is set to fixed and the tilt is set to the optimum tilt as described in the main text. For east-west vertical fixed-tilt systems the azimuth is set to 90° from South, the tracking type is set to fixed, and the module orientation is landscape. In all cases a minimum ground-to-module clearance of 0.25 m is maintained. Other parameters are set to common values across each of these system configuration types. Module electrical parameters are extracted from a model for dual-sided textured silicon heterojunction devices [S6].

Table S2. Summary of DUET Inputs

Environmental	Sky model	Perez sky luminance distribution model
	Environmental data	NREL NSRDB [S1] or CWEC [S2]
Cell geometry	Cell size	M2 (156.75 mm)
	Cell area (cm^2)	238.84
	Metallization shading fraction (%)	7%
	Irradiance sample points per cell	16
Cell *I-V*	Bifaciality (%)	96
	Short-circuit current (A/cell)	8.19
	Responsivity (A/W)	0.343
	Open-circuit voltage (V)	0.712
	Ideality factor	1.08
	Saturation current (nA/cell)	0.35
	Shunt resistance (Ω)	12.6
	Series resistance (Ω)	0.00018
	Temp. coef. short-circuit current (K^{-1})	0.035
	Temp. coef. open-circuit voltage (K^{-1})	-0.00235
	Nominal operating cell temp. (°C)	42
	Incidence angle modifier model	ASHRAE
Module geometry	Number of cells	72
	Module orientation	Portrait
	Frame	Included
Array geometry	Azimuth (° from South)	90
	Number of rows	5
	Row pitch (m)	Depends on GCR
	Number of tables per row	1
	Number of modules per table	31
	Module spacing along row (m)	0.03
	Number of tiers	1
	Ground clearance (m)	Adjusted according to Eq. 3
	Racking	Includes purlins and torque tube
Tracker	Type	Horizontal single-axis tracking, ±60°
	Backtracking	Included
Torque tube	Shape	Round
	Radius (m)	0.05

III. ENERGY DENSITY

In the main text we presented the sensitivity of inter-row energy yield shading loss to GCR by comparing to the energy yield of a module with no neighbouring rows. In some cases, it might be more beneficial to instead consider energy density, as suggested by Verissimo *et al.* [S7]. This could be of more use when, for example, available land for PV is limited and module costs are low. Figure S1 shows a plot of energy yield density as a function of GCR for the 31 locations considered in this work for fixed-tilt arrays (A, B), HSAT arrays (C, D), and east-west vertical fixed-tilt arrays (E, F). All rows have the same scale for ease of comparison between monofacial and bifacial energy yield density. Energy yield density, ρ, is calculated by simply dividing the annual module energy yield, E, by the row pitch, R, associated with each GCR:

$$\rho = E/R \qquad \text{(Eq. S1)}.$$

For HSAT arrays, energy yield density continues to increase towards GCRs of 1.0, despite increased shading losses. If the sole objective is to maximize the energy yield of a given plot of land regardless of module cost, HSAT rows can be placed side-by-side, since losses associated with near constant backtracking are offset by the sheer number of modules on site. However, this is not a practical site layout in most cases as space must be left for operation and management practices. Additionally, since HSAT modules were not constrained to a minimum tilt of 15° like fixed-tilt modules, for GCRs near 1.0, the module tilt will be between 0-15° for most hours of the year. Fixed-tilt energy density, on the other hand, peaks for GCRs between 0.5 and 0.7 for latitudes between 75°N to 17°N. Even with negligible module cost, GCRs beyond these peaks are unlikely to be economically feasible, as reducing row spacing further results in an overall loss to energy yield. Unlike their equator-facing fixed-tilt counterparts, east-west facing

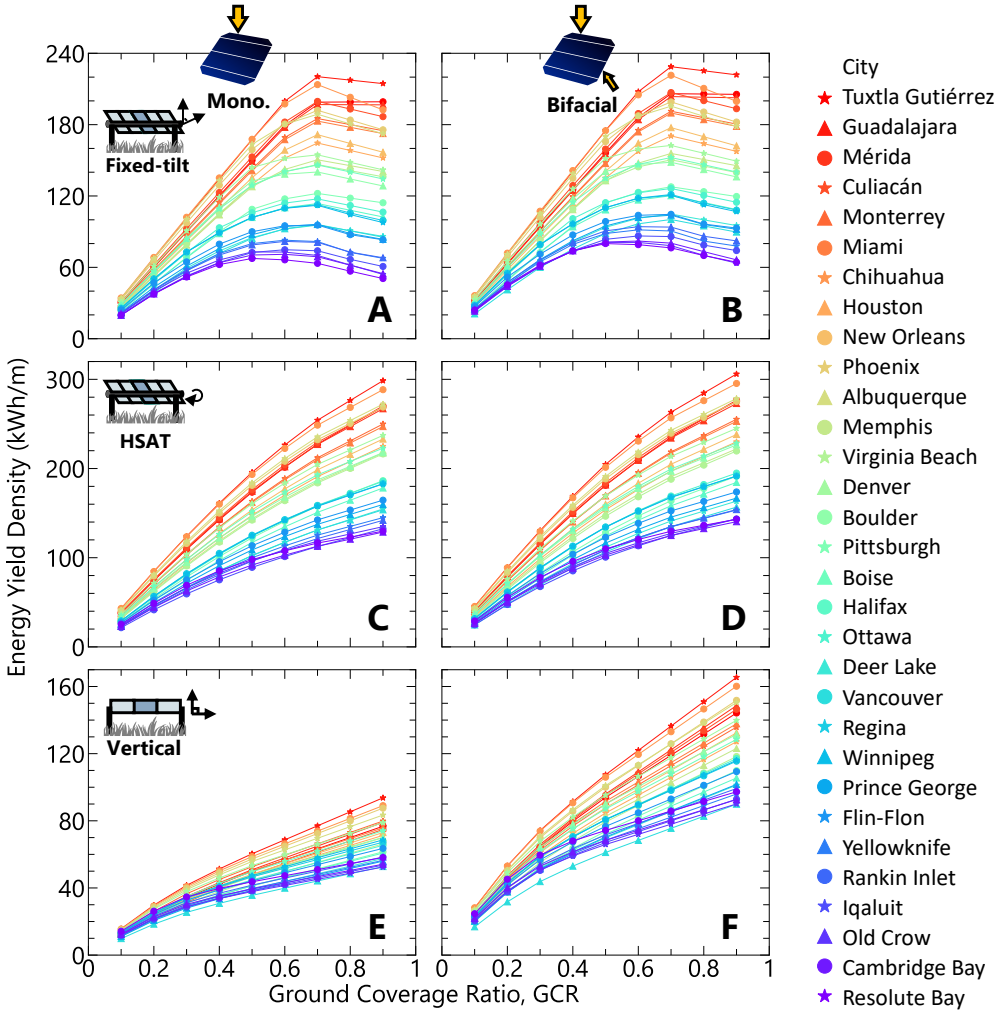

Fig. S1. The effect of GCR on energy yield density for all 31 North American locations for (A, C, E) monofacial systems and (B, D, F) bifacial systems with (A, B) fixed-tilt, (C, D) HSAT, and (E, F) vertical fixed-tilt configurations.

vertical panels do not experience an energy yield density peak for GCRs up to 1.0; it is possible to have GCRs>1 to increase the energy yield density of the PV array [S8].

REFERENCES

[S1]. M. Sengupta, Y. Xie, A. Lopez, a. Habte, G. Maclaurin, and J. Shelby, "The National Solar Radiation Data Base (NSRDB)," *Renewable and Sustainable Energy Reviews*, 89, 51-60 (2018).

[S2]. Environment and Climate Change Canada, "Engineering climate datasets," Online (2022). Available: https://climate.weather.gc.ca/prods_servs/engineering_e.html

[S3]. S. Dubey, J. N. Sarvaiya, and B. Seshadri, "Temperature dependent photovoltaic efficiency and its effect on PV production in the world – a review," *Energy Procedia*, 33, 311-321 (2013).

[S4]. A. Nentwich and A. Szeless, "The Alpsolar project – field testing and optimization of European photovoltaic power plant equipment at high-elevation and Nordic sites," *Prog. in Photovolt.: Res. Appl*., 1, 55-66 (1993).

[S5]. A. C. J. Russell, C. E. Valdivia, C. Bohémier, J. E. Haysom, and K. Hinzer, "DUET: A novel energy yield model with 3D shading for bifacial photovoltaic systems," *IEEE J. of Photovolt*., 12(6), 1576-1585 (2022).

[S6]. E. M. Tonita, C. E. Valdivia, M. Martinez-Szewczyk, M. R. Lewis, M. I. Bertoni, and K. Hinzer, "Effect of air mass on carrier losses in bifacial silicon heterojunction solar cells," *Solar Energy Materials and Solar Cells*, 230(15), 111293 (2021).

[S7]. P. H. A. Verissimo, R. A. Campos, M. V. Guarnieri, J. P. A. Verissimo, L. Rafael do Nascimento, and R. Ruther, "Area and LCOE considerations in utility-scaled, single-axis tracking PV power plant topology optimization," *Solar Energy*, 211, 433-445 (2020).

[S8]. M. H. Riaz, H. Imran, R. Younas, and N. Z. Butt, "The optimization of vertical bifacial photovoltaic farms for efficient agrivoltaic systems," *Solar Energy*, 230, 1004-1012 (2021).

6.2 Effect of spectral albedo on bifacial photovoltaic module measurements and system model predictions

The effects of spectral albedos
Are quantified for measurement & software.
With spectra like uneven rainbows
You may have error up to 3%, beware.
.
Spectral mismatch is increased
For fixed systems in northern locations,
Bandgaps above 1 eV at least,
And bright ground-cover applications.

❄ ❄ ❄

Scope and impact

Quantifying rear incident irradiance is one of the main research challenges for accurate prediction and characterization of bifacial PV performance. Rear irradiance is most heavily influenced by the surrounding ground albedo, with a major uncertainty associated with the use of albedo being the importance of spectral shape. In this article, we present a comprehensive study of spectral albedo effects on (1) bifacial PV device *I-V* measurements, and (2) annual predictions of bifacial PV system performance.

This article has the following novelties:

1. An indoor measurement demonstration of measuring bifacial PV devices under varying illumination conditions corresponding to specific ground covers including snow, grass, and soil using 1-cell bifacial SHJ mini-modules is completed. This is a practical demonstration of the SRI method described in Section 5.2.

2. Spectral albedo irradiance mismatch is calculated in 31 locations spanning 15-75°N and for ten different ground covers.

3. We show that ground-reflected irradiance composes between 2-32% of all annual plane-of-array irradiance on bifacial PV modules, with notably high (>10%) contributions for fixed-tilt arrays above 50°N.

4. Empirical equations are provided for estimating the sensitivity of model energy yield predictions to changes in ground albedo.

5. We quantify how much spectral mismatch can be expected to increase for solar cell technologies with larger bandgaps, such as cadmium telluride (CdTe) and GaAs.

Overall, this article demonstrates the scenarios where omission of spectral effects can lead to measurement and modelling errors on the order of 1-3%. We recommend considering spectral effects for (1) fixed-tilt deployments at high latitudes, (2) wide bandgap technologies, (3) albedos which vary significantly over the technology's absorption range, and (4) high albedos such as snow.

Author contributions

Erin M. Tonita As the lead author of this work, I conceptualized the research project, performed mini-module *I-V* curve measurements and EQE measurements, ran all system-level simulations, analyzed results, and wrote the manuscript.

Christopher E. Valdivia identified references for the other solar cell technologies explored in Section 3.4 in the paper, "Other module technologies", and developed the analysis methodology in this section. He also supervised this research and reviewed and edited the manuscript.

Annie C. J. Russell provided DUET software support, regular guidance, and edited the manuscript.

Michael Martinez-Szewczyk fabricated SHJ mini-modules at Arizona State University and provided edits to the final manuscript.

Mariana I. Bertoni supervised the fabrication of mini-modules in Arizona State University and shipped samples to the University of Ottawa for measurement. She reviewed and edited the manuscript.

Karin Hinzer supervised and funded this project. She guided the development of the manuscript and edited the final version.

Copyright

E. M. Tonita, C. E. Valdivia, A. C. J. Russell, M. Martinez-Szewczyk, M. I. Bertoni, and K. Hinzer, "Quantifying spectral albedo effects on bifacial photovoltaic module measurements and system model predictions," *Progress in Photovoltaics: Research and Applications*, 1-13 (2023). https://doi.org/10.1002/pip.3789

Received: 11 July 2023 | Revised: 6 December 2023 | Accepted: 23 January 2024

DOI: 10.1002/pip.3789

RESEARCH ARTICLE

PROGRESS IN PHOTOVOLTAICS WILEY

Quantifying spectral albedo effects on bifacial photovoltaic module measurements and system model predictions

Erin M. Tonita[1] | Christopher E. Valdivia[1] | Annie C. J. Russell[1] | Michael Martinez-Szewczyk[2] | Mariana I. Bertoni[2] | Karin Hinzer[1]

[1]SUNLAB, University of Ottawa, Ottawa, Canada

[2]DEfECT Lab, Arizona State University, Tempe, Arizona, USA

Correspondence
Erin Tonita, SUNLAB, University of Ottawa, 25 Templeton Street, Ottawa, ON K1N 6N5, Canada.
Email: etoni044@uottawa.ca

Funding information
Natural Sciences and Engineering Research Council of Canada, Grant/Award Numbers: NSERC CGS-D, NSERC STPGP 521894, NSERC CREATE 497981; CMC Microsystems Canada; Canadian Foundation for Innovation; Ontario Research Fund; US Department of Energy Office of Energy Efficiency and Renewable Energy Solar Energy Technologies Office, Grant/Award Number: DE-EE0009346

Abstract

We provide a comprehensive analysis of the effect of spectral albedo on photovoltaic (PV) module measurements and system model predictions. We demonstrate how to account for albedo in indoor bifacial device measurements by adjusting the applied irradiance using the scaled rear irradiance method, exemplified on fabricated silicon heterojunction (SHJ) modules. System model performance is studied using a detailed 3D finite-element model, DUET, for fixed-tilt and horizontal single-axis tracked (SAT) arrays between 15 and 75°N. Spectral effects cause variations in measured SHJ module short-circuit current up to 2% and efficiency variation up to 0.3% abs. We further demonstrate that rear-side spectral mismatch factors (SMMs) resulting from including or omitting spectral albedo in PV system modeling vary between ±13%, while total (front+rear) SMMs vary up to 3%, depending on the deployment configuration and latitude. SAT array SMMs are weakly correlated with latitude, while fixed-tilt array SMMs increase with latitude, driven by an increasing proportion of ground-reflected light on the front-side of modules. Ground-reflections can constitute between 2% and 32% of total incident module irradiance, with notably high (>10%) contributions for fixed-tilt arrays at high latitude. Effects of spectral albedo are most significant for: (1) fixed-tilt deployments at high latitudes, (2) wide bandgap technologies such as perovskite and cadmium telluride cells, (3) albedos which vary steeply over the technology's absorption range, and (4) high albedo ground covers. Overall, we demonstrate that omitting spectral albedo effects can result in PV measurement and system-level modeling uncertainties on the order of several percent in these cases.

KEYWORDS

broadband albedo, energy yield, ground reflected, latitude, scaled rear irradiance, spectral albedo, spectral impact, spectral mismatch

1 | INTRODUCTION

Bifacial photovoltaic (PV) technologies, which absorb radiation on both front and rear faces, are rapidly becoming the mainstream technology deployed worldwide, with over 20 GW deployed as of 2021.[1] By 2050, bifacial technologies are projected to constitute 80% of the global PV market share courtesy of their increased absorptive area and module lifetime compared to conventional monofacial technologies.[1,2] Energy yield gains typically between 5–30% can be achieved compared to monofacial technologies,[2] with bifacial gain driven by the acceptance of rear-side irradiance. Thus, quantifying rear incident irradiance is one of the main research challenges for accurate prediction and characterization of bifacial PV performance.

Direct beam irradiance, diffuse sky irradiance, and ground-reflected irradiance all contribute to the total incident irradiance received on a PV module. In the case of low-latitude monofacial PV modules, ground-reflected irradiance typically accounts for <2% of total incident irradiance,[3] but this number can be >10% for bifacial modules and compose >90% of all rear-incident irradiance.[4,5] Ground-reflected irradiance is determined by the surrounding *albedo* of the environment, where albedo is defined as the bidirectional hemispherical reflectance of a surface and depends on the ground material, topology, and lighting conditions.[5,6] Thus, the characterization and measurement of albedo on bifacial rear-side irradiance over a wide range of conditions, including extending beyond previous low-latitude assumptions, is imperative for both resource assessment & planning, and for monitoring the performance of existing deployments.

How ground-reflected, diffuse sky, and direct beam irradiance sources manifest into rear-side module irradiance profiles depends on numerous parameters. Rear-side non-uniformity arises naturally from the configuration of the PV array, with factors such as module tilt, height, and location in the PV array influencing rear-incident irradiance.[5,7,8] For example, Ayala Pelaez et al. used a ray tracing technique to investigate single-axis tracked (SAT) edge-brightening, finding modules at the end of the tracker experience a 15%–25% increase in rear irradiance compared to central modules in Albuquerque, USA, at 35°N.[9] Alongside non-uniformities arising from module orientation and the surrounding environment, self-shading and self-reflections can also occur to either diminish or enhance energy yield. For instance, Ayala Pelaez et al. found a 2%–8% torque tube rear irradiance shading factor for 2-in-portrait tracked systems in Richmond, USA, at 38°N.[10] Similarly, Coathup et al. examined the complementary effect of torque tube reflections, finding slight annual energy yield prediction increases of 0.1%–0.2% for tracked systems located in Livermore, USA, at 38°N.[11]

Rear-side irradiance non-uniformity leads to current mismatch loss in all cases. McIntosh et al. quantified the current mismatch loss in a SAT array in Golden, USA, at 40°N using a ray tracing model, finding that mismatch losses were higher for edge modules in the array, for single tier arrays, and when the ground albedo was high.[12] Deline et al. investigated rear side irradiance for ground-mounted tracked and rooftop fixed-tilt systems in three mid-latitude locations around the globe and found that mismatch losses increased linearly with module bifaciality.[13] Electrical wiring schemes can be used to reduce mismatch losses, for example, by the addition of more bypass diodes or use of half-cut cells.

Among the areas of uncertainty regarding bifacial PV performance is the importance of the *spectral* nature of albedo on both rear-side irradiance and energy yield. Different ground conditions will preferentially reflect and absorb certain wavelengths, leading to unique spectral albedos. In many cases, an average or broadband albedo is instead used in simulations to reduce measurement and computational complexities.[14–16] In recent years, a few studies have investigated the impact of spectral albedo on bifacial device performance compared to these broadband approximations. For example, Onno et al. described how spectral albedo impacts bifacial tandem devices, considering the albedos of brown loam, white sand, and dry grass,[17] while Russell et al. described the theoretical efficiency limit for bifacial solar cells with and without the spectral dependence of albedo.[18] Russell et al. further modeled that bifacial solar cell power can vary by up to 5% due to spectral effects.[18]

A few studies have explored the impact of spectral albedo on system performance, however they are limited to select locations or do not conduct a yearly energy yield analysis. Brennan et al. investigated the impact of spectral albedo versus broadband albedo for 22 albedos and 7 technologies under a single-spectrum representing a sunny mid-latitude at solar noon.[19] Andrews et al. calculated the effect of spectrally-weighted albedo versus broadband albedo for spectra with varying cloud optical thicknesses, demonstrating that insolation can be under-predicted by up to 7% by ignoring spectral effects.[20] In this paper, Andrews et al. suggested that the use of an external quantum efficiency (EQE) weighted albedo value can be used as a proxy for a full spectral calculation.[20] Vogt et al. adopted this *spectrally-weighted albedo* to further demonstrate a 20% relative discrepancy in bifacial gain compared to using a broadband albedo approximation for Hamelin, Germany.[4] Riedel-Lyngskaer et al. analyzed field data in Denmark of bifacial fixed-tilt and SAT arrays, monitored using different spectroradiometers and pyranometers, finding spectral impacts varying from 0.98 to 1.20.[21]

Here, we present a comprehensive review of the effect of spectral albedo compared to broadband approximations on yearly bifacial PV system performance for 31 North American locations spanning 17–75°N. We consider equator-facing fixed-tilt and SAT systems under 10 different albedo scenarios. Furthermore, we demonstrate how in-lab bifacial PV module measurements are affected by broadband albedo approximations by measuring bifacial silicon heterojunction (SHJ) mini-modules (1-cell modules) using the scaled rear irradiance measurement method.[22] Thus, this paper is composed of two primary sections—in the first, we analyze the impact of spectral albedo on in-lab bifacial module measurements; in the second, we use the measurements of SHJ mini-modules as input into a PV system-level performance model to analyze spectral albedo system model uncertainty. We examine the front, rear, and total spectral mismatch factors arising from spectral albedo as a function of latitude. Finally, we extend our analysis to show relative performance variations for six other technologies in addition to SHJ.

2 | METHODOLOGY

2.1 | Albedo

For both module measurements and system-level modeling, we consider 10 albedo scenarios: snow, white sand, dry grass, light sand, concrete, roof shingle, green grass, red brick, soil, and tundra. The spectral albedos of these ground conditions are plotted in Figure 1A. Albedos of soil and light sand are digitized from the SMARTS database.[23] To exemplify a naturally occurring high-latitude surface, we consider the albedo of tundra to be the measurement of natural surface with soil and rock from Bøggild et al. acquired in Greenland.[24] The remaining spectral albedos are digitized from Russell et al.[18] For comparison, broadband albedo, a_{bb}, is depicted by dashed lines in Figure 1A and calculated using the following formula:

$$a_{bb} = \frac{\int A(\lambda) \times AM1.5G(\lambda)\, d\lambda}{\int AM1.5G(\lambda)\, d\lambda} \quad (1)$$

The spectral albedo, $A(\lambda)$, is weighted by the standard solar spectrum of AM1.5G. Though spectral albedo data is displayed for the silicon absorption range in Figure 1A, this value is calculated over wavelengths, λ, from 280 to 3000 nm representing the absorption range of typical pyranometers.

The shaded background in Figure 1A corresponds to the measured external quantum efficiency (EQE) of a bifacial SHJ mini-module. As suggested by Andrews et al., we calculated a spectrally-weighted albedo, a_λ, using the SHJ EQE to represent performance under spectral albedo conditions[20]:

$$a_\lambda = \frac{\int A(\lambda) \times EQE(\lambda) \times AM1.5G(\lambda) \times \lambda\, d\lambda}{\int EQE(\lambda) \times AM1.5G(\lambda) \times \lambda\, d\lambda} \quad (2)$$

This method reduces the computation time required for a full spectral analysis, while providing comparable results due to incorporating the technology's spectral response.[4,20] An inset table in Figure 1A summarizes a_{bb} and a_λ for our 10 considered ground conditions.

2.2 | Module measurement methodology

Bifacial silicon heterojunction mini-modules were fabricated for albedo performance characterization and input into a system-level model. A schematic of the module layer structure is provided in Figure S1. Four SHJ glass–glass mini-modules were fabricated and measured to have an average efficiency of 21.9 ± 0.9% under front-side standard test conditions (STC) of AM1.5G at 1000 W/m^2 and an

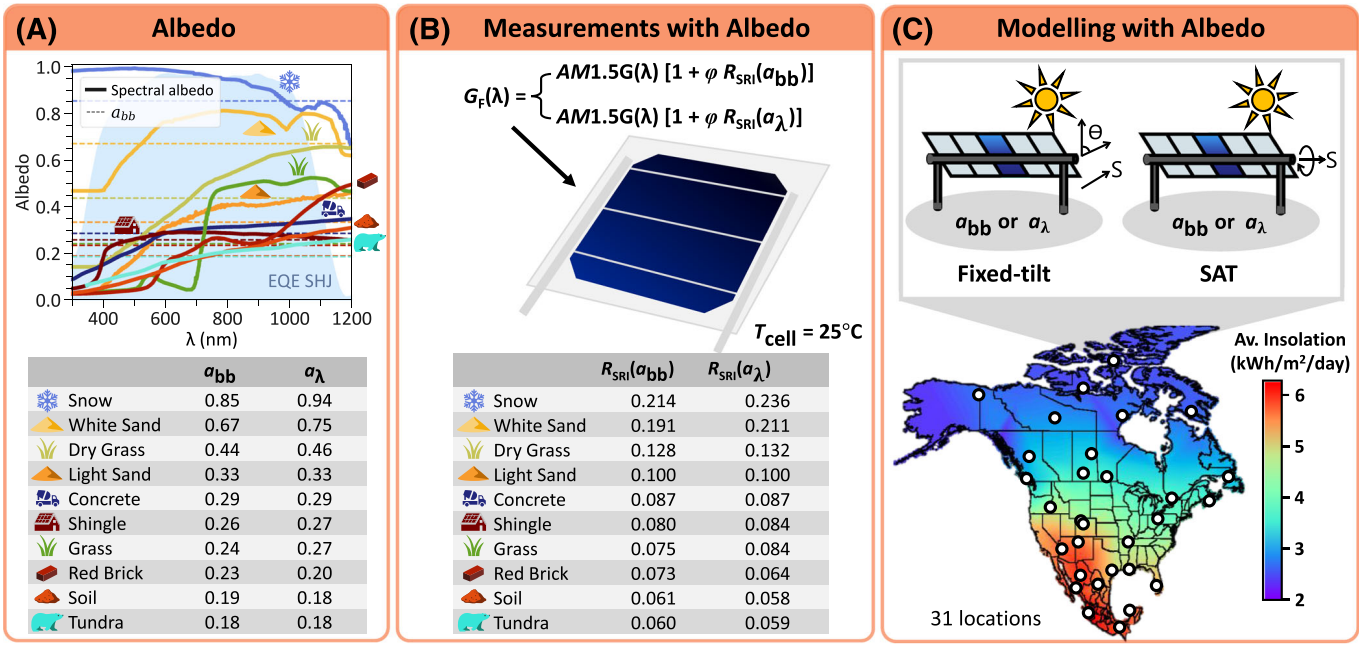

	a_{bb}	a_λ
Snow	0.85	0.94
White Sand	0.67	0.75
Dry Grass	0.44	0.46
Light Sand	0.33	0.33
Concrete	0.29	0.29
Shingle	0.26	0.27
Grass	0.24	0.27
Red Brick	0.23	0.20
Soil	0.19	0.18
Tundra	0.18	0.18

	$R_{SRI}(a_{bb})$	$R_{SRI}(a_\lambda)$
Snow	0.214	0.236
White Sand	0.191	0.211
Dry Grass	0.128	0.132
Light Sand	0.100	0.100
Concrete	0.087	0.087
Shingle	0.080	0.084
Grass	0.075	0.084
Red Brick	0.073	0.064
Soil	0.061	0.058
Tundra	0.060	0.059

FIGURE 1 (A) The spectral albedo and broadband albedos considered in this work, shown for the c-Si absorption range, with silicon heterojunction EQE given by the faded blue background. The table summarizes the broadband and spectrally-weighted albedos for each ground condition. (B) A schematic demonstrating how measurements with albedo are implemented indoors by scaling front-side irradiance, $G_F(\lambda)$, according to the ground albedo, using target irradiance values, R_{SRI}, calculated using Equations (5) and (7) via the scaled rear irradiance method. (C) A schematic showing how system-level modeling is completed using varied albedo across 31 locations for fixed-tilt and SAT modules. Array icons are truncated and represent a 5-row array with 31 modules per row (see Figure 2A). The central module is analyzed in this work, represented by colored shading. The map displays the yearly average daily solar insolation across Mexico, the United States, and Canada.

average bifaciality of 96 ± 2%. Further information can be found in the supporting information, including a summary of mini-module measured parameters in Table S1 and fabrication details.

The performance of bifacial PV mini-modules under varying albedo conditions can be tested indoors using the scaled rear irradiance (SRI) method, developed and described in our prior work.[22] In the SRI method, the International Electrotechnical Commission (IEC) standard 60904-1-2 for measurement of bifacial *I-V* behavior[25] is extended to include effects of albedo. In the simplest measurement case, rear-side irradiance is added to the front-side, modified by the device's bifaciality, φ, in what is referred to as 'an equivalent irradiance method'; the spectra, $G_F(\lambda)$, illuminated on the front-side of a bifacial device is increased to mimic the effect of additional rear-side irradiance:

$$G_F(\lambda) = AM1.5G(\lambda)[1 + \varphi R] \quad (3)$$

Here, R is the value representing the intended rear-side irradiance in suns. The IEC 60904-1-2 standards recommend testing with R between 0.1–0.25 suns (100–250 W/m^2).

In the SRI method, an albedo, a, is calibrated and assigned to a particular R, depending on the system mounting architecture (fixed-tilt or SAT).[22] Thus, it is possible to attribute a physical meaning to the selection of rear-side irradiance values by, for example, applying irradiance that corresponds to outdoor conditions with fresh snow. For fixed-tilt and SAT mounting architectures, the rear irradiance R for an albedo, a, can be calculated using the following two empirical equations, repeated from Tonita et al.[22] These empirical formulae emulate the performance of 1-in-portrait systems located in Boulder, USA, at 40°N:

$$R_{\text{fixed-tilt}}(a) = 0.31a + 0.01 \quad (4)$$

$$R_{\text{SAT}}(a) = 0.27a + 0.01 \quad (5)$$

Since snow falls and accumulates over a subset of hours in a year, snowy albedos are treated separately in the SRI method, leading to two additional equations unique for evaluation of snowy hours:

$$R_{\text{fixed-tilt,snow}}(a) = 0.19a + 0.01 \quad (6)$$

$$R_{\text{SAT,snow}}(a) = 0.24a + 0.01 \quad (7)$$

To demonstrate indoor measurements with albedo, we measure bifacial SHJ mini-modules assuming a planned SAT mounting architecture. Thus, we calculate appropriate measurement conditions, or R values, using SAT equations (Equations 5 and 7). A depiction of the SRI measurement method is provided in Figure 1B, with summarized R_{SAT} values provided for the scenarios where $a = a_{bb}$ or $a = a_\lambda$ in Equations (5) and (7).

2.3 | System model

We modeled the performance of fixed-tilt and SAT PV systems in 31 locations across Mexico, the United States, and Canada under the 10 spectral and broadband albedos provided in Figure 1A. Locations were selected to span a wide range of environmental conditions, with latitudes between 17 and 75°N, longitudes between 57 and 140°W, and diffuse fractions between 0.23 and 0.55. Selected locations are indicated by white circles in Figure 1C, and a summary of location parameters can be found in Table S2. Map color in Figure 1C is given by the year-averaged daily solar insolation received at each location. We retrieved hourly Typical Meteorological Year (TMY) environmental data from the National Solar Radiation Database (NSRDB)[26] for all locations excluding those above 60°N, which were retrieved from the Canada Weather Energy Calculation (CWEC) database.[27] NSRDB datasets contain surface albedo measurement data, which updates at an hourly resolution, whereas CWEC datasets only indicate which

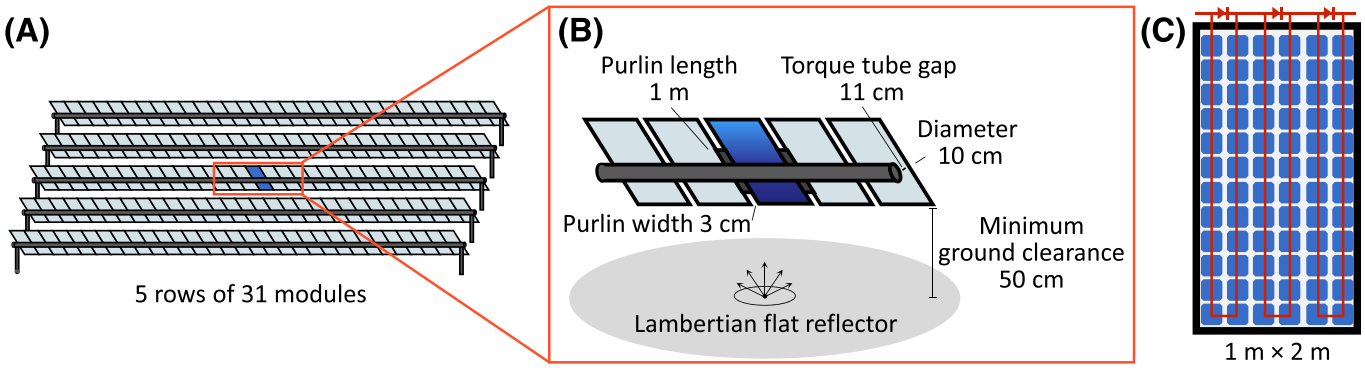

FIGURE 2 (A) The simulated PV array, as viewed from the rear-side, for fixed-tilt and SAT arrays. (B) Supportive structure dimensions around the central module which is analyzed in this work. Purlins, which are supporting module structures installed perpendicular to the torque tube, are modeled around only the central module to reduce computation time. The ground is assumed to be a flat Lambertian reflector with a minimum distance between the ground and module of 50 cm. (C) Module layout with 72-cells and internal wiring indicated by red lines. The bypass diode configuration is shown above the module.

hours of the year have snow cover. To test the impact of spectral albedo versus broadband albedo assumptions on model performance predictions, while capturing to the first order the effects of seasonality, all NSRDB hourly input timesteps are flagged as either 'snow' or 'non-snow' hours as well. This categorization is completed by assigning all timesteps with default TMY albedo >0.7 as 'snow hours', with all other values considered 'non-snow'. Thus, for this albedo analysis, a non-snow albedo such as dry grass is analyzed over a year in each location and array configuration over flagged non-snow hours. Snow albedo is exclusively analyzed for flagged snow hours. In some cases, we additionally present system results using the default, measured hourly albedo values given in NSRDB TMY files. In this case, CWEC albedo snow hours are set to 0.87 and non-snow hours are set to 0.185, corresponding to the broadband albedo of tundra as measured by Bøggild et al.[24]

We modeled the performance of a central module in fixed-tilt and SAT PV arrays using our 3D PV performance prediction software, DUET.[28] Figure 2 depicts a schematic of the PV array layout and module electrical wiring. PV modules are modeled in a 1-in-portrait configuration and centered in a 5-row array, with each row containing 31 modules. Edge effects are negligible on this scale, resulting in module performance that is representative of central modules of utility-scale systems.[29] The spacing between rows is updated according to the location latitude and tracking type using the equations provided in Tonita et al.[30] for 5% inter-row energy yield shading loss. Figure 2B depicts key dimensions assumed in this work for supportive structures, with a 10 cm diameter torque tube to align with dimensions previously modeled in literature.[13,29] Purlins extend to half the length of the module with a width of 3 cm and support the modules perpendicular to the torque tube. The array schematic depicted applies to both fixed-tilt and SAT arrays, though fixed-tilt arrays are oriented to be south-facing, while SAT arrays track east to west. For both system configurations, a minimum ground clearance of 50 cm is maintained between the bottom of the module and the ground. All fixed-tilt arrays are placed at latitude-tilt minus 10°,[30] while SAT arrays have tracking bounds of ±60°. SAT arrays are additionally implemented using a conventional backtracking algorithm to eliminate inter-row shading in morning and evening hours.[31] On the electrical side, each module contains 72-cells connected in series and parallel with three bypass diodes, as provided in Figure 2C. Input module electrical parameters are as measured from fabricated silicon heterojunction mini-modules, and summarized in Tables S1 and S3.

Given environmental parameters, array geometry, and module electrical parameters, DUET calculates hourly front and rear irradiance profiles and module *I-V* curves. Optical modeling is completed per timestep (hour) using a 3D finite-element approach modified to include scene shading using a deterministic ray intersection algorithm.[28] Direct beam radiation, anisotropic diffuse sky radiation, and ground-reflected radiation sources contribute to front and rear module 2D irradiance profiles. The ground is assumed to be a flat, Lambertian reflector with incident irradiance modified by the albedo assigned to the ground. Albedo is assigned in this model as a single-value to reduce computation time—as either a_λ or a_{bb}. Irradiance profiles are converted into per timestep module *I-V* curves using a single-diode model, incorporating effects of cell heating using the Sandia glass-cell-glass model.[32] DUET has been validated against fixed-tilt and tracked bifacial PV systems to within 14–18 mW/Wp mean absolute error for hourly timesteps.[28,33] A summary of all input parameters in DUET is provided in Table S3.

3 | RESULTS

3.1 | Module measurements

The scaled rear irradiance method enables measurements in-lab of the performance of bifacial PV devices under varied albedo conditions by suitably adjusting the rear-side irradiance.[22] Figure 3 displays measurements of a fabricated SHJ mini-module under varying albedo-driven illumination conditions using the scaled equivalent rear irradiance method.[22] These illumination conditions are summarized in Figure 1B. External quantum efficiency (EQE) was measured (Figure 3A) using an Oriel 300 W Xenon Lamp with an Oriel Cornerstone 130 1/8 m Monochromator, while *I-V* curve characteristics were measured (Figure 3B–E) using a Newport 94123A Solar Simulator with a 1600 W Xenon Arc Lamp. EQE measurements were conducted at an ambient room temperature of 22.5 ± 0.5°C. *I-V* curves were measured under ambient room temperatures of 23 ± 0.5°C with ~5 s measurement acquisition times and 5-minute cool-down periods. The module is estimated to be at a temperature between 25–28°C during *I-V* measurements. All measurements were conducted with an absorptive black material placed underneath the module to eliminate rear reflection enhancements.

Figure 3B and C show the measured short-circuit current (J_{sc}) and efficiency (η), respectively, under varied ground conditions. Standard test conditions of front 1000 W/m^2 illumination is provided for comparison. Colored bars are used to emphasize the discrepancy between spectral albedo and broadband albedo assumptions.

Efficiency is calculated in the broadband albedo case as P_{mp} divided by the total incident applied irradiance, P_{inc}. In the spectral albedo case, the rear-side incident irradiance, $P_{inc,r}$, is scaled to compensate for spectral shape through the albedo ratio of a_{bb}/a_λ.[22] Front-side incident irradiance, $P_{inc,f}$, remains the 1000 W/m^2 of AM1.5G:

$$\eta = \frac{P_{mp}}{P_{inc}} = \frac{P_{mp}}{P_{inc,f} + P_{inc,r}} = \frac{P_{mp}}{1000 + \left[\varphi \times R_{SRI}(a_\lambda) \times \frac{a_{bb}}{a_\lambda}\right]} \quad (8)$$

Spectral shape can serve to either enhance the efficiency of photon conversion by proportionally shifting irradiance to wavelengths where EQE is high, or diminish the conversion efficiency by shifting irradiance away from these regions of high EQE. For instance, the spectral shapes of snow and white sand increase the conversion efficiency of our fabricated module by 0.27% and 0.26% abs., respectively, while red brick decreases the efficiency by 0.16% abs.

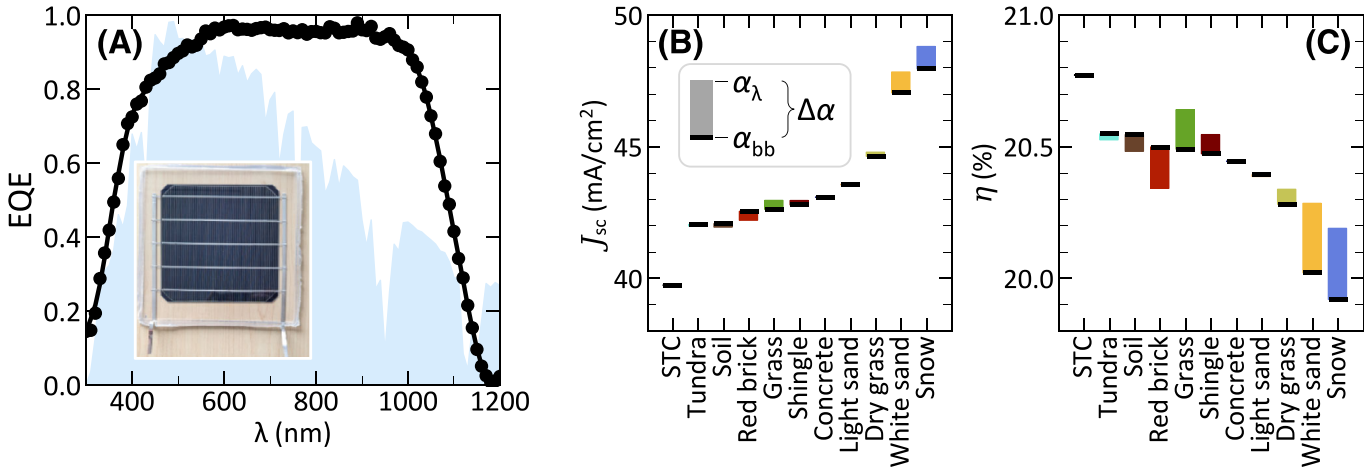

FIGURE 3 (A) Measured external quantum efficiency of a bifacial SHJ mini-module (pictured) with the AM1.5G solar spectrum as a shaded background. Current–voltage performance metrics are provided under varied albedo illumination conditions dictated by the scaled rear irradiance method for (B) J_{sc} and (C) efficiency. Black lines indicate the measured values assuming a broadband albedo approximation. The difference between broadband and spectrally-weighted albedo measurements are given by the colored areas extending from broadband measurement values. Spectral albedo efficiency is calculated using Equation (8), leading to discrepancies as high as 0.3% abs. Spectral albedo effects can serve to increase or decrease measured cell performance metrics.

As J_{sc} increases linearly with albedo, the impact of spectral albedo on J_{sc} is similarly most notable for snow, white sand, green grass, and red brick, causing measurement discrepancies between 0.8% and 1.8%. Soil, roof shingle, and dry grass demonstrate small (<0.4%) differences between broadband and spectrally-weighted albedo measurements, while tundra, concrete, and light sand ground conditions cause a negligible change in J_{sc}. Overall, the inclusion of spectral effects can result in up to a 3% impact on measured cell metrics. Further discussion on the effect of other technologies on these results is provided in Section 3.4.

3.2 | Ground-reflected irradiance

To understand the impact of spectral albedo on system-level modeling, we first quantify the proportion of annual incident irradiance that comes from ground-reflections for fixed-tilt and SAT arrays as a function of latitude. Figure 4 shows the ground-reflected irradiance as a percentage of the total incident irradiance on the front-side (Figure 4A,B), rear-side (Figure 4C,D), and both sides (Figure 4E,F) of a bifacial PV module in a fixed-tilt (4A,C,E) or SAT (4B,D,F) array. Results are displayed as a function of latitude for varying ground albedos between 0.1 and 1. Displayed lines show a second-order polynomial fit to the 31-location dataset, with an average deviation from the fit of ±0.6% abs. Black circles on the plot contextualize these results by indicating the annual proportion of irradiance resulting from ground-reflections when default, hourly updating albedo values given in location TMY files are used instead of a yearly constant value.

The proportion of incident irradiance, which comes from ground-reflections is strongly related to the albedo of the ground, as expected, with an ideal ground-reflector (albedo = 1) contributing 20%–32% (25%–26%) of total irradiance on a bifacial fixed-tilt (SAT) module between 15 and 80°N (see Figure 4E,F). In the low-albedo scenario of 0.1, ground-reflected irradiance contributes 2%–5% (3.2%–3.4%) of total irradiance for bifacial fixed-tilt (SAT) modules. The proportion of total irradiance that comes from the ground increases as a function of latitude particularly for fixed-tilt modules, driven by front-side irradiance. As latitude increases, so does the tilt of fixed-tilt modules (latitude-tilt minus 10°) and the average tilt of SAT modules, resulting in an increasing proportion of the module front-side acceptance angle encompassing the ground. Consequently, the module rear acceptance angle that encompasses the ground decreases, resulting in less ground-reflected light on the rear of the modules for high-latitude locations. For a fixed-tilt array at a latitude of 15°N, 95%–100% of all rear light is ground-reflected. By 80°N, ground-reflected irradiance is reduced and accounts for 0%–65% of all rear-side irradiance, depending on the albedo of the ground. This is in part driven by an increasing diffuse light irradiance component on the rear, with location latitude correlated to diffuse fraction; low-latitude locations often experience less cloud cover and lower humidity compared to high-latitude locations.[34] For high-latitude locations, the sun is also observed over a wider range of azimuth angles, leading to increased direct irradiance on the rear-side of south-facing fixed-tilt modules.

SAT arrays are instead oriented to track the sky from east-to-west, and the proportion of irradiance that comes from ground-reflected light remains similar as a function of latitude; the increasing ground-reflected irradiance component on the front-side of modules is balanced by the associated decrease in rear-side ground reflected light. However, this is the case assuming a constant albedo across all latitudes. When measured surface albedo data given in TMY files is used in place of an annual constant albedo, the proportion of irradiance which comes from ground-reflections increases with latitude. Albedo naturally tends to increase with latitude, driven by an

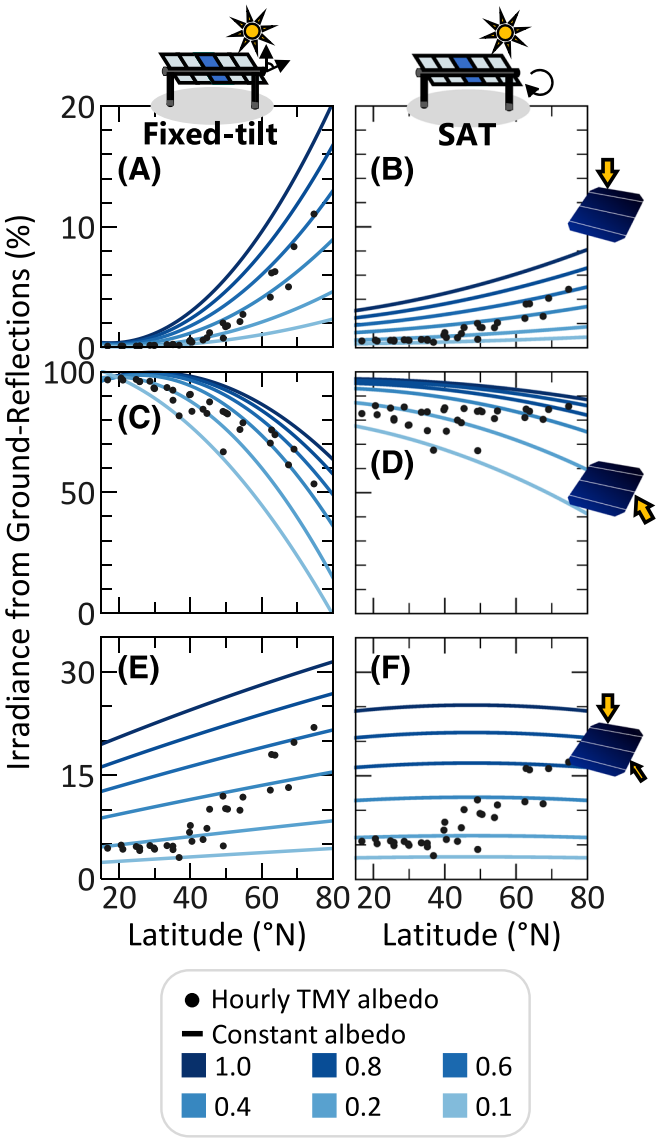

FIGURE 4 The annual proportion of incident irradiance on fixed-tilt (A, C, E) and SAT (B, D, F) photovoltaic modules that originates from ground-reflections as a function of deployment latitude and albedo. The proportion of incident irradiance that comes from the ground is provided for the front-side (A, B), rear-side (C, D), and both sides (E, F) of bifacial modules. Annual hourly TMY albedo results are provided as black dots to contextualize what naturally occurs in the field, while blue lines demonstrate lines of constant albedo across all latitudes.

increasing number of hours with snowy ground conditions. Thus, for both bifacial fixed-tilt and SAT arrays, ground-reflected light is both strongly related to albedo and the deployment latitude, and tends to increase in importance as latitude increases.

Figure 5 shows the annual incident effective plane-of-array irradiance gain when the ground albedo is changed from an albedo of 0 to 1 as a function of latitude for bifacial arrays. These values represent the sensitivity of model predicted incident irradiance to the input albedo. As incident irradiance has a linear dependence with albedo,[16] the plotted values represent the slope of this relationship and can be

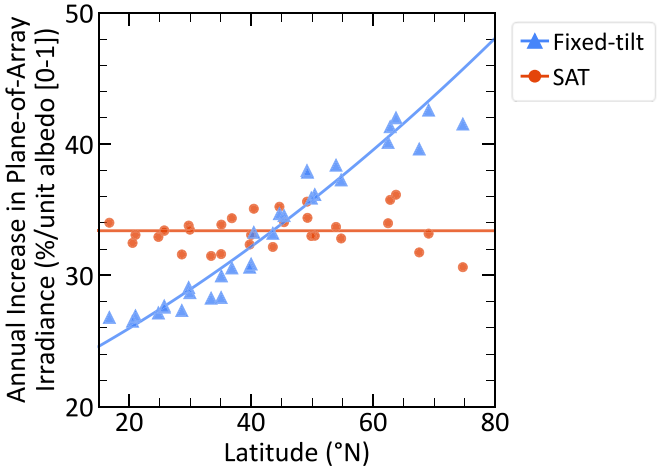

FIGURE 5 The total annual incident plane-of-array irradiance gain for bifacial fixed-tilt and SAT systems when albedo increases from 0 to 1. These values represent the sensitivity of model predicted incident irradiance to the input albedo. Trendlines are depicted as a guide for the eye using best-fit polynomials of order 2 (fixed-tilt) and 1 (SAT), with equations provided in-text (Equations 9 and 10).

used to predict performance variation for any arbitrary change in ground albedo. The total annual plane-of-array irradiance change, ΔG_{POA}, as albedo changes by $\Delta\alpha$ for a location at latitude, β, is described by the following two equations for fixed-tilt and SAT systems:

$$\Delta G_{POA,\text{Fixed}}\,[\%] = \Delta\alpha\left(0.0014\beta^2 - 0.23\beta + 21\right) \quad (9)$$

$$\Delta G_{POA,\text{SAT}}\,[\%] = \Delta\alpha\left(33.4\beta\right) \quad (10)$$

These equations provide an estimate of model uncertainty for any change in albedo for any northern latitude. For example, if albedo increases from 0.1 to 0.2 at 40°N for a fixed-tilt system, the annual incident plane-of-array irradiance increases by 3.2%.

SAT systems are more sensitive to changes in model-input albedo <45°N, while fixed-tilt systems are more sensitive >45°N. Albedo-related benefits increase with latitude for fixed-tilt systems and remain roughly latitude-independent for SAT systems. Thus, high-latitude fixed-tilt PV deployments have greater potential gains from enhanced albedo compared to low-latitude deployments and may also experience greater albedo-related model prediction uncertainty.

3.3 | Albedo-driven spectral mismatch

Following these general albedo trends with latitude, we characterize spectral mismatch factors (SMMs) resulting from use of spectral versus broadband albedo assumptions in our PV system model. SMMs quantify the deviation in incident irradiance received on a PV module under a spectrum of light relative to a reference spectrum. In many

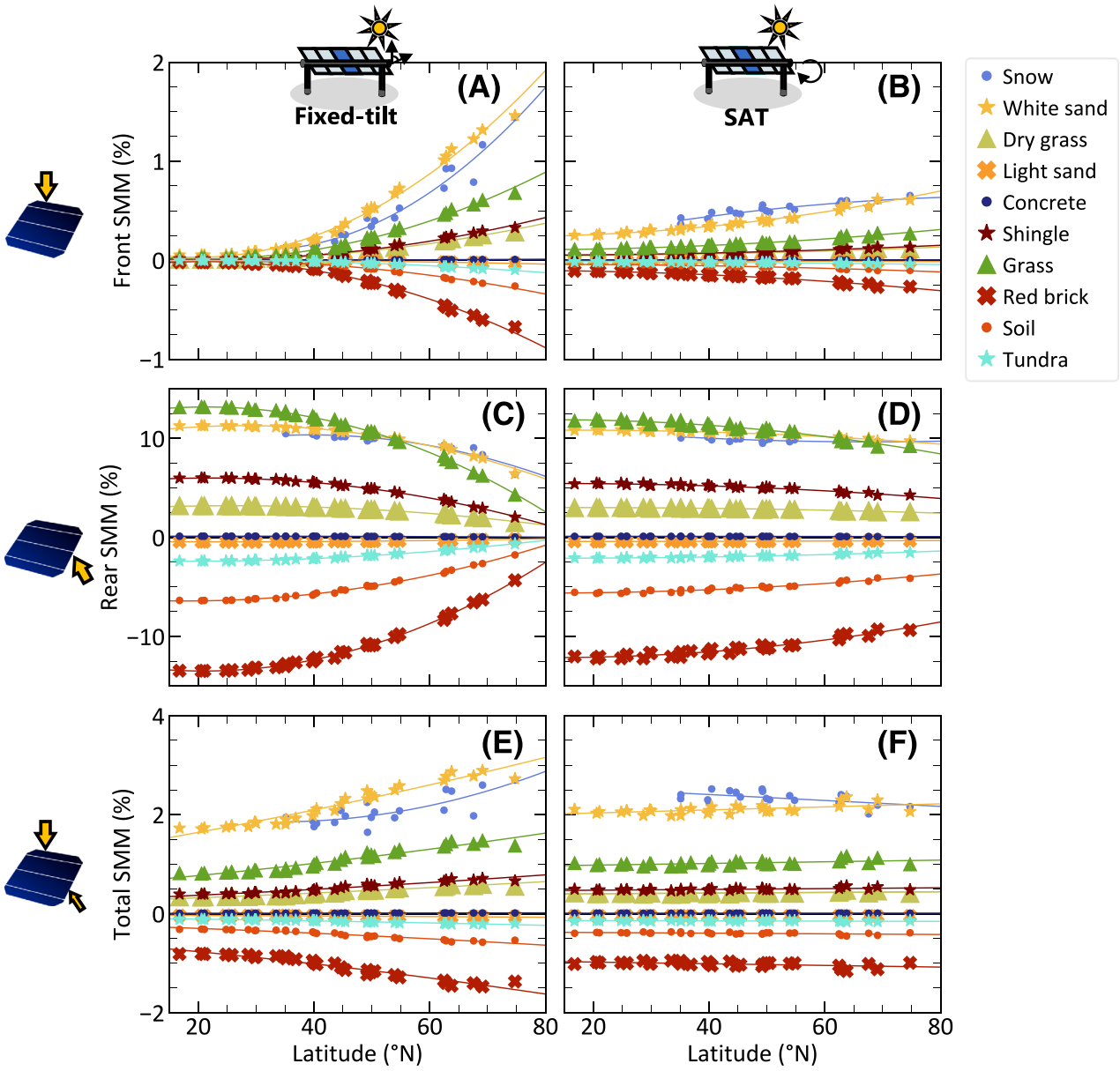

FIGURE 6 Spectral mismatch factors resulting from spectral albedo on fixed-tilt (A,C,E) and SAT (B,D,F) bifacial photovoltaic modules as a function of deployment latitude for 10 ground conditions. SMM is calculated as an irradiance ratio, given by Equation (11), for front-side (A, B), rear-side (C, D), and total (E, F) incident irradiance. SMM > 0% corresponds to spectral shape irradiance enhancements, while <0% corresponds to reductions. The importance of spectral shape depends on the module configuration and latitude, but is most substantially effected by the ground condition considered, with snow, white sand, green grass, and red brick leading to the greatest absolute SMMs.

cases, SMMs are used in PV models to adjust for deviations in front-incident irradiance from the reference solar spectrum of AM1.5G. A SMM > 1 indicates a spectrally-induced short-circuit gain and a SMM < 1 indicates short-circuit loss. In this work, we analyze spectral albedo-driven SMMs, with the reference spectrum being AM1.5G uniformly de-rated by a broadband albedo. As the effect of device spectral responsivity is captured in the definition of a_λ, SMM is calculated by the ratio of incident irradiance when a spectrally-weighted albedo is assumed in system modeling, G_{a_λ}, to incident irradiance when broadband assumptions are used, $G_{a_{bb}}$. We present our results in terms of percent, leading to the following equation:

$$SMM\,[\%] = \left(\frac{G_{a_\lambda}}{G_{a_{bb}}} - 1\right) \times 100 \tag{11}$$

Figure 6 depicts front-side SMM (Figure 6A,B), rear-side SMM (Figure 6C,D), and total SMM (Figure 6E,F) as a function of location latitude for fixed-tilt (Figure 6A,C,E) and SAT (Figure 6B,D,F) array configurations under 10 albedo scenarios. Total SMM corresponds to the sum of front and rear incident irradiance, with rear irradiance modified by the module bifaciality. A black horizontal line is drawn at SMM = 0 to differentiate between spectral enhancements and reductions. Second-order polynomial fitting lines are drawn between

TABLE 1 Spectrally-weighted albedo for other technologies.

		a_λ						
	a_{bb}	SHJ	IBC	TOPCon	CIGS	CdTe	GaAs	PK
Snow	**0.85**	0.94	0.94	0.94	0.94	0.97	0.97	0.98
White sand	**0.67**	0.75	0.74	0.74	0.74	0.73	0.73	0.71
Dry grass	**0.44**	0.45	0.45	0.45	0.45	0.39	0.39	0.35
Light sand	**0.33**	0.33	0.33	0.33	0.33	0.29	0.30	0.27
Concrete	**0.29**	0.29	0.28	0.28	0.29	0.27	0.27	0.26
Roof shingle	**0.26**	0.27	0.27	0.27	0.27	0.27	0.27	0.27
Green grass	**0.24**	0.27	0.28	0.28	0.28	0.19	0.20	0.13
Red brick	**0.23**	0.20	0.20	0.20	0.21	0.16	0.16	0.14
Soil	**0.19**	0.18	0.18	0.18	0.18	0.15	0.15	0.13
Tundra	**0.18**	0.18	0.18	0.18	0.18	0.16	0.16	0.15
	E_g (eV)	1.1	1.1	1.1	1.1	1.4	1.4	1.7

Note: Data in blue indicate spectral albedo enhancement. Data in orange indicate spectral albedo reduction.

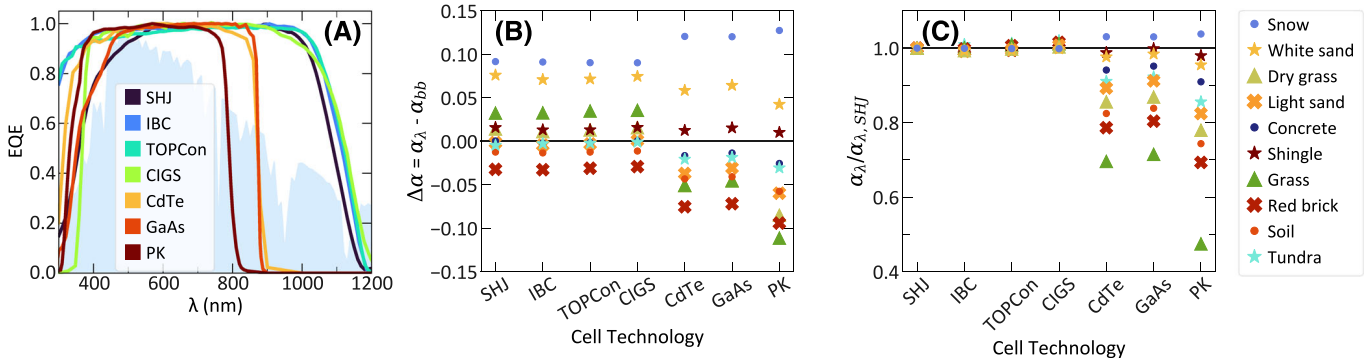

FIGURE 7 (A) Digitized external quantum efficiencies of various common solar cell technologies, for comparison with the measured SHJ EQE in this work. (B) The difference between spectrally-weighted and broadband albedo for each ground condition and technology. (C) The difference between spectrally-weighted and broadband albedo relative to the SHJ technology examined in this work, demonstrating greater discrepancies for higher bandgap technologies and therefore increased sensitivity to spectral effects.

individual location markers as a guide for the eye. Note that the *y*-axis limits are different for each subplot row to best show the data.

The spectral effects of ground albedo have a significant influence on rear-side irradiance, demonstrated by rear SMMs varying between −13.5% and +13.2% from 17 to 75°N. Despite the lower importance of ground-reflected light on front-side irradiance, front SMMs can reach up to 1.5% at high latitudes. Total SMM varies between −1.5% and +2.9% for all latitudes and albedos.

Similar trends can be seen for the impact of spectral effects on module energy yield. For example, in the case of our high-bifaciality (96%) fabricated SHJ modules, the spectral shape of albedo has an impact on energy yield compared to irradiance of between −1.2% and +2.5%. Further information on the impact of spectral albedo on energy yield is presented in Figure S2.

Trends of SMM with latitude are related to the proportion of total incident irradiance which is ground-reflected, as given in Figure 4. In the monofacial case (Figure 6A,B), SMM diverges away from zero as latitude increases, most notably for fixed-tilt modules. For rear-side irradiance (Figure 6C,D), SMM converges toward zero for higher latitudes due to the rear-side of modules facing more toward the diffuse sky than the ground. Combining these effects, total bifacial module SMM (Figure 6E,F) tends to diverge away from zero as a function of latitude for fixed-tilt configurations. As the proportion of rear-side incident irradiance originating from the ground is relatively flat with latitude in the bifacial SAT case, the same trends are present for the SMM in Figure 6F.

The SMM of fixed-tilt and SAT modules is similar between 40 and 50°N, with spectral effects most important for SAT modules at low latitudes and fixed-tilt modules at high latitudes. Below 40°N, SAT modules have higher absolute SMM values by up to 0.4% abs. Greater than 50°N, fixed-tilt modules have higher absolute SMM by up to 0.7% abs.

The importance of spectral versus broadband albedo assumptions depends on the module configuration and latitude but is most substantially effected by the ground condition considered. When the difference between a_λ and a_{bb} is <0.01, the effect of array configuration

and latitude is negligible as, in all cases, SMMs are ≤1%. For instance, albedos of light sand, concrete, tundra, and soil all have discrepancies between a_λ and a_{bb} by <0.01 absolute and thus SMMs near zero. For monofacial (Figure 6A,B) and bifacial (Figure 6E,F) illumination scenarios, SMMs are ordered by the absolute discrepancy between a_λ and a_{bb}, leading to the greatest spectral effects occurring for white sand, snow, green grass, and red brick.

3.4 | Other module technologies

The results presented thus far have been specific to silicon heterojunction solar cell technologies, with the spectrally-weighted albedo given by the external quantum efficiency of fabricated SHJ mini-modules. Table 1 compares a_λ calculated using published EQE data for six other example technologies: interdigitated back-contact (IBC),[35] tunnel oxide passivated contact (TOPCon),[36] copper indium gallium selenide (CIGS),[37] cadmium telluride (CdTe),[38] gallium arsenide (GaAs),[39] and perovskite (PK).[40] TOPCon, CdTe, and GaAs EQE data are retrieved from solar cell efficiency table entries for Jinko Solar,[36] First Solar,[38] and Alta Device[39] technologies, respectively. Table 1 entries are color-coded according to whether the spectrally-weighted albedo is higher (light blue), the same (medium gray), or lower (dark orange) compared to their broadband values.

Figure 7A shows the EQE for the seven solar cell technologies considered. EQEs have all been normalized to peak at 1.0 for this comparison and all EQE data, apart from the measured SHJ EQE, are for unencapsulated cells. Since encapsulant materials tend to be UV-absorptive,[41] the EQE of c-Si based technologies of IBC and TOPCon would become more similar to the measured SHJ mini-module EQE when encapsulated into modules.

Figure 7B shows the difference between spectrally-weighted albedos and broadband albedo for each technology, with the technologies listed in order of increasing bandgap energy. The discrepancy between a_λ and a_{bb} for each ground condition is similar for silicon-based technologies of SHJ, IBC, and TOPCon and for CIGS. Despite differing UV behavior, the effect of similar band-edges (~1.1 eV) dominates. As the bandgap increases for CdTe (1.4 eV), GaAs (1.4 eV), and PK (1.7 eV), so does the discrepancy between a_λ and a_{bb} for most albedos. For the SHJ technology studied in detail in this work, spectrally-weighted albedos deviate from broadband albedo by up to 9%. For wide bandgap technologies that absorb over a narrower bandwidth, spectral effects can change the broadband albedo value by up to 13%. Generally, narrower wavelength bandwidths will lead to greater variation in spectral albedo performance compared to broadband performance, as seen by the discrepancy between a_λ and a_{bb} diverging away from zero for higher bandgap technologies in Figure 7B. For instance, the spectral effects of snow on perovskite module irradiance are anticipated be around 1.4 × higher than that given by SHJ modules, as Δa increases from 0.09 to 0.13. Similarly, Figure 7C shows how the spectrally-weighted albedo varies between technologies compared to the spectrally-weighted SHJ value. High bandgap technology spectrally-weighted albedos tend to diverge away from SHJ values. This aligns with previous related findings in literature, where silicon technologies were found to have the least variation in performance under varied spectra compared to other solar cell technologies.[34]

The technology material also dictates whether spectral effects enhance or diminish the performance of the module. For instance, in the case of green grass, SHJ, IBC, TOPCon, and CIGS technologies all experience gains when the spectral effects are considered. As a contrast, CdTe, GaAs, or PK cells will experience spectral losses in performance. This is because the spectral albedo of green grass is low <700 nm.

The relative differences between SHJ Δa and other technology Δa is related to the relative differences that would be found in spectral mismatch factors for these other technologies, since irradiance linearly scales with ground albedo. Though energy yield is linearly related to albedo as well, the slope will vary with technology due to differences such as bifaciality, temperature response, and resistance. SHJs have the highest bifaciality among the considered technologies, and therefore the strongest relationship between albedo and energy yield. Thus, the reduced collection efficiency of the rear-side of modules for other technologies will partially offset increases in spectral mismatch factor. Regardless, for most albedos, spectral effects are expected to be even more significant than what is demonstrated in this work for PV technologies with bandgap energies higher than silicon.

4 | DISCUSSION

In this work, we demonstrated that omitting the effects of spectral albedo can cause variations in silicon cell measurements up to 2% and system modeled total irradiance up to 3%. A complementary and associated uncertainty arises from albedo monitoring meteorological equipment. In-field measurements of irradiance and albedo may be acquired from silicon pyranometers, thermopile pyranometers, and reference cells. The selection of one irradiance sensor over another can cause discrepancies in predicted bifacial gain of a similar order as the effect of spectral albedo.[3,42] Thus, the suitability and uncertainty of the albedo measurement method must itself be scrutinized when examining the spectral effects of albedo on bifacial PV system performance. The irradiance sensor used for measuring albedo may be selected to appropriately account for spectral effects, for example by selecting a reference cell with a similar spectral responsivity to the modeled deployment. Measurements of albedo must be appropriately documented so users can assess the uncertainty associated with their use in system-level models.

A few simplifying assumptions were made for this analysis. We assumed that ground-reflected irradiance was Lambertian in angular distribution, and that the spectral content of this reflection was the reference spectrum of AM1.5G modified by the ground's spectral albedo. In reality, both the solar spectrum and albedo vary in time, depending on the sun position, moisture content, and atmospheric conditions.[3,34] Ground surfaces tend to behave as Lambertian reflectors when

illuminated diffusely, but experience anisotropy in other illumination conditions commonly experienced in outdoor PV environments.[42–44] Surface reflections, notably those of water and ice, can be highly directional in nature, causing additional uncertainty to the analysis of albedo. Furthermore, we assumed that the albedo of fresh snow is present for all snow hours, in line with standard TMY datasets where snow hours are set to a singular default value of 0.87.[45] The albedo of snow is of particular interest for bifacial PV applications due to its potential for enhancing bifacial gain, but varies quite significantly depending on ambient temperature, grain size, wetness, and impurity content.[19,43,46] Understanding and modeling the varied albedo of snow is an active area of research to reduce overzealous estimations of snow performance. For example, Dumitrascu et al. have also proposed a model for two types of snow—melting and accumulating.[46]

While a thorough understanding of spectral albedo effects is a complex and nuanced problem, it is possible to reduce PV system modeling computational time and complexity by down-sampling spectral albedo to a few selected wavelength bands. For instance, Lindsay et al. found that 12 spectral bands provided enough resolution to capture the effects of spectral albedo compared to a broadband value,[47] though other work has suggested that for certain applications as low as 4–6 bands is sufficient.[21,48] Thus, further studies that incorporate more nuanced albedo effects such as anisotropy or snow-aging models, may benefit from reduced computation time via spectral down-sampling.

5 | CONCLUSION

We have demonstrated that omitting the effects of spectral albedo can cause variations in bifacial PV module short-circuit current measurements of up to 2% using the scaled rear irradiance method. Modeled bifacial PV system irradiance varies up to ±13% on the rear-side and up to 3% in total, resulting in energy yield modeling discrepancies of up to 2.5% for high bifaciality technologies. Spectral mismatch factors resulting from including or omitting spectral albedo vary as a function of deployment latitude and system tracking type. SAT array SMMs show a low correlation with latitude, while fixed-tilt array SMM increases with latitude, driven by an increasing proportion of ground-reflected light on the front-side of modules. Spectral albedo driven SMMs can reach as high as 1.5% for monofacial fixed-tilt systems at high latitude.

The proportion of total incident irradiance coming from ground-reflections increases with latitude for both SAT and south-facing fixed-tilt arrays and depends significantly on the ground albedo. Ground-reflected irradiance can constitute >10% of total irradiance received on the front-side of a fixed-tilt array at high-latitudes. Totaling both front and rear-side irradiance, ground-reflected irradiance contributions vary between 2% up to 32%, depending on the array tracking type, latitude, and albedo of the ground.

Effects of spectral albedo are most significant if the albedo varies over the technology's absorption range. For example, for c-Si technologies, snow, white sand, green grass, and red brick result in the highest absolute SMMs among the ground conditions considered in this work. Other single-junction technologies with wider bandgaps than c-Si will exhibit greater irradiance spectral sensitivity, and this spectral sensitivity is expected to be higher still for two-terminal tandem devices and multijunction cells due to their sub-cell current-matching requirements. Overall, we demonstrated that omission of spectral albedo effects can result in PV measurement and system model uncertainties on the order of several percent, with the greatest spectral effects occurring for fixed-tilt deployments at high latitudes, wide bandgap technologies, and high albedo ground conditions.

AUTHOR CONTRIBUTIONS

Erin M. Tonita: Conceptualization; methodology; software; investigation; formal analysis; data curation; writing—original draft; writing—review & editing; visualization. **Christopher E. Valdivia**: Conceptualization; methodology; software; investigation; formal analysis; data curation; writing—review & editing; supervision. **Annie C. J. Russell**: Software; writing—review & editing. **Michael Martinez-Szewczyk**: Investigation; resources; writing—review & editing. **Mariana I. Bertoni**: Resources; writing—review & editing. **Karin Hinzer**: Conceptualization; writing—review & editing; supervision; funding acquisition.

ACKNOWLEDGEMENTS

The authors would like to extend their thanks to Dr. Salima Alem and Hiroshi Fukutani from the National Research Council of Canada for access to their solar simulator and supportive conversations. The authors gratefully acknowledge the support of CMC Microsystems Canada, Canadian Foundation for Innovation, Ontario Research Fund, and the Natural Sciences and Engineering Research Council of Canada (NSERC CREATE 497981, NSERC STPGP 521894, and NSERC CGS-D). Funding was additionally provided by the US Department of Energy Office of Energy Efficiency and Renewable Energy Solar Energy Technologies Office under award DE-EE0009346. The views expressed in the article do not necessarily represent the views of the DOE or the US Government. The University of Ottawa is located on the unceded territory of the Anishinaabe Algonquin Nation.

DATA AVAILABILITY STATEMENT

The data supporting the findings of this study are available in the main text and supplemental information and are additionally available upon request from the corresponding author. Details regarding the system-level code used in this paper are published in Russell et al.[28]

ORCID

Erin M. Tonita https://orcid.org/0000-0003-4558-2414
Michael Martinez-Szewczyk https://orcid.org/0000-0003-0199-6148

REFERENCES

1. International Technology Roadmap for Photovoltaic (ITRPV), 2021 Results, Ed. 13, Frankfurt, Germany (2022). https://www.vdma.org/international-technology-roadmap-photovoltaic

2. Kopecek R, Libal J. Bifacial photovoltaics 2021: status, opportunities and challenges. *Energies*. 2021;14(8):2076. doi:10.3390/en14082076
3. Riedel-Lyngskaer N, Ribaconka M, Po M et al Spectral albedo in bifacial photovoltaic modeling: what can be learned from onsite measurements? *Proceedings of the IEEE 48th Photovoltaic Specialists Conference (PVSC)*. 2021, 0942–0949.
4. Vogt M. R., Gewohn T, Bothe K, Schinke C, Brendel R. Impact of using spectrally resolved ground albedo data for performance simulations of bifacial modules. *Proceedings of the 35th Euro. Photovolt. Sol. Energy Conference Exhibition*, 2018, 1011–1016.
5. Jager K, Tillmann P, Becker C. Detailed illumination model for bifacial solar cells. *Opt Express*. 2020;28(4):4751-4762. doi:10.1364/OE.383570
6. Ziar H, Sonmez FF, Isabella O, Zeman M. A comprehensive albedo model for solar energy applications: geometric spectral albedo. *Appl Energy*. 2019;255:113867. doi:10.1016/j.apenergy.2019.113867
7. Guerrero-Lemus R, Vega R, Kim T, Kimm A, Shephard LE. Bifacial solar photovoltaics – a technology review. *Renew Sustain Energy Rev*. 2016;60:1533-1549. doi:10.1016/j.rser.2016.03.041
8. Durusoy B, Ozden T, Akinoglu BG. Solar irradiation on the rear surface of bifacial solar modules: a modeling approach. *Sci Rep*. 2020;10(1):13300. doi:10.1038/s41598-020-70235-3
9. Ayala Pelaez S, Deline C, Greenberg P, Stein JS, Kostuk RK. Model and validation of single-axis tracking with bifacial PV. *IEEE J of Photovolt*. 2019;9(3):715-721. doi:10.1109/JPHOTOV.2019.2892872
10. Ayala Pelaez S, Deline C, Stein JS, Marion B, Anderson K, Muller M. Effect of torque tube parameters on rear-irradiance and rear-shading loss for bifacial PV performance on single-axis tracking systems. IEEE 4th Photovoltaics Specialists Conference (PVSC), Chicago, USA, 1–6 (2019).
11. Coathup T, Lewis MR, Russell ACJ, Haysom JE, Valdivia CE, Hinzer K. Impact of torque tube reflection on bifacial photovoltaic single axis tracked system performance. *Opt Express*. 2023;31(4):6155. doi:10.1364/OE.481301
12. McIntosh KR, Abbott MD, Sudbury BA, Meydbray J. Mismatch loss in bifacial modules due to nonuniform illumination in 1D tracking systems. *IEEE J Photovolt*. 2019;9(6):1504-1512. doi:10.1109/JPHOTOV.2019.2937217
13. Deline C, Pelaez SA, MacAlpine S, Olalla C. Estimating and parameterizing mismatch power loss in bifacial photovoltaic systems. *Prog Photovolt Res Appl*. 2020;28(7):691-703. doi:10.1002/pip.3259
14. Sun X, Khan MR, Deline C, Alam MA. Optimization and performance of bifacial solar modules: a global perspective. *Appl Energy*. 2018;212:1601-1610. doi:10.1016/j.apenergy.2017.12.041
15. Jannsen GJM, Van Aken BB, Carr AJ, Mewe AA. Outdoor performance of bifacial modules by measurements and modelling. *Energy Procedia*. 2015;77:364-373. doi:10.1016/j.egypro.2015.07.051
16. Yusufoglu UA, Lee TH, Pletzer TM, et al. Simulation of energy production by bifacial modules with revision of ground reflection. *Energy Procedia*. 2014;55:389-395. doi:10.1016/j.egypro.2014.08.111
17. Onno A, Rodkey N, Asgharzadeh A, et al. Predicted power output of silicon-based bifacial tandem photovoltaic systems. *Joule*. 2020;4(3):580-596. doi:10.1016/j.joule.2019.12.017
18. Russell TCR, Saive R, Augusto A, Bowden SG, Atwater HA. The influence of spectral albedo on bifacial solar cells: a theoretical and experimental study. *IEEE J Photovolt*. 2017;7(6):1611-1618. doi:10.1109/JPHOTOV.2017.2756068
19. Brennan MP, Abramase AI, Andrews RW, Pearce JM. Effects of spectral albedo on solar photovoltaic devices. *Solar Energy Mater Solar Cells*. 2014;124:111-116. doi:10.1016/j.solmat.2014.01.046
20. Andrews RW, Pearce JM. The effect of spectral albedo on amorphous silicon and crystalline silicon solar photovoltaic device performance. *Solar Energy*. 2013;91:233-241. doi:10.1016/j.solener.2013.01.030
21. Riedel-Lyngskaer N, Ribaconka M, Po M, et al. The effect of spectral albedo in bifacial photovoltaic performance. *Solar Energy*. 2022;231:921-935. doi:10.1016/j.solener.2021.12.023
22. Tonita EM, Valdivia CE, Russell ACJ, Martinez-Szewczyk M, Bertoni MI, Hinzer K. A general illumination method to predict bifacial photovoltaic system performance. *Joule*. 2023;7:1-12.
23. Gueymard CA, Myers D, Emery K. Proposed reference irradiance spectra for solar energy systems testing. *Solar Energy*. 2002;73(6):443-467. doi:10.1016/S0038-092X(03)00005-7
24. Bøggild CE, Brandt RE, Brown KJ, Warren SG. The ablation zone in Northeast Greenland: ice types, albedos and impurities. *J Glaciol*. 2010;56(195):101-113. doi:10.3189/002214310791190776
25. IEC 60904–1-2: Photovoltaic devices – Part 1–2: Measurement of current-voltage characteristics of bifacial PV devices, Ed.1.0 2019–01 (2019).
26. Sengupta M, Xie Y, Lopez A, Habte A, Maclaurin G, Shelby J. The National Solar Radiation Data Base (NSRDB). *Renew Sustain Energy Rev*. 2018;89:51-60. doi:10.1016/j.rser.2018.03.003
27. Environment and Climate Change Canada. Engineering climate datasets. Online (2022). Available: https://climate.weather.gc.ca/prods_servs/engineering_e.html
28. Russell ACJ, Valdivia CE, Bohémier C, Haysom JE, Hinzer K. DUET: a novel energy yield model with 3D shading for bifacial photovoltaic systems. *IEEE J Photovolt*. 2022;12(6):1576-1585. doi:10.1109/JPHOTOV.2022.3185546
29. Berrian D, Libal J, Klenk M, Nussbaumer H, Kopecek R. Performance of bifacial PV arrays with fixed tilt and horizontal single-axis tracking: comparison of simulated and measured data. *IEEE J Photovolt*. 2019;9(6):1583-1589. doi:10.1109/JPHOTOV.2019.2924394
30. Tonita EM, Russell ACJ, Valdivia CE, Hinzer K. Optimal ground coverage ratios for tracked and fixed-tilt photovoltaic systems for latitudes up to 75°N. *Solar Energy*. 2023;258:8-15. doi:10.1016/j.solener.2023.04.038
31. Lorenzo E, Narvarte L, Munoz J. Tracking and back-tracking. *Prog Photovolt Res Appl*. 2011;19(6):747-753. doi:10.1002/pip.1085
32. King DL, Kratochvil JA, Boyson WE. Photovoltaic array performance model. *Sandia Report – SAND2004–3535*. 2004;8:1-19.
33. Stein J, Reise C, Castro JB, et al. Bifacial photovoltaic modules and systems: experience and results from international research and pilot applications. *Int Energy Agency Photovolt Power Syst Prog*. 2021;T13-14:2021.
34. Kinsey GS. Solar cell efficiency divergence due to operating spectrum variation. *Solar Energy*. 2021;217:49-57. doi:10.1016/j.solener.2021.01.024
35. Yoshikawa K, Kawasaki H, Yoshida W, et al. Silicon heterojunction solar cell with interdigitated back contacts for a photoconversion efficiency over 26%. *Nat Energy*. 2017;2(5):17032. doi:10.1038/nenergy.2017.32
36. Green MA, Dunlop ED, Hohl-Ebinger J, et al. Solar cell efficiency tables (version 60). *Prog Photovolt Res Appl*. 2022;30(7):687-701. doi:10.1002/pip.3595
37. Nakamura M, Yamaguchi K, Kimoto Y, Yasaki Y, Kato T, Sugimoto H. Cd-free cu(in,Ga)(se,S)2Thin-film solar cell with record efficiency of 23.35%. *IEEE J Photovolt*. 2019;9(6):1863-1867. doi:10.1109/JPHOTOV.2019.2937218
38. Green MA, Emery K, Hishikawa Y, Warta W, Dunlop ED. Solar cell efficiency tables (version 45). *Prog Photovolt Res Appl*. 2015;23(1):1-9. doi:10.1002/pip.2573
39. Green MA, Hishikawa Y, Dunlop ED, et al. Solar cell efficiency tables (version 53). *Prog Photovolt Res Appl*. 2015;27(1):1-9.
40. Xu J, Boyd CC, Yu ZJ, et al. Triple-halide wide-band gap perovskites with suppressed phase segregation for efficient tandems. *Science*. 2020;367(6482):1097-1104. doi:10.1126/science.aaz5074

41. McIntosh KR, Cotsell JN, Cumpston JS, Norris AW, Powell NE, Ketola BM. An optical comparison of silicone and EVA encapsulants for conventional silicon PV modules: a ray-tracing study. *34th IEEE Photovoltaic Specialists Conference (PVSC)*, Philadelphia, USA, 544–549 (2009).
42. Gostein M, Marion B, Stueve B. Spectral effects in albedo and rear-side irradiance measurement for bifacial performance estimation. *Proceedings of the 47th IEEE Photovoltaic Specialists Conference (PVSC)*, 0515–0519 (2020).
43. Gueymard CA, Lara-Fanego V, Sengupta M, Xie Y. Surface albedo and reflectance: review of major definitions, angular and spectral effects, and intercomparison of major data sources in support of advanced solar irradiance modelling over the Americas. *Solar Energy*. 2019;182:194-212. doi:10.1016/j.solener.2019.02.040
44. Martin N, Ruiz JM. A new method for the spectral characterization of PV modules. *Prog Photovolt Res Appl*. 1999;7(4):299-310.
45. Marion B. Measured and satellite-derived albedo data for estimating bifacial photovoltaic system performance. *Solar Energy*. 2021;215:321-327. doi:10.1016/j.solener.2020.12.050
46. Dumitrascu L, Beausoleil-Morrison I. A model for predicting the solar reflectivity of the ground that considers the effects of accumulating and melting snow. *J Build Perform Simul*. 2020;13(3):334-346. doi:10.1080/19401493.2020.1728383
47. Lindsay N, Libois Q, Badosa J, Migan-Dubois A, Bourdin V. Errors in PV power modelling due to the lack of spectral and angular details of solar irradiance inputs. *Solar Energy*. 2020;197:266-278. doi:10.1016/j.solener.2019.12.042
48. Tatsiankou V, Hinzer K, Haysom J, Schriemer H, Emery K, Beal R. Design principles and field performance of a solar spectral irradiance meter. *Solar Energy*. 2016;133:94-102. doi:10.1016/j.solener.2016.03.054

SUPPORTING INFORMATION

Additional supporting information can be found online in the Supporting Information section at the end of this article.

How to cite this article: Tonita EM, Valdivia CE, Russell ACJ, Martinez-Szewczyk M, Bertoni MI, Hinzer K. Quantifying spectral albedo effects on bifacial photovoltaic module measurements and system model predictions. *Prog Photovolt Res Appl*. 2024;1-13. doi:10.1002/pip.3789

6.3 Vertical bifacial photovoltaic system model validation

Five bifacial modelling platforms
Are validated using measured irradiance.
Vertical data is not that norm
And is compared in two places simultaneous.
.
Modelling error is found to be high
For low irradiance hours,
When clouds float across the sky,
And snow covers any flowers.

❄ ❄ ❄

Scope and impact

Bifacial PV irradiance models have been historically validated against field data in traditional south-facing fixed-tilt and single-axis tracking configurations. PV models have yet to be thoroughly validated for emerging east-west vertical systems where direct-beam irradiance swaps sides at solar noon. Vertical PV systems have been deployed in recent years in northern latitudes, and have been used in combination with agricultural practices (agri-PV) and in building-integrated applications [14, 32, 173]. These systems are gaining in popularity for a variety of reasons, including their ability to minimize soiling, eliminate snow accumulation, and improve building self-consumption [143, 146, 147, 147–149]. In our article, we validate five bifacial PV irradiance models for the first time with vertical system PV field data: bifacial_radiance (ray tracing), PVSyst (2D view factor), bifacialVF (2D view factor), SAM (2D view factor), and DUET (finite-element). These models are described in Section 3.4.4 of this thesis.

This article has the following novelties:

1. PV model validation is completed using vertical PV test-site plane-of-array irradiance data for five PV modelling platforms.

2. Model validation is completed for test-site data in two locations: over 6-months in Golden, Colorado (40°N), and over 1-year in Fairbanks, Alaska (65°N). This work represents the highest latitude site model validation to-date in literature, to the authors' knowledge.

3. We find that the four sub-hourly PV irradiance models predict daily and seasonal variations in vertical PV system measured plane-of-array irradiance, with root-mean-square error

(RMSE) varying between 4-28% depending on the system location, orientation, and data filtering conditions. PVSyst, limited by hourly resolution, demonstrates RMSE varying from 12-45%.

4. In all models, RMSE is higher for low irradiance timestamps, on cloudy days, and in the presence of snow.

5. Snow accumulation on south-facing tilted modules in Fairbanks is found to increase model RMSE, by causing model over-estimation in winter months.

6. Regular test-site maintenance is found to decrease model RMSE by up to 3% abs. in Alaska.

7. Trends with latitude show a divergence between model software predictions at higher latitudes. Vertical PV systems are found to result in 2-3× higher model discrepancies than equator-tilted PV systems.

This article demonstrates that bifacial PV models can be used for vertical systems and high latitudes with a higher margin of uncertainty. We recommend practices for test-site data collection in high latitude locations, and outline potential pathways for improving model accuracy for vertical and high latitude PV applications.

Author contributions

Erin M Tonita As the lead author of this work, I led the design, purchasing, assembly, and maintenance of the vertical test-site located at NREL's South Table Mountain campus. I ran simulations in bifacial_radiance, PVSyst, bifacialVF, SAM, and DUET and conducted the validation analysis presented in the paper. I ran quality assurance tests, cleaned, and merged test-site datasets for NREL and ACEP. I helped conceptualize this research project under the supervision of Silvana Ovaitt and Chris Deline. I wrote the original manuscript and generated all figures.

Silvana Ovaitt led the conceptualization of the research project and provided regular guidance and supervision throughout the project. She assisted in the design and assembly of the vertical test-site, provided software support for bifacial_radiance, and helped with NREL weather station and test-site data collection. She provided valuable connections and resources for progressing the research project. She reviewed and edited the manuscript.

Henry Toal maintained and led data-sharing efforts of the ACEP test-site data in Fairbanks. He provided regular feedback on the research directions and supported findings for the ACEP test-site. He reviewed and edited the manuscript.

Karin Hinzer supervised research efforts at the University of Ottawa, provided funding and support for making the exchange to NREL possible, and reviewed and edited the manuscript.

Christopher Pike supervised and guided the model validation efforts using Alaskan test-site data. He supervised and maintained ACEP test-site data and provided maintenance logs and photos of the test-site for use in this study. He provided regular, valuable feedback on the research progression. He reviewed and edited the manuscript.

Chris Deline conceptualized this research and provided software support for bifacial_radiance. He supervised this project at NREL, funded the vertical test-site deployment, and reviewed and edited the manuscript.

Copyright

Vertical bifacial photovoltaic system model validation: Study with field data, various orientations, and latitudes

Erin Tonita[1], Silvana Ovaitt[2], Henry Toal[3], Karin Hinzer[1], Christopher Pike[3], and Chris Deline[2]

[1]SUNLAB, University of Ottawa, Ottawa, Ontario, Canada
[2]National Renewable Energy Laboratory, Golden, Colorado, USA
[3]Alaska Center for Energy and Power, University of Alaska Fairbanks, Fairbanks, Alaska, USA

***Abstract* —Accurate modelling of photovoltaic (PV) systems is critical for the design, financial analysis, and monitoring of solar PV plants. For bifacial PV applications, models must additionally offer robust rear-side irradiance algorithms. However, bifacial PV irradiance models have yet to be sufficiently validated for east-west vertically oriented systems, where direct beam solar irradiation swaps at solar noon. Here, we validate five bifacial irradiance models with field data collected in Golden, Colorado (40°N) and Fairbanks, Alaska (65°N) for east-west vertical, north-south vertical, and south-tilted arrays. There is no clear best performer amongst sub-hourly models; Bifacial_radiance, bifacialVF, the System Advisor Model, and DUET comparably predict seasonal and daily changes in PV production, with root mean square error (RMSE) falling in the range of 11-28% depending on the location and system orientation. PVSyst (v7.4.8), limited by hourly resolution, demonstrates RMSE in the range of 33-45%. The primary causes of high RMSE are similar for all models; using an irradiance cut-off of >100 W/m², clear-sky filtering, and removing timestamps with snow, lowers model RMSE to 4-13% for sub-hourly models and 12-25% for PVSyst. Regular meteorological station servicing is found to further decrease model RMSE by up to 3% abs. in Alaska. Finally, we model bifacial PV systems in over 250 locations between 15-85°N, finding that deviations between model-predicted annual insolation tends to be 2-3× higher for vertical PV systems than south-facing fixed-tilt systems. We discuss potential methods for improving vertical PV modelling, and provide recommendations for high quality field data collection in northern environments.**

Keywords: *bifacial photovoltaics, model validation, ray tracing, view factor, finite element, vertical, bifacial_radiance, bifacialVF, System Advisor Model, DUET, PVSyst, Alaska, high latitude*.

I. Introduction

With rising annual bifacial photovoltaic (PV) deployments each year, there is growing interest in harnessing bifaciality for unique system configurations. One configuration deployed recently in smaller-scale custom arrays (< 1 MW) is vertically-mounted, east-west (E-W) facing bifacial arrays. Vertical E-W bifacial systems offer potential advantages compared to traditional equator-facing fixed-tilt modules including afternoon and morning production which can better match electricity load and improve self-consumption [1][2][3][4], break-even annual energy yield at high-latitudes [1][2][5][6], low soiling loss [7][3], and better shade uniformity for agri-PV applications [8][9][10].

While bifacial PV models are critical for optimizing, predicting, and assessing the performance of various system configurations, limited research exists that compares and validates bifacial PV irradiance models for vertical systems or at high latitudes. A recent IEA Task 13 report [11] identified significant hourly discrepancies in predicted irradiance by PV irradiance models for a single row of simulated vertical E-W modules in three locations (23°S, 24°N, and 53°N). However, to the authors knowledge there are no model validations specifically for vertical PV systems with field data to date. Several studies have been published in recent years that quantify bifacial irradiance model accuracy with measured field data but do not include vertically oriented panels or high latitudes [12][13][14][15]. For example, Ayala Pelaez *et al*. compared the performance of 5 bifacial irradiance models to 3 months of field data for a 10° south-facing fixed-tilt testbed located in Golden, Colorado, finding front irradiance root mean square error (RMSE) <1% and rear irradiance RMSE <2.3% on a clear-sky day [12]. Asgharzadeh *et al*. compared four bifacial irradiance models to measurements of a south-facing fixed-tilt site in Albuquerque, New Mexico (35°N) and a single-axis tracking site in Davis, California (39°N), finding a median percent difference between measurements and model of 17% in Albuquerque [13]. Capelle *et al*. compared front and back irradiance residuals for PVFactors, bifacialVF, PVSyst, bifacial_radiance, and the INES 3D VF model for a bifacial fixed-tilt test-site in France (46°N), finding marginally better performance for ray tracing and 3D VF models [14].

For model validation at high latitudes, there have been some studies published using an open-source dataset of a fixed-tilt and single-axis tracking PV site located in northern Europe in Roskilde, Denmark (55.6°N) [16][17][18]. For example, Riedel-Lyngskaer *et al*. compared eight bifacial irradiance models to 12 months of field data collected in Roskilde for a utility-scale 25° south-facing fixed-tilt system and a utility-scale single-axis tracking system [16]. The authors found that 2D view factor models could predict monthly bifacial gain to within 1% in the fixed-tilt case and 2% for the tracked case. Despite this study occurring at a northern latitude, only six snowfall events happened, with authors noting that snow did not accumulate or remain on the ground for more than a day [16]. This snowfall is not representative of many locations

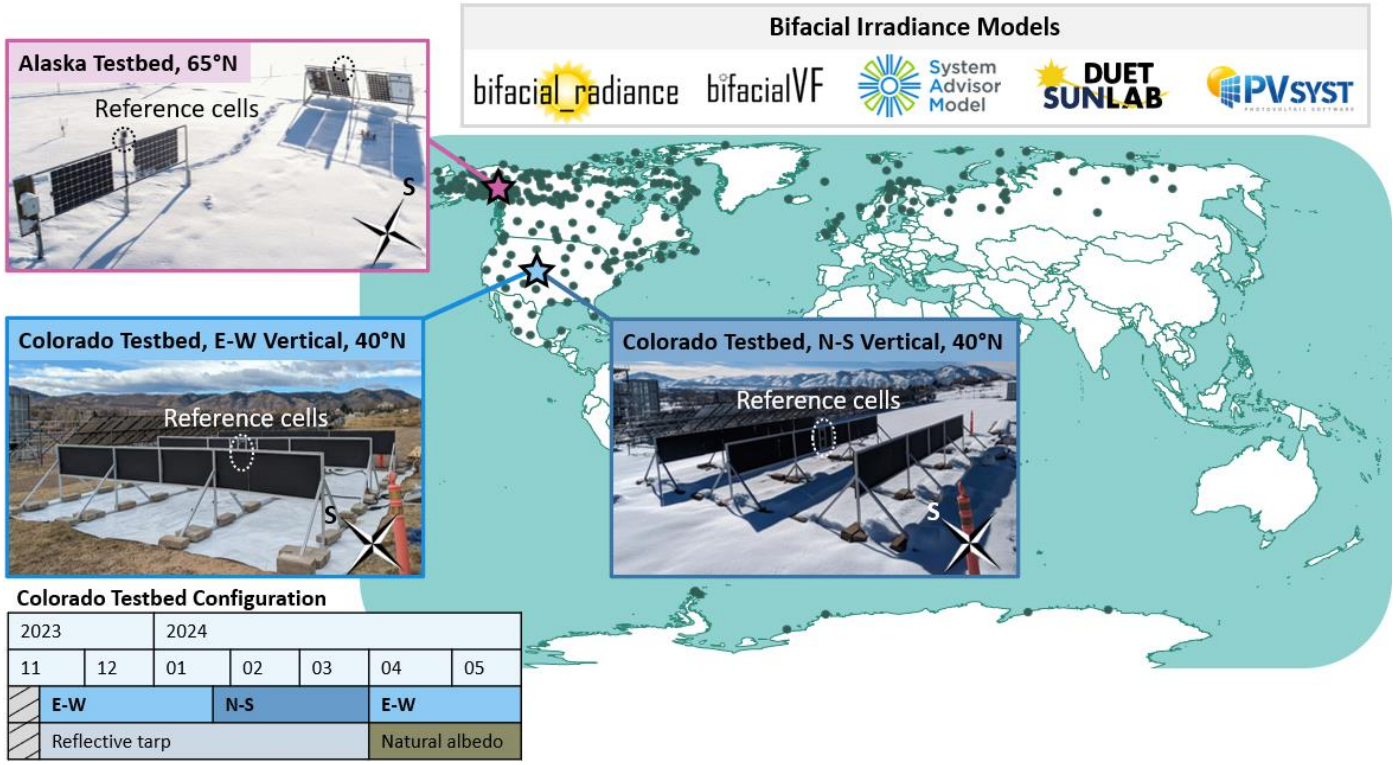

Figure 1. A map of modelled locations with images of the PV sites where models are compared against field data. Reference cells measuring plane-of-array irradiance are labelled in each photo by dashed circles. The Colorado testbed is rotatable between E-W and N-S orientation, with the timeline of the experiments outlined in the inset table. Green circles on the map represent locations where utility-scale bifacial E-W vertical, N-S vertical, and equator-facing fixed-tilt arrays are modelled using TMY data.

around and above 55°N, where snowfall remains on the ground for several months of the year.

Here, we expand upon previous bifacial irradiance model validation studies to additionally quantify model accuracy for bifacial vertical PV systems and at a high latitude location near the Arctic Circle. We compare model-predicted irradiance to measured field data for vertical and south-tilted test-sites in Golden, Colorado (40°N) and Fairbanks, Alaska (65°N). We validate five PV irradiance models: PVSyst [19], bifacial_radiance [20], bifacialVF [21], the System Advisor Model (SAM) [22], and DUET [18]. The vertical test-site in Golden is constructed for this study and is rotated between east-west and north-south (N-S) orientations for model validation. A full year of data is analyzed in Alaska, while in Colorado 124 days are analyzed in E-W orientation and 70 days in N-S orientation. All datasets are analyzed at a 15-minute resolution, apart from PVSyst which is limited to hourly resolution as of v7.4.8. We additionally compare model-predicted irradiance for utility-scale E-W vertical and equator-facing fixed-tilt bifacial PV arrays across 250+ locations, emphasizing locations above 60°N/S. Modelled test-sites and locations are depicted in Figure 1.

II. Methodology

A. Bifacial Photovoltaic Irradiance Models

The five models examined in this work use one of three techniques to predict irradiance: ray tracing, view factor transposition, and finite element analysis. Table 1 outlines the key differences between each model used in this study.

Ray tracing algorithms track individual light ray reflection, transmission, and absorption properties throughout a scene given a defined 3D environment. Custom scenes can be built, considering detailed array descriptions, such as irregular array spacing, custom racking, and the surrounding environment, such as nearby buildings and trees. Material properties are assigned to each object in the scene, allowing for transparency and specular reflection. Bifacial_radiance is an open-source ray tracing model developed by the National Renewable Energy Laboratory (NREL). In bifacial_radiance, the 'Radiance' ray tracing tool suite is adapted and packaged for modelling bifacial PV arrays. Reverse ray tracing is performed on a user-defined object in the 3D scene to determine incident irradiance for each timestamp of interest. Though computationally expensive, bifacial_radiance can analyze custom array geometries, and can thus examine edge effects, rack shading, and the effects of obstructions close to the PV array [20]. Bifacial_radiance can also account for spectral albedo and specular reflections, as shown in Table 1. In this work, broadband albedo values are measured and used, and Lambertian reflection is assumed due to a lack of specular data.

Table 1: Comparison of bifacial PV model functionality

	bifacial_ radiance	bifacialVF	SAM	DUET	PVSyst
Main algorithm	Ray tracing	2D VF	2D VF	3D finite element	2D VF
Spectral albedo	✓	×	×	×	×
Specular reflections	✓	×	×	×	×
Rear-irradiance non-uniformity	✓	×	×	✓	×
Rack shading	✓	×	✓†	✓	✓†
Edge effects	✓	×	×	✓	×
Data resolution	Sub-hourly	Sub-hourly	Sub-hourly	Sub-hourly	Hourly
Albedo resolution	Sub-hourly	Sub-hourly	Sub-hourly	Sub-hourly	Monthly
Speed* (runtime/ timestamp)	6 s	3 s	< 1 s	6 s	< 1 s
Version used	v0.4.2	v0.1.8.1	v4.2.0	v0-research	v7.4.8

*Speed test is completed using the Golden E-W vertical test-site on a Windows 10.0 Dell OptiPlex 7020 computer with an Intel Core i5-4690 processor (4 cores) and 16GB of RAM.
†Rack shading is not calculated by the program but can be implemented by including a user-defined structure shading factor.

View factor (VF) models, on the other hand, rely on simpler, repeating geometries for fast computation of array incident irradiance. In VF models, the fraction of radiant energy emitted or reflected from one surface to another is calculated using a transposition model. Two-dimensional (2D) VF approaches are commonly used in PV modelling tools, including PVSyst [19], bifacialVF [21], and the System Advisor Model (SAM) [22] for fast computation of plane-of-array (PoA) irradiance. Rows of modules are assumed to be of infinite extent, allowing for 2D assumptions.

DUET, developed internally by the University of Ottawa, calculates irradiance transfer between finite elements in a 3D scene by segmenting the sky, ground, and PV array into patches. Shading within the 3D scene is determined using a ray-intersection algorithm. This calculation method is intended to provide an alternative to ray tracing and can thus also capture the effect of finite-array size at the cost of higher computation time [18].

All five models considered in this work use the Perez sky model to calculate the angular distribution of sky irradiance [23]. Bifacial_radiance and DUET model the finite geometries of the PV test-site arrays and PV module frames, while VF models of SAM, bifacialVF, and PVSyst compute irradiance assuming infinite array geometries and flat, frameless modules.

B. Bifacial Test-Sites

(i) Colorado Bifacial Vertical Test-Site

To validate the performance of bifacial PV irradiance models for vertically-oriented PV arrays, we constructed a 2/3rd scale vertical bifacial PV test-site at NREL's South Table Mountain campus (39.7°N, 105.2°W). The test-site consists of three rows, six central reference cells (three east and three west IMT Si-V-1.5TC), black plywood, and aluminium 80/20 frame (see Figure 1). The modular design of this test-site allows for varying the row-spacing of the array and the light-weight plywood enables easier rotation of the array between E-W and N-S orientation. For this analysis, the array has a 0.61 m ground clearance and 3.0 m pitch, corresponding to a scaled-down version of a 1×2m module landscape system with 1 m ground clearance, 5 m pitch, and five modules per row. Data has been collected for 124 days from Nov. 2023 through Jan. 2024 and Apr. 2024 through May 2024 in the E-W orientation, and for 70 days from Jan. 2024 through April 2024 in the N-S orientation. A visualization of the experimental timeline can be found in Figure 1. Data is logged on a Campbell Scientific CR1000 Datalogger at 1-minute intervals and averaged to 1-hour intervals for PVSyst and 15-minute intervals for all other models.

A reflective tarp is placed underneath the array to simulate high albedo conditions in northern, high altitude, and Antarctic latitudes during the winter months of November through April. The reflectivity of the tarp was measured in 10 locations using a Konika Minolta CM-700d handheld reflectometer three times throughout the data acquisition period under varying soiling conditions. When initially placed under the array, the average tarp reflectivity was measured to be 0.66 over the silicon absorption range. The average soiled reflectivity of the tarp throughout the experiment was measured to be 0.62, with the lowest occurring single measurement being 0.40 for a particularly muddy location. Since the albedo of the tarp around the array was not continuously monitored throughout the experiment, we assume a value of 0.60 as the albedo input into all simulations. We estimate the albedo varied between 0.40-0.66 depending on the soiling conditions. This results in a modelled irradiance uncertainty of ±3-10% when the tarp is present. Measurements of albedo and diffuse, direct, and global sky irradiance components are obtained from the NREL Measurement and Instrumentation Data Center (MIDC) located half a kilometer away from the site and averaged to 15-minute resolution [24]. In the case of snowfall, snow covers the tarp, and the measured albedo from MIDC exceeds 0.60. Thus, these measured values replace the tarp reflectivity for snowy timestamps. Outside of the winter months, the tarp is removed and natural albedo is instead used, as measured by MIDC.

(ii) Alaska Bifacial E-W Vertical & South-Tilted Test-Site

We additionally analyze a full year of reference cell irradiance data for the vertical bifacial test-site in Fairbanks, Alaska (64.8°N, 147.7°W) and maintained by the University of Alaska Fairbanks [2]. This test-site consists of two sub-arrays: a two-module, two reference cell E-W vertical array and a four-module, two reference cell 60° south-facing tilted array, as depicted in Figure 1. Reference cells are oriented to measure the irradiance incident on both sides of both sub-arrays. Global, diffuse, and direct irradiance components, wind speed, ambient temperature, and albedo are measured continuously on-site at 1-minute averaged intervals and averaged again to 1-hour intervals for PVSyst and 15-minute intervals for input into bifacial_radiance, bifacialVF, SAM, and DUET. Pyranometers are heated to reduce the effects of snow accumulation. Albedo is calculated by dividing a downward-facing RHI pyranometer by the measured GHI, with a maximum allowed value of 0.85. The site undergoes regular maintenance and cleaning on a roughly weekly schedule. For the period of this study, Sept. 2019 through Sept. 2020, the site was serviced 23 times between March and October and was not serviced outside of these months. Since this time period, maintenance procedures have been adapted and solidified to a regular weekly schedule including the winter months.

Further details on this test-site, including a comparison of module energy yield, can be found in Ref. [2].

III. Results

A. Model Validation

For model validation, each sub-hourly bifacial irradiance model is tested under four scenarios at 15-minute resolution: (1) E-W vertical orientation in Golden, CO (124 days, ~6000 sun-up timestamps); (2) N-S vertical orientation in Golden, CO (70 days, ~3000 timestamps); (3) E-W vertical orientation in Fairbanks, AK (1 year, ~17,700 timestamps); and (4) South-facing 60°-tilt orientation in Fairbanks, AK (1 year, ~17,700 timestamps). In PVSyst, hourly values are used instead, resulting in 1600-5000 non-zero irradiance timestamps depending on the test-site and orientation.

The following results compare modelled to measured PoA irradiance using root mean square error (RMSE) and mean bias error (MBE):

$$RMSE = \frac{\sqrt{(1/N)\sum_{i=1}^{N}(y_i - x_i)^2}}{(1/N)\sum_{i=1}^{N} x_i} \quad (1)$$

$$MBE = (1/N)\sum_{i=1}^{N}(y_i - x_i) \quad (2)$$

where N is the total number of timestamps, y is modelled PoA irradiance, and x is measured PoA irradiance.

For model validation in Colorado, sensors facing the same direction are averaged together and compared to average line-scan irradiance data output by the models. In Alaska, exact sensor positions were modelled due to only having one sensor per direction.

An example clear-sky day for each system configuration is provided in Figure 2. Black solid lines give measured PoA irradiance while modelled results are given by coloured broken lines or open circles. Irradiance is shown for both east and west (A, C), south and north (B), or front and rear (D) sensors. The example clear-sky days in Colorado are relatively close to the winter solstice, while the clear-sky day provided in Alaska is approaching the summer solstice, leading to more than 18 hours of sunlight. Models show larger variation in Colorado near the winter solstice, with RMSE between 4-28% in Colorado compared to 4-13% in Alaska. A few trends are notable from these example clear-sky days. All five bifacial irradiance models over-predict south irradiance for the N-S vertical configuration in Colorado (Figure 2B). South irradiance MBE for the day varies from +27 W/m^2 (DUET) to +43 W/m^2 (PVSyst). All models also over-predict south irradiance for the south-tilted test-site in Alaska (Figure 2D) and under-estimate diffuse light irradiance for both orientations in Alaska (Figure 2C/D). For example, rear irradiance MBE varies from -12 W/m^2 (bifacial_radiance) to -31 W/m^2 (PVSyst) in the south-tilted configuration.

These same under-estimating and over-estimating trends can be observed when all timestamps are considered. Figure 3

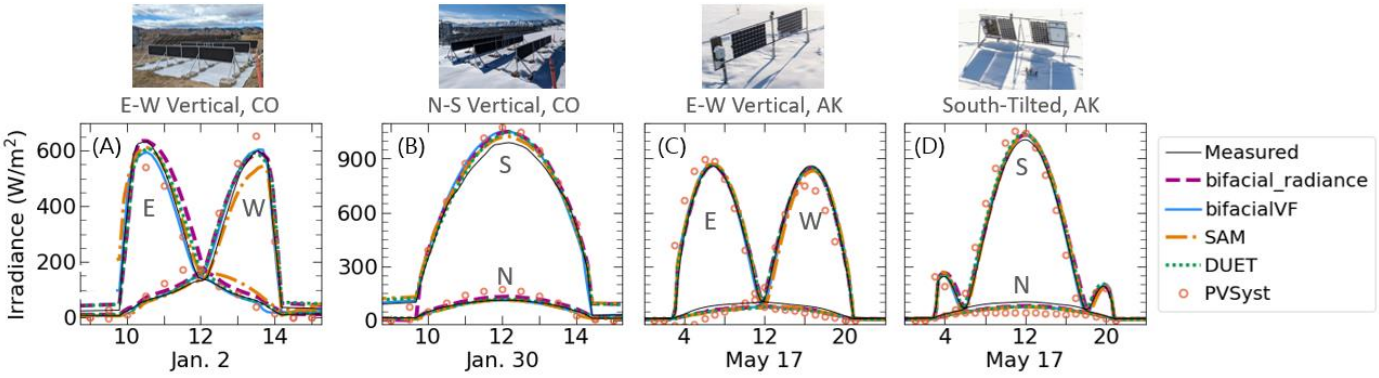

Figure 2. Performance of five bifacial irradiance models during example clear-sky days for (A) the E-W vertical test-site located in Colorado, (B) the N-S vertical test-site in Colorado, (C) the E-W vertical test-site located in Alaska, and (D) the south-tilted test-site located in Alaska. Measured PoA irradiance for each day is given by the solid black lines. Data is provided for both directions and labelled in each subplot.

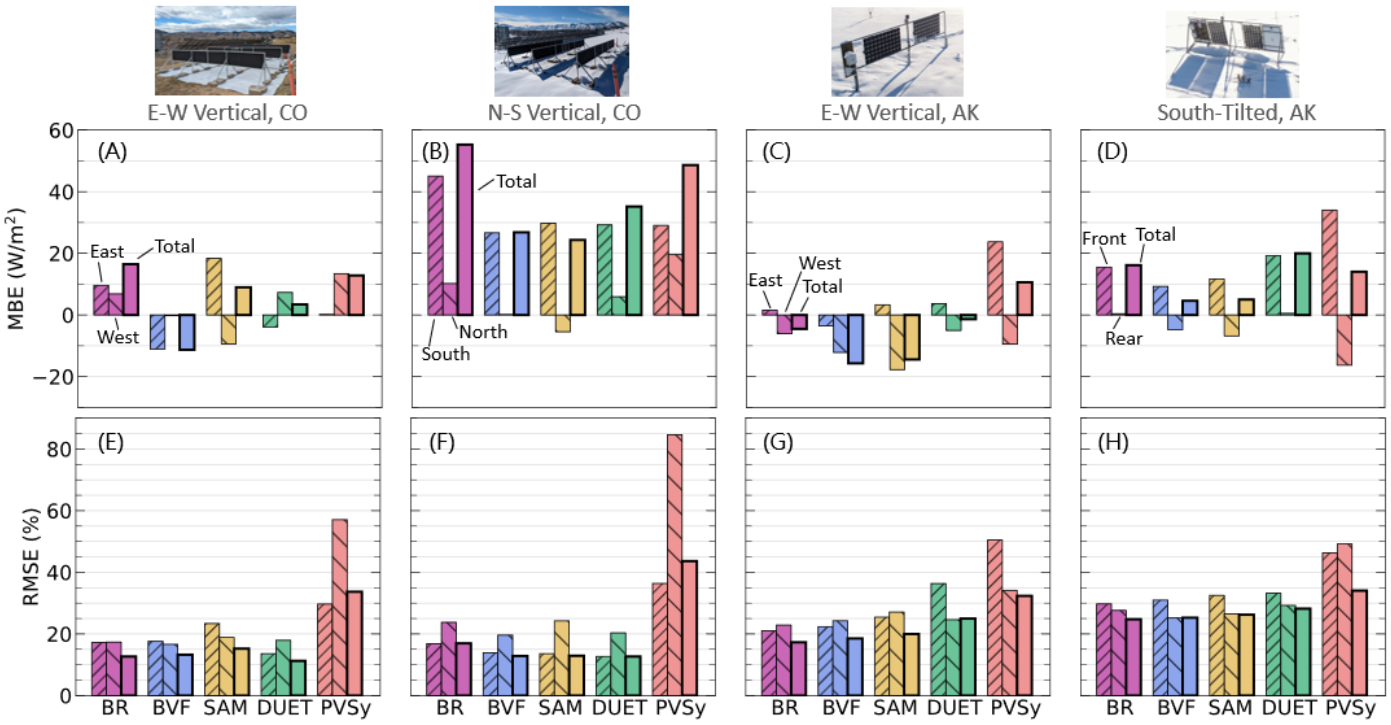

Figure 3. (A-D) Mean bias error and (E-H) root mean square error for the full period of study in each system configuration (no timestamp filtering applied). The system configuration is labelled by the photo and text above each column. Error metrics are calculated separately for each side of the panel, and as a total sum. Bifacial_radiance is abbreviated as BR, bifacialVF is abbreviated as BVF, and PVSyst is abbreviated as PVSy.

summarizes modelling error metrics of (A-D) MBE and (E-H) RMSE for the five bifacial irradiance models and four test-sites over all timestamps. Error metrics are provided for the PoA irradiance for each side of the panel and as a total sum of front PoA irradiance plus rear PoA irradiance. Similar to the clear-sky day example, all models over-estimate south irradiance for the N-S vertical testbed in Colorado and front irradiance for the south-tilted test-site in Alaska. MBE is the highest in the former case, with MBE >25 W/m^2 for all models. Irradiance tends to be under-predicted for the E-W vertical testbed in Alaska and for rear-side irradiance in the south-tilted testbed in Alaska.

RMSE is higher for the test-sites in Alaska compared to Colorado for all models aside from PVSyst. Total RMSE varies from 11-15% for the E-W vertical site in Colorado, 12-17% for the N-S vertical site in Colorado, 16-24% for the E-W vertical site in Alaska, and 24-28% for the south-tilted site in Alaska. PVSyst, on the other hand, experiences similar RMSE in Colorado and Alaska. RMSE for PVSyst falls between 32-44% depending on the location and orientation. This is, in part, due to a lower statistical significance for PVSyst; PVSyst results are computed using a quarter the number of data points as the rest of the models due to hourly time step constraints in v7.4.8. The distribution of residuals has consistently higher standard deviation for PVSyst compared to other models, indicating that the distribution is not as well defined. Further information can be found in the Supplemental Information.

To better understand the effects of environmental conditions on modelling error, we additionally filter timestamps by various conditions. The results of filtering are presented in Figure 4 for (A) the E-W vertical test-site in Colorado, (B) the N-S vertical test-site in Colorado, (C) the E-W vertical test-site in Alaska, and (D) the south-tilted test-site in Alaska. The first column of data in each subplot reproduces the total irradiance RMSE values given by all timestamps, provided in Figure 3. Table 2 describes the percent of total insolation (annual insolation in the case of Alaskan data) included in each filter.

(i) Irradiance Filter

Measured high irradiance (>100 W/m^2) timestamps are filtered from low irradiance (<100 W/m^2) timestamps. The highest calculated RMSE values occur for low irradiance conditions, with RMSE >90% in Alaska and >30% in Colorado. In all cases, considering only timestamps of high irradiance increases model accuracy. These results are not surprising given low irradiance conditions are often associated with low solar elevation or heavy cloud cover, resulting in high angles of incidence, spectral changes, inhomogeneous sky conditions, and in some cases shading from distant objects or the landscape. Despite high RMSE, timestamps with measured irradiance <100 W/m^2 account for ≤5% of total measured insolation (see Table 2).

(ii) Clear-Sky Filter

Timestamps are also filtered by whether the sky is classified as clear. Filtering is accomplished using RdTools coupled with the pvlib detect_clearsky function [25][26]. Measured PoA

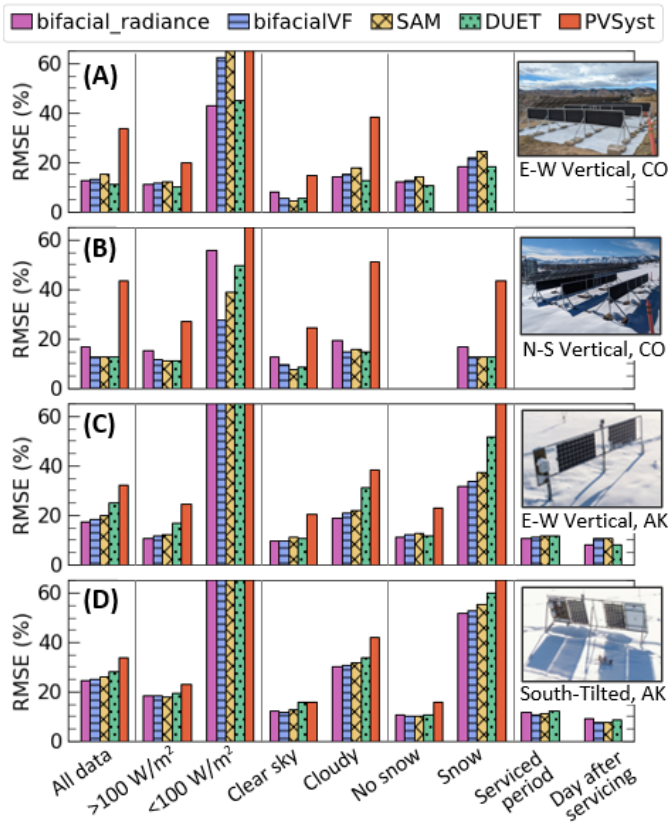

Figure 4. Root mean square error for bifacial_radiance, bifacialVF, SAM, and DUET under varying filtering conditions for the (A) E-W vertical test-site in Colorado, (B) N-S vertical test-site in Colorado, (C) E-W vertical test-site in Alaska, and (D) south-tilted test-site in Alaska. The Alaska test-site and meteorological station was serviced during a subset of the year, outside of the winter season. This period of the dataset is represented by the column labelled 'serviced period'. The N-S vertical system in Colorado was deployed only during winter months, resulting in all data occurring during 'snowy' conditions.

irradiance is compared with the irradiance predicted by a clear-sky model to detect clear-sky timestamps. Timestamps are considered to be 'clear' if the ratio of measured irradiance to modelled clear-sky irradiance is within 10% of unity. In all bifacial irradiance models, clear-sky conditions increase model accuracy. Compared to clear-sky conditions, cloudy RMSE is 2-3× larger in all scenarios.

For the data collection period in Colorado (November through May), clear-sky conditions account for 33% of total insolation. The 28% of total insolation came from clear-sky conditions in Alaska for the full year of data. Generally, cloudy and thus higher error conditions tend to be more prevalent in high-latitude locations on an annual basis.

(iii) Snow Filter

Data is also filtered by the ground condition, with any timestamp with an albedo ≥0.6 considered a snowy timestamp. Due to the addition of the reflective tarp at the Colorado test-site for the winter months, all timestamps for the N-S orientation occur under artificial or real snow conditions. For the E-W vertical configuration in Colorado, roughly half of the experiment takes place under high albedo conditions, leading to 42% of insolation coming from high albedo timestamps. RMSE is 1.4× on average higher in the presence of snow in Colorado for the E-W vertical orientation. In Alaska, where natural ground cover is instead used for a full year of timestamps, the presence of snow causes a significant increase in model error. Model RMSE increases by 3× on average for the E-W vertical array and 5× on average for the south-tilted array. The causes for this increase in error are further explored in Figure 5.

Table 2: Dataset insolation represented by filtering conditions

	Insolation represented by filter (%)		
	<100 W/m²	Clear-sky	Albedo ≥ 0.6
Colorado, EW	2	31	42
Colorado, NS	1	35	100
Alaska	5	28	17

(iv) Site Maintenance Filter

Finally, model error is additionally filtered in Alaska based on the maintenance logs of the test-site. For the period of this study, from Sept. 2019-Sept. 2020, the test-site was serviced roughly weekly between March and October. The column labelled 'serviced period' indicates these months. To examine the effects of sensor cleaning on model error, this servicing period is compared to the day immediately following a service visit. The effect of servicing the meteorological station clearly impacts model accuracy. Model error drops by 14% rel. for the vertical array and 27% rel. for the south-tilted array on average. PVSyst results are not included in this filter due to a low number of data points.

Overall, model error is highest during low irradiance timestamps, cloudy conditions, in the presence of snow, and as more time elapses following meteorological station servicing. These conditions are more common during winter and at high latitudes. Figure 5 demonstrates how MBE in (A) the E-W vertical site and (B) the south-tilted site in Alaska varies for each month of the year. Strong seasonal effects can be seen for vertical and south-tilted systems, with high error from November to March. Increased error over the winter season has also been observed in a relatively southern location of Albuquerque, New Mexico (35°N) [13]. PVSyst significantly over-estimates E-W vertical irradiance between January and April in Alaska, possibly due to high uncertainty caused by assuming monthly average albedos. For all other models, modelled irradiance tends to be underpredicted across most months of the year for the E-W vertical site, which may be related to the Perez sky model under-estimating diffuse irradiance, an effect observed by M. de Simón-Martín *et al.* [27]. On the other hand, modelled irradiance for the south-tilted site tends to overestimate compared to measured irradiance,

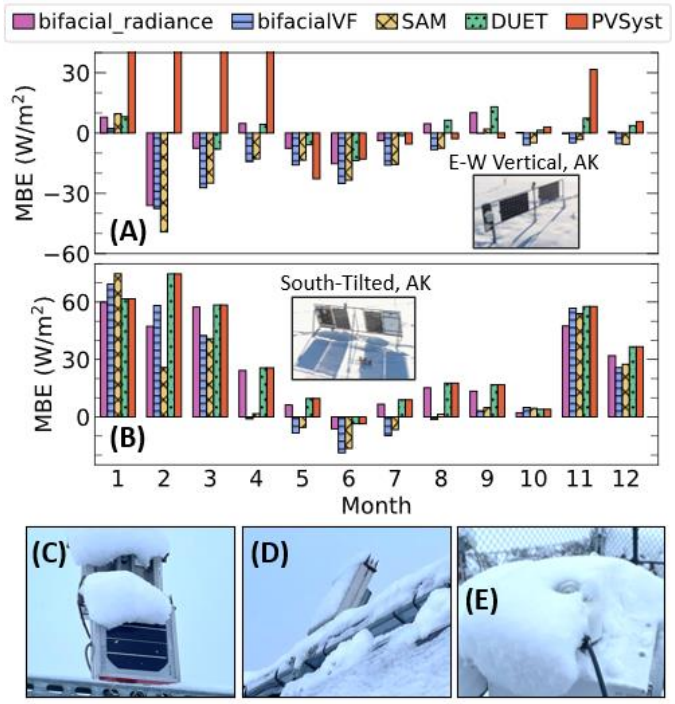

Figure 5. Seasonal mean bias error for (A) the E-W vertical site in Alaska and (B) the south-tilted site in Alaska. Images of snow accumulation for (C) vertical reference cells, (D) south-tilted front-facing reference cell, and (E) a heated pyranometer.

which can be attributed to snow accumulation on south-tilted reference cells.

Images of snow accumulation on sensors are provided in Figure 5 (C-E). Model error in the presence of snow is expected to be higher due to snow accumulation on panels and reference cells, which is not typically accounted for in bifacial irradiance models. Snow accumulation may be modelled by adding a seasonal soiling de-rate factor, or modelled separately with, for example, the Marion snow model [28][29]. As shown in Figure 5E, snow may also accumulate around even heated pyranometers. Therefore, it is interesting that despite possible snow accumulation from the top-down for vertical reference cells (Figure 5C), most of the bifacial irradiance models still under-predict vertical irradiance during winter months, particularly the 2D view factor models.

Figure 6 shows the RMSE of each model in each test-site under 'best case scenario' filtering parameters of irradiance >100 W/m^2, clear-sky conditions, and albedo<0.6 (no snow or reflective tarp present). Overall, the RMSE values are much lower than those in the unfiltered dataset given in Figure 3E-H. Total RMSE in this filtered (unfiltered) dataset varies from 4-12% (11-34%) for the E-W vertical site in Colorado, 8-25% (12-44%) for the N-S vertical site in Colorado, 8-18% (16-32%) for the E-W vertical site in Alaska, and 8-14% (24-34%) for the south-tilted site in Alaska. Thus, when filtering for ideal modelling conditions, model error is comparable between the E-W vertical and south-tilted arrays in Alaska.

B. Model Variation Trends

To expand upon the model validation presented above, we have additionally modelled the annual insolation of a utility-scale (7-row, 21 modules per row) (A) 1-in-landscape vertical E-W array and (B) 1-in-portrait equator-facing fixed-tilt array (latitude-tilt minus 10°) using TMY data in 250 locations using bifacial_radiance, bifacialVF, SAM, and DUET. The locations considered in this study are primarily above 60°N/S (with 6 locations in Antarctica) and are denoted by green circles in Figure 1. Row spacing for each location is determined by the latitude and system type, as developed in Ref. [30]. Total insolation is the sum of east/west or front/rear insolation.

The coefficient of variation Δ_{var} quantifies the spread between model-predicted insolation:

$$\Delta_{var} = \sqrt{\left\{\sum_{j=1}^{M}\left(y_j - \bar{y}\right)^2 / M\right\}} / \bar{y} \qquad (3)$$

where M is the number of models, in this case 4, y is the annual predicted insolation of model j, and $\bar{y}$ is the average predicted insolation of the models. In simple terms, the coefficient of variation is the standard deviation across the bifacial irradiance models, divided by the average.

Figure 7 displays calculated coefficients of variation as a function of location latitude for the (A) E-W vertical array, and (B) equator-facing tilted array. Model discrepancies are higher for vertical arrays than equator-facing tilted arrays. Between 15-50°N/S, the coefficient of variation falls within 3-4% (E-W vertical) and 1.0-1.6% (equator-facing tilted). Above 50°N/S, where more locations are studied, we find a greater spread between model predictions in all three system types, with variation as high as 9%.

These results demonstrate that higher variation amongst model choices should be expected for vertical systems and at high latitudes.

IV. Discussion

Given the modelling error observed in this work for vertical systems and in high latitudes, a few avenues can be recommended for improving model accuracy, outlined below.

(A) Sub-hourly timescale modelling

Generally, sub-hourly timescale resolution provides a more nuanced description of PV performance and can capture more accurately rapid variations in solar resource, which are particularly important for bifacial PV systems [31]. This can also be useful for sufficiently sampling E-W vertical arrays which peak twice over the course of a day. For high latitudes in particular, the ability to model hourly and sub-hourly albedo is critical, as snowy conditions can change significantly from day to day due to melting and accumulating conditions. Monthly-averaged albedo values, as used in PVSyst v7.4.8, will introduce additional uncertainty to PV system modelling in snowy environments [32][33].

(B) Sky model assumptions

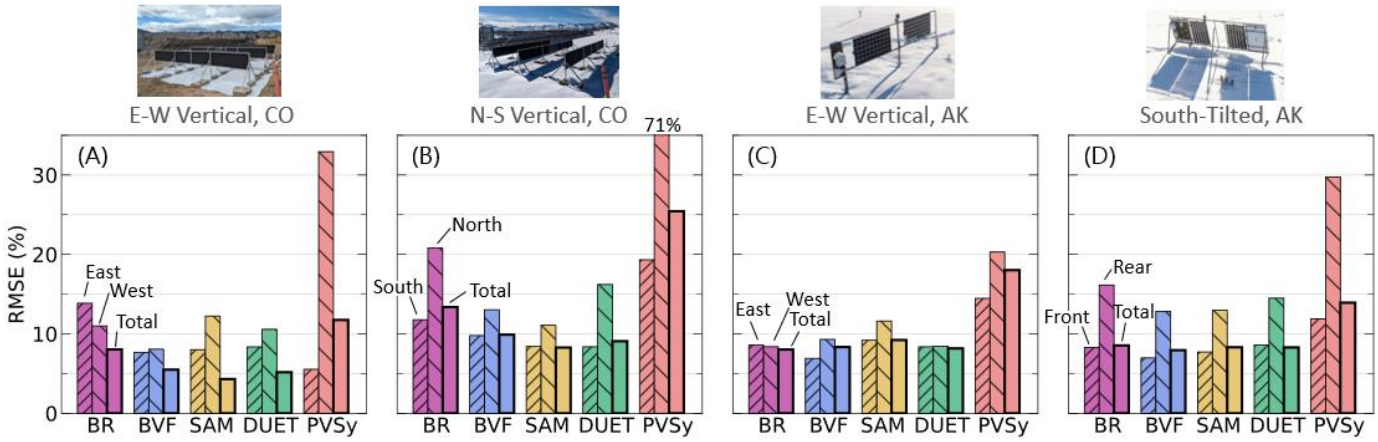

Figure 6. Root mean square error for the (A) E-W vertical system in Colorado, (B) N-S vertical system in Colorado, (C) E-W vertical system in Alaska, and (D) south-tilted system in Alaska with 'best case scenario' filters. These filters are: measured irradiance >100 W/m^2, clear-sky conditions, and without the presence of snow (albedo <0.6). These three conditions are met for 13-19% of all timestamps, depending on the dataset. Error metrics are calculated separately for each side of the panel, and as a total sum. Bifacial_radiance is abbreviated as BR, bifacialVF is abbreviated as BVF, and PVSyst is abbreviated as PVSy.

The 1993 Perez sky luminance distribution model accounts for cloudy conditions by adjusting five general empirical coefficients describing the sky luminance distribution for different sky clearness indexes [23]. These coefficients were determined from a dataset of measured sky scans in Berkeley, California. Bifacial_radiance, bifacialVF, SAM, DUET, and PVSyst use the Perez model. In SAM and PVSyst, users may also use the Hay-Davies-Klucher-Reindl (HDKR) model [34]. For this work, the Perez model is used due to marginally better modelling accuracy compared to the HDKR model.

M. de Simón-Martín *et al*. evaluated 30 solar diffuse transposition models with data measured by pyranometers mounted vertically in the four cardinal directions at the University of Burgos (42°N, 3°W) over eight months [27]. The Perez model was the best-performing parametric model with locally optimized coefficients. Locally optimizing the coefficients rather than using the general coefficients determined in Berkeley, California, significantly improved model accuracy [27]. This indicates that there may be a need for coefficients based on climate classification. Bifacial irradiance modelling error may be improved for vertical systems in Alaska by using empirical coefficients optimized for a high-latitude environment.

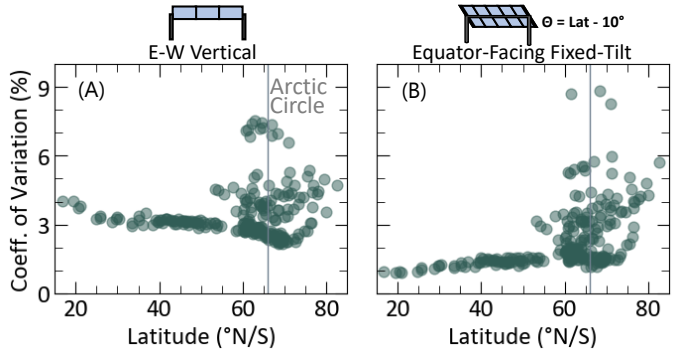

Figure 7. Variation between model predicted insolation for bifacial_radiance, bifacialVF, SAM, and DUET in 250 locations for (A) E-W vertical and (B) equator-facing fixed-tilt bifacial utility scale arrays. The coefficient of variation is calculated using Equation 3. The Arctic Circle is drawn as a vertical line on each plot.

M. de Simón-Martín *et al*. also noted that sky models and, indeed, the modelling of ground-reflected irradiance in bifacial PV models assume isotropic ground reflectance. A natural surface is never perfectly isotropic, and this is particularly true for systems oriented away from the equator and for low solar elevation, leading again to potentially increased error at high latitudes [27]. This effect could be explored further in ray tracing models where specularity can be specified in the simulation. In this work, specularity was set to zero in bifacial_radiance simulations.

(C) Snow monitoring

This study would benefit from continuous monitoring of snow accumulation on reference cells to filter modelling error for conditions when snow is on the ground and reference cells are completely clear, partially, or fully obscured by snow. Modelling error in the presence of snow could then be separately reported for high albedo conditions and for high albedo conditions with sensor obfuscation. This is important to characterize for snow loss studies, where the modelling of PV panels is assumed to be the baseline performance of PV panels, and any deviation from this baseline is attributed to an effect of snow accumulation [28].

(D) Meteorological station servicing

Periodic maintenance of PV systems, rather than responsive maintenance, has been shown to reduce PV module degradation rates [35], and regular cleaning of modules can be economically viable for reducing soiling losses [36]. Maintenance and cleaning of weather station sensors are also required for high-quality monitoring of utility-scale PV plants and experimental PV testbeds. NREL's Best Practices Handbook for the Collection and Use of Solar Resource Data [37], recommends cleaning procedures on the scale of daily to weekly. In this work, we have demonstrated the effect of regular maintenance

and cleaning to have a notable impact on bifacial irradiance model accuracy, decreasing modelling error (RMSE) by up to 30% rel. or 3% abs.

V. Conclusion

In this study, we validated five bifacial irradiance PV models, PVSyst, bifacial_radiance, bifacialVF, the System Advisor Model, and DUET, using test-site data for four PV system configurations in Alaska and Colorado. All models were found to have higher error under the same conditions: low irradiance conditions, clouds, and snow. These conditions are much more prevalent at high latitudes, resulting in increased modelling error in Alaska compared to Colorado. All models were found to overestimate steeply-tilted (≥60° tilt) south PoA irradiance in both Alaska and Colorado. In the Alaska, PoA irradiance was further over-predicted during the winter due to snow accumulation on reference cells. Periods with snow ground cover are critical in Alaska, with 17% of annual insolation occurring during snowy periods. Regular servicing and cleaning of meteorological station sensors and reference cells can decrease model RMSE by up to 30% rel. or 3% abs. We recommend continual snow monitoring, the use of sufficiently high-powered heated pyranometers, and regular meteorological station servicing for high-quality data acquisition in high latitudes. However, site visits during winter can be challenging.

A balance between speed and complexity is necessary when choosing a PV irradiance model. View factor models offer a good compromise between simplicity, speed, and model accuracy. In contrast, a ray tracing model like bifacial_radiance or a finite element model like DUET are preferable for complex situations involving edge effects or nearby obstructions. For E-W vertical PV systems, modelling on a sub-hourly timescale is recommended to sufficiently sample the daily production curve.

We demonstrate that larger error and model variation can be expected for vertical PV systems and at high latitudes. Assumptions about modelling error in one location and system orientation may not be the best representation of performance in other locations or even the same location but with a different design. Larger margins of uncertainty should be used when designing and making financial plans for new northern deployments. This work additionally motivates the need for revisiting model assumptions for vertical and high latitude conditions.

Acknowledgements

The authors would like to extend their gratitude to Byron McDonald and Joshua Parker for their help with testbed design, installation, and data collection in Golden, Colorado. The authors additionally thank Matthew Muller for structural calculations for the vertical testbed in Colorado. A sincere thank you to Tobin Ford, Chong Seok Choi, Heather Mirletz, Daniel Tsvankin, and Gavin Forcade for assisting with shifting the testbed between E-W and N-S orientation. Thank you to Robert Bensin, Daniel Manley, and William Fisher for conducting meteorological station and site maintenance in Alaska during this study. Photos of the sensors provided in Figure 5 were taken by Cole Sudkamp-Walker.

The authors gratefully acknowledge funding support from the Canadian Foundation for Innovation, Ontario Research Fund, and the Natural Sciences and Engineering Research Council of Canada [NSERC CREATE 497981, NSERC STPGP 521894, NSERC CGS-D].

Funding was additionally provided by the Department of Navy award N00014-19-1-2235 issued by the Office of Naval Research.

This work was authored in part by the National Renewable Energy Laboratory (NREL), operated by Alliance for Sustainable Energy, LLC, for the U.S. Department of Energy (DOE) under Contract No. DE-AC36-08GO28308. Partial Funding provided by the U.S. Department of Energy's Office of Energy Efficiency and Renewable Energy (EERE) from the Solar Energy Technologies Office (SETO), under CPS Agreement 38535 and 38258. The views expressed in the article do not necessarily represent the views of the DOE or the U.S. Government. The U.S. Government retains and the publisher, by accepting the article for publication, acknowledges that the U.S. Government retains a nonexclusive, paid-up, irrevocable, worldwide license to publish or reproduce the published form of this work, or allow others to do so, for U.S. Government purposes. The funders had no role in study design, data collection and analysis, decision to publish, or preparation of the manuscript.

The University of Ottawa is located on the unceded territory of the Anishinaabe Algonquin Nation.

Data Availability

The data supporting the findings of this study is available upon request of the authors.

Conflict of Interest

K. Hinzer is the president of Enurgen Inc.

Inclusion and Diversity

One or more of the authors of this paper self-identifies as an underrepresented ethnic minority in science.

Author Contributions

Erin Tonita: Conceptualization, Methodology, Software, Validation, Investigation, Formal Analysis, Data Curation, Writing – Original Draft, Writing – Review & Editing, Visualization. **Silvana Ovaitt**: Conceptualization,

Methodology, Software, Writing – Review & Editing, Supervision. **Henry Toal**: Investigation, Resources, Data Curation, Writing – Review & Editing. **Karin Hinzer**: Writing – Review & Editing, Supervision, Funding Acquisition. **Christopher Pike**: Investigation, Resources, Data Curation, Writing – Review & Editing, Supervision. **Chris Deline**: Conceptualization, Methodology, Software, Writing – Review & Editing, Supervision, Funding Acquisition.

REFERENCES

[1] S. Jouttijärvi, G. Lobaccaro, A. Kamppinen, and K. Miettunen, "Benefits of bifacial solar cells combined with low voltage power grids at high latitudes," *Renewable and Sustainable Energy Reviews*, 161, 112354 (2022). https://doi.org/10.1016/j.rser.2022.112354

[2] C. Pike, E. Whitney, M. Wilber, and J. S. Stein, "Field performance of south-facing and east-west facing bifacial modules in the Arctic," *Energies*, 14(4), 1210 (2021). https://doi.org/10.3390/en14041210

[3] M. R. Khan, A. Hanna, X. Sun, M. A. Alam, "Vertical bifacial solar farms: physics, design, and global optimization," *Applied Energy*, 206, 240-248 (2017). https://doi.org/10.1016/j.apenergy.2017.08.042

[4] S. Reker, J. Schneider, C. Gerhards, "Integration of vertical solar power plants into a future German energy system," *Smart Energy*, 7, 100083 (2022). https://doi.org/10.1016/j.segy.2022.100083

[5] M. Ito, and E. Gerritsen, "Geographical mapping of the performance of vertically installed bifacial modules," in *Proceedings of the 32nd European Photovoltaic Solar Energy Conference and Exhibition*, München, Germany (2016).

[6] S. Guo, T. M. Walsh, and I. M. Peters, "Vertically mounted bifacial photovoltaic modules: A global analysis," *Energy*, 61, 447-454 (2013). https://doi.org/10.1016/j.energy.2013.08.040

[7] S. Bhaduri and A. Kottantharayil, "Mitigation of soiling by vertical mounting of bifacial modules," *IEEE Journal of Photovoltaics*, 9(1), 240-244 (2019). https://doi.org/10.1109/JPHOTOV.2018.2872555

[8] M. H. Riaz, H. Imran, R. Younas, and N. Z. Butt, "The optimization of vertical bifacial photovoltaic farms for efficient agrivoltaic systems," *Solar Energy*, 230, 1004-1012 (2021). https://doi.org/10.1016/j.solener.2021.10.051

[9] Z. Tahir and N. Z. Butt, "Implications of spatial-temporal shading in agrivoltaics under fixed-tilt and bifacial photovoltaic panels," *Renewable Energy*, 190, 167-176 (2022). https://doi.org/10.1016/j.renene.2022.03.078

[10] P. E. Campana, B. Stridh. S. Amaducci, M. Colauzzi, "Optimisation of vertically mounted agrivoltaic systems," *Journal of Cleaner Production*, 325, 129091 (2021). https://doi.org/10.1016/j.jclepro.2021.129091

[11] J. Stein, C. Reise, J. B. Castro, G. Friesen, G. Maugeri, E. Urrejola, and S. Ranta, "Bifacial photovoltaic modules and systems: experience and results from international research and pilot applications," Int. Energy Agency Photovolt. Power Syst. Programme T13-14 (2021). https://doi.org/10.2172/1779379

[12] S. Ayala Pelaez, C. Deline, S. M. MacAlpine, B. Marion, J. S. Stein, and R. K. Kostuk, "Comparison of bifacial solar irradiance model predictions with field validation," *IEEE Journal of Photovoltaics*, 9(1), 82-88 (2019). https://doi.org/10.1109/JPHOTOV.2018.2877000

[13] A. Asgharzadeh, M. A. Anoma, A. Hoffman, C. Chaudhari, S. Bapat, R. Perkins, D. Cohen, G. M. Kimball, D. Riley, F. Toor, and B. Bourne, "A benchmark and validation of bifacial PV irradiance models," in *IEEE 46th Photovoltaic Specialists Conference (PVSC)*, Chicago, IL, USA, 3281-3287 (2019). https://doi.org/10.1109/PVSC40753.2019.8981272

[14] T. Capelle, F. Araya, F. Haffner, J. Sayritupac, and H. Colin, "A comparison of bifacial PV system modelling tools," bifiPV Workshop, Amsterdam (2019). http://npv-workshop.com/fileadmin/layout/images/bifiPV/presentations2019/bifiPV2019-CEA_INES_Capelle.pdf

[15] C. W. Hansen, J. S. Stein, C. Deline, S. MacAlpine, B. Marion, A. Asgharzadeh, and F. Toor, "Analysis of irradiance models for bifacial PV modules," in *IEEE 43rd Photovoltaic Specialists Conference (PVSC)*, Portland, OR, USA, 138-143 (2016). https://doi.org/10.1109/PVSC.2016.7749564

[16] N. Riedel-Lyngskær, D. Berrian, D. A. Mira, A. A. Protti, P. B. Poulsen, J. Libal, and J. Vedde, "Validation of bifacial photovoltaic simulation software against monitoring data from large-scale single-axis trackers and fixed tilt systems in Denmark," *Applied Sciences*, 10(23), 8487 (2020). https://doi.org/10.3390/app10238487

[17] M. Theristis, N. Riedek-Lyngskær, J. S. Stein, L. Deville, L. Micheli, A. Driesse, W. B. Hobbs, S. Ovaitt, R. Daxini, D. Barrie, M. Campanelli, H. Hodges, J. R. Ledesma, I. Lokhat, B. McCormick, B. Meng, B. Miller, R. Motta, E. Noirault, M. Parker, J. Polo, D. Powell, R. Moretón, M. Prilliman, S. Ransome, M. Schneider, B. Schnierer, B. Tian, F. Warner, R. Williams, B. Wittmer, and C. Zhao, "Blind photovoltaic modeling intercomparison: A multidimensional data analysis and lessons learned," *Progress in Photovoltaics: Research and Applications*, 31(11), 1144-1157 (2023). https://doi.org/10.1002/pip.3729

[18] A. C. J. Russell, C. E. Valdivia, C. Bohémier, J. E. Haysom, and K. Hinzer, "DUET: A novel energy yield model with 3D shading for bifacial PV systems," *IEEE Journal of Photovoltaics*, 12(6) (2022). https://doi.org/10.1109/JPHOTOV.2022.3185546

[19] PVSyst Version 7.4.8. Accessed Oct. 2024. https://www.pvsyst.com/

[20] S. Ayala Pelaez and C. Deline, "Bifacial_radiance: a python package for modeling bifacial PV systems," *Journal of Open Source Software*, 5(50), 1865 (2020). https://doi.org/10.21105/joss.01865

[21] B. Marion, S. MacAlpine, C. Deline, A. Asgharzadeh, F. Toor, D. Riley, J. Stein, and C. Hansen, "A practical irradiance model for bifacial PV modules," *in 44th IEEE PVSC*, Washington, DC (2017). https://doi.org/10.1109/PVSC.2017.8366263

[22] System Advisor Model Version 2022.11.21. National Renewable Energy Laboratory. Accessed Nov. 2023. https://sam.nrel.gov

[23] R. Perez, R. Seals, and J. Michalsky, "All-weather model for sky luminance distribution – preliminary configuration and validation," *Solar Energy*, 50(3), 235-245 (1993). https://doi.org/10.1016/0038-092X(93)90017-I

[24] A. Andreas and T. Stoffel, "NREL Solar Radiation Research Laboratory (SRRL): Baseline Measurement System (BMS)," Golden, Colorado (Data), NREL Report No. DA-5500-56488 (1981). http://dx.doi.org/10.5439/1052221

[25] W. F. Holmgren, C. W. Hansen, and M. A. Mikofski, "PVlib python: a python package for modeling solar energy systems," *Journal of Open Source Software*, 3(29), 884 (2018). https://joss.theoj.org/papers/10.21105/joss.00884

[26] M. Deceglie, A. Nag, A. Shinn, G. Kimball, D. Ruth, D. Jordan, J. Yang, K. Anderson, K. Perry, M. Mikofski, M. Muller, W. Vining, and C. Deline, RdTools, version 2.1.7, Computer Software, https://github.com/NREL/rdtools.

[27] M. de Simón-Martín, C. Alonso-Tristán, and M. Díez-Mediavilla, "Diffuse solar irradiance estimation on building's façades: Review, classification and benchmarking of 30 models under all sky conditions," *Renewable and Sustainable Energy Reviews*, 77, 783-802 (2017). https://doi.org/10.1016/j.rser.2017.04.034

[28] M. B. Øgaard, B. L. Aarseth, A. F. Skomedal, H. N. Riise, S. Sartori, and J. H. Selj, "Identifying snow in photovoltaic monitoring data for improved snow loss modeling and snow detection," *Solar Energy*, 223, 238-247 (2021). https://doi.org/10.1016/j.solener.2021.05.023

[29] B. Marion, R. Schaefer, H. Caine, and G. Sanchez, "Measured and modeled photovoltaic system energy losses from snow for Colorado and Wisconsin locations," *Solar Energy*, 97, 112-121 (2013). https://doi.org/10.1016/j.solener.2013.07.029

[30] E. Tonita, A. C. J. Russell, C. E. Valdivia, and K. Hinzer, "Optimal GCRs for tracked, fixed-tilt, and vertical PV systems for latitudes up to 75°N," *Solar Energy*, 258, 8-15 (2023). https://doi.org/10.1016/j.solener.2023.04.038

[31] M. Z. Zapata, K. Lappalainen, A. Kankiewicz, and J. Kleissl, "Comparing solar inverter design rules to subhourly solar resource simulations," *J.*

Renewable Sustainable Energy, 15, 053501 (2023). https://doi.org/10.1063/5.0151042

[32] J. Lopez-Lorente, A. Neubert, and M. Hamer, "Uncertainty considerations in bifacial photovoltaic systems with high albedo seasonality," *IEEE 50th Photovoltaic Specialists Conference (PVSC)*, San Juan, PR, USA, 1-7 (2023). https://doi.org/10.1109/PVSC48320.2023.10359862

[33] S. Ayala Pelàez, C. Deline, B. Marion, B. Sekulic, B. McDanold, J. Parker, M. Monarch, and J. S. Stein, "Ultimate bifacial showdown: 75kW field results," bifiPV Workshop, Virtual (2020). https://www.osti.gov/biblio/1669536

[34] P. Gilman, A. Dobos, N. DiOrio, J. Freeman, S. Janzou, and D. Ryberg, "SAM Photovoltaic model technical reference update," NREL: Golden, CO, USA (2018).

[35] B. Aboagye, S. Gyamfi, E. A. Ofosu, and S. Djordjevic, "Investigation into the impacts of design, installation, operation and maintenance issues on performance and degradation of installed solar photovoltaic (PV) systems," Energy for Sustainable Development, 66, 165-176 (2022). https://doi.org/10.1016/j.esd.2021.12.003

[36] L. Micheli, E. F. Fernández, J. T. Aguilera, F. Almonacid, "Economics of seasonal photovoltaic soiling and cleaning optimization scenarios," Energy, 215(A), 119018 (2021). https://doi.org/10.1016/j.energy.2020.119018

[37] M. Sengupta, A. Habte, S. Wilbert, C. Gueymard, and J. Remund, "Best practices handbook for the collection and use of solar resource data for solar energy applications: third edition," National Renewable Energy Laboratory, Technical Report NREL/TP-550-47465. https://www.nrel.gov/docs/fy21osti/77635.pdf

6.4 Long-term photovoltaic system performance in cold, snowy climates

In cold, snowy locations
PV systems are deployed.
The systems show slow degradation
And long lifetimes can be enjoyed.
.
This study suggests
That low temperatures are beneficial.
However, further northern tests
Are required for conclusions to be official.

❄ ❄ ❄

Scope and impact

As PV costs continue to decline, there is increasing interest in deploying PV plants to help decarbonize northern communities. However, a barrier towards large-scale adoption in northern regions such as Alaska, Canada, and the Nordics, is long-term performance uncertainty under cold climate environmental conditions, including snowfall, freeze-thaw cycles, and low temperatures. This is, in part, driven by limited existing studies on the performance of PV systems in high latitude and alpine regions. In this article, we provide a comprehensive review of published silicon PV degradation and performance loss rates (PLRs) in cold climates of humid continental, subarctic, and tundra Köppen-Geiger climate code classification. As a contrast to previous literature surveys which discuss degradation of PV arrays in northern climates, this survey includes studies from colder Köppen-Geiger climate codes (Dfc & ET) and Photovoltaic Climate Zone (PVCZ) temperature zones (T1-T3), and includes PV sites across the USA, Canada, Poland, Norway, Sweden, Finland, and the Alps mountain range. We additionally present new analysis of three northern PV sites, previously not presented in the literature.

This article has the following novelties:

1. Year-on-year system degradation rates are calculated for four PV systems located >60°N, each with between 5-15 years of field data:
    - A 100 kW fixed-tilt PV array located in Fort Simpson, Canada.
    - Four double-axis tracking PV arrays located in Fairbanks, Alaska.

- Two south-facing fixed-tilt PERC modules located in Fairbanks, Alaska.
- Four E-W vertical SHJ modules located in Fairbanks, Alaska.

2. The sites located at 65°N in Fairbanks, Alaska represent the highest latitude analyzed PV degradation rates to date.

3. Performance metrics of data availability, tracking availability, monthly performance ratio, and specific yield are provided for each of the analyzed PV sites.

4. A compendium of cold climate PV degradation is presented, covering 27 unique PV systems located in cold climates. The distribution of cold climate degradation peaks at -0.1 to -0.2%/year but has a large tail with systems degrading faster than -0.5%/year. The median degradation rates for cold climate PV is -0.33%/year.

5. Statistics are provided, categorizing cold climate PV systems by Köppen-Geiger climate code, PVCZ temperature zone, degradation analysis methodology, system configuration, PV capacity, field exposure, and deployment year.

6. High latitude data limitations are discussed, and degradation mechanisms reported in the literature are discussed.

These results suggest that PV systems in cold climates tend to degrade slower than in warm climates where median degradation rates typically fall between -0.5% to -0.9%/year. As more PV is deployed in northern latitudes, it is important to understand the long-term reliability of PV systems under cold climatic conditions. These results can help identify potential reliability concerns for any location with significant snowfall.

Author contributions

Erin M Tonita As the lead author of this work, I led the literature review and collection and analysis of test-site data in RdTools. I compiled North American test-site data from multiple sources, ran quality assurance tests, cleaned, and merged data files. I analyzed site data and synthesized results from literature. I developed a new routine for analyzing double-axis tracking PV sites in RdTools. I wrote the original manuscript and generated all figures and tables.

Dirk C. Jordan provided training, example scripts, and guidance on the running of year-on-year analyses with RdTools. He also provided literature references and analysis from prior work involving cold climate PV locations for roughly half of the locations presented in the

compendium. He provided supervision and research direction throughout the research project. He reviewed and edited the manuscript.

Silvana Ovaitt led the conceptualization of this research project, alongside Dirk Jordan. She supervised the development of the manuscript, and provided connections to ACEP and the Cold Climate Housing Research Center, now known as NREL's Alaska campus. She reviewed and edited the manuscript.

Henry Toal provided PV site data for the ACEP deployment in Fairbanks, including module-level data streams and weather files. He provided regular feedback on the development of the manuscript.

Karin Hinzer supervised the research efforts at the University of Ottawa and provided funding. She reviewed and edited the manuscript.

Christopher Pike supervised the data collection and maintenance of the ACEP vertical and south-tilted PV site in Fairbanks. He helped conceptualize and develop Section 4.1 of the paper on site data and tracking availability. He reviewed and edited the manuscript.

Chris Deline supervised this research project at NREL and provided project funding. He reviewed and edited the manuscript.

Copyright

E. M. Tonita, D. C. Jordan, S. Ovaitt, H. Toal, K. Hinzer, C. Pike, and C. Deline, "Long-term photovoltaic system performance in cold, snowy climates," Submitted for publication August 22, 2024. Revision submitted January 13, 2025.

Long-term photovoltaic system performance in cold, snowy climates

Erin M. Tonita[1,*], Dirk C. Jordan[2], Silvana Ovaitt[2], Henry Toal[3], Karin Hinzer[1], Christopher Pike[3], and Chris Deline[2]

[1] SUNLAB, University of Ottawa, Ottawa, ON, Canada
[2] National Renewable Energy Laboratory, Golden, CO, USA
[3] The Alaska Center for Energy and Power, University of Alaska Fairbanks, Fairbanks, AK, USA

Abstract

As countries around the world transition towards renewable energy, there is increasing interest in using photovoltaic (PV) technologies to help decarbonize northern and alpine communities due to their scalability and affordability. However, a barrier to large-scale adoption of PV in cold climates is long-term performance uncertainty under snowfall, freeze-thaw cycles, low temperatures, and high winds. In this work, we provide a comprehensive review of published silicon degradation rates in cold Köppen-Geiger climate classifications of Dfb (humid continental), Dfc (subarctic), and ET (tundra). We first analyze the system degradation rates of three ground-mounted photovoltaic sites >60°N in North America using the RdTools year-on-year method: an Al-BSF double-axis tracking site in Fairbanks, Alaska (65°N); a PERC and silicon heterojunction bifacial vertical and south-tilted site in Fairbanks, Alaska; and a PERC south-facing fixed-tilt site in Fort Simpson, Northwest Territories (62°N). Degradation rates of these newly analyzed sites vary between −0.4%/year to −1.5%/year. Combining this data with previously reported cold climate degradation rates, we show that the distribution of cold climate degradation peaks at −0.1 to −0.2%/year but has a large tail with rates above −0.5%/year. The average reported cold climate degradation rate is −0.45%/year, while the median value is −0.33%/year. These results suggest that despite exposure to high snow loads and frequent freeze-thaw cycles, PV systems in cold climates tend to degrade slower than PV systems in warmer climates due to the benefits of operating at cooler temperatures. The limited sample size of reported degradation rates in cold climates (27) motivates the need for further data acquisition and monitoring efforts as new technologies are deployed.

KEYWORDS
High latitude; photovoltaics; degradation; performance loss; performance ratio; specific yield; polar; continental.

*Correspondence
Erin Tonita, University of Ottawa, 25 Templeton Street, Ottawa, ON K1N 6N5, Canada.
Email: etoni044@uottawa.ca.

1 | INTRODUCTION

Photovoltaic (PV) systems have been deployed in high latitude and mountainous regions as early as the 1980s to provide clean, distributed, and scalable energy for buildings and equipment[1,2]. However, it is only in recent years that the cold climate PV market has begun to see regular PV deployments >100kWp in these climatic regions with total regional installed PV capacities in the few to hundreds of MWp range[3-8]. PV systems are being deployed in diverse configurations in high latitudes and altitudes, including in rooftop residential applications[9], building-integrated applications[10,11], hybrid microgrids[12,13], and centralized grids[14]. Integration of PV into cold climate infrastructure can reduce electricity bills[12,15], offset diesel consumption and associated greenhouse gas emissions[15,16,17,18], peak shave[17], offer dual-land purpose[11,19], and prepare existing grids for growing electricity demand[20].

Cold climates are known for their low ambient temperatures, moderate to high seasonal snowfall, frequent freeze-thaw cycles, and, in the case of high-latitude cold climates, strong seasonal variations in solar resource. All of these effects may impact the long-term performance of PV systems in cold climates.

Cold climate operating conditions primarily exert mechanical stresses on PV modules. For example, snow and ice accumulation on PV arrays exerts a load that is typically non-uniform, irregular in frequency, can last for up to months at a time[21,22], and is difficult to measure[22,23]. Snow load can lead to cell cracking, while moisture ingress from melt can lead to delamination and corrosion[21]. Additionally, snow removal practices can cause damage to module surfaces, leading to potential module breakage[24]. Snow also acts as a soiling mechanism for PV modules, leading to potentially higher

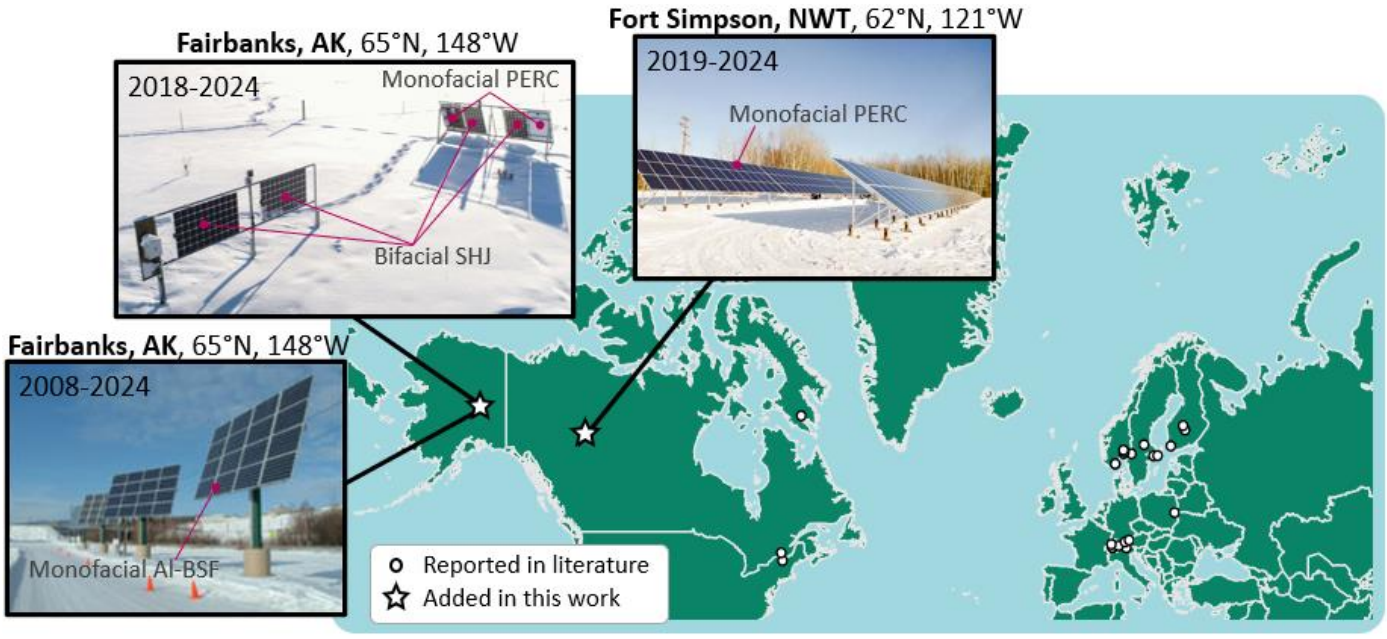

FIGURE 1. Locations of PV sites discussed in this work. Newly analyzed PV systems are pictured and denoted by stars. Silicon PV systems located in cold climates (Köppen Geiger climate codes of Dfb, Dfc, and ET) which have published degradation rates for ≥3 years of field exposure are given by the circles on the map. Previous studies primarily analyze PV in the Nordic countries and in the European Alps.

reported performance loss rates (PLRs) in regions with regular seasonal snowfall.

Temperature also plays a role in panel durability. Schneller *et al*. have shown that a single exposure to −40°C can permanently reduce the fracture strength of crystalline silicon (c-Si) cells[25]. Other components of the PV system may also experience failures outside of their rated temperature zones. For example, PV materials such as encapsulants and backsheets may experience a glass transition in cold climates[26]. Kempe *et al*. measured a glass transition temperature of ethylene-vinyl acetate (EVA) at −15°C [27], while Blieske *et al*. quoted a glass transition temperature for EVA of −35°C [26]. Variations between EVA polymers and additives can cause discrepancies in glass transition temperatures. Cell connectors have also been found to be susceptible to failure during cold temperature thermal cycling down to −40°C [28].

Despite mechanical weakening under exposure to cold temperatures, cold operating temperatures generally benefit PV system performance and reliability. For example, maximum power temperature coefficients of c-Si modules today typically lie in the range of −0.25%/°C to −0.40%/°C, causing photovoltaic energy conversion efficiency to increase for colder temperatures[29]. For example, a silicon solar panel that operates at 20% efficiency at 25°C with a −0.3%/°C temperature coefficient will have an efficiency of 22.1% at −10°C. Moreover, cold environments will suppress major thermally-activated degradation processes, such as mechanisms related to chemical reactions and diffusion[30].

Cooler, high-latitude climates are also associated with lower solar elevation angles, resulting in increased atmospheric absorption of ultraviolet light (UV). UV-induced degradation mechanisms, such as encapsulant discoloration, will be less common at high latitudes[31], but could still occur in alpine climates[32].

Previous reviews of PV performance around the globe have examined the effects of climate type on module degradation rates and/or system performance loss rates. Climate-dependent conditions including temperature, solar radiation, humidity, precipitation, and wind can all influence PV module degradation[32,33,34]. Several studies have been published which analyze PV module degradation in hot and humid, hot and dry, and warm and temperate climates[32], with degradation rates ranging around −0.75 to −1.2%/year[35,36,37,38]. However, existing literature on PV degradation and PLR in cold climates is relatively limited, especially for subarctic and arctic tundra climates.

In 2020, Jordan *et al*. analyzed 100,000 PV systems in the continental USA, with just under 9% of these sites experiencing significant winter snowfall[39]. In 2022, Jordan *et al*. analyzed PLR for sites deployed in the continental USA and separated results by temperature zone, finding slower PLR for the coolest USA temperature zone that had significant PV system data[35]. The coolest temperature zone PV arrays degraded with a median rate of −0.48%/year, compared to two other hotter climate zones (−0.78%/year and −0.88%/year). The coolest temperature zone roughly corresponded to the northern third of the continental USA, excluding continental Alaska, mountainous regions, and many regions close to the Northern border with Canada[40].

Bogdanski *et al*. analyzed degradation rates of PV modules in 4 sites with different climates: a warm, moderate climate, arid climate, tropical climate, and a cold, high-mountain climate, finding the fastest maximum power degradation rate for the cold mountain climate of −2.0%/year[41]. Dhimish *et al.*

calculated the degradation rates of seven PV sites in the United Kingdom, finding degradation rates between −0.4%/year to −1.0%/year and reporting issues related to hoarfrost, hotspots, microcracks, and glass damage[42]. Ascencio-Vasquez *et al*. calculated degradation rates worldwide according to Köppen-Geiger climate classification zones[43] considering three degradation mechanisms: hydrolysis degradation, photo-degradation, and thermo-mechanical degradation[44]. All three degradation mechanisms were found to be reduced in cold climates, resulting in the lowest predicted degradation rates occurring in cold and polar climates with average predicted degradation rates of −0.2%/year. However, the authors warned that these calculations do not include external effects like snow and wind, which may cause increased degradation rates and PLRs in practice[44]. Finally, Jordan *et al*. reported a median degradation rate of −0.35%/year (−0.62%/year average) for 39 PV systems and sub-strings in snowy climates with x-Si technology (a-Si, c-Si, etc.)[36].

In this work, we analyze the degradation rates of four diverse PV systems located at three sites above 60°N in Alaska and Northern Canada, each with ≥5 years of hourly or sub-hourly data. We analyze the degradation rates of the PV systems using a robust year-on-year degradation methodology, which can handle the strong seasonal variation present at high latitudes[20,45]. Finally, we include these degradation rates in a compendium of published PV degradation rates in cold climates with either Dfb, Dfc, or ET Köppen-Geiger climate codes. We limit our study to only multi-crystalline silicon (mc-Si) and c-Si technologies with ≥3 years of outdoor field exposure.

2 | PHOTOVOLTAIC SITES

Figure 1 shows a map of the three PV sites studied in this work alongside locations of existing degradation rate studies in cold climates detailed in the compendium (Section 5). Each PV system is described in detail in the following sections. Together, these PV systems represent the three highest latitude PV sites analyzed for degradation to-date and the first two instances of PV degradation analysis in Alaska. In addition, we present the first long-term performance analysis of a double-axis tracking PV system located in a subarctic Dfc climate. Environmental conditions at these three sites are summarized in Table S1 of the Supplemental Information.

2.1 | Fort Simpson, Canada

The analyzed array in Fort Simpson, Canada (61.9°N, 121°W) consists of a 100 kW ground-mounted fixed-tilt array at a tilt of 35° and an azimuth of 190°. The array, maintained by the Northwest Territories Power Corportation[46], was installed in two phases starting in 2012 and completed in February of 2013 and consists of 258 Conergy ON 235P-235 modules and 178 Conergy ON 245P-245 modules. AC Power data is retrieved at the inverter level for the whole array (inverter model Enphase M215 208 V).

Meteorological data collection of module temperature, plane-of-array (PoA) irradiance, and global horizontal irradiance (GHI) began in 2017. Wind speed and ambient temperature are collected at a nearby airport weather station (Fort Simpson A, Climate ID 2202103). Measured power, energy, and meteorological data is at a resolution of 15 minutes and covers six years, from 2017−2023. Thermopile, PoA, and GHI pyranometers are calibrated yearly at the site. Snow is removed periodically in March from the array.

2.2 | Fairbanks, USA – Fixed-tilt

The ground-mounted south-facing and east-west vertical fixed-tilt site in Fairbanks, Alaska (64.8°N, 147.7°W) consists of 6 modules, each connected to an Enphase IQ6 microinverter. PV production is measured on the AC side. The east-west vertical modules and two of four south-facing 60° tilted modules are silicon heterojunction (SHJ) modules, Sunpreme Maxima GxB-310 with 94% bifaciality. The remaining two south-facing tilted modules are monofacial passivated emitter rear-contact (PERC) modules, Suniva OPT270-60-4-1B0. All modules were flash-tested before outdoor exposure, with the average maximum power under standard test conditions of the bifacial and monofacial modules being 288 W and 251 W, respectively. The Alaska Center for Energy and Power of the University of Alaska, Fairbanks, maintains the array. Further details on the site, including a performance comparison of east-west vertical to south-tilted modules, can be found in Ref. 47.

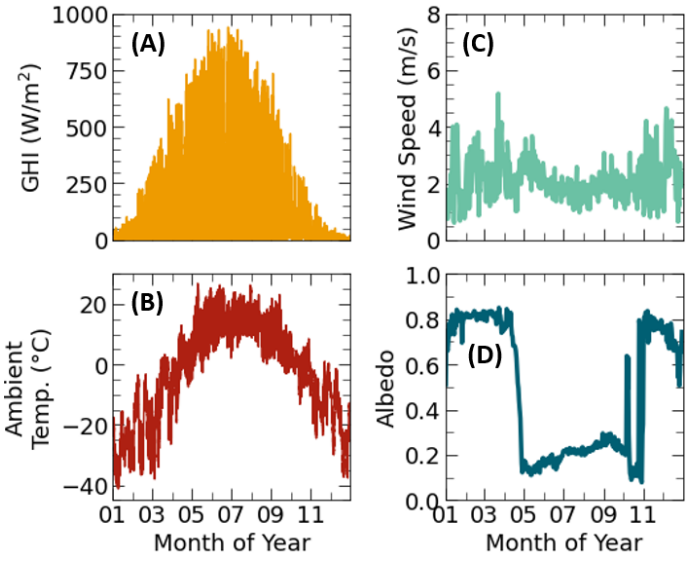

FIGURE 2. An example year of meteorological station data for the fixed-tilt Alaskan array of 6 modules. (A) Measured GHI, (B) ambient temperature, (C) wind speed, and (D) albedo. Data has been shifted to accommodate a full year without data gaps; August-December months come from 2019 and January-July from 2020. To better show the wind speed and albedo values, daily averages are plotted.

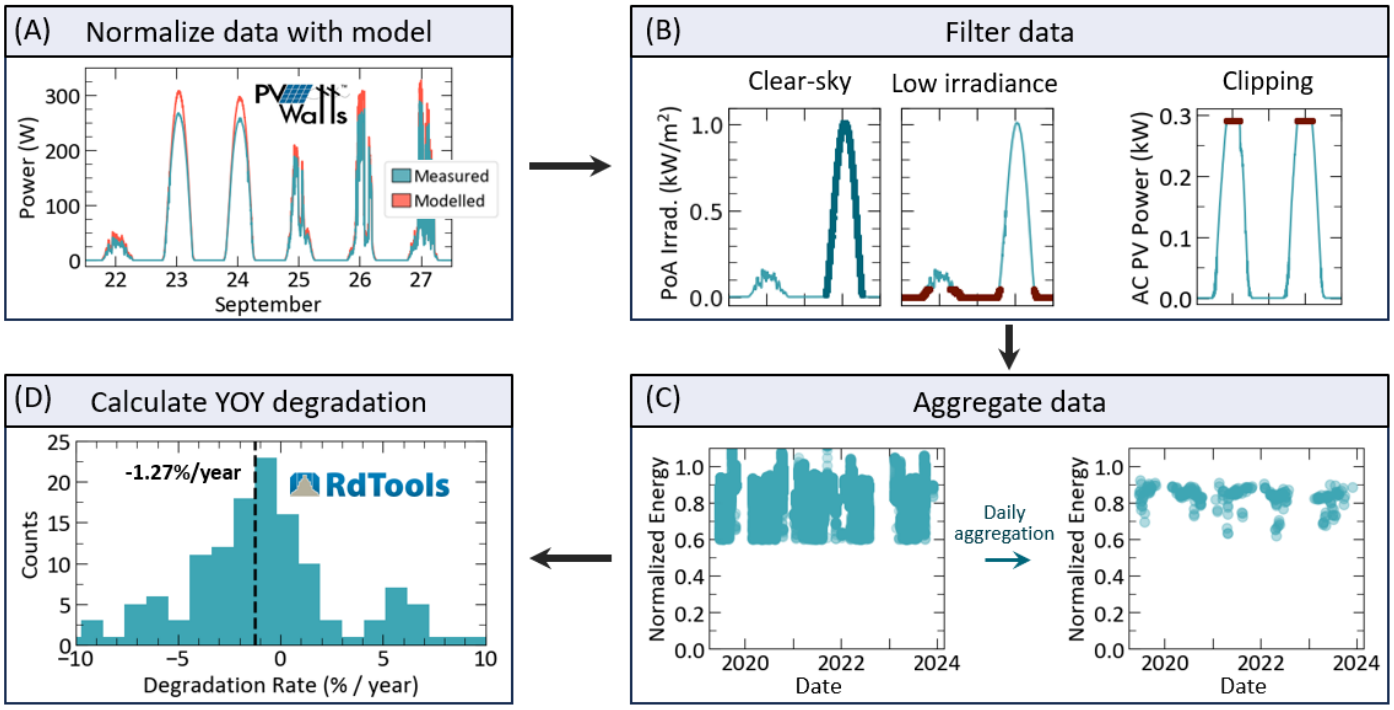

FIGURE 3. Schematic outlining the main four steps in the year-on-year degradation methodology: (A) normalization, (B) data filtering, (C) data aggregation, and (D) the calculation of degradation rate distribution. YOY=year-on-year.

Meteorological and PV production data has been collected at 1-minute resolution for five years from 2019−2024. Ambient temperature, wind speed, albedo, GHI, and PoA irradiance are measured on-site. An example year of meteorological data for this site is provided in Figure 2, demonstrating strong seasonal effects for GHI (Fig. 2A), ambient temperature (Fig. 2B), and albedo (Fig. 2D). The site and meteorological station are serviced on a roughly weekly schedule.

2.3 | Fairbanks, USA – Double-axis tracking

A second ground-mounted site in Fairbanks, Alaska, is analyzed in this work. This site consists of four double-axis trackers commissioned in 2007 by the Cold Climate Housing Research Center (CCHRC), now known as the National Renewable Energy Laboratory (NREL) Alaska Campus. The arrays have been continuously monitored at an hourly resolution since their commissioning, resulting in 16 years of data from 2008−2024. Data for this site is publicly available and can be found at Ref. 48. For this analysis, we only analyze 3 of the 4 arrays, neglecting the array which has an experimental design combining mc-Si cells with concentrating optics.

Each of the three studied trackers consist of 16 modules and are referred to as Array 1 through 3 in this work. Array 1 and Array 2 consist of SolarWorld 165 mc-Si modules with a rated power of 2640 W each. Array 3 uses Sharp 170 mc-Si modules with a rated power of 2720 W. These arrays were originally constructed to demonstrate the difference in energy payback periods for double-axis trackers compared to south-facing fixed-tilt trackers. A direct comparison between Array 1 and Array 2 was done for this purpose[49], with Array 1 performing double-axis tracking and Array 2 purposefully fixed to a south-facing tilt for the first two years of operation. After this experiment, all arrays were set to perform double-axis tracking, except for winter months, where the arrays are south-facing at a fixed-tilt (roughly October through March each year).

PV production data is collected from 3 SMA Sunny Boy inverters. Module temperature and PoA irradiance are collected on site, while wind speed and ambient temperature are measured at a nearby rooftop meteorological station. Due to long-term data quality issues with the available AC power data, the following degradation analysis is completed using measured AC current. This should introduce only modest uncertainty, to the extent that grid voltage remains stable over the measurement period.

3 | YEAR-ON-YEAR METHODOLOGY

To analyze the degradation rates of the three PV sites, the open-source python-based package RdTools is used[50]. This tool uses a year-on-year methodology to calculate PV array degradation and statistics. This method calculates a system degradation rate that excludes certain performance factors, but includes others. To achieve a relatively stable performance estimate, system production is corrected for solar resource and module temperature. Exogenous factors such as grid and maintenance outages are removed. Module degradation driven by changes in chemical composition, cell cracking, and permanent soiling are retained. System degradation losses such as other DC health degradation (string or module failures)

and tracker errors are also typically retained. RdTools attemps to remove snow loss effects described further in this section. Thus, as RdTools output includes some performance loss factors and excludes others such as outages, clipping, and seasonal shade or soiling losses, it has been suggested that it doesn't match other definitions of system PLR[51]. We therefore provide some specifics of the analysis process here.

The RdTools year-on-year methodology relies on four main steps: data normalization, data filtering, data aggregation, and, finally, calculation of year-on-year degradation. Figure 3 shows a schematic representation of each of these steps using data for a bifacial SHJ south-facing tilted module in Fairbanks, Alaska.

First, data is normalized against a PV energy yield model, PVWatts[52], to account for changes in temperature and solar insolation from year to year using inputs of measured PoA irradiance, module temperature, the module temperature coefficient, the nameplate DC power, the array longitude and latitude, location time zone, and PV array orientation and tilt. Year-to-year variation from changes in solar spectral content and albedo is not captured by this model. An example of the measured versus PVWatts modelled module power is displayed in Figure 3A for a few days in September of 2019.

Data is then filtered to only include clear-sky timestamps using a built-in function *detect_clearsky* in pvlib[53,54]. Effectively, measured PoA is compared to a clear-sky model with moving windows where a point is judged clear-sky if agreement is reached within specific tolerances[55]. Next, any clipping events are filtered from the data by removing data points where output power is within 99% of the maximum measured power. Low irradiance timestamps <50 W/m^2 are then removed. A range of low irradiance cut-offs have been recommended in the literature[20,45,56]. Karttunen *et al*. observed that an irradiance cut-off of 200 W/m^2 would exclude >50% of their measured datapoints in Turku, Finland, limiting seasonal analysis and potentially decreasing PLR accuracy. Thus, for this work where PV arrays are located above 60°N, we select an irradiance cut-off of 50 W/m^2. Finally, data where PV system energy yield is <60% of the model-predicted energy yield is removed from the analysis. This filters out significant snow accumulation events, shading from nearby objects, and PV system outages.

Data is then aggregated to daily irradiance and temperature-weighted averages to reduce high error data from morning and evening timestamps. This step is visualized in Figure 3C. Data aggregation has been shown to reduce degradation rate calculation uncertainty[45].

Finally, the year-on-year degradation rate is calculated by comparing daily aggregated values from year-to-year, resulting in the distribution of degradation rates as shown in Figure 3D. We report the average of this distribution as the long-term degradation of the system.

As it has been shown that diffuse fraction increases with latitude in the United States and Canada[57]. Thus, clear-sky filtering in RdTools in high latitude regions results in fewer daily aggregated points and higher degradation rate uncertainties. Calculating the system's year-on-year degradation rate after more years of field exposure will compensate for this data loss. Overall, the year-on-year method is robust to seasonal changes and data outliers and has the benefit that it does not rely on the need to flash test modules in potentially remote areas where access to specialized testing equipment may be limited. Thus, this algorithm is an appropriate choice for assessing PV system degradation rates in cold climates when sufficient field data is present.

4 | RESULTS

Here, we report on site data availability, tracking availability, specific yield, and year-on-year degradation for each new high latitude PV site introduced in Section 2 and visualized in Figure 1. We have additionally calculated average monthly performance ratios for these PV systems, which is presented in the Supplemental Information.

4.1 | Site Availability and Tracking Availability

Table 1 outlines the availability of site power data and site meteorological station data for the duration of the data acquisition periods. Availability is calculated as the number of timestamps with data divided by the number of timestamps within the data acquisition period. Meteorological station availability is determined by the lowest value between essential temperature and irradiance variable availability.

Since power and weather data from Fort Simpson for the south-tilted array were provided together, the availability of data is the same for both site data and meteorological data at 91%. For the east-west vertical and south-facing fixed-tilt site in Fairbanks, site data availability is 95%, while meteorological

TABLE 1. Summary of site power and meteorological data availability.

Site	Years in Operation	Data Resolution	Site Data Availability (%)	Met. Station Availability (%)
Fort Simpson, Canada South fixed-tilt array	6	15-minute	2001 days/ 2191 days = **91**	2001 days/ 2191 days = **91**
Fairbanks, USA Fixed-tilt modules	5	1-minute	1572 days / 1656 days = **95**	1391 days / 1656 days = **84**
Fairbanks, USA Double-axis tracker heads	16	1-hour	5326 days / 5582 days = **95**	3653 days / 5582 days = **65**

TABLE 2. Summary of annual Alaskan double-axis tracking site tracker availability. Tracking is disabled in the winter, leading to a maximum annual availability of 61%.

	Double-Axis Tracking Availability (%)	
	Annual	Non-Winter Months
Array 1	51	86
Array 2	43	63
Array 3	37	48

station availability is 84%. Since 2008, the double-axis tracking site in Fairbanks has had a data availability of 95%, and a meteorological station availability of 65%. Data gaps primarily occur from 2014–2018 for the PoA sensors. There was an additional loss in data around 2015–2017 in wind speed and ambient temperature. This data loss may be due to issues with long-term maintenance of the site database.

We additionally report on the availability of the tracking system for the double-axis tracking site in Fairbanks over the past 16 years in Table 2. The azimuth and elevation of each tracker were monitored throughout the study with the same data availability as the meteorological station. When the arrays are not tracking, each tracker is fixed to an azimuth of between ~150–180° and a tilt of ~60–74°. Array tracking is disabled each year from roughly October through March to reduce reliability concerns with moving parts during the winter months. Given this constraint, the best annual tracking availability possible is 61% of the year. When tracking is enabled, the double-axis tracking arrays successfully tracked the sun between 48-86% of the time, depending on the array. Array 3 experienced a tracking failure in 2019 and has not been tracking since, resulting in an annual tracking availability of 48%.

4.2 | Specific Yield

Figure 4 shows the calculated annual specific yield from each site in each configuration. Specific yield is calculated as the yearly average energy produced by the PV array divided by the rated power. For the east-west vertical and south-tilted site in Fairbanks (Figure 4A), bifacial east-west vertical panels and bifacial south-tilted panels have comparable performance with a specific yield of ~1200 kWh/kWp. These two bifacial configurations have a gain in energy yield of between 27–34% annually compared to the monofacial modules.

The annual specific yield for the dual-axis tracking site in Fairbanks is given in Figure 4B for fixed-tilt and dual-axis tracking configurations. These values are calculated using the annual energy yield for the first two years between Array 1 and Array 2, as reported in Ref. 49. Double-axis tracking leads to a 41% increase in annual energy yield, which is interestingly the same value reported by Burnham *et al*. for a double-axis tracking site located at 44°N in Vermont[58].

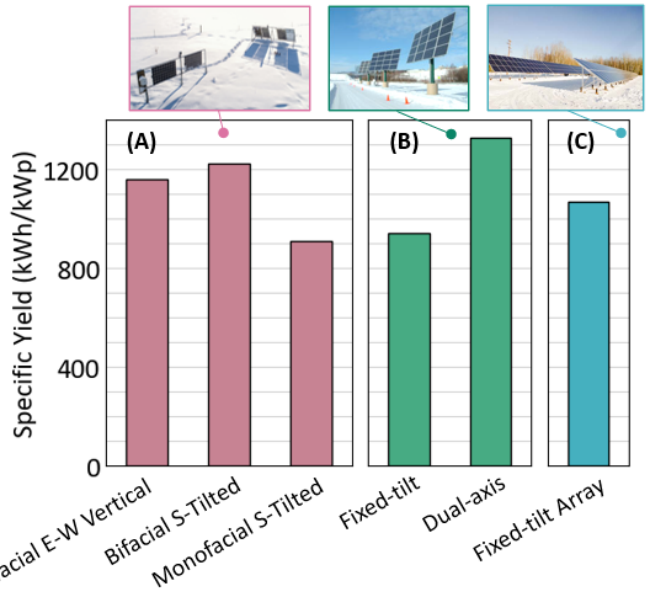

FIGURE 4. Specific yield for the various configurations at each site. (A) Average specific yield for pairs of modules in bifacial east-west vertical, bifacial south-tilted, and monofacial south-tilted configurations in Fairbanks, Alaska. (B) Specific yield of Alaskan double-axis trackers Array 1 and Array 2 from 2007-2009 when in south-facing fixed-tilt and dual-axis tracking modes. (C) Specific yield of the monofacial south-tilted site in Fort Simpson, Canada.

The specific yield of the monofacial south-tilted site in Fort Simpson is 1067 kWh/kWp, visualized in Figure 4C.

4.3 | Year-on-Year Degradation Rates

Finally, degradation rates are calculated for each site using the methodology outlined in Section 3. A degradation rate is calculated per module in the east-west vertical and south-tilted Fairbanks PV site, per tracker in the double-axis tracking Fairbanks PV site, and for the overall fixed-tilt PV array in Fort Simpson.

Figure 5 shows the degradation rate calculated for (A) the fixed-tilt site in Fairbanks, (B) the double-axis tracking site in Fairbanks, and (C) the fixed-tilt site in Fort Simpson. A dashed line is provided at a rate of zero. Each data point is provided with error bars given by a 68.2% confidence interval. Degradation rates are averaged and provided at the bottom of Figure 5.

For the fixed-tilt site in Fairbanks (Figure 5A), we average degradation rates for the bifacial SHJ modules and the monofacial PERC modules separately. With this small sample size (4), there is no clear difference between modules of the same type oriented either vertically (P1, P2) or south-tilted (P3, P4). As a contrast, the bifacial SHJ modules do appear to be degrading faster than the monofacial PERC modules in

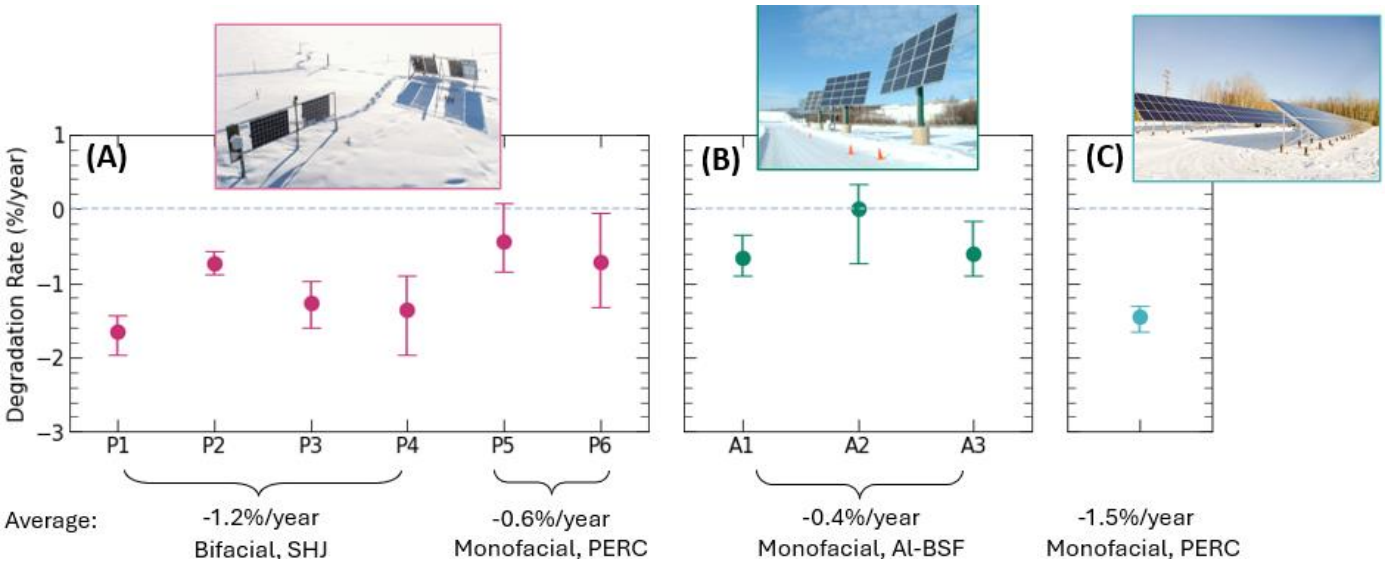

FIGURE 5. Year-on-year degradation rates for (A) east-west vertical (P1, P2) and south-tilted (P3-P6) modules in Fairbanks, Alaska; (B) double-axis tracking arrays in Fairbanks, Alaska; and (C) the fixed-tilt array in Fort Simpson, Northwest Territories. Error bars are given by a confidence interval of 68.2% for each data point.

Fairbanks. The PERC modules are degrading on average by −0.58%/ year compared to −1.25%/year for the SHJ modules. Monofacial PERC degradation rates are reported to typically fall between −0.5 to −0.9%/year[39,61]. Thus, the degradation observed in Fairbanks is in the lower range of typical observations. For SHJ cell technologies, a literature survey on SHJ module reliability reported a median degradation rate of −0.8%/year, with most data falling between −0.5 to −1.0%/year[60]. While the Fairbanks SHJ modules (Sunpreme GxB 310) are degrading faster than this range at -1.25%/year, the degradation rates of similar modules (Sunpreme HxB 400) in a warmer climate have been degrading quicker at a rate of −1.9%/year[62]. Further studies on new bifacial SHJ modules are recommended in other climate zones to determine the impact of climate on observed degradation.

The double-axis tracking arrays in Fairbanks are degrading on average at a rate of −0.4%/year in AC current (Figure 5B). There have been some noted observations of glass damage to the modules caused by the impact of gravel from the nearby gravel road. In remote locations where gravel roads are common, it is recommended to provide greater distance between PV arrays and roads.

In Fort Simpson (Figure 5C), the array degradation is found to be −1.5%/year. Since data is collected and analyzed on the AC side of the inverter, this degradation rate may include degradation from inverter electronics.

The degradation rates determined in this section demonstrate a diversity in PV system configuration in cold climate locations, system age, technology, and ultimately a diversity in degradation, with PV systems degrading between −0.4 to −1.5%/year.

5 | COMPENDIUM OF COLD CLIMATE DEGRADATION RATES

Here, we review existing literature on the degradation of mc-Si and c-Si PV systems located in Köppen-Geiger Dfb, Dfc, and ET climate codes with ≥3 years of field exposure[43]. A literature survey has been conducted for this purpose to the best of the authors' ability, finding 19 publications covering 23 PV systems in cold climates[1,2,20,41,63-77]. Any arrays with sub-string degradation rates are reported here as a median value for the PV system to highlight differences between systems and reduce data bias towards PV arrays with multiple strings of data. Including the four unique PV systems studied in this work, the total number of analyzed PV systems is 27.

The reported studies in this compendium include both degradation rates, for example for studies conducted using measured I-V parameters before and after field exposure, PLRs, and analysis methodologies which fall in-between these two, such as RdTools described in Section 3. Studies primarily aim to analyze degradation rate methodologies via module I-V flash-testing or sophisticated year-on-year approaches, however, a mix of other approaches for filtering data and removing seasonal effects are present in the literature. This is further discussed in Section 5.1.2 below. For simplicity, in this article, we refer to all these results together as degradation rates.

Details on each PV system included in this compendium is summarized in Table 3 in order of latitude. Table 3 includes information on array location, Köppen-Geiger climate code, years of analysis, degradation analysis method, installed system capacity, system orientation and mounting, and observed issues mentioned in the publication relating to

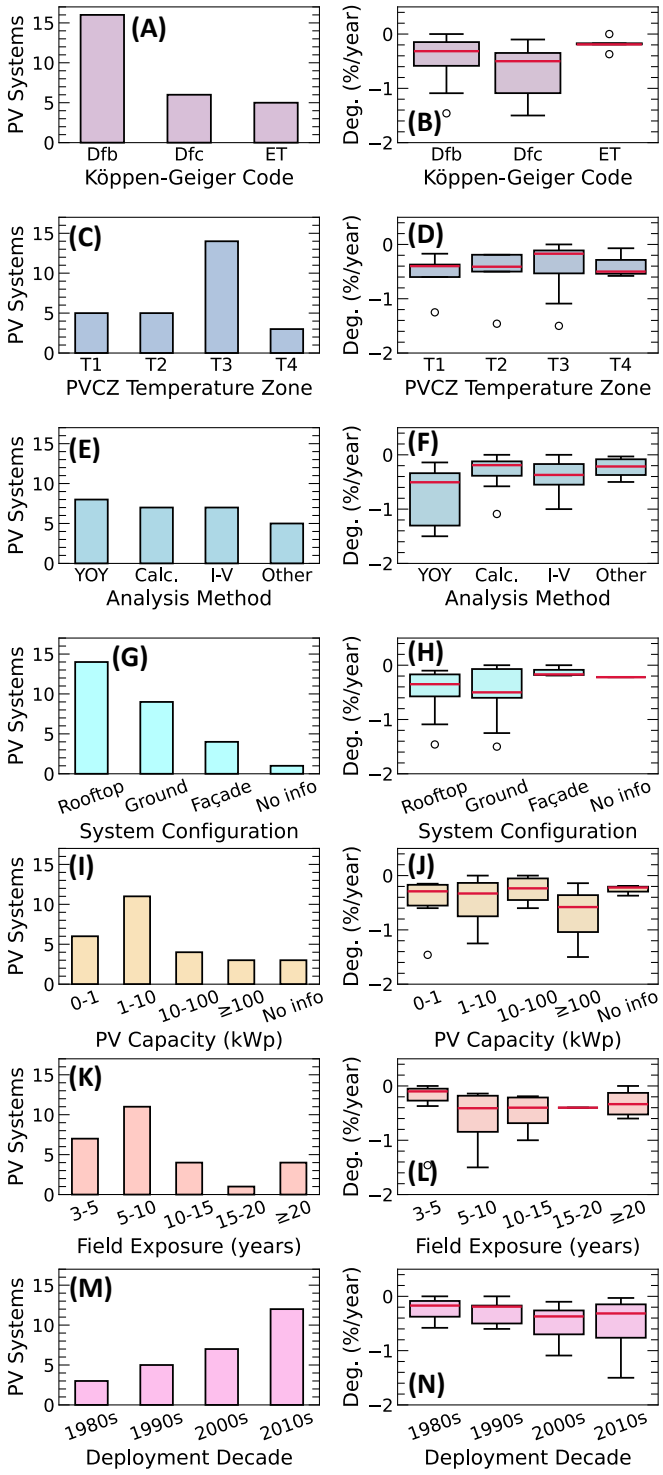

FIGURE 6. The distribution of cold climate PV systems and boxplots by various categories: (A,B) Köppen-Geiger climate classification, (C,D) PVCZ temperature zone classification, (E,F) degradation analysis methods, (G,H) system configurations, (I,J) PV system capacity, (K,L) field exposure, and (M,N) deployment decade. Horizontal red lines in the boxplots denote the median value for each category. In subplots (E,F) degradation analysis methods are abbreviated, with 'Calc.' referring to the number of PV systems where degradation rates were calculated by the authors of this work from data provided in publications. 'I-V' refers to the measurement of current-voltage parameters before and after field exposure.

system performance. In Table 3, the column labelled "data" describes which variable the degradation analysis was conducted on, for example, AC or DC power.

5.1 | Characteristics of Cold Climate Studies

5.1.1 | Site Locations and Climates

Studied PV systems span latitudes from 44°N to 65°N (this work) and include systems in the USA[63], Canada[64,77], Poland[68], Norway[69,70,74,73], Sweden[2,71,72,75], Finland[20,76], and the Alps mountain range in Switzerland[1,66,65], Germany[41,67], and Italy[63]. Figure 6A summarizes the distribution of Köppen-Geiger climate codes for the PV system locations, and Figure 6B shows a boxplot of degradation rates per climate code. Over fifty percent of the studied systems are of Dfb climate (mild summer humid continental). Other cold climates present in the literature are Dfc (cool summer subarctic) and ET (tundra). Due to a small number of systems per climate code category, it is difficult to ascertain if there are distinct degradation trends between climate codes. However, in all cases, the median degradation rates relatively slow, at −0.32%/year (Dfb), −0.50%/year (Dfc), and −0.19%/year (ET).

A separate climate classification for PV systems has been proposed by Karin *et al*. to replace Köppen-Geiger climate codes called the Photovoltaic Climate Zones (PVCZ)[40]. The PVCZ open-rack temperature zones are provided for comparison in Figure 6C/D using the PVCZ python package. Temperature zones were calculated by Karin *et al*. by modelling the Arrhenius-weighted module temperature for a module in a horizontal open-rack configuration with a polymer backsheet using grided land data for ambient temperature, irradiance, and wind speed. Temperature zones for the locations in this work are limited by the resolution of the grid (0.25°), particularly in alpine locations where a small spatial distance can result in a significantly different climate due to altitude. Temperature zones correspond to average modelled module temperatures of <14°C (T1), 14–19°C (T2), 19–24°C (T3) and 24–29°C (T4). Half of the locations identified as T4 are in alpine regions which the limited spatial resolution of the dataset may have misidentified.

5.1.2 | Analysis Methodology

Figure 6E/F summarizes the analysis methodology used for calculating the degradation rate of each cold climate PV system. In seven studies, a degradation rate was not specifically reported; however, it was possible to digitize the published data to calculate the performance loss. In these cases, the analysis method is described as "calculated from paper," abbreviated as "Calc." in Figure 6C. Often, these calculations were done by analyzing several years of published monthly performance ratio data, thus these values represent a PLR rather than an irreversible degradation rate as this analysis does not filter out effects such as soiling, snow

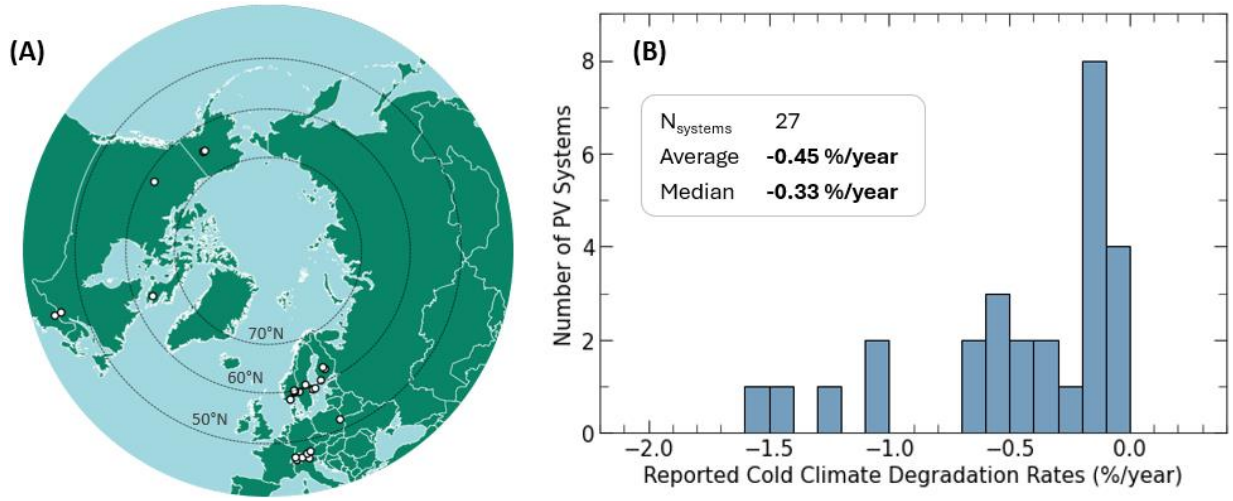

FIGURE 7. (A) The location of reported degradation rates for all 27 mc-Si and c-Si PV systems with ≥3 years of field exposure in Dfb, Dfc, or ET climates. (B) The distribution of reported degradation rates in cold climates in this work covering Dfb, Dfc, and ET Köppen-Geiger climates. The sample size, average, and median are inset.

accumulation, or shading. The true degradation rate of these reported systems likely is lower than what has been calculated, due to inclusion of these performance-decreasing effects.

The most common method for degradation analysis in the literature for cold climates is using a year-on-year approach, closely followed by comparing I-V measurements before and after field exposure. These two methodologies aim to report the underlying degradation rate of the PV system, with year-on-year methodologies requiring a sophisticated approach to filter out common reversible PV system effects (see Section 3).

Several other analysis methods were found in the studies, offering a mix of PLR calculations and more sophisticated approaches for data filtering. Mutungi used an autoregressive integrated moving average (ARIMA) method to calculate the degradation rates for two sites in Finland[76]. This methodology removes outages and includes some seasonality. Rinio *et al*. analyzed 6 clear sky days per year for a 10 year-old site in Sweden to calculate site performance loss[72]. France *et al*. reported the degradation rate for two cold climate sites by taking an average of several analysis methods and data filters, including using a year-on-year approach and seasonal and trend decomposition with Loess[63]. The diverse methodologies highlight the variability in degradation analysis approaches, underscoring the need for standardized methods to improve comparability and accuracy across studies.

5.1.3 | PV System Configuration & Capacity

Cold climate degradation studies have primarily been conducted to-date on small rooftop deployments. Figure 6G categorizes the number of studies conducted on rooftop, ground-mounted, and façade PV systems, while Figure 6H summarizes the degradation rates reported for each configuration. The mounting environment of a PV system will impact the thermal environment of the modules, and thus can influence module degradation rates[36,78,79]. As rooftop PV systems tend to operate at higher temperatures, degradation rates for roof-mounted PV can be higher[36,78,79]. In this dataset of Dfb, Dfc, and ET climate code PV systems, we find that rooftop PV systems have a median degradation rate of −0.35%/year compared to ground-mounted PV systems at −0.50%/year. More data is required to draw stronger conclusions on the effect of mounting configuration in cold climates.

The distribution of PV capacities studied is given in Figure 6I/J. In several cases, no data was provided on the system size. This is denoted as “no info”. Around 20% of all studies were conducted for small and experimental systems <1 kWp and 40% of the studies were conducted on PV arrays with capacities between 1−10 kWp. The largest studied PV system in a Dfb, Dfc, or ET climate zone is a 120 kWp rooftop array in Vestby, Norway[73].

5.1.4 | Field Exposure & Deployment Decade

Figure 6K shows the number of years of field exposure of the PV systems studied, and Figure 6L shows the degradation rates for each exposure bin. Since we have excluded any studies with less than three years of data, field exposure time is categorized unevenly from 3−5, 5−10, 10−15, and 20+ years. Only five systems have been studied in Dfb, Dfc, or ET climates after ≥15 years of field exposure: a rooftop array in Varennes, Canada[64], a rooftop and façade array in Stockholm, Sweden[2], a façade array in Huvudsta, Sweden[71], a rooftop array in Borlänge, Sweden[75], and the double-axis tracking site presented in this work in Fairbanks, Alaska. Most studies in the compendium are for PV systems with field exposure between 5−10 years in length.

The decade of PV system deployment is provided in Figure 6M/N, with PV systems deployment dates ranging from 1981 to 2019 in this compendium. Figure 6N demonstrates a rise in PV degradation rates in time, with median (average) degradation rates increasing from −0.17%/year (−0.25%/year) in the 1980s to −0.32%/year (−0.54%/year) in the 2010s. The number of PV systems studied is also increasing in recent decades (Figure 6M), which is an indication of the rise in interest in PV system deployments in cold climates in time.

The observed increase in PV system degradation in time may be due to historic trends in module architecture towards larger formats, thinner silicon wafers, and thinner glass sheets. Together, these effects can reduce the mechanical durability of modules and result in more cell-cracking, glass-cracking, and module contortion in time[30,80]. Continued reliability testing and development of appropriate standards for cold climate conditions is required to ensure module durability for emerging designs.

5.1.5 | Degradation Rates

Finally, the location and distribution of all reported degradation rates for mc-Si and c-Si PV arrays in cold climate zones of Dfb, Dfc, and ET with ≥3 years of field exposure is provided in Figure 7. The locations of cold climate degradation studies are shown in Figure 7A, and a histogram of reported rates is provided in Figure 7B.

Most studies report a degradation rate of between −0.1 to −0.2%/year; however, there is a long tail in the distribution with faster observed degradation rates. The median degradation rate of cold climate sites is found to be −0.33%/year, while the mean is −0.45%/year, reflecting the influence of this long tail.

5.1.6 | Observed Degradation Mechanisms

Issues related to moisture ingress were identified in several of the cold-climate PV sites[1,2,64,65] . Bogdanski *et al*. reported on a module frame that was destroyed by snow and ice freeze-thaw in Zugspitze, Germany[41]. Cell and glass damage has also been reported in a couple of instances[41], including damage noted by the authors of this work for the double-axis tracking PV site located in Fairbanks, Alaska, near a gravel road.

5.2 | Global Context

The number of PV system degradation studies in cold climates is relatively limited compared to other, warmer climates. Figure 8 summarizes the reported median degradation rates for three other published reviews which include cold climate data in Köppen-Geiger continental or polar climate codes.

Lindig *et al*. reported the average PLR of Dfb Köppen-Geiger climate code PV systems in Europe from the PV PEARL database (purple circle in Figure 8)[81]. The median PLR was found to be −0.17%/year for 19 mc-Si, c-Si, and thin film systems with an average field exposure of 2.8 years. The authors also examined warmer temperate climate zones of Cfa, Cfb, and Csa, reporting PLRs between −0.63%/year to −1.55%/year for these climate zones using a year-on-year analysis[78,81].

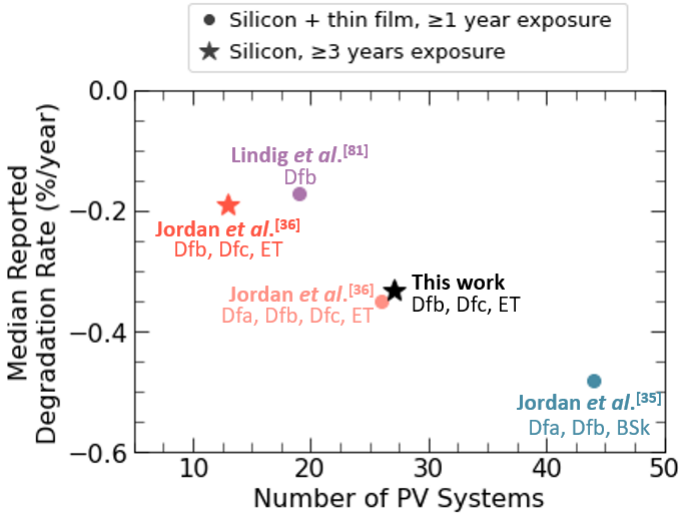

FIGURE 8. Reported median degradation rates for cold climate locations in the literature. The Köppen-Geiger climate zones associated with each study are listed next to each reference point. Dfa and BSk represent warmer climate zones in the continental USA. Circles denote analysis which includes thin film technologies and PV systems with field exposure <3 years, while stars denote analysis of only silicon PV systems with ≥3 years of field exposure.

In 2022, Jordan *et al*. analyzed 1700 utility-scale PV systems in the continental USA[35]. A subset of the sites was analyzed for PLRs by PVCZ temperature zone, finding lower PLRs for the northern third of the USA (44 sites, blue circle in Figure 8)[35]. PV arrays located in this region degraded with a median PLR of −0.48%/year, compared to the middle (−0.78%/year) and southern (−0.88%/year) third of the continental USA. The northern third of the USA primarily consists of Dfa, Dfb, and BSk Köppen-Geiger climate zones, as noted in Figure 8, though other climates may also be included in this analysis.

In 2016, Jordan *et al*. published a summary of reported degradation rates around the globe, finding around 200 studies and 11,000 degradation rates, but with only 39 data points attributed to snowy regions (Dfa, Dfb, Dfc, and ET climates)[36]. The 39 snowy data points reported by Jordan *et al.* consisted of thin-film, mc-Si, and c-Si studies with multiple strings of data with a median degradation rate of −0.35%/year (−0.62%/year average)[36]. These 39 data points represent 26 unique PV systems, as plotted in Figure 8. Moderate, hot and humid, and desert climate types were also reported with degradation rates of −0.42%/year, −0.60%/year, and −0.71%/year, respectively.

A secondary point is plotted for this study in Figure 8 to represent the same selection criteria used in this work. Removing thin-film technologies, systems with field exposure

<3 years, and systems in Dfa climate zones, instead results in 13 PV systems with a median degradation rate of −0.19%/year.

In this work, we examined PV system degradation across continental and polar climate zones of Dfb, Dfc, and ET. We limited our literature review of cold climate degradation rates to only sites with ≥3 years of data and mc-Si or c-Si technologies to improve data quality and comparability. The median degradation rate was found to be −0.33%/year (−0.45%/year on average). This represents the most thorough report of cold climate degradation analysis to date which includes tundra and subarctic climates.

5.3 | Data Limitations

A thorough understanding of long-term PV performance in cold climates is limited by the slower uptake of the PV industry at high latitudes and altitudes, compounded by a lack of collocated instrumentation near existing PV sites, sparse ground irradiance stations, and lower satellite data quality at high latitudes[82,83,84]. In the presented compendium, the degradation rates of 27 unique silicon PV systems in Dfb, Dfc, and ET climate zones are analyzed.

There are notable data gaps in the compendium relating to PV system configuration and location. PV systems with reported degradation rates in cold climates are typically small rooftop deployments with <10 years of field exposure. Furthermore, no reports on PV site degradation were found for Dfb, Dfc, or ET climates in Russia, Greenland, and several other countries, which may be due to limited PV deployments in these regions to-date[85,86].

Additionally, we observed a trend towards higher degradation rates for PV systems deployed in recent decades compared to systems deployed in the 1980s and 1990s. More data is required to corroborate this finding.

A few studies were found for PV systems in Eastern Europe and the USA that did not specify latitude and longitude coordinates, resulting in their exclusion from this analysis. However, these systems may be located in Dfb, Dfc, or ET Köppen-Geiger climate zones. J. Larrivee reported the degradation rates of several PV systems in Germany[87]. Belik *et al.* reported degradation rates between −0.7% to −1.3%/year for unnamed c-Si PV plants in the Czech Republic and Ukraine[88]. Murgescu *et al.* reported the PLR of several PV plants in Romania without geographical coordinates[89]. Finally, Raupp *et al*. reported an average degradation rate of −0.7%/year for two rooftop systems in New York State, which may belong to either continental or temperate climate zones[90].

Nonetheless, the results presented in this review represent the most thorough compilation of degradation studies in Dfb, Dfc, and ET climates to-date. Lessons learned from PV systems deployed in arctic and tundra climates can inform the performance of PV systems in warmer climates, which are experiencing more frequent extreme weather events including heavy snowfall, ice storms, and high wind events[34].

6 | CONCLUSION

In this work, we collected a compendium of PV system degradation rates in cold continental and polar Köppen-Geiger climate zones (Dfb, Dfc and ET) with c-Si or mc-Si technology and ≥3 years of field exposure. The 27 PV sites presented have a median degradation rate of −0.33%/year and an average degradation rate of −0.45%/year. Snow load, high winds, and freeze-thaw cycles with temperatures as low as -40°C can cause cell and frame strain and embrittlement in these climates. However, the benefits of lower PV system operating temperatures and reduced UV-light exposure are suspected to outweigh these mechanical stresses, leading to the overall lower observed degradation rates. Compared to previous reviews of PV system degradation in warmer climates, PV systems in Dfb, Dfc, and ET climate zones tend to degrade slower, providing lasting power to high latitude and alpine communities.

Included in this review is the examination of three new ground-mounted PV sites located >60°N in Alaska and Canada, representing the three highest-latitude PV sites in the compendium and the first PV systems analyzed in Alaska for degradation.

We show that the specific yield of these high-latitude, North American sites varied between 911 kWh/kWp and 1329 kWh/kWp, depending largely on the system configuration and cell technology. Site PV power data availability was >90% in all cases, while meteorological data experienced more outages, with availabilities of 65%, 84%, and 95% over the systems' lifetimes.

One of the newly analyzed sites is a 16-year old double-axis tracking system located in Fairbanks, Alaska (65°N), where tracking is enabled each year outside of the winter months (October through March). While tracking was enabled, the double-axis arrays demonstrated tracking availabilities of 48-86%. The tracking of one of three arrays failed after 12 years of operation.

Overall, the newly analyzed North American PV sites showcase a wide range of degradation rates from −0.4%/year to −1.5%/year due to their widely varying system configurations, module technologies, and deployment age. These results are included in the compendium and were calculated using a robust year-on-year method with RdTools, which captures seasonal effects and attempts to remove effects commonly included in PLR calculations such as outages, clipping, and effects of snow accumulation.

A diverse range of methodologies for calculating degradation rates are present in the compendium, highlighting the variability of degradation analyses, and underscoring the need for standardized calculation methods to improve comparability and accuracy across future studies. Year-on-year approaches are recommended in particular for high latitude locations which experience strong seasonality and remote locations which may be more prone to data outages.

New PV systems and test-sites deployed in cold climates should seek to collect and store information over the long term to facilitate reliability studies and regular degradation monitoring. This is particularly important in remote locations, where access to I-V flash testing equipment may be limited. However, long-term data collection in cold climates for year-on-year degradation analyses can be challenging in cold climates due to small regional PV workforces, outdoor operation and maintenance challenges in winter months, and higher data-outage potential. In the case where I-V tracing equipment is available, flash-testing modules before and after field exposure are recommended as a supplement to year-on-year methodologies, or when continuous data collection is not possible.

Further studies on new bifacial technologies, such as SHJ and TOPCon modules, are required across different climate zones to determine their degradation rates and mechanisms under varied outdoor stressors, including freeze-thaw cycles and snow loading. A trend towards higher degradation rates for PV systems deployed in recent decades is observed in the compendium, which may be due to larger and thinner module architectures in recent years. Continued development of reliability standards and testing are critical to maintaining module durability under cold climate stressors of snow load, wind load, and freeze-thaw cycles.

Overall, we have presented a compendium of degradation rates for PV systems located in Dfb (mild summer humid continental), Dfc (cool summer subarctic), and ET (tundra) Köppen-Geiger climate zones, representing the most thorough compilation of PV systems in these climate zones to-date and supporting existing trends that PV systems degrade slower in colder climates.

ACKNOWLEDGEMENTS

The authors would like to extend their thanks to Qwerty Mackey and Robbin Garber-Slaght from the NREL's Alaska Campus for assistance with data curation for the double-axis tracking site in Fairbanks, Alaska. Thank you to the Northwest Territories Power Corporation and Christopher Baldus-Jeursen from CanmetENERGY for providing data for the PV site in Fort Simpson, Northwest Territories. Thank you to Kirsten Perry and Robert White from NREL for porting data and assisting with data cleaning routines.

This work was authored in part by the University of Ottawa with the support of the Canadian Foundation for Innovation, Ontario Research Fund, and the Natural Sciences and Engineering Research Council of Canada [NSERC CREATE 497981, NSERC STPGP 521894, NSERC CGS-D]. The University of Ottawa is located on the unceded territory of the Anishinaabe Algonquin Nation.

This work was authored in part by the Alaska Center for Energy and Power, University of Alaska Fairbanks with funding additionally provided by the Department of Navy award N00014-19-1-2235 issued by the Office of Naval Research.

This work was also authored in part by the National Renewable Energy Laboratory (NREL), operated by Alliance for Sustainable Energy, LLC, for the U.S. Department of Energy (DOE) under Contract No. DE-AC36-08GO28308. Partial funding is provided by the U.S. Department of Energy (DOE)'s Office of Energy Efficiency and Renewable Energy (EERE) from the Solar Energy Technologies Office (SETO), under CPS Agreement 385258, and as part of the Durable Module Materials Consortium 2 (DuraMAT 2) funded by the U.S. DOE, Office of EERE, SETO, agreement number 38259. The views expressed in the article do not necessarily represent the views of the DOE or the U.S. Government. The U.S. Government retains and the publisher, by accepting the article for publication, acknowledges that the U.S. Government retains a nonexclusive, paid-up, irrevocable, worldwide license to publish or reproduce the published form of this work, or allow others to do so, for U.S. Government purposes. The funders had no role in study design, data collection and analysis, decision to publish, or preparation of the manuscript.

DATA AVAILABILITY STATEMENT

The data supporting the findings of this study are available publicly online and by request. Power data for Fort Simpson can be found publicly online by the Northwest Territories Power Corporation portal[46], while associated meteorological station can be requested from CanmetENERGY. All data for the double-axis tracking site in Fairbanks maintained by NREL-Alaska (formerly the Cold Climate Housing Research Center) is publicly available[48]. Data is available upon request for the east-west vertical and south-tilted PV site in Fairbanks by reaching out to the Alaska Center for Energy and Power at the University of Alaska Fairbanks. RdTools is available as an open-source Python package for the calculation of year-on-year degradation rates and associated statistics[45].

INCLUSION AND DIVERSITY

One or more of the authors of this paper self-identifies as an underrepresented ethnic minority in science.

AUTHOR CONTRIBUTIONS

Erin M. Tonita: Conceptualization, Software, Investigation, Formal Analysis, Investigation, Data Curation, Writing – Original Draft, Visualization. **Dirk Jordan**: Conceptualization, Methodology, Software, Formal Analysis, Investigation, Data Curation, Writing – Review & Editing, Supervision. **Silvana Ovaitt**: Conceptualization, Writing – Review & Editing, Supervision. **Henry Toal**: Conceptualization, Resources, Data Curation. **Karin Hinzer**: Writing – Review & Editing, Supervision, Funding Acquisition. **Christopher Pike**: Conceptualization, Resources, Data Curation, Writing – Review & Editing, Supervision. **Chris Deline**: Writing – Review & Editing, Supervision, Funding Acquisition.

REFERENCES

1. U. Jahn and W. Nasse, "Analysis of long-term performance and reliability of photovoltaic systems," IEA Task 2 Draft Report (2003).
2. J. Hedström and L. Palmblad, "Performance of old PV modules: measurement of 25 year old crystalline silicon modules," Technical Report ELFORSK-01-71 (2006).
3. M. Lindh, "Country report: Sweden," in *2024 High Latitude Photovoltaics Workshop*, Piteå, Sweden, 1-11 (2024). https://www.sandia.gov/app/uploads/sites/243/dlm_uploads/2024/03/3.1-LindhMattias_Sweden_20240314.pdf
4. E. S. Marstein, "Country report: Norway," in *2024 High Latitude Photovoltaics Workshop*, Piteå, Sweden, 1-17 (2024). https://www.sandia.gov/app/uploads/sites/243/dlm_uploads/2024/03/3.2-Marstein-Norway-20240314-1.pdf
5. S. Ranta, "PV Progress in Finland," in *2024 High Latitude Photovoltaics Workshop*, Piteå, Sweden, 1-15 (2024). https://www.sandia.gov/app/uploads/sites/243/dlm_uploads/2024/03/3.3-RantaSamuli-Finland-20240314.pdf
6. E. Larsen, "Country Report: Denmark & Greenland," in *2024 High Latitude Photovoltaics Workshop*, Piteå, Sweden, 1-19 (2024). https://www.sandia.gov/app/uploads/sites/243/dlm_uploads/2024/03/3.4-LarsenEsben-Denmark-Greenland-20240314.pdf
7. C. Pike, "High latitude solar workshop country report: United States," in *2024 High Latitude Photovoltaics Workshop*, Piteå, Sweden, 1-11 (2024). https://www.sandia.gov/app/uploads/sites/243/dlm_uploads/2024/03/3.5-PikeChris-UnitedStates-20240314.pdf
8. E. M. Tonita, "Status of PV in Canada," in *2024 High Latitude Photovoltaics Workshop*, Piteå, Sweden, 1-18 (2024). https://www.sandia.gov/app/uploads/sites/243/dlm_uploads/2024/03/3.6-TonitaErin_Canada_20240314.pdf
9. M. Dhimish, "Performance ratio and degradation rate analysis of 10-year field exposed residential photovoltaic installations in the UK and Ireland," *Clean Technologies*, 2, 170-183 (2020). https://doi.org/10.3390/cleantechnol2020012
10. H. Haeberlin, "Grid connected PV plant Jungfraujoch (3454m) in the Swiss Alps: 10 years of trouble-free operation with record energy yields," *19th European Photovoltaic Solar Energy Conference*, Paris, France, June 2004.
11. H. Gholami, H. N. Røstvik, N. M. Kumar, and S. S. Chopra, "Lifecycle cost analysis (LCCA) of tailor-made building integrated photovoltaics (BIPV) façade: Solsmaragden case study in Norway," *Solar Energy*, 211, 488-502 (2020). https://doi.org/10.1016/j.solener.2020.09.087
12. A. Boute, "Off-grid renewable energy in remote Arctic areas: An analysis of the Russian Far East," *Reviews*, 59, 1029-1037 (2016). https://doi.org/10.1016/j.rser.2016.01.034
13. E. Usher, G. Jean, and G. Howell, "The use of photovoltaics in a northern climate," *Solar Energy Materials and Solar Cells*, 34, 73-81 (1994). https://doi.org/10.1016/0927-0248(94)90026-4
14. S. Rönnberg, M. Bollen, and A. Larsson, "Grid impact from PV-installations in Northern Scandinavia," *22nd International Conference and Exhibition on Electricity Distribution (CIRED 2013)*, Stockholm, 1-4 (2013). https://doi.org/10.1049/cp.2013.1046
15. I. Das and C. A. Canizares, "Renewable energy integration in diesel-based microgrids at the Canadian Arctic," *Proceedings of the IEEE*, 107(9), 1838-1856 (2019). https://doi.org/10.1109/JPROC.2019.2932743
16. A. Wills, C. Banister, M. Pellissier, and J. Berquist, "A multi-year analysis of Canadian Arctic historical weather data in support of solar and wind renewable energy deployment," *E3S Web of Conferences*, 246, 03006 (2021). https://doi.org/10.1051/e3sconf/202124603006
17. D. Dumas and L. Gosselin, "Optimizing photovoltaic systems to decarbonize residential arctic buildings considering real consumption data and temporal mismatch," *Solar Energy*, 275, 112560 (2024). https://doi.org/10.1016/j.solener.2024.112560
18. S. V. Obydenkova and J. M Pearce, "Technical viability of mobile solar photovoltaic systems for indigenous nomadic communities in northern latitudes," *Renewable Energy*, 89, 253-267 (2016). https://doi.org/10.1016/j.renene.2015.12.036
19. P. E. Campana, B. Stridh, T. Hörndahl, S. Svensson, S. Zainali, S. M. Lu, T. E. K. Zidane, P. De Luca, S. Amaducci, and M. Colauzzi, "Experimental results, integrated model validation, and economic aspects of agrivoltaics systems at northern latitudes," *Journal of Cleaner Production*, 437, 140235 (2024). https://doi.org/10.1016/j.jclepro.2023.140235
20. L. Karttunen, S. Jouttijärvi, A. Poskela, H. Palonen, H. Huerta, M. Todorović, S. Ranta, and K. Miettunen, "Comparing methods for long-term performance assessment of bifacial photovoltaic modules in Nordic conditions," *Renewable Energy*, 219, 119473 (2023). https://doi.org/10.1016/j.renene.2023.119473
21. E. Andenæs, B. P. Jelle, K. Ramlo, T. Kolås, J. Selj, and S. E. Foss, "The influence of snow and ice coverage on the energy generation from photovoltaic solar cells," *Solar Energy*, 159, 318-328 (2018). https://doi.org/10.1016/j.solener.2017.10.078
22. D. Riley, L. Burnham, W. Snyder, B. King, and P. Dice, "Measurement of snow loading on a tilted PV module in Northern Michigan," *IEEE 49th Photovoltaic Specialists Conference (PVSC)*, Philadelphia, USA, 1343-1345 (2022). https://doi.org/10.1109/PVSC48317.2022.9938704
23. L. Burnham, D. Riley, B. H. King, J. Braid, P. Dice, A. Dyreson, W. Snyder, and C. Pike, "Dedicated cold-climate field laboratory for photovoltaic system and component studies: the Michigan Regional Test Center as a case study," *IEEE 49th Photovoltaic Specialists Conference (PVSC)*, Philadelphia, USA, 333-335 (2022). https://doi.org/10.1109/PVSC48317.2022.9938861
24. J. D. Brearly, "Designing PV systems for environmental extremes," SolarPro Magazine, 8(5) (2015).
25. E. J. Schneller, H. Seigneur, J. Lincoln, and A. M. Gabor, "The impact of cold temperature exposure in mechanical durability testing of PV modules," *IEEE 46th Photovoltaic Specialists Conference (PVSC)*, Chicago, USA, 1521-1524 (2019). https://doi.org/10.1109/PVSC40753.2019.8980533
26. U. Blieske and G. Stollwerck, "Chapter Four – Glass and other encapsulation materials," *Semiconductors and Semimetals*, 89, 199-258 (2013). https://doi.org/10.1016/B978-0-12-381343-5.00004-5
27. M. D. Kempe, G. J. Jorgensen, K. M. Terwilliger, T. J. McMahon, C. E. Kennedy, and T. T. Borek, "Acetic acid production and glass transition concerns with ethylene-vinyl acetate used in photovoltaic devices," *Solar Energy Materials and Solar Cells*, 91(4), 315-329 (2007). https://doi.org/10.1016/j.solmat.2006.10.009
28. W. Hermann and N. Bogdanski, "Outdoor weathering of PV modules – effects of various climates and comparison with accelerated laboratory testing," *IEEE 37th Photovoltaic Specialists Conference (PVSC)*, Seattle, USA, 2305-2311 (2011). https://doi.org/10.1109/PVSC.2011.6186415
29. J. Lopez-Garcia, D. Pavanello, and T. Sample, "Analysis of temperature coefficients of bifacial crystalline silicon PV modules," *IEEE Journal of Photovoltaics*, 8(4), 960-968 (2018). https://doi.org/10.1109/JPHOTOV.2018.2834625
30. M. Aghaei, A. Fairbrother, A. Gok, S. Ahmad, S. Kazim, K. Lobato, G. Oreski, A. Reinders, J. Schmitz, M. Theelen, P. Yilmaz, and J. Kettle, "Review of degradation and failure phenomena in photovoltaic modules," *Renewable and Sustainable Energy Reviews*, 159, 112160 (2022). https://doi.org/10.1016/j.rser.2022.112160
31. A. Sinha, H. Gopalakrishna, A. B. Subramaniyan, D. Jain, J. Oh, D. Jordan and G. Tamizh Mani, "Prediction of climate-specific degradation rate for photovoltaic encapsulant discoloration," *IEEE J. of Photovolt.*, 10(4), 1093 (2020). https://doi.org/10.1109/JPHOTOV.2020.2989182
32. A. Omazic, G. Oreski, M. Halwachs, G. C. Eder, C. Hirschl, L. Neumaier, G. Pinter, and M. Erceg, "Relation between degradation of polymeric components in crystalline silicon PV module and climatic conditions: A literature review," *Solar Energy Materials and Solar Cells*, 192, 123-133 (2019). https://doi.org/10.1016/j.solmat.2018.12.027
33. T. Rahman, A. A. Mansur, M. S. H. Lipu, M. S. Rahman, R. H. Ashique, M. A. Houran, R. M. Elavarasan, and E. Houssain, "Investigation of degradation of solar photovoltaics: A review of aging factors, impacts, and future directions toward sustainable energy management," *Energies*, 16(9), 3706 (2023). https://doi.org/10.3390/en16093706
34. M. Bošnjaković, M. Stojkov, M. Katinić, and I. Lacković, "Effects of extreme weather conditions on PV systems," *Sustainability*, 15(22), 16044 (2023). https://doi.org/10.3390/su152216044

35. D. C. Jordan, K. Anderson, K. Perry, M. Muller, M. Deceglie, R. White, and C. Deline, "PV fleets degradation insights," *Progress in Photovoltaics: Research and Applications*, 30(10), 1166-1175 (2022). https://doi.org/10.1002/pip.3566
36. D. C. Jordan, S. R. Kurtz, K. VanSant, and J. Newmiller, "Compendium of photovoltaic degradation rates," *Progress in Photovoltaics: Research and Applications*, 24(7), 978-989 (2016). https://doi.org/10.1002/pip.2744
37. P. Ingenhoven, G. Belluardo, G. Makrides, G. E. Georghiou, P. Rodden, L. Frearson, B. Herteleer, D. Bertani, and D. Moser, "Analysis of photovoltaic performance loss rates of six module types in five geographical locations," *IEEE Journal of Photovoltaics*, 9(4), 1091-1096 (2019). https://doi.org/10.1109/JPHOTOV.2019.2913342
38. K. Kunaifi, A. Reinders, S. Lindig, M. Jaeger, and D. Moser, "Operational performance and degradation of PV systems consisting of six technologies in three climates," *Applied Sciences*, 10(16), 5412 (2020). https://doi.org/10.3390/app10165412
39. D. C. Jordan, B. Marion, C. Deline, T. Barnes, and M. Bolinger, "PV field reliability status – analysis of 100 000 solar systems," *Progress in Photovoltaics: Research and Applications*, 28, 739-754 (2020).
40. T. Karin, C. B. Jones, and A. Jain, "Photovoltaic degradation climate zones," *IEEE 49th Photovoltaic Specialists Conference (PVSC)*, Chicago, USA, 687-694 (2019). https://doi.org/10.1109/PVSC40753.2019.8980831
41. N. Bogdanski, W. Herrmann, F. Reil, M. Köhl, K. A. Weiss, and M. Heck, "Results of 3 years' PV module weathering in various open-air climates," *Proc. SPIE 7773, Reliability of Photovoltaic Cells, Modules, Components, and Systems III*, 77730L (2010). https://doi.org/10.1117/12.859807
42. M. Dhimish and A. Alrashidi, "Photovoltaic degradation rate affected by different weather conditions: A case study based on PV systems in the UK and Australia," *Electronics*, 9, 650 (2020). https://doi.org/10.3390/electronics9040650
43. R. Geiger, Überarbeitete Neuausgabe von Geiger, R.: Köppen-Geiger / Klima der Erde. (Wandkarte 1:16 Mill.) – Klett-Perthes, Gotha (1961).
44. J. Ascencio-Vásquez, I. Kaaya, K. Brecl, K-A. Weiss, and M. Topič, "Global climate data processing and mapping of degradation mechanisms and degradation rates of PV modules," *Energies*, 12, 4749 (2019). https://doi.org/10.3390/en12244749
45. D. C. Jordan, C. Deline, S. R. Kurtz, G. M. Kimball, and M. Anderson, "Robust PV degradation methodology and application," *IEEE Journal of Photovoltaics*, 8(2), 525-531 (2018). https://doi.org/10.1109/JPHOTOV.2017.2779779
46. Northwest Territories Power Corporation, "Fort Simpson Solar Energy Project," website accessed June 28, 2024 (2024). https://www.ntpc.com/energy-alternatives/current-alternative-energy-projects/fort-simpson-solar-energy-project
47. C. Pike, E. Whitney, M. Wilber, and J. S. Stein, "Field performance of south-facing and east-west facing bifacial modules in the Arctic," *Energies*, 14(4), 1210 (2021). https://doi.org/10.3390/en14041210
48. Cold Climate Housing Research Center, "RTF Solar PV," website accessed June 28, 2024 (2024). http://cchrc.rcs.alaska.edu
49. R. Colgan, N. Wiltse, M. Lilly, B. LaRue, and G. Egan, "Performance of photovoltaic arrays – Cold Climate Housing Research Center (CCHRC)," CCHRC Snapshot RS 2010-10 (2010). https://cchrc.org/media/Solar_Photovoltaics.pdf
50. M. Deceglie, A. Nag, A. Shinn, G. Kimball, D. Ruth, D. Jordan, J. Yan, K. Anderson, K. Perry, M. Mikofski, M. Muller, W. Vining, and C. Deline, RdTools, Version 2.1.7, Computer Software, https://github.com/NREL/rdtools.
51. M. G. Deceglie, K. Anderson, D. Fregosi, W. B. Hobbs, M. A. Mikofski, M. Theristis, and B. E. Meyers, "Perspective: performance loss rate in photovoltaic systems," *SolarRRL*, 7(15), 2300196 (2023). https://doi.org/10.1002/solr.202300196
52. A. P. Dobos, "PVWatts Version 5 Manual," NREL/TP-6A20-62641, National Renewable Energy Lab (2014). https://doi.org/10.2172/1158421
53. K. Anderson, C. Hansen, W. Holmgreen, A. Jensen, M. Mikofski, and A. Driesse, "pvlib python; 2023 project update," *Journal of Open Source Software*, 8(92), 5994 (2023). https://doi.org/10.21105/joss.05994
54. M. J. Reno and C. W. Hansen, "Identification of periods of clear sky irradiance in time series of GHI measurements," *Renewable Energy*, 90, 520–531 (2016). https://doi.org/10.1016/j.renene.2015.12.031
55. D. C. Jordan and C. Hansen, "Clear-sky detection for PV degradation analysis using multiple regression," *Renewable Energy*, 209, 393–400 (2023). https://doi.org/10.1016/j.renene.2023.04.035
56. A. Phinikarides, N. Kindyni, G. Makrides, and G. E. Georghiou, "Review of photovoltaic degradation rate methodologies," *Renewable and Sustainable Energy Reviews*, 40, 143-152 (2014). https://doi.org/10.1016/j.rser.2014.07.155
57. E. Tonita, A. Russell, C. Valdivia, and K. Hinzer, "Optimal ground coverage ratios for tracked, fixed-tilt, and vertical photovoltaic systems for latitudes up to 75°N," *Solar Energy*, 258, 8-15 (2023). https://doi.org/10.1016/j.solener.2023.04.038
58. L. Burnham, D. Riley, B. Walker, and J. M. Pearce, "Performance of bifacial photovoltaic modules on a dual-axis tracker in a high-latitude, high-albedo environment," in *IEEE 46th Photovoltaic Specialists Conference (PVSC)*, Chicago, IL, USA, 1320-1327 (2019). https://doi.org/10.1109/PVSC40753.2019.8980964
59. T. Dierauf, A. Growitz, S. Kurtz, J. L B. Cruz, E. Riley, and C. Hansen, "Weather-corrected performance ratio," NREL/TP-5200-57991, National Renewable Energy Lab, Golden, CO, USA (2013). https://doi.org/10.2172/1078057
60. O. Arriaga Arruti, A. Virtuani, and C. Ballif, "Long-term performance and reliability of silicon heterojunction solar modules," *Prog. in Photovolt.: Res. Appl.*, 31(7), 664-677 (2023). https://doi.org/10.1002/pip.3688
61. D. Jordan, D. B. Sulas-Kern, S. Johnston, H. R. Moutinho, C. Xiao, C. S. Jiang, M. Young, A. G. Norman, C. Deline, I. Repins, R. Bhoopathy, O. Kunz, Z. Hameiri, and C. Sainsbury, "High efficiency module degradation – from atoms to systems," *37th European Photovoltaic Solar Energy Conference*, 828-833 (2020).
62. C. Deline, D. Jordan, B. Sekulic, J. Parker, B. McDanold, and A. Anderberg, "PV lifetime project – 2024 NREL annual report," Golden, CO: National Renewable Energy Laboratory, NREL/TP-5K00-90651 (2024). https://www.nrel.gov/docs/fy24osti/90651.pdf
63. R. H. French *et al.*, "Assessment of performance loss rate of PV power systems," IEA PVPS Task 13, Report IEA-PVPS T13-22:2021 (2021). https://iea-pvps.org/key-topics/assessment-of-performance-loss-rate-of-pv-power-systems/
64. Christopher Baldus-Jeursen, Alexandre Côté, Tanya Deer, and Yves Poissant, "Analysis of photovoltaic module performance and life cycle degradation for 23 year-old array in Quebec, Canada," *Renewable Energy*, 174, 547-556 (2021). https://doi.org/10.1016/j.renene.2021.04.013
65. H. Haeberlin, "Grid connected PV plant Jungfraujoch (3454m) in the Swiss Alps: 10 years of trouble-free operation with record energy yields," in *19th European Photovoltaic Solar Energy Conference*, Paris, France (2004).
66. H. Haeberlin and P. Schaerf, "Newtech – 3 different thin film PV plants of 1kWp under direct long-term comparison (2002-2009)," in *25th European Photovoltaic Solar Energy Conference*, Valencia, Spain (2010).
67. H. Wilk, A. Szeless, A. Beck, H. Meier, M. Heikkilä, and C. Nyman, "Eureka Project EU 333 Alpsolar: field testing and optimization of photovoltaic solar power plant equipment, progress report 1994," *12th European Photovoltaic Solar Energy Conference (EUPVSEC)*, Amsterdam (1994).
68. A. Zdyb and S. Gulkowski, "Performance assessment of four different photovoltaic technologies in Poland," *Energies*, 13, 196 (2020). https://doi.org/10.3390/en13010196
69. D. Verma, M. Tayyib, T. O. Saetre, and O. Midtgård, "Outdoor performance of 10 year old a-Si and poly-Si modules in southern Norway conditions," in *IEEE 38th Photovoltaic Specialists Conference*, Austin, TX, USA, 2368-2371 (2012). https://doi.org/10.1109/PVSC.2012.6318074
70. B. R. Paudyal and A. G. Imenes, "Performance assessment of field deployed multi-crystalline PV modules in Nordic conditions," in *46th IEEE Photovoltaic Specialists Conference (PVSC)*, Chicago, IL, USA, 1377-1383 (2019). https://doi.org/10.1109/PVSC40753.2019.8980629
71. L. Palmblad, C. Martinsson, J. Hedstrom, and M. Andersson, "Long-term performance of PV modules – results from Swedish case studies," *22nd European Photovoltaic Solar Energy Conference (EUPVSEC)*, Milan, Italy (2007).

72. M. Rinio, U. Enarsson, and C. Hansen, "A fast software check for PV systems," *8th World Conference on Photovoltaic Energy Conversion*, Milano, Italy, 1085-1088 (2022). https://doi.org/10.4229/WCPEC-82022-4DO.2.4
73. E. B. Sveen, M. B. Øgaard, J. H. Selj, and G. Otnes, "PV system degradation rates in the Nordics," *37th European Photovoltaic Solar Energy Conference (EUPVSEC)*, 1563-1566 (2020).
74. C. Seiffert, "PV module degradation rates in Norway," in High Latitude PV Workshop, Piteå, Sweden (2024).
75. E. Psimopoulos, J. Plautz, F. Fiedler, and A. Augusto, "Performance of PV system operating for 30-years in Scandinavia," *in 51st IEEE Photovoltaic Specialists Conference (PVSC)*, Seattle, IL, USA (2024). https://doi.org/10.1109/PVSC57443.2024.10748925
76. Dereck Musyimi Mutungi, "Degradation of photovoltaics in central Finland: A comparative study of polycrystalline and heterojunction with intrinsic thin layer technologies," Masters Thesis, University of Jyväskylä (2013).
77. Y. Poissant, D. Thevenard and D. Turcotte, "Performance monitoring of the Nunavut arctic college PV system: nine years of reliable electricity generation," CanmetENERGY (2004).
78. D. C. Jordan, C. Deline, M. Deceglie, T. J. Silverman, and W. Luo, "PV degradation – mounting & temperature," in *46th IEEE Photovoltaic Specialists Conference (PVSC)*, Chicago, IL, 673-679 (2019). https://doi.org/10.1109/PVSC40753.2019.8980767
79. N. Bansal, S. P. Jaiswal, and G. Singh, "Comparative investigation of performance evaluation, degradation causes, impact and corrective measures for ground mount and rooftop solar PV plants – A review," *Sustainable Energy Technologies and Assessments*, 47, 101526 (2021). https://doi.org/10.1016/j.seta.2021.101526
80. J. Zuboy, M. Springer, E. C. Palmiotti, J. Karas, B. L. Smith, and M. Woodhouse, "Getting ahead of the curve: Assessment of new photovoltaic module reliability risks associated with projected technological changes," *IEEE Journal of Photovoltaics*, 14(1), 4-22 (2024). https://doi.org/10.1109/JPHOTOV.2023.3334477
81. S. Lindig, D. Moser, A. J. Curran, and R. H. French, "Performance loss rates of PV systems of Task 13 database," in *46th IEEE Photovoltaic Specialists Conference (PVSC)*, Chicago, IL, 1363-1367 (2019). https://doi.org/10.1109/PVSC40753.2019.8980638
82. N. Matsui, C. N. Long, J. Augustine, D. Halliwell, T. Uttal, D. Longenecker, O. Niebergall, J. Wendell, and R. Albee, "Evaluation of Arctic broadband surface radiation measurements," *Atmospheric Measurement Techniques*, 5(2), 429-438 (2012). https://doi.org/10.5194/amt-5-429-2012
83. B. Babar, L. T. Luppino, T. Boström, S. N. Anfinsen, "Random forest regression for improved mapping of solar irradiance at high latitudes," *Solar Energy*, 198, 81-92 (2020). https://doi.org/10.1016/j.solener.2020.01.034
84. H. N. Riise, M. M. Nygård, B. Aarseth, A. Dobler, and E. Berge, "Benchmark of modelled solar irradiance data at high latitude locations," SSRN Preprint (2024). http://dx.doi.org/10.2139/ssrn.4804004
85. M. Ross and J. Royer, "PV-hybrid power systems for radio links in Greenland," in Photovoltaics in Cold Climates, 1st Edition, Routledge, pp. 126-127 (1998).
86. A. Pantaleo, M. R. Albert, H. T. Snyder, S. Doig, T. Oshima, N. E. Nagelqvist, "Modeling a sustainable energy transition in northern Greenland: Qaanaaq case study," *Sustainable Energy Technologies and Assessments*, 54, 102774 (2022). https://doi.org/10.1016/j.seta.2022.102774
87. J. Larrivee, "An analysis of degradation rates of PV power plants at the system level," Masters Thesis, Utrecht University (2013).
88. M. Belik, J. Timr, and O. Rubanenko, "Prediction of the degradation process of mono-Si photovoltaic panels in Ukrainian and Czech conditions," *23rd International Scientific Conference on Electric Power Engineering (EPE)*, Brno, Czech Republic, 1-6 (2023). https://doi.org/10.1109/EPE58302.2023.10149312
89. I. Murgescu, L. A. El-Leathey, and R. A. Chihaia, "Guaranteed versus real service life of PV panels in Romania," *Journal of Engineering Sciences and Innovation*, 3(4), 375-392 (2018). https://doi.org/10.56958/jesi.2018.3.4.375
90. C. Raupp, C. Libby, S. Tatapudi, D. Srinivasan, J. Kuitche, B. Bicer, and G. TamizhMani, "Degradation rate evaluation of multiple PV technologies in 59,000 modules representing 252,000 modules in four climatic regions of the United States," *IEEE 43rd Photovoltaic Specialists Conference (PVSC)*, Portland OR, USA, 255-260 (2016). https://doi.org/10.1109/PVSC.2016.7749590

TABLE 3: Existing cold climate degradation studies in the literature

Ref.	Location	Köppen-Geiger Code	PLR (%/year)	Years Covered	Analysis Method	Data	Module Information	System Configuration	Reported Issues
This work	Fairbanks, USA (64.8°N, 148°W)	Dfc	**-1.2±0.4**	5 years, 2019-2024	Year-on-year, RdTools	AC power, minutely	1.15 kWp c-Si, bifacial SHJ	Ground, 60° tilt, 180° azimuth and 90° tilt, 90/270° azimuth	
	Fairbanks, USA (64.8°N, 148°W)	Dfc	**-0.6±0.2**	5 years, 2019-2024	Year-on-year, RdTools	AC power, minutely	502 Wp c-Si, monofacial and bifacial PERC	Ground, 60° tilt, 180° azimuth	
	Fairbanks, USA (64.8°N, 148°W)	Dfc	**-0.4±0.4**	16 years, 2008-2024	Year-on-year, RdTools	AC current, hourly	10 kWp mc-Si, Al-BSF	Ground, 4 dual-axis trackers	Some visual damage of modules due to gravel impact from nearby road; JX Crystals array failed after 4 years.
[77]	Iqaluit, Canada (63.8°N, 69°W)	ET	**-0.17**	9 years, 1995-2004	Calculated from paper	AC energy, annual	3.2 kWp c-Si	Façade, 230° azimuth	
[76]	Saarijärvi, Finland (62.7°N, 25°E)	Dfc	**-0.33**	7 years, 2005-2013	ARIMA	AC power, minutely	6.27 kWp c-Si, SHJ	Rooftop	Small interruptions from inverter errors.
	Jyväskylä, Finland (62.2°N, 26°E)	Dfc	**-0.1**	3 years, 2009-2013	ARIMA	AC power, minutely	2.6 kWp mc-Si	Rooftop, 40° tilt, 180° azimuth	Small interruptions from inverter errors.
This work	Fort Simpson, Canada (61.9°N, 121°W)	Dfc	**-1.5**	6 years, 2018-2024	Year-on-year, RdTools	AC power, 15-minute	100 kWp c-Si, monofacial PERC	Ground, 35° tilt, 190° azimuth	Missing first 5 years of operation data.
[75]	Borlänge, Sweden (60.6°N, 16°E)	Dfb	**-0.5**	30 years, 1994-2024	IV before & after	IV parameters	3.2 kWp mc-Si	Rooftop, 60° tilt, 210° azimuth	Light module yellowing, with otherwise no visual damage reported.
[20]	Turku, Finland (60.5°N, 22°E)	Dfb	**-1.46**	4 years, 2017-2021	Year-on-year	DC power, minutely	375 Wp c-Si, bifacial	Rooftop, 90° tilt, 90° azimuth	Suspected possible PID.

TABLE 3 Cont.: Existing cold climate degradation studies in the literature

Ref.	Location	Köppen-Geiger Code	PLR (%/year)	Years Covered	Analysis Method	Data	Module Information	System Configuration	Reported Issues
[74]	Oslo, Norway (60.0°N, 11°E)	Dfb	**-0.41**	6 years, 2017-2023	Year-on-year, RdTools	AC power	720 Wp mc-Si	Rooftop, 10° tilt	
	Oslo, Norway (59.8°N, 11°E)	Dfb	**-0.15**	8 years, 2015-2023	Year-on-year, RdTools	AC power	370 Wp mc-Si	Rooftop, 10° tilt	
[73]	Vestby, Norway (59.6°N, 11°E)	Dfb	**-0.14**	5 years, 2015-2019	Year-on-year	DC power, 5-minute	120 kWp mc-Si	Rooftop, 10° tilt, 112° azimuth	
[72]	Glava, Sweden (59.6°N, 13°E)	Dfb	**-0.22**	10 years, 2012-2022	Clear sky peak power degradation	Power, 6 days per year	No info	No info	Missing first 3 years of operation data.
[71]	Huvudsta, Sweden (59.3°N, 18°E)	Dfb	**0**	21 years, 1985-2007	IV before & after	IV parameters	2.1 kWp mc-Si	Façade	No visual defects.
[2]	Stockholm, Sweden (59.3°N, 19°E)	Dfb	**-0.17**	25 years, 1981-2006	IV before & after	IV parameters	660 Wp mc-Si	Rooftop/façade	Some encapsulant bubbling, corroded contact grids; one case of minor delamination; one module with hotspot failure.
[70]	Grimstad, Norway (58.3°N, 8°E)	Dfb	**-0.17**	4 years, 2014-2018	IV near STC	IV parameters	940 W mc-Si	Rooftop, 39° tilt	Degradation mostly from short-circuit current.
[69]	Grimstad, Norway (58.3°N, 8°E)	Dfb	**-1.0**	10 years	IV before & after	IV parameters	1.0 kWp mc-Si	Rooftop, 58° tilt, 180° azimuth	
[68]	Poland (51.9°N, 23.2°E)	Dfb	**-0.07**	4 years, 2015-2018	Calculated from paper	Specific yield, annual	21.3 kWp mc-Si	Ground, 34° tilt, 180° azimuth	

TABLE 3 Cont.: Existing cold climate degradation studies in the literature

Ref.	Location	Köppen -Geiger Code	PLR (%/year)	Years Covered	Analysis Method	Data	Module Information	System Configuration	Reported Issues
[67]	Wendelstein, Germany (47.7°N, 12°E)	ET	**0**	3 years, 1991-1994	Calculated from paper	PR, monthly	31.5 kWp mc-Si and c-Si	Ground, 60° tilt	
[41]	Zugspitze, Germany (47.4°N, 11°E)	ET	**-0.37**	3 years	IV before & after	IV parameters	7 modules	Rooftop, 45° tilt	Some cell breakage; one metal frame destroyed by snow and ice; high snowfall and wind.
[65]	Burgdorf, Switzerland (47.1°N, 8°E)	Dfb	**-1.09**	8 years, 2002-2010	Calculated from paper	DC efficiency, monthly	3.18 kWp c- Si	Rooftop, 30° tilt	
[1]	Domat, Switzerland (46.8°N, 9°E)	Dfb	**-0.58**	12 years, 1989-2002	Calculated from paper	Energy yield, monthly	104 kWp mc-Si	Sound barrier, 45° tilt, 180° and 155° azimuth	Leakage current found under wet conditions; inverter failure after 11 years; 21 modules damaged and 12 modules stolen during operation.
[66]	Birg, Switzerland (46.6°N, 8°E)	ET	**-0.19**	8 years, 2002-2010	Calculated from paper	DC efficiency, monthly	c-Si	Rooftop, 90° tilt	
[65]	Jungfraujoch, Switzerland (46.6°N, 8°E)	ET	**-0.19**	10 years, 1993-2004	Calculated from paper	PR, 5-minute	1.15 kWp c-Si	Façade, 192° and 207° azimuths	Windstorms of 250km/h; irradiance peaks >1700W/m^2; some instances of delamination from moisture ingress.
[63]	Bolzano, Italy (46.5°N, 11.3°E)	Dfb	**-0.5**	8 years, 2011-2019	Average of various methods	AC power	4.2 kWp mc-Si	Ground, 30° tilt, 180° azimuth	Missing first 6 months of operational data
[64]	Varennes, Canada (45.7°N, 73°W)	Dfb	**-0.6**	23 years, 1992-2015	IV before & after	IV parameters	16.7 kWp c-Si	Rooftop, 45° tilt	Freeze-thaw led to moisture ingress, busbar corrosion.
[63]	Williston, USA (44.4°N, 73.1°W)	Dfb	**-0.03**	3 years, 2015-2018	Average of various methods	AC power	3.2 kWp mc-Si	Ground, 35° tilt, 180° azimuth	

Chapter 7

Summary & outlook

The path forward in the next few years
Will bring to light more technological advances.
Solar energy will reach new frontiers
To mitigate CO_2 damages.

❄ ❄ ❄

Due to their scalability and affordability, PV technologies are poised to help decarbonize high latitude and alpine regions. The results presented as a part of this thesis support on-going efforts to characterize, predict, and optimize PV cell and system level performance under high latitude operating conditions found throughout northern regions, such as in the presence of snow, cool temperatures, low solar elevation angles, high air mass, and strong seasonal fluctuations in solar resource.

This thesis consists of six research articles, published or submitted for publication in scientific peer-reviewed journals. In Section 5.1, the impact of high air mass illumination was characterized for high efficiency and high bifaciality SHJ solar cells. Research efforts, such as this, demonstrate that location-specific device optimization is possible as a contrast to optimizations that are typically performed under the standard solar spectrum of AM1.5G. In the case of SHJ devices, passivating layers could be made thicker at higher latitudes due to less UV light content. This would add the benefit of further passivation to front and rear surfaces with a smaller trade-off to parasitic absorption in these layers. Further studies in the field on SHJ modules would need to be conducted to confirm cell optimization routines. These results suggest that design changes could be made on the solar cell level to better tailor for performance in high latitudes. However, given the importance of energy security and reliability in

high latitude locations, in practice the design parameters which may be best to optimize are on the system-level.

In Section 5.2, an extension to current drafted IEC bifacial measurement standards was speculated. To incorporate the method I proposed in this article, adaptations would need to be made to align with standard-creation protocols. For instance, rather than calibrating the method using a year of hourly data, the calibration would need to be instead done with a single normal-incidence illumination of AM1.5G on the front surface of a "standard" module. An appropriate selection would need to be made regarding standard module parameters (module size, frame, ground clearance, and tilt) and reviewed by the international community. The resulting rear plane-of-array irradiance could be calculated for different ground albedos and incorporated into an official standard. Nonetheless, indoor measurement standards are designed for technology inter-comparisons and predicting accurately the performance of the technologies in the field requires detailed PV energy yield models.

In Section 6.1, an analysis of the effect of row spacing, tilt, and inter-row shading losses was examined as a function of latitude, up to 75°N. This research has helped develop an understanding of system sensitivity to row spacing in mid-to-high latitudes. With emerging E-W vertical PV systems, this work has also provided further guidelines on how these systems must be spaced in comparison with conventional equator-facing fixed-tilt systems and SAT systems. This research could be developed further such that the empirical equations provided are a function of target shading loss and latitude. This would allow users additional flexibility in determining appropriate row spacing for their needs in mid-and-high latitudes.

In Section 6.2, the irradiance modelling uncertainty associated with broadband and spectral albedo assumptions was characterized as a function of latitude. Particularly for bifacial PV systems with high bifaciality $>$80%, an understanding of the sensitivity of performance predictions to rear-side environmental inputs is critical. In this work, I demonstrated that ground reflections compose a significant portion of total irradiance received on bifacial and monofacial modules in high latitude locations. This emphasizes the importance of high quality albedo inputs in cold and snowy locations. Operational characteristics like inhomogeneous ground cover, uneven ground, and specular reflections will cause further uncertainty in practice. Understanding the spectral nature of rear-side irradiance is anticipated to be even more important for emerging bifacial tandem structures.

In Section 6.3, a model validation was performed using vertical PV field data collected in two locations for five PV system-level models - bifacial_radiance, bifacialVF, SAM, PVSyst, and DUET. Models, such as these, are being used to simulate emerging vertical PV systems for design, planning, and monitoring purposes. However, these models have been developed and validated for equator-facing fixed-tilt systems and/or SAT systems at low-to-mid latitudes.

In this work, I demonstrated model validation at 65°N and showed that the PV models all experience higher RMSE during cloudy conditions, in the presence of snow, and at low irradiance light levels - conditions more common at high latitudes and especially during winter months. Vertical PV systems tend to result in higher modelling uncertainty due to a higher dependence on ground-reflected and diffuse light, as well as high angles-of-incidence during high irradiance hours of the day. To improve test-site and weather station data quality, continuous snow monitoring and regular maintenance and cleaning was suggested. This work supports research into location-specific optimization of sky models for high latitude locations.

In Section 6.4, an analysis and review of PV degration rates in cold, snowy climates was presented. This manuscript highlights the gap in northern PV field data to-date in high latitude, cold climate regions. High quality weather station and PV site monitoring is challenging in these environments and long-term data is scarce due to the relatively young age of most deployed PV systems. When longer-term data exists, it may be hard to know if it is relevant for modern modules, which now have significantly larger areas, half-cut and bifacial cells, thinner glass, and higher efficiencies. Continuous research efforts are required in this field to monitor recent and up-coming deployments over the next few decades. This review supports the finding that PV systems tend to degrade slower in colder environments, benefiting primarily from cooler operating temperatures. Effects such as snow load, freeze-thaw stress, and moisture ingress are failure modes to be cautious of in cold climates.

❄ ❄ ❄

LE POEM DU SOLEIL

Artization, M.K.[1]; writing – original draft, E.M.T.

i – TWO-FACED

Plants have cells
and solar panels have cells
Coincidence?
The cells on the grass
give their leftover light to
the solar cells
Is it kindness?
Or simple rear irradiance?

ii – BIFACIAL

The two-faced sun, which illuminates the same hand that it burns you with,
which regularly gives too much,
then too little,
as seen by dry grass and
snow hours. . .
The sun's spectral faces are really
A DUET

[1]Poem by Monika Kitor

References

[1] International Energy Agency, Photovoltaic Power Systems Programme, "Snapshot of Global PV Markets - 2023," *Report IEA-PVPS T1-42:2024*, pp. 1–25, 2024.

[2] N. M. Haegel, H. Atwater, T. Barnes, C. Breyer, A. Burrell, Y.-M. Chiang, S. De Wolf, B. Dimmler, D. Feldman, S. Glunz, J. C. Goldschmidt, D. Hochschild, R. Inzunza, I. Kaizuka, B. Kroposki, S. Kurtz, S. Leu, R. Margolis, K. Matsubara, A. Metz, W. K. Metzger, M. Morjaria, S. Niki, S. Nowak, I. M. Peters, S. Philipps, T. Reindl, A. Richter, D. Rose, K. Sakurai, R. Schlatmann, M. Shikano, W. Sinke, R. Sinton, B. Stanbery, M. Topic, W. Tumas, Y. Ueda, J. Van De Lagemaat, P. Verlinden, M. Vetter, E. Warren, M. Werner, M. Yamaguchi, and A. W. Bett, "Terawatt-scale photovoltaics: Transform global energy," *Science*, vol. 364, no. 6443, pp. 836–838, May 2019. doi: 10.1126/science.aaw1845. https://www.science.org/doi/10.1126/science.aaw1845

[3] U. Jahn and W. Nasse, "Analysis of Long-term Performance and Reliability of Photovoltaic Systems," *IEA Task 2 Draft Report*, pp. 1–65, 2003.

[4] J. Hedström and L. Palmblad, "Performance of old PV modules: measurement of 25 year old crystalline silicon modules," *Technical Report ELFORSK-01-71*, pp. 1–20, 2006.

[5] I. E. Agency, "World Energy Outlook 2022," IEA, Paris, Tech. Rep., 2022. https://www.iea.org/reports/world-energy-outlook-2022

[6] International Energy Agency, "IEA50 Countries and Regions," 2024. https://www.iea.org/countries

[7] A. Toktarova, V. Walter, L. Göransson, and F. Johnsson, "Interaction between electrified steel production and the north European electricity system," *Applied Energy*, vol. 310, p. 118584, Mar. 2022. doi: 10.1016/j.apenergy.2022.118584. https://linkinghub.elsevier.com/retrieve/pii/S0306261922000654

[8] L. Karttunen, S. Jouttijärvi, A. Poskela, H. Palonen, H. Huerta, M. Todorović, S. Ranta, and K. Miettunen, "Comparing methods for the long-term performance assessment of bifacial photovoltaic modules in Nordic conditions," *Renewable Energy*, vol. 219, p. 119473, Dec. 2023. doi: 10.1016/j.renene.2023.119473. https://linkinghub.elsevier.com/retrieve/pii/S0960148123013885

[9] M. B. Øgaard, B. L. Aarseth, A. F. Skomedal, H. N. Riise, S. Sartori, and J. H. Selj, "Identifying snow in photovoltaic monitoring data for improved snow loss modeling and snow detection," *Solar Energy*, vol. 223, pp. 238–247, Jul. 2021. doi: 10.1016/j.solener.2021.05.023. https://linkinghub.elsevier.com/retrieve/pii/S0038092X21003868

[10] C. Baldus-Jeursen, A. L. Petsiuk, S.-A. Rheault, S. Pelland, A. Côté, Y. Poissant, and J. M. Pearce, "Snow Losses for Photovoltaic Systems: Validating the Marion and Townsend Models," *IEEE Journal of Photovoltaics*, vol. 13, no. 4, pp. 610–620, Jul. 2023. doi: 10.1109/JPHOTOV.2023.3264644. https://ieeexplore.ieee.org/document/10124088/

[11] C. Pike, D. Riley, H. Toal, and L. Burnham, "Presenting a Model to Predict Changing Snow Albedo for Improving Photovoltaic Performance Simulation," *Solar*, vol. 4, no. 3, pp. 422–439, Aug. 2024. doi: 10.3390/solar4030019. https://www.mdpi.com/2673-9941/4/3/19

[12] R. E. Pawluk, Y. Chen, and Y. She, "Photovoltaic electricity generation loss due to snow – A literature review on influence factors, estimation, and mitigation," *Renewable and Sustainable Energy Reviews*, vol. 107, pp. 171–182, Jun. 2019. doi: 10.1016/j.rser.2018.12.031. https://linkinghub.elsevier.com/retrieve/pii/S1364032118308268

[13] P. E. Campana, B. Stridh, T. Hörndahl, S.-E. Svensson, S. Zainali, S. M. Lu, T. E. K. Zidane, P. De Luca, S. Amaducci, and M. Colauzzi, "Experimental results, integrated model validation, and economic aspects of agrivoltaic systems at northern latitudes," *Journal of Cleaner Production*, vol. 437, p. 140235, Jan. 2024. doi: 10.1016/j.jclepro.2023.140235. https://linkinghub.elsevier.com/retrieve/pii/S0959652623043937

[14] P. E. Campana, B. Stridh, S. Zainali, S. M. Lu, U. Andersson, J. Nordstrom, P. Bergdahl, T. Horndahl, and S.-E. Svensson, "Evaluation of the first agrivoltaic system in Sweden," *Future Energy Center Report*, pp. 1–60, 2023.

[15] H. Haeberlin and B. Fachhochschule, "Grid Connected PV Plant Jungfraujoch (3454m) in the Swiss Alps: 10 Years of trouble-free Operation with Record Energy Yields," *19th European Photovoltaic Solar Energy Conference*, pp. 1–4, 2004.

[16] H. Gholami, H. Nils Røstvik, N. Manoj Kumar, and S. S. Chopra, "Lifecycle cost analysis (LCCA) of tailor-made building integrated photovoltaics (BIPV) façade: Solsmaragden case study in Norway," *Solar Energy*, vol. 211, pp. 488–502, Nov. 2020. doi: 10.1016/j.solener.2020.09.087. https://linkinghub.elsevier.com/retrieve/pii/S0038092X20310409

[17] A. Boute, "Off-grid renewable energy in remote Arctic areas: An analysis of the Russian Far East," *Renewable and Sustainable Energy Reviews*, vol. 59, pp. 1029–1037, Jun. 2016. doi: 10.1016/j.rser.2016.01.034. https://linkinghub.elsevier.com/retrieve/pii/S1364032116000642

[18] E. Usher, G. Jean, and G. Howell, "The use of photovoltaics in a northern climate," *Solar Energy Materials and Solar Cells*, vol. 34, no. 1-4, pp. 73–81, Sep. 1994. doi: 10.1016/0927-0248(94)90026-4. https://linkinghub.elsevier.com/retrieve/pii/0927024894900264

[19] I. Das and C. A. Canizares, "Renewable Energy Integration in Diesel-Based Microgrids at the Canadian Arctic," *Proceedings of the IEEE*, vol. 107, no. 9, pp. 1838–1856, Sep. 2019. doi: 10.1109/JPROC.2019.2932743. https://ieeexplore.ieee.org/document/8798665/

[20] A. Wills, C. Banister, M. Pellissier, and J. Berquist, "A multi-year analysis of Canadian Arctic historical weather data in support of solar and wind renewable energy deployment," *E3S Web of Conferences*, vol. 246, p. 03006, 2021. doi: 10.1051/e3sconf/202124603006. https://www.e3s-conferences.org/10.1051/e3sconf/202124603006

[21] D. Dumas and L. Gosselin, "Optimizing photovoltaic systems to decarbonize residential arctic buildings considering real consumption data and temporal mismatch," *Solar Energy*, vol. 275, p. 112560, Jun. 2024. doi: 10.1016/j.solener.2024.112560. https://linkinghub.elsevier.com/retrieve/pii/S0038092X24002548

[22] S. V. Obydenkova and J. M. Pearce, "Technical viability of mobile solar photovoltaic systems for indigenous nomadic communities in northern latitudes," *Renewable Energy*, vol. 89, pp. 253–267, Apr. 2016. doi: 10.1016/j.renene.2015.12.036. https://linkinghub.elsevier.com/retrieve/pii/S0960148115305425

[23] M. Tawalbeh, A. Al-Othman, F. Kafiah, E. Abdelsalam, F. Almomani, and M. Alkasrawi, "Environmental impacts of solar photovoltaic systems: A critical

review of recent progress and future outlook," *Science of The Total Environment*, vol. 759, p. 143528, Mar. 2021. doi: 10.1016/j.scitotenv.2020.143528. https://linkinghub.elsevier.com/retrieve/pii/S0048969720370595

[24] A. Skarin, P. Sandström, and M. Alam, "Out of sight of wind turbines—Reindeer response to wind farms in operation," *Ecology and Evolution*, vol. 8, no. 19, pp. 9906–9919, Oct. 2018. doi: 10.1002/ece3.4476. https://onlinelibrary.wiley.com/doi/10.1002/ece3.4476

[25] M. De Witt, H. Stefánsson, A. Valfells, and J. N. Larsen, "Energy resources and electricity generation in Arctic areas," *Renewable Energy*, vol. 169, pp. 144–156, May 2021. doi: 10.1016/j.renene.2021.01.025. https://linkinghub.elsevier.com/retrieve/pii/S0960148121000318

[26] N. Ninad, D. Turcotte, and Y. Poissant, "Analysis of PV-Diesel Hybrid Microgrids for Small Canadian Arctic Communities," *Canadian Journal of Electrical and Computer Engineering*, vol. 43, no. 4, pp. 315–325, 2020. doi: 10.1109/CJECE.2020.2995750. https://ieeexplore.ieee.org/document/9240086/

[27] C. Baldus-Jeursen, A. Côté, T. Deer, and Y. Poissant, "Analysis of photovoltaic module performance and life cycle degradation for a 23 year-old array in Quebec, Canada," *Renewable Energy*, vol. 174, pp. 547–556, Aug. 2021. doi: 10.1016/j.renene.2021.04.013. https://linkinghub.elsevier.com/retrieve/pii/S0960148121005255

[28] A. Zdyb and S. Gulkowski, "Performance Assessment of Four Different Photovoltaic Technologies in Poland," *Energies*, vol. 13, no. 1, p. 196, Jan. 2020. doi: 10.3390/en13010196. https://www.mdpi.com/1996-1073/13/1/196

[29] D. Verma, M. Tayyib, T. O. Saetre, and O.-M. Midtgard, "Outdoor Performance of 10 year Old a-Si and Poly-Si Modules in southern Norway conditions," in *2012 38th IEEE Photovoltaic Specialists Conference*. Austin, TX, USA: IEEE, Jun. 2012. doi: 10.1109/PVSC.2012.6318074. ISBN 978-1-4673-0066-7 978-1-4673-0064-3 978-1-4673-0065-0 pp. 002 368–002 371. http://ieeexplore.ieee.org/document/6318074/

[30] B. R. Paudyal and A. Gerd Imenes, "Performance assessment of field deployed multi-crystalline PV modules in Nordic conditions," in *2019 IEEE 46th Photovoltaic Specialists Conference (PVSC)*. Chicago, IL, USA: IEEE, Jun. 2019. doi: 10.1109/PVSC40753.2019.8980629. ISBN 978-1-72810-494-2 pp. 1377–1383. https://ieeexplore.ieee.org/document/8980629/

[31] E. B. Sveen, M. B. Øgaard, J. H. Selj, and G. Otnes, "PV System Degradation Rates in the Nordics," *37th European Photovoltaic Solar Energy Conference and Exhibition*, pp. 1–4, 2020.

[32] Y. Poissant, D. Thevenard, and D. Turcotte, "Performance Monitoring of the Nunavut Arctic College PV System: Nine Years of Reliable Electricity Generation," *CanmetENERGY*, 2004.

[33] D. C. Jordan, B. Marion, C. Deline, T. Barnes, and M. Bolinger, "PV field reliability status—Analysis of 100 000 solar systems," *Progress in Photovoltaics: Research and Applications*, vol. 28, no. 8, pp. 739–754, Aug. 2020. doi: 10.1002/pip.3262. https://onlinelibrary.wiley.com/doi/10.1002/pip.3262

[34] M. B. Øgaard, H. N. Riise, H. Haug, S. Sartori, and J. H. Selj, "Photovoltaic system monitoring for high latitude locations," *Solar Energy*, vol. 207, pp. 1045–1054, Sep. 2020. doi: 10.1016/j.solener.2020.07.043. https://linkinghub.elsevier.com/retrieve/pii/S0038092X20307751

[35] A. Granlund, M. Lindh, T. Vikberg, and A. M. Petersson, "Evaluation of Snow Removal Methods for Rooftop Photovoltaics," *8th World Conference on Photovoltaic Energy Conversion*, pp. 1122–1128, 2022.

[36] A. Peinado Gonzalo, A. Pliego Marugán, and F. P. García Márquez, "Survey of maintenance management for photovoltaic power systems," *Renewable and Sustainable Energy Reviews*, vol. 134, p. 110347, Dec. 2020. doi: 10.1016/j.rser.2020.110347. https://linkinghub.elsevier.com/retrieve/pii/S1364032120306353

[37] F. Bockelmann, A.-K. Dreier, J. Zimmermann, and M. Peter, "Renewable energy in Antarctica - Photovoltaic for Neumayer Station III," *Solar Energy Advances*, vol. 2, p. 100026, 2022. doi: 10.1016/j.seja.2022.100026. https://linkinghub.elsevier.com/retrieve/pii/S2667113122000146

[38] A. Reinders, P. Verlinden, W. v. Sark, and A. Freundlich, Eds., *Photovoltaic solar energy: from fundamentals to applications*, first edition ed. Chichester, West Sussex: Wiley, 2017. ISBN 978-1-118-92746-5

[39] NREL, "NREL Best Research-Cell Efficiency Chart," Aug. 2024. https://www.nrel.gov/pv/cell-efficiency.html

[40] J. Zuboy, M. Springer, E. Palmiotti, J. Karas, B. Smith, M. Woodhouse, and T. Barnes, "DuraMAT Technology Scouting Report: Assessing Module Reliability Risks Associated with Projected Technological Changes," 2023.

[41] VDMA, "International Technology Roadmap for Photovoltaics (ITRPV): 15th Edition," p. 82, 2024.

[42] M. Bolinger and G. Bolinger, "Land Requirements for Utility-Scale PV: An Empirical Update on Power and Energy Density," *IEEE Journal of Photovoltaics*, vol. 12, no. 2, pp. 589–594, Mar. 2022. doi: 10.1109/JPHOTOV.2021.3136805. https://ieeexplore.ieee.org/document/9676427/

[43] C. Yu, W. Van Sark, and E. Alsema, "Unraveling the photovoltaic technology learning curve by incorporation of input price changes and scale effects," *Renewable and Sustainable Energy Reviews*, vol. 15, no. 1, pp. 324–337, Jan. 2011. doi: 10.1016/j.rser.2010.09.001. https://linkinghub.elsevier.com/retrieve/pii/S1364032110002881

[44] D. Feldman, J. Zuboy, K. Dummit, D. Stright, M. Heine, S. Grossman, and R. Margolis, "Spring 2024 Solar Industry Update," Tech. Rep. NREL/PR–7A40-90042, 2376145, MainId:91820, May 2024. https://www.osti.gov/servlets/purl/2376145/

[45] C. D. Rodríguez-Gallegos, H. Liu, O. Gandhi, J. P. Singh, V. Krishnamurthy, A. Kumar, J. S. Stein, S. Wang, L. Li, T. Reindl, and I. M. Peters, "Global Techno-Economic Performance of Bifacial and Tracking Photovoltaic Systems," *Joule*, vol. 4, no. 7, pp. 1514–1541, Jul. 2020. doi: 10.1016/j.joule.2020.05.005. https://linkinghub.elsevier.com/retrieve/pii/S2542435120301884

[46] J. S. Stein, D. Riley, M. Lave, C. Hansen, C. Deline, and F. Toor, "Outdoor Field Performance from Bifacial Photovoltaic Modules and Systems," in *2017 IEEE 44th Photovoltaic Specialist Conference (PVSC)*. Washington, DC: IEEE, Jun. 2017. doi: 10.1109/PVSC.2017.8366042. ISBN 978-1-5090-5605-7 pp. 3184–3189. https://ieeexplore.ieee.org/document/8366042/

[47] E. Molin, B. Stridh, A. Molin, and E. Wackelgard, "Experimental Yield Study of Bifacial PV Modules in Nordic Conditions," *IEEE Journal of Photovoltaics*, vol. 8, no. 6, pp. 1457–1463, Nov. 2018. doi: 10.1109/JPHOTOV.2018.2865168. https://ieeexplore.ieee.org/document/8449214/

[48] M. T. Patel, R. A. Vijayan, R. Asadpour, M. Varadharajaperumal, M. R. Khan, and M. A. Alam, "Temperature-dependent energy gain of bifacial PV farms: A global perspective,"

Applied Energy, vol. 276, p. 115405, Oct. 2020. doi: 10.1016/j.apenergy.2020.115405. https://linkinghub.elsevier.com/retrieve/pii/S030626192030917X

[49] Climate Watch, "Historic GHG Emissions," 2021. https://www.climatewatchdata.org/ghg-emissions?end_year=2021&sectors=total-excluding-lucf&start_year=1990

[50] Canada Energy Regulator, "Canada's Energy Future Data Appendices: Electricty Generation," 2023. https://apps.cer-rec.gc.ca/ftrppndc/dflt.aspx?GoCTemplateCulture=en-CA

[51] Canada Energy Regulator, "Provincial and territorial energy profiles," 2024. https://www.cer-rec.gc.ca/en/data-analysis/energy-markets/provincial-territorial-energy-profiles/

[52] Natural Resources Canada, "Photovoltaic potential and solar resource maps of Canada," 2024. https://natural-resources.canada.ca/energy/energy-sources-distribution/renewables/solar-photovoltaic-energy/tools-solar-photovoltaic-energy/photovoltaic-and-solar-resource-maps/18366

[53] Canadian Renewable Energy Association, "NEWS RELEASE: New 2023 data shows 11.2% growth for wind, solar & energy storage," 2024. https://renewablesassociation.ca/news-release-new-2023-data-shows-11-2-growth-for-wind-solar-energy-storage/

[54] D. W. McKenney, S. Pelland, Y. Poissant, R. Morris, M. Hutchinson, P. Papadopol, K. Lawrence, and K. Campbell, "Spatial insolation models for photovoltaic energy in Canada," *Solar Energy*, vol. 82, no. 11, pp. 1049–1061, Nov. 2008. doi: 10.1016/j.solener.2008.04.008. https://linkinghub.elsevier.com/retrieve/pii/S0038092X08000996

[55] E. Becquerel, "Mémoire sur les effets électriques produits sous l'influence des rayons solaires," *Comptes Rendus*, vol. 9, pp. 561–567, 1839.

[56] C. Fritts, "On the Fritts selenium cell and batteries," *Van Nostrands Engineering Magazine*, vol. 32, pp. 388–395, 1885.

[57] D. M. Chapin, C. S. Fuller, and G. L. Pearson, "A New Silicon *p-n* Junction Photocell for Converting Solar Radiation into Electrical Power," *Journal of Applied Physics*, vol. 25, no. 5, pp. 676–677, May 1954. doi: 10.1063/1.1721711. https://pubs.aip.org/jap/article/25/5/676/160783/A-New-Silicon-p-n-Junction-Photocell-for

[58] J. Pankove, *Optical Processes in Semiconductors*. New York: Dover Publications Inc., 1971.

[59] J. Nelson, *The Physics of Solar Cells*. Imperial College, UK: Imperial College Press, 2003.

[60] M. Beattie, "Semiconductor Materials and Devices for High Efficiency Broadband and Monochromatic Photovoltaic Energy Conversion," Ph.D. dissertation, University of Ottawa, 2021.

[61] W. Zulehner, "Czochralski Growth of Silicon," *Journal of Crystal Growth*, vol. 65, pp. 189–213, 1983. doi: https://doi.org/10.1016/0022-0248(83)90051-9

[62] I. Institute, "Semiconductors on NSM." https://www.ioffe.ru/SVA/NSM/Semicond/

[63] C. Kittel, *Introduction to solid state physics*, 8th ed. Hoboken, NJ: Wiley, 2005. ISBN 978-0-471-41526-8

[64] A. Schenk, *Advanced Physical Models for Silicon Device Simulation*, ser. Computational Microelectronics, S. Selberherr, Ed. Vienna: Springer Vienna, 1998. ISBN 978-3-7091-7334-3 978-3-7091-6494-5. http://link.springer.com/10.1007/978-3-7091-6494-5

[65] M. S. Kim, J. H. Lee, and M. K. Kwak, "Review: Surface Texturing Methods for Solar Cell Efficiency Enhancement," *International Journal of Precision Engineering and Manufacturing*, vol. 21, no. 7, pp. 1389–1398, Jul. 2020. doi: 10.1007/s12541-020-00337-5. http://link.springer.com/10.1007/s12541-020-00337-5

[66] W. Shockley and H. J. Queisser, "Detailed Balance Limit of Efficiency of *p-n* Junction Solar Cells," *Journal of Applied Physics*, vol. 32, no. 3, pp. 510–519, Mar. 1961. doi: 10.1063/1.1736034. https://pubs.aip.org/jap/article/32/3/510/505950/Detailed-Balance-Limit-of-Efficiency-of-p-n

[67] M. A. Green, E. D. Dunlop, M. Yoshita, N. Kopidakis, K. Bothe, G. Siefer, D. Hinken, M. Rauer, J. Hohl-Ebinger, and X. Hao, "Solar cell efficiency tables (Version 64)," *Progress in Photovoltaics: Research and Applications*, vol. 32, no. 7, pp. 425–441, Jul. 2024. doi: 10.1002/pip.3831. https://onlinelibrary.wiley.com/doi/10.1002/pip.3831

[68] C. A. Gueymard, D. Myers, and K. Emery, "Proposed Reference Irradiance Spectra for Solar Energy Systems Testing," *Solar Energy*, vol. 73, no. 6, pp. 443–467, 2002. doi: https://doi.org/10.1016/S0038-092X(03)00005-7

[69] M. P. Thekaekara, "Survey of the Literature on the Solar Constant and the Spectral Distribution of Solar Radiant Flux," *NASA SP-74*, pp. 1–47, 1965.

[70] G03 Committee, "Tables for Reference Solar Spectral Irradiances: Direct Normal and Hemispherical on 37 Tilted Surface," 2020. http://www.astm.org/cgi-bin/resolver.cgi?G173-03R20

[71] P. Blanc, B. Espinar, N. Geuder, C. Gueymard, R. Meyer, R. Pitz-Paal, B. Reinhardt, D. Renné, M. Sengupta, L. Wald, and S. Wilbert, "Direct normal irradiance related definitions and applications: The circumsolar issue," *Solar Energy*, vol. 110, pp. 561–577, Dec. 2014. doi: 10.1016/j.solener.2014.10.001. https://linkinghub.elsevier.com/retrieve/pii/S0038092X14004824

[72] E. M. Tonita, C. E. Valdivia, A. C. J. Russell, M. Martinez-Szewczyk, M. I. Bertoni, and K. Hinzer, "Quantifying spectral albedo effects on bifacial photovoltaic module measurements and system model predictions," *Progress in Photovoltaics: Research and Applications*, vol. 32, no. 7, pp. 468–480, Jul. 2024. doi: 10.1002/pip.3789. https://onlinelibrary.wiley.com/doi/10.1002/pip.3789

[73] C. A. Gueymard, V. Lara-Fanego, M. Sengupta, and Y. Xie, "Surface albedo and reflectance: Review of definitions, angular and spectral effects, and intercomparison of major data sources in support of advanced solar irradiance modeling over the Americas," *Solar Energy*, vol. 182, pp. 194–212, Apr. 2019. doi: 10.1016/j.solener.2019.02.040. https://linkinghub.elsevier.com/retrieve/pii/S0038092X19301653

[74] T. C. R. Russell, R. Saive, A. Augusto, S. G. Bowden, and H. A. Atwater, "The Influence of Spectral Albedo on Bifacial Solar Cells: A Theoretical and Experimental Study," *IEEE Journal of Photovoltaics*, vol. 7, no. 6, pp. 1611–1618, Nov. 2017. doi: 10.1109/JPHOTOV.2017.2756068. http://ieeexplore.ieee.org/document/8063403/

[75] A. W. Walker, "Bandgap engineering of multi-junction solar cells using nanostructures for enhanced performance under concentrated illumination," Ph.D. dissertation, University of Ottawa, 2013.

[76] Synopsys, "Sentaurus™ Device User Guide Version O-2018.06," pp. 1–1488, 2018.

[77] Synopsys, "Sentaurus Technology Template: EQE and I-V Curve Calculation of Textured Solar Cells Using Raytracer," 2009.

[78] G. Létay, "Reducing Optical Generation Profiles from 3D to 1D," 2015.

[79] H. Mori, "Radiation energy transducing device," US/JAPAN Patent US3 278 811A, 1966.

[80] A. Cuevas, A. Luque, J. Eguren, and J. Del Alamo, "50 per cent more output power from an albedo-collecting flat panel using bifacial solar cells," *Solar Energy*, vol. 29, no. 5, pp. 419–420, 1982. doi: 10.1016/0038-092X(82)90078-0. https://linkinghub.elsevier.com/retrieve/pii/0038092X82900780

[81] R. Hezel, "Novel applications of bifacial solar cells," *Progress in Photovoltaics: Research and Applications*, vol. 11, no. 8, pp. 549–556, Dec. 2003. doi: 10.1002/pip.510. https://onlinelibrary.wiley.com/doi/10.1002/pip.510

[82] S. Ayala Pelaez, C. Deline, S. M. MacAlpine, B. Marion, J. S. Stein, and R. K. Kostuk, "Comparison of Bifacial Solar Irradiance Model Predictions With Field Validation," *IEEE Journal of Photovoltaics*, vol. 9, no. 1, pp. 82–88, Jan. 2019. doi: 10.1109/JPHOTOV.2018.2877000. https://ieeexplore.ieee.org/document/8534404/

[83] I. E. Commission, "IEC 60904: Photovoltaic devices - Part 1-2: Measurement of current-voltage characteristics of bifacial photovoltaic (PV) devices," 2019.

[84] S. Ayala Peláez, "Bifacial solar modules system design, modeling, and performance," Ph.D. dissertation, University of Arizona, 2019.

[85] J. Stein, C. Reise, J. Castro, G. Friesen, G. Maugeri, E. Urrejola, and S. Ranta, "Bifacial Photovoltaic Modules and Systems: Experience and Results from International Research and Pilot Applications," International Energy Agency, Tech. Rep. SAND–2021-4835R, IEA–PVPS T13-14:2021, 1779379, Apr. 2021. https://www.osti.gov/servlets/purl/1779379/

[86] R. Kopecek and J. Libal, "Bifacial Photovoltaics 2021: Status, Opportunities and Challenges," *Energies*, vol. 14, no. 8, p. 2076, Apr. 2021. doi: 10.3390/en14082076. https://www.mdpi.com/1996-1073/14/8/2076

[87] D. Berrian, J. Libal, M. Klenk, H. Nussbaumer, and R. Kopecek, "Performance of Bifacial PV Arrays With Fixed Tilt and Horizontal Single-Axis Tracking: Comparison of Simulated and Measured Data," *IEEE Journal of Photovoltaics*, vol. 9, no. 6, pp. 1583–1589, Nov. 2019. doi: 10.1109/JPHOTOV.2019.2924394. https://ieeexplore.ieee.org/document/8809374/

[88] L. Kreinin, N. Bordin, A. Karsenty, A. Drori, D. Grobgeld, and N. Eisenberg, "PV module power gain due to bifacial design. Preliminary experimental and simulation data," in *2010 35th IEEE Photovoltaic Specialists Conference*. Honolulu, HI, USA: IEEE, Jun. 2010. doi: 10.1109/PVSC.2010.5615874. ISBN 978-1-4244-5890-5 pp. 002 171–002 175. http://ieeexplore.ieee.org/document/5615874/

[89] I. Shoukry, J. Libal, R. Kopecek, E. Wefringhaus, and J. Werner, "Modelling of Bifacial Gain for Stand-alone and in-field Installed Bifacial PV Modules," *Energy Procedia*, vol. 92, pp. 600–608, Aug. 2016. doi: 10.1016/j.egypro.2016.07.025. https://linkinghub.elsevier.com/retrieve/pii/S1876610216304520

[90] H. Tang, S. Ma, Y. Lv, Z. Li, and W. Shen, "Optimization of rear surface roughness and metal grid design in industrial bifacial PERC solar cells," *Solar Energy Materials and Solar Cells*, vol. 216, p. 110712, Oct. 2020. doi: 10.1016/j.solmat.2020.110712. https://linkinghub.elsevier.com/retrieve/pii/S0927024820303111

[91] S. Park, H. Park, Y. Kang, H.-S. Lee, and D. Kim, "Analysis of aluminum back surface field at different wafer specifications in crystalline silicon solar cells," *Current Applied Physics*, vol. 16, no. 9, pp. 1062–1068, Sep. 2016. doi: 10.1016/j.cap.2016.05.016. https://linkinghub.elsevier.com/retrieve/pii/S1567173916301298

[92] A. Cuevas, A. Luque, J. Eguren, and J. Del Alamo, "High efficiency bifacial back surface field solar cells," *Solar Cells*, vol. 3, no. 4, pp. 337–340, Jul. 1981. doi: 10.1016/0379-6787(81)90024-7. https://linkinghub.elsevier.com/retrieve/pii/0379678781900247

[93] T. Dullweber, H. Schulte-Huxel, S. Blankemeyer, H. Hannebauer, S. Schimanke, U. Baumann, R. Witteck, R. Peibst, M. Köntges, R. Brendel, and Y. Yao, "Present status and future perspectives of bifacial PERC+ solar cells and modules," *Japanese Journal of Applied Physics*, vol. 57, no. 8S3, p. 08RA01, Aug. 2018. doi: 10.7567/JJAP.57.08RA01. https://iopscience.iop.org/article/10.7567/JJAP.57.08RA01

[94] T. S. Liang, M. Pravettoni, C. Deline, J. S. Stein, R. Kopecek, J. P. Singh, W. Luo, Y. Wang, A. G. Aberle, and Y. S. Khoo, "A review of crystalline silicon bifacial photovoltaic performance characterisation and simulation," *Energy & Environmental Science*, vol. 12, no. 1, pp. 116–148, 2019. doi: 10.1039/C8EE02184H. http://xlink.rsc.org/?DOI=C8EE02184H

[95] T. Mishima, M. Taguchi, H. Sakata, and E. Maruyama, "Development status of high-efficiency HIT solar cells," *Solar Energy Materials and Solar Cells*, vol. 95, no. 1, pp. 18–21, Jan. 2011. doi: 10.1016/j.solmat.2010.04.030. https://linkinghub.elsevier.com/retrieve/pii/S0927024810002205

[96] D. K. Ghosh, S. Bose, G. Das, S. Acharyya, A. Nandi, S. Mukhopadhyay, and A. Sengupta, "Fundamentals, present status and future perspective of TOPCon solar cells: A comprehensive review," *Surfaces and Interfaces*, vol. 30, p. 101917, Jun.

2022. doi: 10.1016/j.surfin.2022.101917. https://linkinghub.elsevier.com/retrieve/pii/S2468023022001973

[97] H. Lin, M. Yang, X. Ru, G. Wang, S. Yin, F. Peng, C. Hong, M. Qu, J. Lu, L. Fang, C. Han, P. Procel, O. Isabella, P. Gao, Z. Li, and X. Xu, "Silicon heterojunction solar cells with up to 26.81% efficiency achieved by electrically optimized nanocrystalline-silicon hole contact layers," *Nature Energy*, vol. 8, no. 8, pp. 789–799, May 2023. doi: 10.1038/s41560-023-01255-2. https://www.nature.com/articles/s41560-023-01255-2

[98] S. Glunz, B. Steinhauser, J.-I. Polzin, C. Luderer, B. Grubel, T. Niewelt, A. Okasha, M. Bories, H. Nagel, K. Krieg, F. Feldmann, A. Richter, M. Bivour, and M. Hermle, "Silicon-based passivating contacts: The TOPCon route," *Progress in Photovoltaics: Research and Applications*, vol. 31, pp. 341–359, 2023. doi: https://doi.org/10.1002/pip.3522. https://doi.org/10.1002/pip.3522

[99] E. Urrejola, F. Valencia, E. Fuentealba, C. Deline, S. A. Pelaez, J. Meydbray, T. Clifford, R. Kopecek, and J. S. Stein, "bifiPV2020 Bifacial Workshop: A Technology Overview," *Renewable Energy*, 2020.

[100] J. Jang and K. Lee, "Practical Performance Analysis of a Bifacial PV Module and System," *Energies*, vol. 13, no. 17, p. 4389, Aug. 2020. doi: 10.3390/en13174389. https://www.mdpi.com/1996-1073/13/17/4389

[101] J. D. Huyeng, E. Lohmüller, B. Shabanzadeh, C. Reichel, T. Rößler, J. Weber, M. Hofmann, D. Von Kutzleben, N. Abdel Latif, A. Kraft, H. Neuhaus, F. Clement, and R. Preu, "Challenges and advantages of cut solar cells for shingling and half-cell modules," *EPJ Photovoltaics*, vol. 15, p. 22, 2024. doi: 10.1051/epjpv/2024019. https://www.epj-pv.org/10.1051/epjpv/2024019

[102] B. Weller and L. Tautenhahn, "Mechanical challenge of frameless PV-modules," in *2010 12th IEEE Intersociety Conference on Thermal and Thermomechanical Phenomena in Electronic Systems*. Las Vegas, NV, USA: IEEE, Jun. 2010. doi: 10.1109/ITHERM.2010.5501292. ISBN 978-1-4244-5342-9 pp. 1–5. http://ieeexplore.ieee.org/document/5501292/

[103] K. Geiger, "Ana Dyreson: solar energy in cold climates," Feb. 2023. https://blogs.mtu.edu/engineering/2023/02/15/ana-dyreson-solar-energy-in-cold-climates/

[104] C. C. H. R. Center, "RTF Solar PV," 2007. http://cchrc.rcs.alaska.edu/project.php?name=FglONjYo

[105] A. C. J. Russell, C. E. Valdivia, C. Bohemier, J. E. Haysom, and K. Hinzer, "DUET: A Novel Energy Yield Model With 3-D Shading for Bifacial Photovoltaic Systems," *IEEE Journal of Photovoltaics*, vol. 12, no. 6, pp. 1576–1585, Nov. 2022. doi: 10.1109/JPHOTOV.2022.3185546. https://ieeexplore.ieee.org/document/9813738/

[106] L. Fernández-Ahumada, J. Ramírez-Faz, R. López-Luque, M. Varo-Martínez, I. Moreno-García, and F. Casares De La Torre, "A novel backtracking approach for two-axis solar PV tracking plants," *Renewable Energy*, vol. 145, pp. 1214–1221, Jan. 2020. doi: 10.1016/j.renene.2019.06.062. https://linkinghub.elsevier.com/retrieve/pii/S0960148119308900

[107] C. Deline, S. Ayala Pelaez, S. MacAlpine, and C. Olalla, "Estimating and parameterizing mismatch power loss in bifacial photovoltaic systems," *Progress in Photovoltaics: Research and Applications*, vol. 28, no. 7, pp. 691–703, Jul. 2020. doi: 10.1002/pip.3259. https://onlinelibrary.wiley.com/doi/10.1002/pip.3259

[108] P. Ineichen, R. Perez, R. Seal, E. L. Maxwell, and A. Zalenka, "Dynamic global-to-direct irradiance conversion models," *ASHRAE Transactions*, vol. 98, no. 1, pp. 354–369, 1992. https://archive-ouverte.unige.ch//unige:38583

[109] E. L. Maxwell, "A quasi-physical model for converting hourly global horizontal to direct normal insolation," Solar Energy Research Institution, United States, Tech. Rep. SERI/TR-215-3087; ON: DE87012273, 1987. https://www.osti.gov/biblio/5987868

[110] M. De Simón-Martín, C. Alonso-Tristán, and M. Díez-Mediavilla, "Diffuse solar irradiance estimation on building's façades: Review, classification and benchmarking of 30 models under all sky conditions," *Renewable and Sustainable Energy Reviews*, vol. 77, pp. 783–802, Sep. 2017. doi: 10.1016/j.rser.2017.04.034. https://linkinghub.elsevier.com/retrieve/pii/S1364032117305312

[111] R. Perez, R. Seals, and J. Michalsky, "All-weather model for sky luminance distribution—Preliminary configuration and validation," *Solar Energy*, vol. 50, no. 3, pp. 235–245, Mar. 1993. doi: 10.1016/0038-092X(93)90017-I. https://linkinghub.elsevier.com/retrieve/pii/0038092X9390017I

[112] R. Perez, P. Ineichen, R. Seals, J. Michalsky, and R. Stewart, "Modeling daylight availability and irradiance components from direct and global irradiance," *Solar Energy*, vol. 44, no. 5, pp. 271–289, 1990. doi: 10.1016/0038-092X(90)90055-H. https://linkinghub.elsevier.com/retrieve/pii/0038092X9090055H

[113] M. F. Modest and S. Mazumder, "View Factors," in *Radiative Heat Transfer*. Elsevier, 2022, pp. 127–159. ISBN 978-0-323-98406-5. https://linkinghub.elsevier.com/retrieve/pii/B9780128181430000122

[114] J. Appelbaum, "The role of view factors in solar photovoltaic fields," *Renewable and Sustainable Energy Reviews*, vol. 81, pp. 161–171, Jan. 2018. doi: 10.1016/j.rser.2017.07.026. https://linkinghub.elsevier.com/retrieve/pii/S1364032117310924

[115] PVSyst, "PVSyst 7.4 Documentation," 2022. https://www.pvsyst.com/help/index.html?contents_table.htm

[116] N. R. E. Laboratory, "System Advisor Model Version 2022.11.21," https://https://sam.nrel.gov, Nov. 2022. https://https://sam.nrel.gov

[117] B. Marion, S. MacAlpine, C. Deline, A. Asgharzadeh, F. Toor, D. Riley, J. Stein, and C. Hansen, "A Practical Irradiance Model for Bifacial PV Modules," in *2017 IEEE 44th Photovoltaic Specialist Conference (PVSC)*. Washington, DC: IEEE, Jun. 2017. doi: 10.1109/PVSC.2017.8366263. ISBN 978-1-5090-5605-7 pp. 1537–1542. https://ieeexplore.ieee.org/document/8366263/

[118] U. A. Yusufoglu, T. H. Lee, T. M. Pletzer, A. Halm, L. J. Koduvelikulathu, C. Comparotto, R. Kopecek, and H. Kurz, "Simulation of Energy Production by Bifacial Modules with Revision of Ground Reflection," *Energy Procedia*, vol. 55, pp. 389–395, 2014. doi: 10.1016/j.egypro.2014.08.111. https://linkinghub.elsevier.com/retrieve/pii/S1876610214013368

[119] R. E. Cardose, "Irradiance simulation of PV system in urban environments," Master's thesis, Delft University of Technology, 2020.

[120] A. Russell, "A bifacial photovoltaic energy yield model with 3D shading: development, validation, and applications in tracked and mid-to-high latitude systems," Ph.D. dissertation, University of Ottawa, 2024.

[121] J. Arvo, "Backward ray tracing," *Developments in Ray Tracing, Computer Graphics, Proc. of ACM SIGGRAPH 86*, vol. Course Notes, pp. 259–263, 1986.

[122] S. Ayala Pelaez and C. Deline, "bifacial_radiance: a python package for modeling bifacial solar photovoltaic systems," *Journal of Open Source Software*, vol. 5, no. 50, p. 1865, Jun. 2020. doi: 10.21105/joss.01865. https://joss.theoj.org/papers/10.21105/joss.01865

[123] PVLighthouse, "SunSolve Yield," 2024. https://sunsolve.info/yield/features/advancedalgorithms/

[124] M. Alonso García and J. Balenzategui, "Estimation of photovoltaic module yearly temperature and performance based on Nominal Operation Cell Temperature calculations," *Renewable Energy*, vol. 29, no. 12, pp. 1997–2010, Oct. 2004. doi: 10.1016/j.renene.2004.03.010. https://linkinghub.elsevier.com/retrieve/pii/S0960148104001260

[125] D. Faiman, "Assessing the outdoor operating temperature of photovoltaic modules," *Progress in Photovoltaics: Research and Applications*, vol. 16, no. 4, pp. 307–315, Jun. 2008. doi: 10.1002/pip.813. https://onlinelibrary.wiley.com/doi/10.1002/pip.813

[126] D. King, W. E. Boyson, and J. Kratochvil, "Photovoltaic array performance model." Tech. Rep. SAND2004-3535, 919131, Aug. 2004. https://www.osti.gov/servlets/purl/919131/

[127] A. Dobos, "PVWatts Version 5 Manual," Tech. Rep. NREL/TP-6A20-62641, 1158421, Sep. 2014. http://www.osti.gov/servlets/purl/1158421/

[128] B. Meyers and M. Mikofski, "Accurate Modeling of Partially Shaded PV Arrays," in *2017 IEEE 44th Photovoltaic Specialist Conference (PVSC)*. Washington, DC: IEEE, Jun. 2017. doi: 10.1109/PVSC.2017.8521559. ISBN 978-1-5090-5605-7 pp. 3354–3359. https://ieeexplore.ieee.org/document/8521559/

[129] M. A. Mikofski, B. Meyers, and C. Chaudhari, "PVMismatch Project: https://github.com/SunPower/PVMismatch," GitHub, 2018. https://github.com/SunPower/PVMismatch

[130] W. De Soto, S. Klein, and W. Beckman, "Improvement and validation of a model for photovoltaic array performance," *Solar Energy*, vol. 80, no. 1, pp. 78–88, Jan. 2006. doi: 10.1016/j.solener.2005.06.010. https://linkinghub.elsevier.com/retrieve/pii/S0038092X05002410

[131] B. Marion, S. Rummel, and A. Anderberg, "Current–voltage curve translation by bilinear interpolation," *Progress in Photovoltaics: Research and Applications*, vol. 12, no. 8, pp. 593–607, Dec. 2004. doi: 10.1002/pip.551. https://onlinelibrary.wiley.com/doi/10.1002/pip.551

[132] M. Sengupta, Y. Xie, A. Lopez, A. Habte, G. Maclaurin, and J. Shelby, "The National Solar Radiation Data Base (NSRDB)," *Renewable and Sustainable*

Energy Reviews, vol. 89, pp. 51–60, Jun. 2018. doi: 10.1016/j.rser.2018.03.003. https://linkinghub.elsevier.com/retrieve/pii/S136403211830087X

[133] "NASA Earth Observations (NEO)." https://neo.gsfc.nasa.gov/

[134] K. S. Anderson, C. W. Hansen, W. F. Holmgren, A. R. Jensen, M. A. Mikofski, and A. Driesse, "pvlib python: 2023 project update," *Journal of Open Source Software*, vol. 8, no. 92, p. 5994, Dec. 2023. doi: 10.21105/joss.05994. https://joss.theoj.org/papers/10.21105/joss.05994

[135] S. Nann and C. Riordan, "Solar Spectral Irradiance under Clear and Cloudy Skies: Measurements and a Semiempirical Model," *Journal of Applied Meteorology*, vol. 30, no. 4, pp. 447–462, Apr. 1991. doi: 10.1175/1520-0450(1991)030¡0447:SSIUCA¿2.0.CO;2. http://journals.ametsoc.org/doi/10.1175/1520-0450(1991)030⟨0447:SSIUCA⟩2.0.CO;2

[136] "World of Change: Global Temperatures," Jan. 2020. https://earthobservatory.nasa.gov/world-of-change/global-temperatures#:~:text=According%20to%20an%20ongoing%20temperature,1.9%C2%B0%20Fahrenheit)%20since%201880.

[137] B. Marion, "Albedo Data Sets for Bifacial PV Systems," in *2020 47th IEEE Photovoltaic Specialists Conference (PVSC)*. Calgary, AB, Canada: IEEE, Jun. 2020. doi: 10.1109/PVSC45281.2020.9300470. ISBN 978-1-72816-115-0 pp. 0485–0489. https://ieeexplore.ieee.org/document/9300470/

[138] L. Dumitrascu and I. Beausoleil-Morrison, "A model for predicting the solar reflectivity of the ground that considers the effects of accumulating and melting snow," *Journal of Building Performance Simulation*, vol. 13, no. 3, pp. 334–346, May 2020. doi: 10.1080/19401493.2020.1728383. https://www.tandfonline.com/doi/full/10.1080/19401493.2020.1728383

[139] M. Brennan, A. Abramase, R. Andrews, and J. Pearce, "Effects of spectral albedo on solar photovoltaic devices," *Solar Energy Materials and Solar Cells*, vol. 124, pp. 111–116, May 2014. doi: 10.1016/j.solmat.2014.01.046. https://linkinghub.elsevier.com/retrieve/pii/S0927024814000658

[140] S. Solar, "The benefits of solar even in the dead of winter," Jan. 2023. https://silfabsolar.com/the-benefits-of-solar-even-in-the-dead-of-winter/

[141] A. Council, "Powered by nature: the Old Crow solar project," Dec. 2020. https://arctic-council.org/news/the-old-crow-solar-project/

[142] C. D. Rodríguez-Gallegos, M. Bieri, O. Gandhi, J. P. Singh, T. Reindl, and S. Panda, "Monofacial vs bifacial Si-based PV modules: Which one is more cost-effective?" *Solar Energy*, vol. 176, pp. 412–438, Dec. 2018. doi: 10.1016/j.solener.2018.10.012. https://linkinghub.elsevier.com/retrieve/pii/S0038092X18309915

[143] C. Pike, E. Whitney, M. Wilber, and J. S. Stein, "Field Performance of South-Facing and East-West Facing Bifacial Modules in the Arctic," *Energies*, vol. 14, no. 4, p. 1210, Feb. 2021. doi: 10.3390/en14041210. https://www.mdpi.com/1996-1073/14/4/1210

[144] M. Ito and E. Gerritsen, "Geographical mapping of the performance of vertically installed bifacial modules," *Proceedings of the European Photovoltaic Solar Energy Conference and Exhibition*, pp. 1–35, 2016.

[145] S. Guo, "Vertically mounted bifacial photovoltaic modules: A global analysis," *Energy*, vol. 61, pp. 447–454, 2013.

[146] S. Jouttijärvi, G. Lobaccaro, A. Kamppinen, and K. Miettunen, "Benefits of bifacial solar cells combined with low voltage power grids at high latitudes," *Renewable and Sustainable Energy Reviews*, vol. 161, p. 112354, Jun. 2022. doi: 10.1016/j.rser.2022.112354. https://linkinghub.elsevier.com/retrieve/pii/S1364032122002659

[147] M. R. Khan, A. Hanna, X. Sun, and M. A. Alam, "Vertical bifacial solar farms: Physics, design, and global optimization," *Applied Energy*, vol. 206, pp. 240–248, Nov. 2017. doi: 10.1016/j.apenergy.2017.08.042. https://linkinghub.elsevier.com/retrieve/pii/S0306261917310589

[148] S. Reker, J. Schneider, and C. Gerhards, "Integration of vertical solar power plants into a future German energy system," *Smart Energy*, vol. 7, p. 100083, Aug. 2022. doi: 10.1016/j.segy.2022.100083. https://linkinghub.elsevier.com/retrieve/pii/S2666955222000211

[149] S. Bhaduri and A. Kottantharayil, "Mitigation of Soiling by Vertical Mounting of Bifacial Modules," *IEEE JOURNAL OF PHOTOVOLTAICS*, vol. 9, no. 1, 2019.

[150] E. M. Tonita, A. C. Russell, C. E. Valdivia, and K. Hinzer, "Optimal ground coverage ratios for tracked, fixed-tilt, and vertical photovoltaic systems for latitudes up to 75°N," *Solar Energy*, vol. 258, pp. 8–15, Jul. 2023. doi: 10.1016/j.solener.2023.04.038. https://linkinghub.elsevier.com/retrieve/pii/S0038092X23002682

[151] L. Burnham, D. Riley, B. Walker, and J. M. Pearce, "Performance of Bifacial Photovoltaic Modules on a Dual-Axis Tracker in a High-Latitude, High-Albedo

Environment," in *2019 IEEE 46th Photovoltaic Specialists Conference (PVSC)*. Chicago, IL, USA: IEEE, Jun. 2019. doi: 10.1109/PVSC40753.2019.8980964. ISBN 978-1-72810-494-2 pp. 1320–1327. https://ieeexplore.ieee.org/document/8980964/

[152] K. S. Hayibo, A. Petsiuk, P. Mayville, L. Brown, and J. M. Pearce, "Monofacial vs bifacial solar photovoltaic systems in snowy environments," *Renewable Energy*, vol. 193, pp. 657–668, Jun. 2022. doi: 10.1016/j.renene.2022.05.050. https://linkinghub.elsevier.com/retrieve/pii/S0960148122006917

[153] A. Singh and D. Jones, "Snow Shedding properties of Bifacial PV Panels," in *2022 IEEE 49th Photovoltaics Specialists Conference (PVSC)*. Philadelphia, PA, USA: IEEE, Jun. 2022. doi: 10.1109/PVSC48317.2022.9938947. ISBN 978-1-72816-117-4 pp. 0646–0648. https://ieeexplore.ieee.org/document/9938947/

[154] E. M. Tonita, C. E. Valdivia, A. C. Russell, M. Martinez-Szewczyk, M. I. Bertoni, and K. Hinzer, "A general illumination method to predict bifacial photovoltaic system performance," *Joule*, vol. 7, no. 1, pp. 5–12, Jan. 2023. doi: 10.1016/j.joule.2022.12.005. https://linkinghub.elsevier.com/retrieve/pii/S2542435122005761

[155] R. W. Andrews and J. M. Pearce, "Prediction of energy effects on photovoltaic systems due to snowfall events," *Proceedings of the IEEE Photovoltaic Specialists Conference*, pp. 3386–3391, 2012.

[156] N. Heidari, J. Gwamuri, T. Townsend, and J. M. Pearce, "Impact of Snow and Ground Interference on Photovoltaic Electric System Performance," *IEEE Journal of Photovoltaics*, vol. 5, no. 6, pp. 1680–1685, 2015.

[157] I. Frimannslund, "Resolving snow challenges for increased deployment of photovoltaic systems," Ph.D. dissertation, Norwegian University of Life Sciences, 2022.

[158] D. Riley, L. Burnham, B. Walker, and J. M. Pearce, "Differences in Snow Shedding in Photovoltaic Systems with Framed and Frameless Modules," in *2019 IEEE 46th Photovoltaic Specialists Conference (PVSC)*. Chicago, IL, USA: IEEE, Jun. 2019. doi: 10.1109/PVSC40753.2019.8981389. ISBN 978-1-72810-494-2 pp. 0558–0561. https://ieeexplore.ieee.org/document/8981389/

[159] T. Tanahashi, T. Chiba, S. Adachi, Y. Tsuno, K. Ikeda, and T. Oozeki, "Mitigation of Heavy Snow Loads on PV Modules," *Proceedings of the High Latitude PV Workshop*, 2024.

[160] M. Lindh, "Snow loads and coatings," *Proceedings of the High Latitude PV Workshop*, 2024.

[161] A. Sinha, H. Gopalakrishna, A. Bala Subramaniyan, D. Jain, J. Oh, D. Jordan, and G. TamizhMani, "Prediction of Climate-Specific Degradation Rate for Photovoltaic Encapsulant Discoloration," *IEEE Journal of Photovoltaics*, vol. 10, no. 4, pp. 1093–1101, Jul. 2020. doi: 10.1109/JPHOTOV.2020.2989182. https://ieeexplore.ieee.org/document/9093139/

[162] A. Dhouib and S. Filali, "Operating temperatures of photovoltaic panels," in *Energy and the Environment*. Elsevier, 1990, pp. 494–498. ISBN 978-0-08-037539-7. https://linkinghub.elsevier.com/retrieve/pii/B9780080375397500855

[163] E. M. Tonita, C. E. Valdivia, M. Martinez-Szewczyk, M. R. Lewis, M. I. Bertoni, and K. Hinzer, "Effect of air mass on carrier losses in bifacial silicon heterojunction solar cells," *Solar Energy Materials and Solar Cells*, vol. 230, p. 111293, Sep. 2021. doi: 10.1016/j.solmat.2021.111293. https://linkinghub.elsevier.com/retrieve/pii/S0927024821003354

[164] M. Dhimish and A. Alrashidi, "Photovoltaic Degradation Rate Affected by Different Weather Conditions: A Case Study Based on PV Systems in the UK and Australia," *Electronics*, vol. 9, no. 4, p. 650, Apr. 2020. doi: 10.3390/electronics9040650. https://www.mdpi.com/2079-9292/9/4/650

[165] N. Bogdanski, W. Herrmann, F. Reil, M. Köhl, K.-A. Weiss, and M. Heck, "Results of 3 years' PV module weathering in various open-air climates," N. G. Dhere, J. H. Wohlgemuth, and K. Lynn, Eds., San Diego, California, Aug. 2010. doi: 10.1117/12.859807 p. 77730L. http://proceedings.spiedigitallibrary.org/proceeding.aspx?doi=10.1117/12.859807

[166] D. C. Jordan, K. Anderson, K. Perry, M. Muller, M. Deceglie, R. White, and C. Deline, "Photovoltaic fleet degradation insights," *Progress in Photovoltaics: Research and Applications*, vol. 30, no. 10, pp. 1166–1175, Oct. 2022. doi: 10.1002/pip.3566. https://onlinelibrary.wiley.com/doi/10.1002/pip.3566

[167] S. Lindig, D. Moser, A. J. Curran, and R. H. French, "Performance Loss Rates of PV systems of Task 13 database," in *2019 IEEE 46th Photovoltaic Specialists Conference (PVSC)*. Chicago, IL, USA: IEEE, Jun. 2019. doi: 10.1109/PVSC40753.2019.8980638. ISBN 978-1-72810-494-2 pp. 1363–1367. https://ieeexplore.ieee.org/document/8980638/

[168] D. C. Jordan, S. R. Kurtz, K. VanSant, and J. Newmiller, "Compendium of photovoltaic degradation rates," *Progress in Photovoltaics: Research and Applications*, vol. 24, no. 7, pp. 978–989, Jul. 2016. doi: 10.1002/pip.2744. https://onlinelibrary.wiley.com/doi/10.1002/pip.2744

[169] N. Matsui, C. N. Long, J. Augustine, D. Halliwell, T. Uttal, D. Longenecker, O. Niebergall, J. Wendell, and R. Albee, "Evaluation of Arctic broadband surface radiation measurements," *Atmospheric Measurement Techniques*, vol. 5, no. 2, pp. 429–438, Feb. 2012. doi: 10.5194/amt-5-429-2012. https://amt.copernicus.org/articles/5/429/2012/

[170] B. Babar, L. T. Luppino, T. Boström, and S. N. Anfinsen, "Random forest regression for improved mapping of solar irradiance at high latitudes," *Solar Energy*, vol. 198, pp. 81–92, Mar. 2020. doi: 10.1016/j.solener.2020.01.034. https://linkinghub.elsevier.com/retrieve/pii/S0038092X20300426

[171] H. N. Riise, M. M. Nygård, B. Aarseth, A. Dobler, and E. Berge, "Benchmark of modelled solar irradiance data at high latitude locations," *SSRN*, 2024. doi: http://dx.doi.org/10.2139/ssrn.4804004. http://dx.doi.org/10.2139/ssrn.4804004

[172] IRENA, "Session 2b: Solar power spatial planning techniques," 2014. https://www.irena.org/-/media/Files/IRENA/Agency/Events/2014/Jul/15/10_Solar_power_spatial_planning_techniques_Cairo_Egypt.pdf

[173] P. E. Campana, B. Stridh, S. Amaducci, and M. Colauzzi, "Optimisation of vertically mounted agrivoltaic systems," *Journal of Cleaner Production*, vol. 325, p. 129091, Nov. 2021. doi: 10.1016/j.jclepro.2021.129091. https://linkinghub.elsevier.com/retrieve/pii/S0959652621032807

Glossary

acceptor A dopant atom that when substituted into a semiconductor lattice forms a p-type region, such as boron and aluminium in a silicon lattice. 16, 17

albedo The broadband bi-hemispherical reflectance of a surface, with a value between 0 (completely absorptive) and 1 (completely reflective). 37, 67

AM0 Standard extraterrestrial solar spectrum. 36

AM1.5G Standard global terrestrial solar spectrum. 36

bandgap Forbidden energy gap between valence and conduction bands in a semiconductor or insulating material. 11

bifacial gain Gain in energy, power, or insolation of a bifacial compared to a monofacial photovoltaic device. 44

bifacial photovoltaics Photovoltaic devices which absorb light from both sides of the semiconductor p-n junction. 5, 43

bifaciality The ratio of rear efficiency to front efficiency under the same standard illumination conditions. This variable can also be reported for other I-V curve parameters. 44

blackbody radiator Absorbs all incident electromagnetic radiation, regardless of frequency or angle of incidence, and emits radiation according to Plank's Law. 35

Boltzmann approximation When the Fermi level is sufficiently far from the band edges, this approximation simplifies the Fermi-Dirac distribution function. 16

bypass diode A diode connected in parallel to a series of solar cells which provides an alternate path for current flow during shading scenarios where reverse biasing cells could cause reverse bias breakdown. 47

conduction band The electronic band which represents the lowest available vacant states at absolute zero. 11

conductivity A material property quantifying the ability of the material to conduct electric current. 18

conductor Materials with free electrons in the conduction band without external excitation. 11

continuity equations The equations that ensure electron and hole numbers are conserved. 24

covalent bond An atomic bond arising from the sharing of electrons, resulting in a lower energy state than the atoms separated. 12

Czochralski process A method for growing bulk semiconducting crystals using a seed crystal in a crucible. 12

dangling bonds An unsatisfied valence band state in an immobile atom, often occurring at the surface of semiconducting materials and causing higher local recombination rates. 23

depletion approximation The interface of a p-n junction is assumed to be fully depleted of charge carriers. 26

detailed balance limit The maximum theoretical photoconversion efficiency of a 1-junction solar cell under AM1.5G illumination where the only loss mechanism is radiative recombination. 33

diffusion current The movement of charge carriers due to diffusion from a concentration gradient. 19

direct bandgap A bandgap where the momentum between the valence and conduction band is the same. 13

donor A dopant atom that when substituted into a semiconductor lattice forms an n-type region, such as phosphorus and arsenic in a silicon lattice. 16

dopants The deliberate addition of an impurity to a semiconductor. 16

drift current The movement of charge carriers due to the presence of an external electric field. 19

effective mass A simplifying picture wherein electrons or holes move with different mass than their vacuum state mass, as influenced by their existence within an energy band structure. 14

electron affinity The amount of energy required to remove an electron entirely from a semiconducting material. 14

Fermi level The energy level of an electron where at thermodynamic equilibrium electrons have a 50% chance of occupation. 11

first Brillouin zone The primitive repeating cell of a crystalline structure in reciprocal space. 13

generation An electronic excitation event that increases the number of free charge carriers available to move within a semiconducting lattice. 20

indirect bandgap A bandgap where a momentum difference exists between the valence and conduction band. 13

insulator Materials with large zones of forbidden energy states (bandgap $>$3 eV) that result in a negligible density of charge carriers in the conduction band. 11

intrinsic semiconductor A perfect semiconducting material crystal without any impurities or dopants. 16

Lambertian surface A surface which reflects light equally over all hemisphere angles. 33

maximum power point The maximum power output by a solar cell as a function of voltage. 30

mobility A material property quantifying how quickly an electron can move in a material in the presence of an electric field. Units are often $cm^2/(Vs)$. 19

momentum space The Fourier Transform of position space, describing momentum vectors in a physical system. 12

monofacial Photovoltaic devices which absorb light from only one side of the semiconductor p-n junction. 5, 45

n-type semiconductor A semiconductor which has been doped to have higher relative concentration of electrons compared to holes. 17

open-circuit voltage The voltage where light and dark current cancel. 30

p-n junction Asymmetry provided by the interface of two differently doped semiconducting materials. 25

p-type semiconductor A semiconductor which has been doped to have higher relative concentration of holes compared to electrons. 17

parabolic band approximation Near the conduction or valence band edges, valleys can be approximated as parabolic, simplifying the mathematics involved with calculating quantities such as density of states, carrier concentrations, and carrier effective mass. 14

phonon Quantized lattice vibration. 13

photogeneration The process where the absorption of a photon results in the excitation of an electron from a lower energy state to a higher energy state. 20

photovoltaic effect The effect where a voltage or current is generated in a material under exposure to light. 10

quasi thermal equilibrium A quasi-equilibrium state that occurs from the thermodynamic balance of photoexcitation and relaxation. 17

recombination An event which results in the loss of electron excitation through the decay of an excited electron to a lower energy state. 20

semiconductor A class of materials exhibiting tunable electronic properties between that of conductors and insulators. 11

short-circuit current The current generated in a photovoltaic device at a voltage of zero. 28

snow loss Energy yield loss due to snow accumulation on PV modules. 72

spectral albedo The wavelength-dependent bidirectional hemispherical reflectance of a surface. 38

surface recombination velocity Describes the surface recombination of charge carriers per unit area per unit time, and relies on the movement of carriers from the bulk towards the surface. 23

thermalization The process where energy transferred from a photon to an excited electron is lost to lattice interactions, resulting in the electron energy relaxing to the band edge. 20

valence band The electronic band which represents the highest occupied states at absolute zero. 11